# Particle and data-driven approaches for reactive micrometric processes : application to CO2 mineral storage with uncertainty quantification.

Sarah Perez

UNIVERSITE DE PAU ET DES PAYS DE L'ADOUR

ECOLE DOCTORALE 211 SEA

SCIENCES EXACTES ET LEURS APPLICATIONS

Presented and defended on November 30th, 2023 by

Sarah PEREZ

to obtain the degree of

**PhD in Applied Mathematics**

of the University of Pau and Pays Adour (UPPA)

# Particle and data-driven approaches for reactive micrometric processes: application to $CO_2$ mineral storage with uncertainty quantification

## Evaluation board

| | | |
|---|---|---|
| Reviewers : | | |
| | Grégoire ALLAIRE | Professor at Ecole Polytechnique |
| | Philippe CHATELAIN | Professor at Université Catholique de Louvain |
| | Monica RIVA | Professor at Polytechnico di Milano |
| Examinators : | | |
| | Ivo F. SBALZARINI | Professor at TU Dresden & Max Planck Institute CBG |
| | Martin VOHRALÍK | Research Director at INRIA (EPC Serena) |
| President : | | |
| | Hélène BARUCQ | Research Director at INRIA (EPC Makutu) |
| PhD Advisor : | | |
| | Philippe PONCET | Professor at UPPA |

UNIVERSITÉ DE PAU ET DES PAYS DE L'ADOUR

e2s UPPA

energy environment solutions

## Particle and data-driven approaches for reactive micrometric processes: application to $CO_2$ mineral storage with uncertainty quantification


### Abstract:

Studying reactive flows in porous media is essential to manage the geochemical effects of $CO_2$ capture and storage in natural underground reservoirs. Through homogenization of the submicrometer porous medium and appropriate modeling, one can simulate the reactive processes occurring at the pore scale and predict their impact on the macro-scale properties, namely the macro-porosity and bulk permeability. Geochemical processes enable understanding of the mineral storage mechanisms, $CO_2$ interactions with the aquifer structure, and query reservoir safety. They encompass $CO_2$ mineral trapping due to carbonate precipitation and crystallization or dissolution of the surrounding porous environment associated with flow and transport mechanisms.

Direct Numerical Simulation (DNS) of reactive processes in intricate pore space geometries is challenging, as this requires efficient numerical methods that withstand multi-scale effects and strongly coupled Partial Differential Equation (PDE) systems. We adopt a semi-Lagrangian approach combining a particle description of the chemical transport equations with Eulerian formulation for the hydrodynamics. Flow modeling relies on a micro-continuum description of the medium, combined with a two-scale Darcy-Brinkman-Stokes formulation. The implementation benefits from an operator-splitting strategy and is provided in a hybrid CPU-GPU context. The numerical framework is improved to incorporate particle-based approximation on GPU devices of heterogeneous diffusion operators, which stems from Archie's law. This DNS method is used to investigate the effects of $CO_2$ mineral trapping through a novel two-step model for calcite crystallization.

However, ensuring reliable calibration of the PDE model parameters is crucial to provide suitable evolution of the macro-scale properties due to geochemical processes. This sometimes requires intuitive tuning of the model parameters to match laboratory experiments, especially considering the wide discrepancies observed in mineral reactivity and kinetic parameters in natural systems. Furthermore, the characterization of the 3D pore-scale geometries by X-ray microtomography (CT) is subject to measurement uncertainties and artifacts. These imaging limitations induce morphological biases, such as unresolved features and approximations in the micro-porosity acquisition, that require embedding uncertainty quantification (UQ). This aims to ensure reliable pore-scale modeling: quantifying the orders of magnitude of the deviations on the macro-scale properties becomes essential and establishes UQ methods as complementary partners to DNS.

In this direction, a direct approach based on asymptotic development analysis and slip-length formalism is developed to quantify the permeability deviation relying on unresolved roughness and approximated wall position. These deviations are computed from porous geometries derived from X-ray CT and provide uncertainty ranges at the macro-scale.

We address inverse problems for the microtomography of reactive flows in porous media introducing a novel data assimilation approach based on Artificial Intelligence tools. The objective is to combine a data-driven approach, based on dynamical experiments, with physics-based models to characterize the uncertainties in the micro-porosity field and kinetic parameters by observing the porous material dissolution.

For this purpose, we develop a novel deep learning strategy that robustly addresses physics-based and multitask Bayesian inference, assuming unknown priors on the measurement noise distribution and model adequacy. The Bayesian Physics-Informed Neural Network formulation, involving the PDEs of the model as tasks, has been investigated and a new method of automatic task balancing, computationally cost-free, is developed in this work. We finally apply this framework to reactive inverse problems in pore-scale imaging of calcite dissolution to quantify morphological and chemical uncertainties.

## Méthodes particulaires et approches supervisées par les données pour les processus micrométriques réactifs: application au stockage minéral du $CO_2$ avec quantification des incertitudes


**Résumé:**

L'étude des écoulements réactifs dans les milieux poreux est essentielle pour gérer les effets géochimiques de la capture et du stockage du $CO_2$ dans les réservoirs souterrains naturels. Grâce à l'homogénéisation du milieu poreux sub-micrométrique et une modélisation appropriée, on peut simuler les processus réactifs à l'échelle des pores et prédire leur impact sur les propriétés macroscopiques. Les processus géochimiques permettent de comprendre les mécanismes du stockage minéral du $CO_2$ et d'interroger la sécurité du réservoir. Ils englobent la capture minérale du $CO_2$ due à la précipitation et à la cristallisation de carbonates ainsi que la dissolution de l'environnement poreux environnant, associées aux mécanismes d'écoulement et de transport.

La Simulation Numérique Directe (DNS) des processus réactifs dans les géométries complexes de l'espace poreux est un défi, car nécessite des méthodes numériques efficaces capables de gérer les effets multi-échelles et systèmes d'Equations aux Dérivées Partielles (EDP) fortement couplées. On adopte une approche semi-Lagrangienne couplant une description particulaire des équations de transport chimique avec une formulation Eulérienne de l'hydrodynamique et utilisant une stratégie de splitting d'opérateurs. La modélisation de l'écoulement repose sur une description à deux échelles de Darcy-Brinkman-Stokes. Le cadre numérique est amélioré pour inclure une approximation particulaire des opérateurs de diffusion hétérogènes dans un contexte hybride CPU-GPU. On l'utilise pour étudier les effets de la capture minérale du $CO_2$ à travers un nouveau modèle en deux étapes pour la cristallisation de calcite.

Cependant, il est essentiel de garantir une calibration fiable des paramètres du modèle d'EDP pour obtenir une évolution adéquate des propriétés à l'échelle macro due aux processus géochimiques. Cela nécessite parfois un réglage intuitif des paramètres du modèle pour correspondre aux expériences, en particulier compte tenu des importantes disparités observées dans la réactivité minérale et les paramètres cinétiques dans les systèmes naturels. De plus, la caractérisation des géométries par micro-tomographie à rayons X est sujette à des incertitudes de mesure et à des artefacts. Ces limitations induisent des biais morphologiques, tels que des caractéristiques non résolues et des approximations dans l'acquisition de la microporosité, qui nécessitent de quantifier les incertitudes. Et ce, afin de garantir une modélisation fiable à l'échelle poreuse : estimer l'ordre de grandeur des écarts sur les macro propriétés devient essentiel.

Dans ce sens, une approche directe basée sur un développement asymptotique et un formalisme de longueur de glissement est développée pour quantifier les écarts de perméabilité dus à ces incertitudes morphologiques. Ces écarts sont calculés sur des géométries poreuses réelles et fournissent des plages d'incertitude à l'échelle macro.

Nous abordons des problèmes inverses pour la micro-tomographie des écoulements réactifs grâce à une nouvelle méthode d'assimilation de données basée sur des outils d'Intelligence Artificielle. L'objectif est de combiner une approche axée sur les données avec des modèles physiques pour mesurer les incertitudes sur le champ de microporosité et les paramètres cinétiques, en observant la dissolution du matériel.

À cette fin, une nouvelle stratégie d'apprentissage profond est développée, qui aborde de manière robuste l'inférence bayésienne multi-tâches basée sur la physique, en supposant des a priori inconnus sur la distribution du bruit de mesure et l'adéquation du modèle. La formulation de Réseau de Neurones Bayésien, impliquant les EPDs du modèle en tant que tâches, a été étudiée, et une nouvelle méthode d'équilibrage automatique des tâches est développée. On l'applique finalement à des problèmes inverses réactifs de dissolution de calcite pour quantifier les incertitudes morphologiques et chimiques.

*To my beloved parents,*
*and in loving memory of my grandfather*

## Acknowledgments

First and foremost, I would like to express my gratitude to Grégoire Allaire, Philippe Chatelain, and Monica Riva for their interest in this work and for agreeing to review this manuscript. Additionally, I would like to acknowledge Hélène Barucq, Ivo F. Sbalzarini, and Martin Vohralik for being part of my thesis committee.

I am particularly grateful to Ivo for providing me with the opportunity to visit the Max Planck Institute of Molecular Cell Biology and Genetics in Dresden, for hosting me in the MOSAIC group, and for his enthusiasm to initiate new collaborations, yet far from the life sciences and biological world. It has been three immersive months of incredible encounters and beneficial experiences in a stimulating environment.

I would like to extend special thanks to Surya for his enthusiasm towards our project, his guidance, and the insightful discussions we had during these three months and far beyond, despite our different time zones between Pau and his new position in New York.

I am also immensely grateful to Justina, Tina, Anastasia, Alexandra, Dominik, Juan, Lenny, Nandu, Hannes, Mateusz, Pietro, Aryaman, Abhinav, ... all the (un)official MOSAIC group. I really had the feeling of being part of an incredible, dynamic, and diverse family, both scientifically and humanely. I will never forget all the enjoyable moments spent together and your undeniable support in a difficult moment of my life. I am grateful and proud to be currently one piece of this MOSAIC. And I won't forget Katja for her absolute kindness and for still keeping a "Sarah's coffee cup" waiting for me.

I would also like to thank Didier and the whole France InterPore Chapter team for their confidence, enabling me to be the first doctoral representative within the FIC. I am deeply grateful for the opportunities to be involved in interesting initiatives, such as the organization of a Regional InterPore Workshop, the life of the savant society, and for having introduced me to the InterPore Young Academy.

In particular, I am immensely thankful to the Porous Media Tea Time Talks team, including Marcel, Mohammad, Catherine, Chiara, Nara, Federico, Kamal, Sang... for being such a cheerful, inspiring and motivating team. In addition to great scientists, I have met thoughtful and supportive people. You all rock!

I am also grateful to the members of the LMAP laboratory, those who have followed me as a student, and those who introduced me to the exciting world of Mathematics. Thanks to Jean-Matthieu, who has led me through my first steps within HySoP, and for his thoughtful advice. Thanks to Peter, Hannelore, and the DMEX team for the introduction to the microtomography technique, the valuable data, and the side discussions. Thanks to Clarisse for giving me the chance to be part of the CMI multi-disciplinary projects and to initiate part of our students to some of my research concerns.

I would also like to thank my PhD colleagues, present and past: those who warmly welcomed me in the office, those who advised me in my first steps of the doctoral journey, and with whom I had the opportunity to initiate enthusiastic debates. A special thought to Laurène, whose footsteps I followed, for her kindness and precious advice. Thank you all, the "Not Pisco" team, for being a great source of positivity in our office. I have made great friends, always willing to go dancing, swimming, play pool, and engage in various extra activities together. I am delighted to have shared these doctoral years with you.

Thanks to my friends, whether near or far, who have shown their support, those who were there before, those who stayed during, and those who will remain after.

I would not have enough words to express my gratitude to my loving parents for their unwavering support at every step of my life, for being an endless source of energy during tough times, and for their unbounded trust and love. I also want to thank my dear grandparents, who have followed my adventures with overflowing enthusiasm and love. I would have a thought for my grandfather, who did not live to see the end and for whom a single glance was worth a thousand words.

Last but not least, I am also immensely grateful to Philippe for his guidance to and throughout my doctoral years, his enthusiastic involvement, his support, and his human qualities, including his patience, benevolence, and dedication. These are some of the reasons why it is a great pleasure to work with such a committed researcher, and I consider myself fortunate to have had such a dedicated thesis advisor.

To those who wonder, this is not the end, just the start of a new chapter.

# Contents

# List of Acronyms

# Résumé développé en français

## Méthodes particulaires et approches supervisées par les données pour les processus micrométriques réactifs: application au stockage minéral du $CO_2$ avec quantification des incertitudes

Cette thèse s'inscrit dans l'étude des écoulements réactifs dans les milieux poreux micrométriques et s'intéresse, plus particulièrement, aux problématiques de fiabilisation des modèles mathématiques à l'échelle des pores et à la quantification des incertitudes qui y sont reliées.

**Contexte général:**

Dans le contexte environnemental actuel et face à l'urgence de réduire les émissions de gaz à effet de serre, le stockage du $CO_2$ dans les réservoirs souterrains naturels a émergé comme une alternative prometteuse pour atténuer l'impact carbone [33]. L'analyse des différents mécanismes géochimiques impliqués dans ce procédé et l'étude de leurs effets sur la structure poreuse du réservoir reste un défi majeur pour prédire le comportement à long terme et ainsi assurer un stockage perenne et efficace. Entre autres, les enjeux concernent, d'une part, l'évaluation des capacités de stockage, liées aux phénomènes de capture minérale du $CO_2$ sous forme de précipitation et de cristallisation, et d'autre part, les problématiques liées à l'altération de la structure par érosion acide et dissolution.

La modélisation mathématique des différents procédés géochimiques et mécanismes de piégeage est alors considérée pour réaliser des simulations numériques directes à l'échelle du réservoir [81]. Ces dernières nécessitent une description de la formation poreuse, sur plusieurs dizaine de kilomètres, en terme de propriétés macroscopiques telles que des distributions spatiales de macro-porosité $\phi$ et de macro-permeabilité $\kappa_0$. L'avantage de telles prédictions à grande échelle réside dans une représentativité du comportement global du réservoir. Cependant, la disponibilité des descriptions macroscopiques de la structure poreuse demeure un sujet de préoccupation qui a conduit à l'émergence de questionnements quant à la fiabilité de ces prédictions. En ce sens, les études de sensibilité en terme de structure macroscopique, résultant d'écarts dans les estimations de macro-perméabilité et macro-porosité, semblent primordiales pour assurer une gestion raisonnée du stockage du $CO_2$ dans les réservoirs naturels [138, 195].

Parallèlement, les procédés réactifs découlant de la capture et du stockage du $CO_2$ impliquent des intéractions locales avec le milieu poreux pour lesquelles l'échelle des pores demeure une échelle d'étude pertinente [232, 280]. A cette échelle micrométrique, un volume représentatif élémentaire du milieu poreux, issu par exemple d'une carotte de roche, est considéré et sa géométrie 3D complexe est explicitement décrite. Les propriétés intrinsèques au milieu sont définies localement en termes de micro-porosité $\varepsilon$ et micro-permeabilité $K_\varepsilon$, où $\varepsilon := \varepsilon_f = 1-\varepsilon_s$ avec $\varepsilon_f$ et $\varepsilon_s$ les fractions volumiques locales d'espace vide et solide, respectivement (voir Figure 1.1 page 3). Le passage à l'échelle, aussi appelé homogénéisation ou upscaling, assure la transition des propriétés microscopiques hétérogènes ($\varepsilon$ et $K_\varepsilon$) vers une modélisation homogène des macro-propriétés ($\phi$ et $\kappa_0$) du volume représentatif [250, 251]. En ce sens, l'étude des processus réactifs à l'échelle des pores fournissent, par homogénéisation, une évolution des propriétés à l'échelle macroscopique due aux mécanismes géochimique du stockage du $CO_2$.

L'échantillon 3D micrométrique est analysé par micro-tomographie à rayons X ($\mu$CT), qui est un procédé d'imagerie fournissant une cartographie initiale du milieu poreux en terme de niveau de gris [23, 24]. Ces derniers caractérisent la densité locale du matériau et par extension le champ de micro-porosité $\varepsilon$, jusqu'à une résolution d'un voxel *i.e.* d'un pixel volumique (voir Figure 1.3 page 6). La $\mu$CT permet ainsi de décrire de manière non-destructive la géométrie locale de l'échantillon poreux, et est ensuite combinée à des modèles mathématiques et simulations numériques à l'échelle des pores [204, 220]. Cette échelle d'observation établit ainsi une complémentarité significative entre les expériences réalisées en laboratoire et la modélisation mathématique, ce qui lui confère un avantage notable dans le contexte des applications en géosciences.

**Motivation et objectifs:**
Des limitations sont en prendre en compte découlant d'incertitudes morphologiques issues du procédé de micro-tomographie, mais aussi d'incertitudes de modélisation dans les modèles réactifs à l'échelle des pores.

D'une part, plusieurs artefacts d'imagerie perturbent la description de la morphologie de l'espace poreux, et par conséquent, la détermination des propriétés effectives du milieu qui en découlent. En effet, la résolution finie des scans de $\mu$CT génère des incertitudes géométriques tant au niveau de la caractérisation des interfaces de pores, qui peuvent apparaître floues dû à des changement d'intensités progressifs s'étendant sur plusieurs voxels, qu'en terme d'hétérogénéités de petites tailles présentes au sein d'un même voxel (voir Figure 1.3 page 6). Ce dernier phénomène, connu sous le nom d'effet de volume partiel [214], résulte d'un compromis entre le volume d'échantillon étudié qui se doit d'être suffisamment large pour être représentatif et la résolution des scans de $\mu$CT, qui se doit d'être suffisamment fine pour capter les différentes échelles de pores. Il en résulte une micro-porosité ou une rugosité des parois de l'espace poreux non résolues et par conséquent une approximation de la véritable morphologie de sorte que l'on considère une borne inférieure sur le champ de porosité avec $\varepsilon(x,t) \geq \varepsilon_0 > 0$. Quantifier la porosité sous-résolue $\varepsilon_0$ et mesurer son impact sur la modélisation numérique et la simulation à l'échelle des pores demeure un enjeu en terme de fiabilisation des modèles prédictifs basés sur les données de micro-tomographie [69, 172].

D'autre part, l'étalonnage des modèles mathématiques en terme de calibration des paramètres cinétiques pose un second défi, notamment si l'on considère les écarts significatifs dans les gammes de réactivités minérales rencontrées dans la littérature [217]. Ces derniers génèrent des incertitudes considérables dans l'estimation des taux de réactions dans les modèles d'EDP, mettant en évidence la nécessité de prendre en compte ces incertitudes de modélisation. L'objectif est alors de fournir des intervalles de confiance robustes sur les paramètres cinétiques par des problèmes inverses dans un cadre Bayésien et ce afin d'assurer un étalonnage fiable des modèles réactifs.

Cette thèse aborde les deux considérations précédentes et incorpore les préoccupations liées à la quantification des incertitudes dans le contexte de la modélisation à l'échelle des pores pour des applications reliées au stockage minéral du $CO_2$. Les divers niveaux d'incertitudes sont traités dans les différents chapitres du manuscrit et incluent:

- la modélisation et la simulation numérique directe du mécanisme de capture minérale par précipitation et cristallisation, assumant des incertitudes morphologiques et de modélisation minimales (Chapitre 2),

- la quantification des déviations de macro-perméabilité $\kappa_0$ induite par les incertitudes d'imagerie purement morphologiques et basée sur une approche déterministe découlant de la théorie mathématique de l'upscaling (Chapitre 3),

- le développement d'une méthodologie robuste d'apprentissage profond pour l'assimilation de données et les problèmes inverses incorporant des incertitudes inconnues de modélisation potentiellement couplées à des incertitudes de mesures (Chapitre 4),

- l'étude de problèmes inverses de dissolution permettant une estimation conjointe des incertitudes géométrique sur le champ de micro-porosité $\varepsilon$ (incluant la porosité sous-résolue $\varepsilon_0$) et des gammes de paramètres cinétiques du modèle réactif (Chapitre 5).

**Contributions:**
Le développement de modèles mathématiques appropriés et d'une méthode numérique efficace pour l'étude des écoulements réactifs à l'échelle des pores est l'une des préoccupations de cette thèse, avec un accent porté sur la précipitation et la cristallisation de carbonates qui assurent un piégeage minéral du $CO_2$ en milieu basique. Ces processus ont un impact significatif sur l'écoulement à l'échelle des pores, entraînant une restructuration des trajets d'écoulement et des changements morphologiques qui altèrent, entre autres, la distribution de la taille des pores et la

rugosité de l'interface en raison d'un colmatage partiel ou complet de l'espace des pores. Ces altérations à l'échelle microscopique influent, par la suite, sur l'estimation des propriétés à l'échelle macroscopique.

La modélisation de ce phénomène de capture minérale combine un modèle pour l'hydrodymamique de type Darcy-Brinkman-Stokes, basé sur le formalisme de vitesse superficielle introduite par Quintard et Whitaker dans les années 1980 [250, 251] et introduisant une description à deux échelles du milieu, avec un système de convection-diffusion-réaction pour les intéractions chimiques (Section 2.3 Chapitre 2). En particulier, un nouveau modèle de cristallisation de calcite est proposé, décomposant le processus chimique en deux étapes: une première étape déterministe de nucléation initiale utilisant la théorie de l'état de transition et formant des précipités de calcite qui seront transportés dans l'espace des pores, et une deuxième étape probabiliste d'agrégation de ces nuclei à la surface minérale sous la forme d'une réaction chimique d'autocatalyse. Cette deuxième étape introduit une probabilité non-uniforme du taux d'attachement du précipité à l'interface en fonction d'une fréquence d'adsorption et de la fraction volumique locale du minéral, impliquant une convolution à support compact de la micro-porosité (Section 2.7.2 Chapitre 2). Ce modèle intègre ainsi la dépendance géométrique du milieu poreux en adoptant une formulation volumique de la croissance des cristaux de calcite dans des zones préférentielles situées dans un voisinage fluide de la surface du minéral.

Une approche numérique hybride, dite Semi-Lagrangienne, est utilisée couplant une formulation particulaire de la chimie avec des méthodes Eulériennes pour la résolution de l'hydrodynamique sur une grille sous-jacente (Section 2.4 Chapitre 2). En particulier, l'équation de Darcy-Brinkman-Stokes assure une pénalisation de la matrice poreuse en introduisant la micro-perméabilité $K_\varepsilon$, explicitement reliée à la micro-porosité $\varepsilon$ par la loi empirique de Kozeny-Carman (équation 2.2 page 25). De plus, cette équation est résolue dans une formulation vitesse-tourbillon qui garantit la condition d'incompressibilité du fluide. L'approche Lagrangienne, quant à elle, présente un avantage significatif pour modéliser les phénomènes de transport des espèces chimiques, mais aussi dans l'approximation, par une méthode de noyau intégral dite Particle-Strength-Exchange (PSE), des termes de diffusion hétérogène issus de la loi d'Archie (Section 2.5.3 Chapitre 2). Ces derniers tiennent compte d'une diffusion réduite des espèces chimiques dans la matrice poreuse, assurant un meilleur contrôle de la diffusion à l'interface, sous certaines contraintes de stabilités (Section 2.5.4 Chapitre 2). L'ensemble est intégré au sein d'une bibliothèque de calcul haute performance, dénommée HySoP [112], qui fournit un cadre efficace pour la modélisation de l'hydrodynamique réactive en utilisant des méthodes Semi-Lagrangiennes sur des configurations matérielles hybrides. En particulier, une des contributions de cette thèse consiste en l'implémentation pérenne d'une méthode PSE pour l'approximation des opérateurs de diffusion hétérogènes sur des accélérateurs GPU. L'implémentation de la méthode numérique est ainsi réalisée dans un contexte hybride combinant l'utilisation de CPU et GPU.

Cette approche est, finalement, appliquée à la modélisation de capture minérale du $CO_2$ sous la forme de cristallisation de calcite au sein de géométries issues de micro-tomographie à rayons X. Nous identifions des effets de colmatage des pores dans la géométrie à l'échelle des pores et établissons leur impact sur l'évolution des propriétés macroscopiques (Figure 2.9 page 53). En particulier, nous démontrons l'effet significatif de l'agrégation des cristaux, *i.e.* de l'adsorption des noyaux à la surface minérale, sur les formes de réactions. Il a été mis en évidence que considérer uniquement les taux de transport et de nucléation, à travers les nombres sans dimension de Péclet et Damköhler usuels, n'est pas suffisant pour caractériser le colmatage des pores (Figure 2.10 page 54). Dans ce sens, nous proposons une nouvelle caractérisation des régimes de cristallisation basée sur l'analyse conjointe de trois nombres sans dimension (équations 2.73 page 51), ce qui permet de prendre en compte les taux d'adsorption des noyaux dans la caractérisation des différents régimes.

Dans un second temps, cette thèse s'intéresse à la caractérisation des déviations induites par les incertitudes morphologiques issues de l'imagerie $\mu$CT. L'objectif est de garantir des évolutions fiables des propriétés à l'échelle macroscopique, résultant des réactions chimiques à l'échelle des

pores, en assurant une quantification des biais d'imagerie. Une première approche déterministe est proposée pour l'étude des déviations de macro-perméabilité $\kappa_0$ et prend en compte les incertitudes morphologiques, telles que la rugosité sous-résolue et l'approximation de la position de l'interface, sous la forme de condition aux limites effective. Un formalisme de longueur de glissement $\beta$ est utilisé et nous proposons deux stratégies pour analyser en pratique les déviations de perméabilités en géométries réelles (Section 3.3.1 Chapitre 3).

La première vise directement à résoudre un écoulement de Stokes dans l'espace poreux avec des conditions aux limites de Navier caractérisées par une longueur de glissement $\beta$ prescrite à l'interface fluide/solide. Il en résulte une estimation de la perméabilité $\kappa_\beta$, utilisée pour estimer la plage d'incertitude $[\kappa_0, \kappa_\beta]$. La deuxième établit théoriquement la déviation de perméabilité comme une extension de $\kappa_\beta$ par des termes de correction de glissement du premier et du deuxième ordre, respectivement notés $L_0$ et $L_1$ et issus de la résolution de problèmes de Stokes à des ordres successifs. Ces problèmes successifs sont déterminés par une méthode de développement asymptotique et impliquent des conditions aux limites de type Dirichlet non homogènes, dépendant directement de la solution du problème de Stokes d'ordre inférieur (Section 3.4 Chapitre 3). On obtient ainsi des gammes de perméabilité basées sur les déviations d'ordre 1 ou 2, respectivement données par les intervalles $[\kappa_0, \kappa_0 + \beta L_0]$ et $[\kappa_0, \kappa_0 + \beta L_0 + \frac{\beta^2}{2} L_1]$.

L'estimation de la longueur de glissement caractéristique est reliée à la taille d'un voxel $h$, avec $0 < \beta \leqslant h$, en fonction de l'incertitude associée au niveau de gris et, par conséquent, de la fraction volumique résiduelle $\varepsilon_0$ dans une zone supposée solide (Section 3.6.1 Chapitre 3). Plusieurs échantillons poreux 3D sont analysés numériquement pour fournir une estimation des plages d'incertitude sur la perméabilité et nous comparons les déviations linéaires du premier ordre $\kappa_0 + \beta L_0$ avec la déviation de perméabilité globale $\kappa_\beta$ (Section 3.7.1 Chapitre 3). D'une part, nous identifions un rapport sans dimension (équation 3.53 page 87) dépendant de la déviation relative de la perméabilité et de la surface spécifique, susceptible de servir de critère de représentativité pour les échantillons poreux. D'autre part, nous observons des effets non-linéaires dans les estimations de premier ordre, résultant de l'extension de $\kappa_\beta$, ce qui nous a amené à considérer la déviation d'ordre deux (Section 3.7.2 Chapitre 3). Ces résultats soulignent, en particulier, la pertinence de la déviation du deuxième ordre pour expliquer les effets macroscopiques apparents sur la perméabilité dans les géométries réelles. Ainsi, nous fournissons un cadre numérique pertinent pour étudier les écarts de perméabilité générés par les incertitudes d'imagerie dans des échantillons poreux de $\mu$CT, ce qui permet d'interroger la fiabilité de leurs évolutions au cours d'un procédé réactif.

Cependant, les préoccupations concernant les incertitudes de modélisation, en particulier reliée à l'estimation d'intervalle de confiance sur les paramètres réactifs, ainsi les incertitudes morphologique sur le champ de micro-porosité persistent. L'idée développée dans cette thèse est, alors, de considérer un processus dynamique pour fournir une description locale, précise et robuste, des matériaux poreux en observant leur dissolution à travers des expériences dynamiques de $\mu$CT. Il en résulte une assimilation de données en 4D (3D+temps) dont l'objectif est à la fois de combiner un modèle d'écoulement réactif a-priori, ayant des paramètres cinétiques inconnus, avec des données imparfaites et bruitées d'imageries issues du processus dynamique de dissolution. Ceci permet d'explorer de manière conjointe les incertitudes morphologiques dues à la micro-porosité sous résolue $\varepsilon_0$, en particulier au sein du milieu poreux initial, ainsi que le problème inverse de détermination des paramètres du modèle avec leurs incertitudes (Chapitre 5). En ce sens, il est donc apparu nécessaire de développer une méthodologie dédiée permettant d'aborder les incertitudes de modélisation dans un contexte d'assimilation de données et de problème inverse.

Nous proposons une approche basée sur les réseaux de neurones informés par la physique dans un contexte Bayésien, communément appelée B-PINN [173, 328], qui tient compte de manière robuste des considérations multi-tâches et multi-échelles pour les problèmes d'inférence Bayésienne couplant principes physiques et données (Chapitre 4). L'objectif est d'échantillonner à l'aide d'un processus de Markov la distribution cible a-posteriori, notée $\mathcal{P}(\Theta|\mathcal{D}, \mathcal{M})$, d'un ensemble

de paramètres $\Theta$ (paramètres du réseau de neurones et paramètres inverses) qui sont vus comme des variables aléatoires ayant des distributions a-priori $\mathcal{P}(\Theta)$. La distribution cible se décompose, alors, suivant la règle de Bayes $\mathcal{P}(\Theta|\mathcal{D},\mathcal{M}) \propto \mathcal{P}(\mathcal{D}|\Theta)\mathcal{P}(\mathcal{M}|\Theta)\mathcal{P}(\Theta)$ introduisant des termes stochastiques de vraisemblance aux données $\mathcal{D}$ et d'adéquation au modèle $\mathcal{M}$, pondérés par leurs incertitudes respectives. L'échantillonnage est assuré par une méthode de Monte Carlo Hamiltonienne qui offre des propriétés de mise à l'échelle efficaces pour des problèmes d'inférence en haute dimension, ce qui est essentiel dans le cadre des B-PINN [48].

Néanmoins, cet échantillonneur introduit une énergie potentielle $U(\Theta)$ qui est directement reliée à la distribution cible par la relation $U(\Theta) = -\ln\mathcal{P}(\Theta|\mathcal{D},\mathcal{M})$. Il en résulte une expression pondérée et multi-objectifs de l'énergie potentielle pour laquelle garantir une inférence Bayésienne robuste repose sur une estimation correcte des poids des différentes tâches, intégrant les différentes sources d'incertitudes. En particulier, une pondération inadéquate dans des problèmes impliquant des tâches conflictuelles ou des préoccupations multi-échelle favorisera, a fortiori, le sur-entrainement ou sous-entrainement de certains termes et générera un échantillonnage biaisé.

Dans cette thèse, une nouvelle formulation de la méthode de Monte-Carlo Hamiltonien est donc proposée, avec une pondération automatique et adaptative de la distribution a-posteriori basée sur l'exploitation des variances de gradient des différentes tâches (Section 4.4.1 Chapitre 4). Cela permet de concentrer, après la procédure d'adaptation, l'échantillonnage sur l'exploration du front de Pareto et évite ainsi le déséquilibre entre les tâches tout en garantissant un coût de calcul raisonnable, allant dans le sens de la sobriété énergétique des méthodes d'apprentissage profond. Notre approche, appelée AW-HMC, bénéficie d'une convergence et d'une stabilité accrues par rapport aux échantillonneurs conventionnels et réduit le biais d'échantillonnage en évitant le réglage manuel des paramètres de pondération critiques. Cette nouvelle alternative a également démontré son efficacité dans la gestion de la sensibilité à l'échelle des différents termes, que ce soit par rapport aux distributions de bruit ou aux problèmes multi-échelles (respectivement Sections 4.6.1 et 4.5 Chapitre 4). En effet, les poids ainsi adaptés fournissent des informations intrinsèques sur les incertitudes des tâches distinctes. Cela améliore la fiabilité des estimations liées au bruit et à l'adéquation du modèle, car les incertitudes sont quantifiées avec un minimum d'hypothèses a-priori sur leur échelle.

Dans une perspective globale d'Intelligence Artificielle (IA), cette thèse démontre la nécessité et l'efficacité du développement d'une stratégie de pondération adaptative qui renforce la robustesse des BPINNs et offre ainsi une alternative prometteuse en tant que stratégie globale d'assimilation de données. Cela permet d'étendre les applications des BPINNs à des problèmes d'inférence complexes et d'obtenir une inférence Bayésienne fiable dans des problèmes inverses multi-tâches du monde réel.

En particulier, nous utilisons cette nouvelle stratégie pour aborder des problèmes inverses réactifs intégrant la quantification des incertitudes, comme évoqué précédemment. Nous examinons une formulation multi-tâche des problèmes inverses de dissolution de calcite et établissons une méthode de renforcement séquentiel qui incorpore successivement les contraintes du système d'EDP dans le procédé d'assimilation de données (Section 5.5 Chapitre 5). En complément de l'estimation de l'incertitude morphologique sur le champ de micro-porosité $\varepsilon$, nous caractérisons les taux de réaction expérimentaux et les régimes de dissolution en identifiant les nombres sans dimension appropriés (Section 5.4 Chapitre 5). Par conséquent, nous dérivons des plages d'incertitude sur les paramètres cinétiques en combinant des modèles d'EDP prescrits et des expériences de dissolution, ce qui rend fiable l'étalonnage des taux de réaction pour les simulations numériques directes. Cela évite également d'utiliser des paramètres réactifs estimés uniquement à partir d'expériences en laboratoire, qui peuvent ne pas être représentatifs de la dynamique à l'échelle des pores ou être sujets à de larges incertitudes. Nous appliquons cette méthodologie à des problèmes de dissolution de noyau de calcite en 1D+Temps et 2D+Temps basés sur des images de $\mu$CT synthétiques, bruitées et présentant des niveaux de micro-porosité variables (Sections 5.6 et 5.7 Chapitre 5). Finalement, nous estimons à partir de la dynamique de dissolution des intervalles de confiance sur la micro-porosité sous-résolue $\varepsilon_0$, et des incertitudes locales sur le champ

$\varepsilon$ qui peuvent ensuite se traduire par des distributions sur la macro-porosité $\phi$ à l'échelle de Darcy.

Comparé aux alternatives d'IA en géosciences, la principale nouveauté de ce travail, en ce qui concerne les problèmes inverses réactifs du dernier Chapitre 5, réside dans l'évaluation robuste des incertitudes liées aux caractéristiques morphologiques non résolues et à la réactivité minérale en intégrant des modèles basés sur la physique avec des techniques d'assimilation de données. Dans cette perspective, cela offre une compréhension plus approfondie de la relation entre les données expérimentales et la théorie de la modélisation mathématique à l'échelle des pores. A terme, nous pourrions accroître la fiabilité des approches de simulation numérique directe pour la modélisation du stockage de $CO_2$, en proposant des distributions réalistes des macro-propriétés $\phi$ et $\kappa_0$. Ces distributions pourraient ainsi être exploitées dans des analyses de sensibilité menées à une large échelle et s'appuyant sur une estimation des incertitudes à l'échelle des pores.

CHAPTER 1

# Introduction

## Contents



## 1.1 General context and motivation

### 1.1.1 $CO_2$ mineral storage

Current concerns about climate change have raised an urgent need to develop efficient solutions for sustainable and low-carbon alternative energy sources. Meanwhile, emissions of greenhouse gases and their release into the atmosphere have emerged as one of the most significant aspects of managing environmental issues. In 2021, the International Energy Agency (IEA), which regularly provides official and public data on energy-related topics, published a report projecting scenarios to achieve carbon neutrality by 2050. The latter, entitled "Net Zero Emission by 2050: A Roadmap for the Global Energy Sector" [136], established the critical need to reduce the concentration of carbon dioxide ($CO_2$) released into the atmosphere as part of an overall ecological transition. By 2030, it is estimated that net-zero emissions will require 1.6 gigatons (Gt) of captured $CO_2$ per year, reaching 7.6 Gt of annual storage by 2050 to cope with the increasingly severe rise of emissions. Indeed, the IEA reported 2021 as the year with the highest increase in global $CO_2$ emission, facing a jump of 1.9 Gt for the energy sector. This resulted in total emissions of 36.6 Gt $CO_2$, and the predictive trends are not declining.

The idea of carbon sequestration in natural formations has consequently appeared as a viable and promising strategy to facilitate the elimination of excess $CO_2$ from the atmosphere, reduce the carbon footprint, and mitigate its impact on global warming. Over the past decades, extensive studies have been conducted on these crucial environmental solutions involving, *inter alia*, $CO_2$ mineral storage [7, 70, 81, 196]. Such a research field aims to understand and predict long-term carbon sequestration in underground geological reservoirs, often referred to as Carbon Capture

and Storage (CCS) or Carbon Capture, Use and Storage (CCUS) technologies. The geological structures involved in this sequestration process are of a wide variety and currently range from depleted oil or gas reservoirs to coal seams and deep saline aquifers. Depending on the kind of sink formations, the main features commonly discussed include the geological storage assessment and trapping capabilities, although safety likewise raises sensitive issues. Overall, suitable sites should be equipped with an impermeable cap rock to prevent $CO_2$ leakage, unlike the porous environment of the reservoir should present high porosity and permeability to ensure efficient storage and high injection capacity. In this regard, saline aquifers offer ideal sequestration sites with a broad geographical distribution and a promising potential to store up to several thousand Gt of $CO_2$ [33, 181].

Saline reservoirs generally consist of heterogeneous porous media, like sandstones and limestones, saturated with salty water that occupies the pore space (or void space) delimited by the rock matrix. Regarding carbon sequestration in these geological structures, multiple physical and chemical mechanisms occur, requiring consideration of a range of simultaneous factors. For instance, part of the injected $CO_2$ will migrate upward, due to its density difference with the saline fluid, and become trapped by the low-permeability cap rock: this is known as structural or physical trapping. Other parts will dissolve in the aqueous phase leading to permanent solubility trapping, and interact with the chemical environment of the brine and the reservoir rocks. Such reactions will eventually result in solid carbonate precipitation, also called $CO_2$ mineral trapping, occurring at various time scales. Finally, supercritical $CO_2$ can also be trapped in the aquifer pore spaces as droplets through the physical effect of capillary trapping. Studying the previous trapping effects is a major concern of $CO_2$ storage in natural reservoirs. Another critical aspect of $CO_2$ mineral storage lies in safety issues in the sense that dissolution of the carbonate species already present in the aquifer, due to an acidification of the medium, may compromise the cap rock integrity. In addition to the previous mechanisms, the underlying physic usually falls within the framework of multi-component, multi-phase flows, coupled with geochemical and thermal effects. The study of the overall system in these porous environments is thereby challenging as it suffers from non-linearity, high complexity of the fluid-rock interactions, and involves multiple phenomena.

Understanding the impact of $CO_2$ sequestration on the reservoir's intrinsic properties, as well as its interactions within the geological sinks, is essential for predicting long-term behaviors and wisely managing storage potential. To meet such requirements, research is conducted in a complementary way on laboratory experiments, mathematical modeling, and numerical simulations of the related hydro-chemical processes. On the one hand, *in situ* experiments offer the opportunity to study these phenomena under reservoir conditions, with high pressure and temperature constraints, and provide comprehensive baselines for comparison or validation [20, 317]. For example, this enables the characterization of structural and petrophysical changes during chemical reactions, reaction rate assessment, and stress management in real-world conditions. On the other hand, numerical simulations rely on appropriate mathematical models derived from physical principles to abstract complex natural behaviors. They intend to generate long-term predictions and benchmarks, which are of key importance for reservoir risk management and efficiency [168, 225]. Nonetheless, the challenge remains to implement appropriate modeling hypotheses and to establish their sufficiency to explain the overall mechanisms. And, mathematical-based models remain intrinsically related to experiments in the sense experimental data can be either used for posterior validations or prior identifications of physical parameters. These two lines of research have, therefore, emerged as complementary approaches for a wide range of real-world applications in geosciences.

At an applicative level, this thesis investigates, on the one hand, the ability to compute and predict the trapping process of $CO_2$ into calcite in an alkaline medium and, on the other hand, the characterization, stability, and alteration of calcite due to acidic erosion and dissolution. In this spirit, we especially explore the relationship between laboratory experiments and mathematical modeling theory. This thesis has been conducted at the Laboratory of Mathematics and their Applications of Pau (LMAP, UMR CNRS 5142, UPPA), in the context of the I-Site project E2S-UPPA Energy, Environment and Solutions.

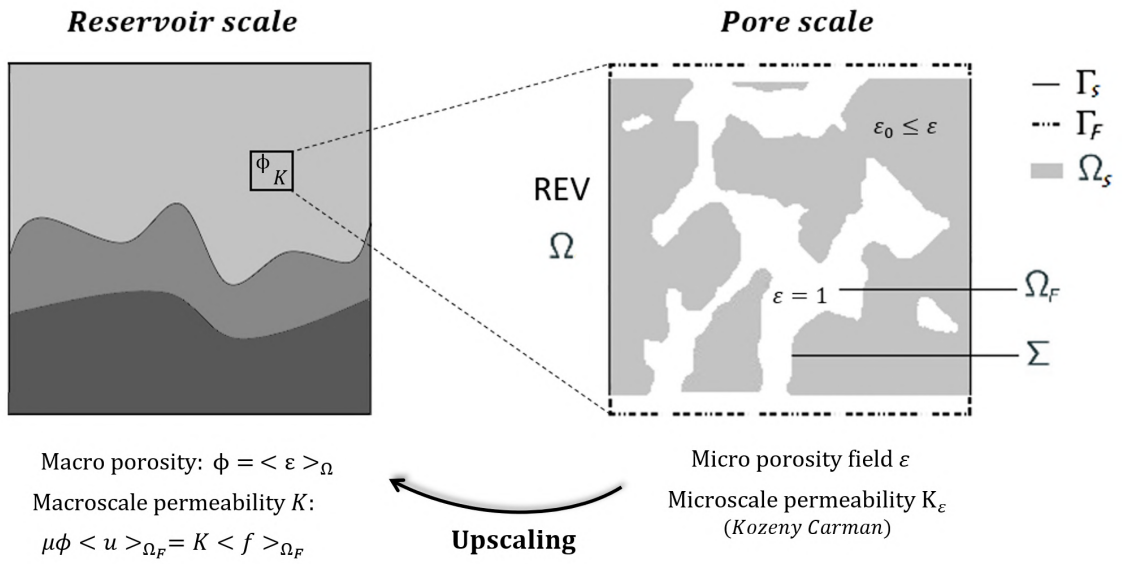


**Figure 1.1: From the pore-scale to the reservoir scale: an upscaling principle.** Schematic representation of a reservoir scale structure, on the left, with its inherent averaged macro-properties $\phi$ and $\kappa_0$ computed on a representative elementary volume (REV). Local micro-continuum description of the pore-scale heterogeneities in this REV, on the right, along with its intrinsic micro-scale properties. These properties are the local micro porosity field $\varepsilon$ (lower bounded by a sub-resolved porosity $\varepsilon_0 > 0$ in the porous matrix $\Omega_S$) and the micro-scale permeability $K_\varepsilon$, based on the Kozeny-Carman relationship developed in equation 2.2 of Chapter 2 (page 25).

### 1.1.2 A question of scale

The meaningful combination of laboratory experiments and mathematical modeling has to be considered to investigate the mechanisms of $CO_2$ mineral storage and assess their global implications on the sequestration process. The question of the scales on which these analyses are carried out, however, remains fundamental.

Indeed, part of the trapping processes, like capillary and mineral trapping, involve local interactions with the aquifer rocks. These reactions occur in the pore space, which can be of varying sizes and distributions, although it commonly refers to small scales (*e.g.*, from a few nanometers to centimeters). Inferring the behavior of these mechanisms has thereby required the development of pore-scale models, in addition to efficient scientific computing tools, to perform predictive numerical simulations [232, 280]. Such pore-scale phenomena are also particularly convenient for experimental studies, which are naturally limited, in some sense, to human physical size and time [21]. In contrast, the long-term predictions of $CO_2$ storage are rather interesting to study at the field scale, corresponding to the entire aquifer behavior over several kilometers. 3D reservoir simulations thereby represent another attractive research area and aim to evaluate global phenomena such as injection capacities, pressure changes, or $CO_2$ plume migration over several hundred years [146, 150].

At first sight, two worlds differ: a pore-scale environment and a large reservoir structure respectively endowed with micro and macro-scale properties. At the sub-micrometer scale, the hydro-chemical implications are finely described based on local characterizations of the medium. On the contrary, the porous medium relies on a continuum description at the field scale, and mathematical models require averaged evaluations of its main properties. However, these two worlds provide crucial insights and are directly related to each other through homogenization techniques that offer an efficient mathematical framework for bridging the gap between these scales (*e.g.* see Figure 1.1). Indeed, upscaling of the governing equations remains an intrinsic and active field of research since the pioneering work in volume averaging developed by Quintard and Whitaker [26, 250, 251, 316]. Volume averaging introduces the concept of Representative Elementary Volume (REV) as the characteristic minimal volume on which the microscopic variables

can be averaged [32]. It allows the transfer from the pore scale to the Darcy scale by referring to representative criteria of the domain in terms of averaged properties, such as the macro-porosity $\phi$, permeability $K$, specific surface area $A_s$, etc. These bulk parameters are derived from the evolving micro-structures through upscaling principles, as illustrated in Figure 1.1. Indeed, at the continuum Darcy scale, the upscaled porosity and permeability are respectively defined by:

$$\phi = < \varepsilon >_\Omega \text{ and } \mu\phi < u >_{\Omega_F} = K < f >_{\Omega_F} \text{ where } K \in \mathcal{M}_{3,3}(\mathbb{R}), \tag{1.1}$$

where $< . >$ represents the average on the respective fluid domain $\Omega_F$ and porous matrix $\Omega_S$, described at the pore scale in a representative volume $\Omega$. The notation $\varepsilon$ refers to the corresponding micro-porosity field, $u$ is the pore-scale velocity, $\mu$ is the dynamic viscosity, and $f$ is the volumic driving force of the flow. In the case of an isotropic permeability, where $K = \kappa_0 I$, it is sufficient to consider the flow in a main direction. For example, along the $z$-axis, this yields:

$$\kappa_0 = \frac{\mu\phi < u_z >_{\Omega_F}}{< f_z >_{\Omega_F}}, \tag{1.2}$$

where $u_z$ and $f_z$ represent the vertical components of the velocity and driving force, respectively. The micro-porosity field description at the pore scale can either account for each individual solid grain or consider a hybrid pore scale-continuum scale formalism, referred to as micro-continuum. In the hybrid case, the pore space is explicitly described, unlike sub-resolved features present within the porous matrix $\Omega_S$ that are, meanwhile, regarded as averaged volume fractions of the material — introducing the local volume-averaged porosity — and characterized by a lower bound on the residual porosity $\varepsilon \geqslant \varepsilon_0 > 0$ in Figure 1.1 [204, 227, 279]. Despite a straightforward conceptualization, the notion of REV can, however, become ambivalent and challenging when dynamical reactions occur. In particular, the alterations in the pore space may affect its unique definition over time and require special considerations [220, 275].

Determining the proper size of this REV is also critical for applications to Digital Rock Physics, which has appeared as a performing approach in porous media studies and combines imaging experiments with pore-scale modeling [52]. The experimental part is supported by advances in X-ray microtomography (X-ray $\mu$CT) which non-destructively describes a representative volume of the material. Such imaging techniques are becoming increasingly valuable tools for providing appropriate internal descriptions of microstructural properties. Indeed, X-ray microtomography reconstructs a high-resolution 3D image of the heterogeneous structure that can be used straightforwardly as complex geometrical input in pore-scale simulations. The micrometric sample geometry serves, for instance, as a basis to perform numerical predictions of reactive flows within the porous media and, afterward, measure their impact on the macro-scale properties through homogenization. Dynamical scans may also be performed over time to directly track evolving interfaces during reactive experiments such as mineral dissolution or precipitation. Afterward, 4D $\mu$CT is either coupled with pore-scale simulations for comparisons [204, 220] or is used to experimentally evaluate reactivity and kinetic parameters [62, 218].

The present thesis explores the pore-scale considerations of $CO_2$ mineral storage through, on one side, the mathematical modeling and Direct Numerical Simulation (DNS) of reactive micrometric processes. Besides, it intends to investigate the relationship between micro-tomography experiments (stationary or dynamic), modeling, and numerical applications. The focus is on enhancing the reliability of direct predictions by building models on experimental data wherein the uncertainties are quantified. The essence of this work, thereby, finds its place in the proper balance between $\mu$CT experiments and mathematical modeling theory.

### 1.1.3 From a microtomography perspective: the imaging challenges

Independently of the modeling considerations, pore-scale simulations are intrinsically related to X-ray $\mu$CT as the latter provides, beforehand, scans of the complex shape geometry on a representative elementary volume. Pore-scale numerical simulations of reactive dynamical processes are then performed on this REV initial geometry tracking the dynamical interface evolutions and

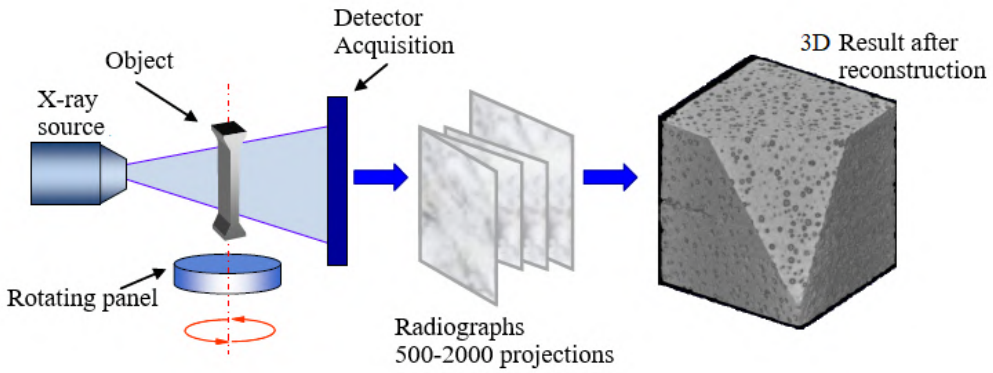


**Figure 1.2: X-ray $\mu$CT data acquisition principle [170]:** The porous sample is positioned on a rotating panel between the X-ray source and the detector, which acquires a series of 2D projections over a rotation of 360°corresponding to the intensity of the transmitted X-ray beam through the sample. The 3D grey scale dataset is subsequently reconstructed from these projections based on, for instance, a back-projection algorithm [119].

micro-properties changes. These afterward translate into petrophysical evolutions through upscaling principles, as introduced in Sect. 1.1.2. Therefore, trustable measurement of the impact of the reactive processes on the porous medium macro-properties requires ensuring reliable quantification of the changes in the micro-properties. This can be achieved under the constraint of having a fine description of the pore space, with correct knowledge of the surrounding solid matrix defined by the local micro-porosity field $\varepsilon$. An efficient representation of the porous sample at the pore scale is necessary to guarantee reliable estimation of the macro-properties evolutions along the reactive processes.

Advances in X-ray microtomography offer such an opportunity. X-ray $\mu$CT is regarded as a powerful non-invasive and high-resolution imaging technique able to determine the inner structure of a porous sample up to a characteristic scale, which defines the voxel size. The voxels are small elementary volumes (of a few $\mu$m) that compose the overall 3D reconstructed sample geometry and are identified by different grey levels characterizing the local attenuation of the material. The $\mu$CT workflow, illustrated in Figure 1.2, describes the intensity of the transmitted X-ray beam, which is material-dependent and determines the absorption ability of the different components through the sample. The resulting 3D dataset can either be segmented to separate the pore space — namely the fluid phase $\Omega_F$ — from the surrounding solid matrix $\Omega_S$ or directly benefit from the information related to the greyscale values of the different voxels. The segmented images lend themselves to numerical simulations that require an explicit representation of the fluid-solid interfaces (*e.g.* Lattice-Boltzmann [4]) or directly account for the voxel greyscale estimations (*e.g.* Darcy-Brinkman Stokes formulation [59, 279]). Indeed, these grey-level shades, depicting the material local attenuation, are correlated to the micro-porosity field description and can be taken into account in the Darcy-Brinkman Stokes formulation. The latter is a hybrid model that combines continuum-scale and pore-scale approaches and relies on the micro-continuum representation of the medium, as introduced in the previous Sect. 1.1.2, along with the empirical Kozeny Carman relationship for the micro-scale permeability (see Sect. 2.3.1 from Chapter 2). This introduces Digital Rock Physics applications as the joint use of high-resolution X-ray computed microtomography and advanced simulation techniques to characterize, *inter alia*, the rock petrophysical properties and their evolutions [23, 24]. Pure imaging alternatives readily regard the resulting dataset to derive the sample's effective physical properties (porosity, permeability, dispersivity...) but also geochemical rates and mineral reactivity in dynamical processes [217, 276]. Therefore, X-ray microtomography is both a complementary means to numerical modeling at the pore scale and a fundamental imaging process on its own to study the $CO_2$ storage implications on porous material.

However, limitations in the $\mu$CT imaging process may affect the determination of the medium effective properties, and query the reliability of the predictive models based on these datasets. In

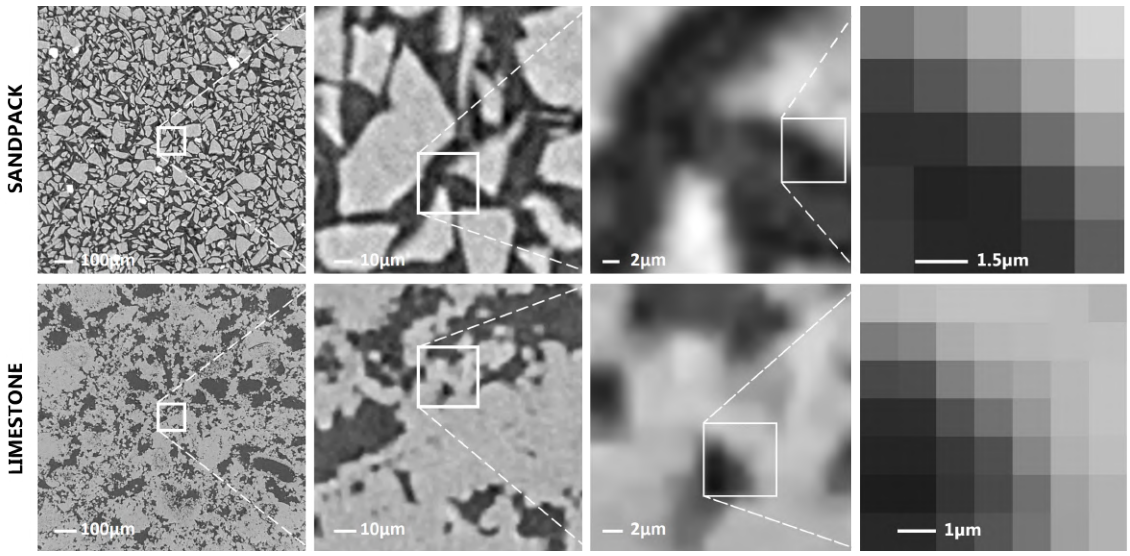


**Figure 1.3: High-resolution X-ray scans of two samples.** Data are numerically magnified up to voxel scale using successive interpolated zoom up to the final zoom on the right, at the physical size of the pixel (voxel sizes are respectively 1.5$\mu$m and 1$\mu$m for the Sandpack and the limestone). This illustrates the presence of a grey-scale gradient instead of a sharp interface.

fact, several imaging artifacts exist and disrupt the efficient description of the pore space morphology. Firstly, the finite resolution of the $\mu$CT pipeline is challenging, as the interfaces appear blurry and do not manifest themselves as sharp intensity steps in the images, but rather as gradual intensity changes spanning over several voxels [266] (see Figure 1.3). Actually, the local attenuation signal within a voxel is influenced by the material heterogeneity in its neighborhood, then the resulting grey scale value represents averaged properties: this is known as the Partial Volume Effect [214]. This phenomenon is also involved when morphological features of interest are smaller than the characteristic voxel size, resulting in unresolved micro-porosity or roughness of the pore space walls. Quantifying sub-resolution porosity, which is a prevalent imaging artifact in $\mu$CT, and measuring its impact on numerical modeling and simulation is identified as critical for geosciences applications [69, 172, 276]. Such an issue is well-known and arises from a compromise between the sample volume being investigated and the scan resolution. For porous media covering a wide range of pore scales, this trade-off can readily result in voxel sizes that are not able to capture fully resolved morphological features of the pore space. Finally, in the presence of sharp density transitions, the different refraction index at either side of the interface furthermore leads to so-called edge enhancement which manifests itself as an over- and undershoot of the grey level immediately next to the interface [37]. Consequently, the position of the material interface is prone to uncertainty, in addition to the roughness of the pore space walls, and therefore results in an approximation of the true morphology.

While the mentioned effects can be minimized, they cannot be eliminated and add uncertainties to the estimation of the effective properties, the characterization of the void/solid interfaces, and the reliability of the numerical models. In addition, the accuracy of X-ray $\mu$CT images is challenged by additional artifacts coming from both inherent physical and technical limitations [144]. It includes, among them, instrumental noise, beam hardening [318] which results in cupping (an underestimation of the attenuation at the center of the object compared to its edges) or drag/streak appearances (due to an underestimation between two areas of high attenuation), beam fluctuations along the scanning process and scatter radiations coming from the object and/or the detector. These variations can manifest as noise, ring or streak artifacts, and halos that are often hard to distinguish from real features and therefore hinder the identification of sample heterogeneities at multiple scales. Ubiquitous limiting factors remain in the X-ray $\mu$CT imaging process, and the assessment of their related uncertainties is fundamental to developing more accurate predictive models.

Incorporating Uncertainty Quantification (UQ) in the workflow of pore-scale modeling is,

therefore, a major concern of the present thesis. In this sense, this intends to improve the relevance of dynamical forecasts through reliable quantification of the macro-properties changes along geochemical transformations in $CO_2$ mineral storage. We especially want to ensure that the evolving petrophysical properties observed through DNS of reactive flows at the pore-scale result from meaningful chemical interactions rather than $\mu$CT imaging biases previously introduced. Quantifying uncertainties in image-based models from a pore-scale perspective is, therefore, of considerable interest and can provide a better understanding of both the modeling aspects and experimental datasets.

Moreover, scaling and stiffness issues, the use of simplified models, and the coarse or inaccurate description of the porous medium, *inter alia*, lead to uncertainties in the numerical results that can be estimated over several DNS approaches as an inherent UQ analysis. Consequently, together with UQ methodologies, confronting several DNS methods also provides insights into the numerical uncertainties, and benchmarks involving multiple numerical methods still contribute to gaining confidence in numerical results and parameter estimations. Nonetheless, a misleading calibration of the mathematical model parameters, namely in the mineral reactivities and kinetic parameters, cannot be identified and quantified in this way. This highlights the need to robustly calibrate reactive Partial Differential Equation (PDE) models by inverse problems integrating confidence in the estimations.

## 1.2 State of the art

### 1.2.1 Hydrodynamics at the pore scale: modeling and numerical considerations

Many mathematical models and DNS methods have been developed to investigate reactive micrometric processes and establish the relationship between pore scale phenomena and continuum macro-scale parameters. However, modeling reactive hydrodynamics in the 3D pore structures arising from X-ray $\mu$CT experiments and understanding how pore-scale heterogeneity affects the reaction rates are currently still challenging.

Firstly, the complexity of the pore structure adds significant intricacy to the flow and transport modeling within these materials. In pore-scale modeling of hydrodynamics, two prominent categories exist: one entails conceptual simplification of the pore structure such as Pore Network models (PNM), while the other directly incorporates the proper 3D morphology of the medium [198]. In particular, PNM rely on a simplified representation of the intricate pore geometry, which is approximated as a network of interconnected pores bodies — represented by nodes — and throats — represented by links (see Figure 1.4). The accuracy of such modeling, however, depends to a large extent on how well the pore network approximation corresponds to the actual pore structure of the medium [323]. In return, their computational efficiency, inherent to the morphological simplifications, and their ability to include numerous heterogeneity in larger rock volumes make PNM popular in porous media research. In particular, a Python open-source framework — called OpenPNM [125, 126] — has been developed to address pore-network models for simulating various processes in porous media including, *inter alia*, transport, single-phase and multiphase flows, and reactive phenomena [169, 197, 257].

On the contrary, explicit descriptions of the complex pore-scale geometry can be incorporated into DNS through conventional discretization methods based on Eulerian formulation.

These DNS approaches intend to discretize and approximate the solutions of PDE systems that arise from mathematical modeling of the fundamental laws governing fluid dynamics. In particular, the hydrodynamics of a single-phase Newtonian fluid within a porous medium can be accurately described, in the fluid domain $\Omega_F$, by the Navier-Stokes or Stokes equations — depending on the flow regime — associated with the continuity equation derived from mass conservation. These models are coupled with appropriate boundary conditions, reactive or not, and can also incorporate the time dependency of the porous medium. An important aspect, therefore, lies in modeling the interactions at the fluid-solid interfaces, which can explicitly describe each solid grain's boundaries within the pore space. This results in a two-domain formulation, which divides the domain into a fluid region and a solid one. Such a modeling approach requires special

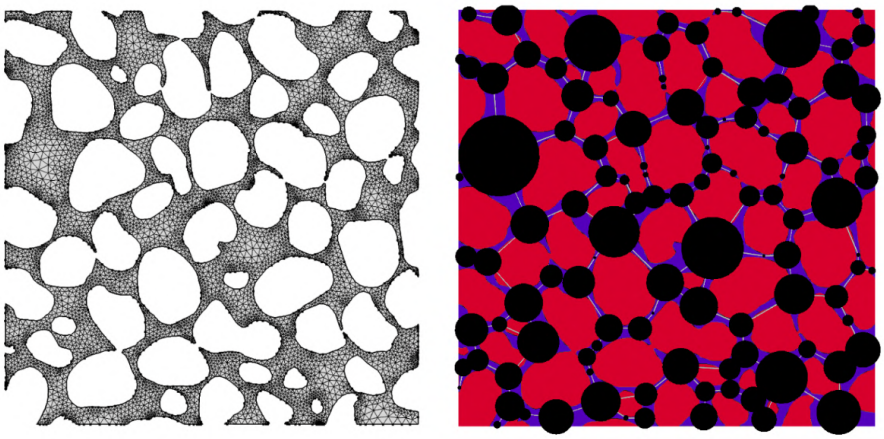

(a) FEM mesh (b) Equivalent PNM

**Figure 1.4: Pore-network abstraction of a porous medium [125]**: a) Unstructured meshing of the porous complex morphology used in Finite Element Methods (FEM). b) Pore-network model (PNM) approximation of the medium, which is reduced to interlinked nodes.

consideration of the surface boundary conditions for accurately capturing the dynamic behavior of the overall system [203].

Meanwhile, other mathematical models consider a volumic description of the micro-scale heterogeneities, introducing the local volume-averaged porosity $\varepsilon$ within control volumes — *e.g.* representing the voxels of the $\mu$CT images — of the pore space. Instead of solving a full Navier-Stokes or Stokes equation in the fluid domain, these approaches account for the micro-continuum description of the medium through the Darcy-Brinkman Stokes (DBS) equation, which models Stokes flow in the void regions $\Omega_F$ and a Darcy *addendum* in the region of the porous matrix $\Omega_S$. This consists of a single set of equations imposed over the whole domain without distinction and, therefore, relies on a penalization principle of the porous matrix [26, 65]. In particular, the empirical Kozeny-Carman permeability-porosity relationship, which is explicitly detailed in equation (2.2) page 25, acts as a moderate penalization term (though physical) in the DBS formulation that facilitates the transition from Darcian regime to Stokes flow as the micro-porosity field changes [128, 278]. Such micro-continuum models lie on the volume averaging theory developed in the late 1980s by Quintard and Whitaker [250], which introduces the superficial velocity $u$, also known as Darcy velocity or filtration velocity. The latter is defined as $\phi < v >_{\Omega_F} \simeq < v >_{\Omega}$ with $< v >_{\Omega_F}$ the interstitial velocity or intrinsic velocity, that is to say the pore-scale velocity $v$ averaged over the fluid domain $\Omega_F$.

Moreover, Bousquet *et al.* [56] established a superficial model that completes the DBS equation with the second Brinkman correction that explicitly involves the micro-porosity gradients, for heterogeneous porous media exhibiting substantial changes of the porosity rates. Besides, the diffusion part of the DBS model can be considered, in practice, under its conservative [305] or non-conservative formulation [128, 278]. Whether the formulation is conservative or not, the formulation is equivalent in the fluid region but differs where the porosity is spatially variable. While both these formulations are acceptable, we can notice that the conservative form is more convenient to Galerkin methods based on the variational formulation of these models, and the non-conservative form is more suitable to grid-based and hybrid Lagrangian methods such as the one developed in Chapter 2.

Furthermore, thermal, mechanical, rheological effects, chemical potential effects at the nanometer scale, and fluid-structure interaction (FSI) can also be incorporated to complete the mathematical modeling of hydrodynamics. The coupling with chemistry and reactive processes, especially, are developed below in Sect. 1.2.2, in Sect. 2.3 from Chapter 2 and in Chapter 5.

Conventional discretizations of such mathematical models, in Eulerian formalism, include Computational Fluid Dynamics (CFD) well-established methods such as finite elements [6, 309], or finite volumes [64, 235] which have been extended to hydrodynamic simulations at the pore

scale. In particular, the use of such traditional CFD methods in pore-scale reactive flow has been supported by the development of efficient open-source libraries such as OpenFOAM [279, 315], Chombo [3, 303] and PoreFlow [295]. These numerical methods combine efficiently with unstructured meshing strategies that allow efficient capture of the pore interfaces (*e.g.* see Figure 1.4a) but require successive mesh adaptations when investigating dynamical interfaces. On the contrary, structured meshes are more computationally efficient and easy to implement, rendering them widely used in practice. However, this requires dedicated methodologies to handle the pore interface representation such as the immersed boundary or the embedded boundary methods. The immersed boundary method, initially developed by Peskin in the 1970s [239], has been recognized as a useful and efficient approach to fluid-structure interaction problems, wherein the interfaces are represented using a Lagrangian formulation [44, 63, 248]. Indeed, this allows for modeling complex and moving interfaces without the need for mesh adaptation or refinement but by directly enforcing the effects of the immersed boundaries on the flow. These methods have subsequently been generalized by LeVeque *et al.* [166] in 1994 to the so-called immersed interfaces, which currently encompass a broad range of discrete forcing methods [121, 324]. The embedded boundary method also allows for the utilization of structured meshing while simultaneously capturing intricate surface geometries [201]. Unlike immersed boundary methods, this introduces cut cells of smaller size, which result from intersecting the intricate interfaces with structured meshing and account for fluid partial volumes along with fractions of interfacial area [206, 303].

Meanwhile, grid-based methods such as finite differences involve discrete operators on structured grids, that can either use collocation or staggered arrangements. In the former, all the variables (*e.g.* velocity, pressure, density ...) are located at the same grid points while, in the latter, these variables are stored at different locations within the grid cells (*e.g.* in the cell centers or at the edges). Grid-based methods can subsequently combine with other dedicated approaches to address particular flow features in the context of hybrid formalism, coupling Eulerian and Lagrangian formulations, for instance.

In contrast with the previous Eulerian approaches, Lagrangian methods wherein the fields are evaluated on moving particles have, indeed, garnered considerable interest in modeling transport-dominant regimes. They offer robust alternatives to address complex fluid dynamics, multi-phase flows, and reactive transport in complex porous media geometries and include, *inter alia*, vortex methods [72] or smoothed particle hydrodynamics [296]. These meshless Lagrangian formulations rely on the description of the fluid motion as the tracking along time of a large number of particles, carrying information about their position, velocity, mass, and other intrinsic properties. Due to their ability to follow the movement of individual particles, these approaches are particularly effective in advection-dominated regimes and alleviate stability issues inherent to the discretization of transport terms in structured grid methods. Such numerical models can also effectively handle complex interactions between particles such as collisions, chemical reactions, surface growth, and precipitation [297]. However, particle methods can be computationally expensive, especially for large systems involving numerous interacting particles, and therefore, require massive parallelization using High-Performance-Computing (HPC) devices.

Finally, the development of hybrid formalism, mixing Eulerian and Lagrangian approaches, has also garnered considerable interest in modeling micrometric processes in porous media [74, 113, 202]. This effectively combines particle-based techniques, usually used for advection phenomena, with an underlying grid structure and is commonly referred to as semi-Lagrangian methods [71, 73, 88, 110]. The latter allows the interpolation and remeshing of the particle locations directly on the grid and makes it possible to mitigate the accumulation or scarcity issues in the particle distribution [189]. Besides, the underlying mesh facilitates the computation of differential operators through dedicated grid-based solvers, resulting in an operator-splitting formulation of the overall PDE system. This hybrid Lagrangian formalism simultaneously overcomes stability conditions related to transport and addresses the ill-conditioning of the linear systems used to discretize the remaining operators in the splitting formulation.

Similar to particle hybrid formalism, the Lattice Boltzmann method has emerged as an alternative to the resolution of Navier-Stokes equations by accounting for the Boltzmann equation

derived from gas kinetic theory [149]. Indeed, this approach is not meant to solve continuum fluid mechanics equations but relies on a distinct conceptualization. The latter describes the flow motion by tracking statistical particle distributions at given locations in space. An underlying lattice is considered to describe the probabilities of particles moving in specific directions at certain velocities, but also to account for particle collisions based on kinetic interactions [31, 142]. The Lattice Boltzmann method has, therefore, emerged as an efficient DNS alternative to address pore-scale modeling of reactive flows [152, 293].

Overall, all the previous modeling and numerical approaches present intrinsic advantages and drawbacks, and in this sense, their variety is a valuable strength in porous media research. Indeed, this variety offers the opportunity to perform extensive cross-validation and benchmarks while comparing the numerical simulations with laboratory experiments. Besides, HPC considerations and computational efficiency remain a significant part of the development of effective numerical simulations. Finally, recent concerns have also emerged about managing the energetic resources of the HPC numerical libraries themselves, and this is also an important aspect not to neglect when developing new methodologies.

### 1.2.2 Geochemical modeling and reactive processes

Incorporating geochemical interactions in the previous numerical approaches introduces additional challenges, which require careful consideration in the modeling and numerical aspects.

Firstly, such reactive processes often involve multiple species with complex chemical interactions, which can manifest as reversible equilibrium reactions or irreversible non-equilibrium reactions. Modeling these geochemical processes hence requires a deep understanding of the reaction patterns, rate constants, and their interactions with the surrounding porous medium. Indeed, morphological features of the pore space, including the pore size and distribution, sub-resolved micro-porosity, and reactive surface area, can have a significant impact on the dynamical reaction rates [42, 104]. Mineralogical heterogeneity also plays a crucial role and affects reactive processes such as mineral dissolution or precipitation [183]. Modeling reactive hydrodynamics presents another substantial challenge due to the intricate interplay between the transport and flow of chemical species, the alterations in pore-scale structures, and the evolution of petrophysical properties. Indeed, alterations of the pore morphology and connectivity due to the chemical reactions affect the porosity, permeability, and tortuosity, which in turn impact the flow and solute transport. In this sense, dynamical tracking of the evolving rock-water interfaces is essential in geochemical modeling at the pore scale in order to manage the petrophysical property changes [220].

Historically, mathematical modeling of chemical reactions has been investigated according to two formulations, namely under the assumption of local equilibrium or kinetic reactions [285]. The local equilibrium approximation strongly assumes that the chemical system has locally reached an equilibrium state, wherein the rates of forward and reverse reactions are equal, and the reactant species concentrations remain constant over time. Local equilibrium reactions, therefore, simplify the modeling of reactive transport by assuming that variations in concentrations and reaction rates can be neglected within a given spatiotemporal region. In particular, this approach seems reasonable for modeling homogeneous reactions between aqueous species, for which the chemical reactions tend to occur much more rapidly than the solute transport by the fluid flow. Such modeling assumption also presents a significant computational advantage in the sense that it makes it possible to considerably decrease the number of chemical species in the overall reactive system. In this sense, in large chemical systems involving numerous species, local equilibrium assumption can be a relevant partner to kinetic formulations which are more relevant to handling heterogeneous water-rock interactions. Such trade-off is commonly applied when considering fully coupled reactive systems for $CO_2$ storage in reservoir simulations, and results in a partitioning of the system between primary and secondary chemical species [5, 116, 282].

Kinetic formulations, on the other hand, consider detailed chemical reaction rates of the primary species, describing their dependence on factors such as reactant concentrations, temperature, mineral morphological features, etc. They offer more suitable modeling of long-term or mineral reactions and are commonly based on laboratory experiments, theoretical chemical kinet-

ics, or a combination thereof [77, 156]. In particular, the Transition State Theory (TST), originally developed by Erying in 1935 and popularized by Lasaga in the 1980s, is a well-established theoretical framework for understanding the fundamental expressions of kinetic reaction rates and the factors influencing them. Since then, this formalism has been widely applied in DNS to model reactive processes related to $CO_2$ storage, including mineral dissolution and precipitation [206, 222, 286, 327]. It has also been extensively used to experimentally determine reaction rate constants of ground mineral samples in fluidized bed reactors [77], which are subsequently used in pore-scale models as surface rates using the reactive surface area.

Nonetheless, the bulk TST formulation also presents some limitations that have raised queries about its applicability, in particular, to capture the complex transition patterns of precipitation and crystal growth phenomena [131, 240, 286]. Indeed, the kinetics of mineral precipitation involve a combination of several factors and phenomena. This includes *inter alia* the supersaturation state, the transport rate of the chemical species to the mineral surface, and the attachment rate of ions on this surface — including the consideration of preferentially growing sites — but also the probabilistic nucleation, which is the first stage of any crystal growth process. In this sense, classical nucleation theory has also emerged as a valuable theoretical framework for developing new probabilistic models for mineral nucleation and crystallization [223, 320]. Investigating proper precipitation and crystallization models at the pore scale in the context of $CO_2$ mineral storage is, therefore, challenging as this needs to account for the kinetics of nucleation, growth, and crystal aggregations while considering the role of the porous medium interfaces.

Besides, experimental identification of mineral reactivities remains a major concern in the geochemical modeling of reactive processes for $CO_2$ mineral storage. Reaction rate parameters measured in laboratory experiments are associated with considerable uncertainties and may not align with field rates observed in natural systems [190]. Among the factors that influence such discrepancies, one can find the effects of surface-controlled parameters at the pore scale, particularly reactive surface areas, which can significantly affect the reaction rates. Accounting for these uncertainties in the kinetic reaction rates is, therefore, crucial to ensure reliable calibration of the pore-scale modeling and comparison with laboratory experiments.

From a numerical perspective, there exists several open-source software dedicated to geochemical modeling, namely CrunchFlow [283] developed by Steefel in the early 2000s to address reactive transport or PHREEQC [228], to name just a few of them [282]. This has subsequently led to the development of flow and reactive transport HPC libraries coupled to these geochemical packages such as, for instance, Chombo-Crunch [302] developed by Trebotich *et al.* since 2010 [205]. However, such coupling of existing software requires special programming considerations to deal with communication interfaces between the libraries and, therefore, alleviate compatibility issues.

### 1.2.3 Machine learning and data-driven approaches in geosciences

Recent advances in developing new Artificial Intelligence (AI) systems that can perform tasks typically requiring human intelligence, such as natural language processing or facial recognition, have drawn attention in the research community for their ability to solve complex problems in a wide range of applications. As subsets of the AI overarching concept, machine learning, and deep learning technologies are the most commonly investigated approaches in geosciences (see Figure 1.5). Machine learning, in particular, is described as the development of new algorithms and models that enable computers to learn from data and make predictions or decisions [13]. Advances in this domain have been motivated by the growth in available data and the continuous emergence of increasingly powerful computing resources. In this sense, data-driven inferences have become valuable partners to merely theory-driven paradigms and traditional DNS approaches. Deep learning, on the other hand, is a dedicated subset of machine learning that focuses on Artificial Neural Networks (ANN), inspired by brain-like logical structures and consisting of interconnected layers of artificial neurons [124]. Currently, numerous deep-learning methodologies exist, ranging from Physics-Informed Neural Networks (PINNs) [254], Convolutional Neural Networks (CNN) [262] and Generative Adversarial Neural Networks (GAN) [210] to Autoencoders [336].

Machine learning and data-driven approaches have, therefore, garnered increasing interest in

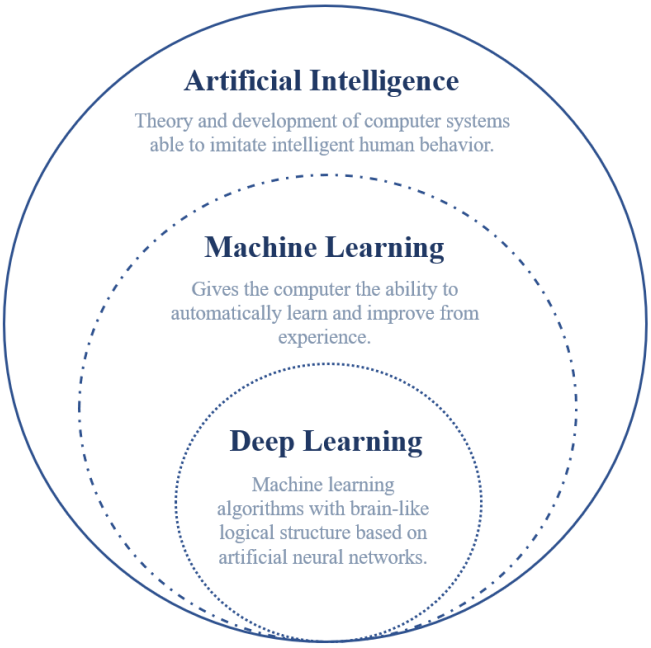


**Figure 1.5: From Artificial Intelligence to Deep Learning:** hierarchical relationship and conceptualization.

geosciences to analyze large datasets generated from laboratory experiments or simulations, but also improve the predictive capabilities through fast surrogate modeling techniques [103]. We subsequently introduce some of the current concerns and developments of AI methodologies for geosciences, depending on the amount of data available, together with physical assumptions on the underlying PDE models.

First, machine learning offers the opportunity to accelerate image and data treatment analyses to predict the petrophysical properties of a porous material. Extensive investigations have been carried out on the development of fast and efficient deep learning computational methodologies for estimating permeability and porosity based on X-ray $\mu$CT images [15, 28, 299]. This can be achieved through CNN, which is a powerful image analysis and recognition framework able to extract hierarchical features from the data using convolution principles. In particular, CNN are well-suited for image classification and segmentation, capturing spatial patterns, and are thus of great interest for mapping morphological pore-scale structures with material properties [14, 241]. In this sense, they have also been extended to multi-scale feature extraction, such as heterogeneous porosity, to provide super-resolved segmentation of $\mu$CT images that aim to identify sub-resolution porosity [16]. Finally, multi-scale image reconstruction from low-resolution $\mu$CT scans can also be performed using GAN, which are particularly efficient for data augmentation problems [271, 330]. Overall, these methodologies fall into pure image treatment analysis and regard the measurement data independently of any physical consideration.

Meanwhile, unlike traditional modeling techniques that historically rely on deriving governing equations, predictive physical-based models can sometimes hardly be available or reliable, and this encourages the shift to data-driven approaches. In this sense, deducing governing equations directly from data when no physical priors exist is also a major research area of machine learning. It covers inference approaches such as symbolic regression, automated model selection, ensemble methods, and sparse regression that aim to identify a parsimonious symbolic structure of the PDE model from (noisy) data [141, 233, 265]. These methods emphasize the improvement of the models' generalizability and interpretability while eventually inferring hidden physics principles directly from the observations. This highlights, at the same time, concerns about the PDE model reliability, whose partial prior knowledge can be associated with intrinsic uncertainties.

Finally, PINNs are among the machine learning paradigms allowing for the integration of physics-based PDE models with available measurement data [254]. These versatile models pro-

vide an effective alternative to purely data-driven methods by embedding known physical laws directly into their neural network architecture. They learn from available measurements, making them data-driven while ensuring that the predictive solutions satisfy the underlying physics of the problem. In particular, this is achieved by considering a multi-objective optimization problem that involves a weighted combination of tasks related to the data and physics constraints. PINNs also offer computational efficiency compared to traditional numerical methods in the sense that they can be used as fast surrogate models — also called proxies — to perform extensive sensitivity analyses for instance, which require a large number of evaluations of the PDE model. Moreover, PINNs are particularly suitable for inverse problems, model parameter estimations, and data assimilation problems, making them a promising framework for a broad spectrum of scientific applications [39, 18, 100, 120]. Apart from machine learning methodologies, traditional data assimilation techniques based on well-established mathematical frameworks, such as variational data assimilation, remain extensively studied [17, 129]. Variational data assimilation relies on solving an adjoint problem that investigates the sensitivity of an objective function with respect to the model parameters or initial conditions of the system. This is used to adjust the mismatch between the model predictions and observations, and overall improve the accuracy of the predictions. This can, however, become highly demanding in computational resources, and machine learning can thus be a valuable alternative for addressing complex data assimilation problems, where back-propagation plays a crucial role in evaluating gradients with respect to the model parameters. Besides, sequential data assimilation and online learning also offer the opportunity to continuously update the model as new measurements become available and incorporate recent observations into the machine learning framework.

Overall, machine learning methodologies have increasingly drawn interest in geoscience for various applications, including purely data-driven methods, model inference, physics-based inverse problems, and data assimilation. Nonetheless, intrinsic uncertainties in terms of model accuracy, reliability of the predicted inverse parameters, and data corruption with noise or imaging artifacts also query the necessity of uncertainty quantification in the previous methodologies.

### 1.2.4 Uncertainty Quantification and Bayesian Inference for data assimilation

Developing efficient data assimilation techniques is crucial to performing extensive parameter estimations, uncertainty quantification, and improving the reliability of model predictions. In particular, inverse problems are often subject to various sources of uncertainty that need to be quantified to ensure trustable estimations. This includes approximate model accuracy whose reliability can be questioned, with sparse or noisy data exhibiting measurement variability. Integrating physical principles, such as conservation laws or PDE models, in these inverse problems can though compensate for the lack of massive or accurate measurements through additional regularization constraints [199]. At the same time, embedding these physical regularizations allows addressing model accuracy in the total uncertainty quantification, especially when misleading a-priori uncertainty is assumed on the physical constraints [249]. Combining physics-based and data-driven methods can efficiently overcome the limitations of each approach individually, making them complementary partners in data assimilation and inverse modeling incorporating uncertainty quantification.

Several approaches were developed to address uncertainty concerns in the context of data assimilation. These uncertainty quantification problems either require stochastic PDE models [35, 137] widely used in sensitivity analysis, or probabilistic approaches such as Markov Chain Monte Carlo (MCMC) methods. The latter can be used in Bayesian Inference, which is a formal framework for addressing uncertainties and making probabilistic statements about model predictions, to sample from a target posterior distribution that usually requires numerous evaluations of the forward PDE model. In this sense, developing efficient MCMC methodologies remains challenging since repeatedly solving a complex coupled PDE system is computationally expensive and therefore can quickly become prohibitive for uncertainty assessments. These computational concerns have motivated the emergence of surrogate models in Bayesian Inference to speed up the forward model evaluation. This covers methods ranging from Polynomial

Chaos Expansions [193, 325] which rely on a representation of the physical model by a series of low-order polynomials of random variables, to neural network proxies previously introduced in Sect. 1.2.3 [8, 326]. Both approaches present the advantage of creating a surrogate model that can be evaluated inexpensively compared to solving the forward problem through usual DNS. Nonetheless, Polynomial Chaos expansions suffer from truncation errors due to the low order of the polynomials yielding inaccurate estimates of the posterior distributions [180]. On the contrary, deep learning methods have shown effectiveness in building surrogate models for a wide range of complex and non-linear PDEs encoding the underlying physical principles. Developing fast surrogate models based on machine learning has garnered increasing interest in accelerating Bayesian inference for scientific applications [86, 103].

A popular framework in deep learning integrating physics regularization, measurement data, and uncertainty quantification is Bayesian Physics-Informed Neural Networks (BPINNs) [173, 328]. BPINNs benefit from the combined advantages of neural network structures in building parameterized surrogate models based on physical principles and Bayesian inference standards in integrating uncertainty quantification. This paradigm, therefore, offers the opportunity to query the confidence in the predictions, the reliability in the estimations of inverse parameters, and the model adequacy in inverse problems incorporating UQ. Efficiently sampling from the posterior distribution in the BPINNs paradigm is essential for performing probabilistic inference and is commonly achieved through Variational Inference [322] or MCMC methods. In particular, one of the most popular MCMC schemes for BPINNs is the Hamiltonian Monte Carlo (HMC) which is a gradient-based MCMC sampler that provides efficient scaling properties for high-dimensional inference problems [48].

Despite their effectiveness, BPINNs can be difficult to use correctly in complex real-world Bayesian inference as they are prone to a range of pathological behaviors. These instabilities arise in multi-objective inverse problems which likely involve conflicting tasks or multiscale issues. In particular, such a multi-objective paradigm directly translates to a weighted multitask posterior distribution for which achieving successful and unbiased sampling is challenging. Ensuring robust Bayesian inference in this context hinges on properly estimating the distinct task weights, which integrate the various sources of uncertainties. For instance, the tasks referring to the deterministic PDE model are completed by stochastic representations of the model adequacy and physical constraint discrepancies, and the data-fitting likelihood terms are supplemented by stochastic modeling of the experimental noise. In this sense, BPINNs intend to capture and estimate the various sources of uncertainties whether aleatoric — arising from variability or randomness in the observations like sensor noise — or epistemic — caused by imperfect modeling hypothesis or ignorance in the model adequacy.

Automatic management of these uncertainties, though, remains challenging as this relies on the appropriate setting of the critical weighting parameters arising from the expression of the multitask or multi-objective problem. Unsuitable choices of these weights can result in biased predictions, vanishing task behavior, or substantial instabilities in the HMC formalism. This can even prevent the sampler from identifying the highest posterior probability region, namely the Pareto front neighborhood, corresponding to predictions that correctly balance all the different tasks and are close to the optimum. While manual calibration of the critical weights is still commonplace [173, 199, 207], robust Bayesian inference strategies should not rely on a-priori hand-tuning or biased calibration of the posterior distribution. Appropriately setting these parameters is neither easy nor computationally efficient, especially for multi-objective inverse problems arising from real-world data. Indeed, Psaros *et al.* recently investigated an alternative for adjusting the noise-related weight parameters [249], but this suffers, *inter alia*, from additional computational costs related to the pre-training of a Generative Adversarial Neural Network (GAN). Developing an alternative that accounts for this multitasking consideration becomes crucial to ensure robust sampling when dealing with coupled physics-based and data-driven inference.

### 1.2.5 Machine learning software and libraries

From a numerical perspective, several popular software libraries and tools are commonly used for developing, training, and deploying machine learning models, among which TensorFlow [298] and PyTorch [151] are the most widely spread. Both libraries present similar accuracy and efficiency, are open-source, and can leverage Graphics Processing Unit (GPU) devices to accelerate the training. While TensorFlow has an extensive library of pre-built deep learning models including, for instance, Convolutional Neural Networks (CNN) and, in this sense, is widely used for production applications, PyTorch is an easier and more flexible framework for developing new AI tools. Indeed, the latter mainly relies on the Python underlying libraries and object-oriented paradigm, which renders the library especially attractive for developers.

In particular, an open-source library designed for probabilistic programming and Bayesian inference, which is called Hamiltorch, was developed within the PyTorch framework by Cobb in the late 2010s [82, 83, 84]. This combines the flexibility and automatic differentiation capabilities of PyTorch to achieve back-propagation of the gradients with Bayesian inference approaches for sampling from complex posterior distributions. Various sampling schemes are part of the library among them stochastic MCMC methods such as Hamiltonian Monte Carlo [48], Riemannian Manifold Hamiltonian Monte Carlo [123] and No-U-Turn Sampler [132], but also Variational Inference [177, 322]. Unlike MCMC, the latter is a deterministic technique in Bayesian Inference that aims to approximate the target posterior distribution by minimizing the Kullback-Leibler divergence between the target and the parameterized approximation of the distribution. In this sense, Hamiltorch offers the opportunity to perform Bayesian Inference over neural networks and is, therefore, a valuable support to address BPINNs implementation within a well-suited PyTorch environment. This also presents the flexibility to compare several sampling strategies but also readily incorporate new samplers as part of the library.

Nonetheless, the sampling schemes implemented within the Hamiltorch package do not account for the task-splitting of the posterior distribution and, therefore, neglect the consideration of balanced sampling around the maximum posterior probability region. Indeed, the weighted posterior distribution is regarded as a single-term expression where the weights are manually tuned and a priori estimated. As introduced in Sect. 1.2.4, this can be particularly challenging and prone to biased predictions when considering Bayesian Inference on a multi-objective data assimilation problem, including a PDE model, physical law constraints (*e.g.* incompressibility condition), and data measurements. Such considerations are, however, crucial to ensure robust Bayesian Inference since multitasking becomes a common issue when considering PDE physics-based and data-driven formalism.

## 1.3 Contributions

### 1.3.1 Toward an efficient DNS method for reactive flows at the pore scale

The development of suitable mathematical models and efficient DNS methods for modeling reactive hydrodynamics at the pore scale is an essential aspect in investigating and managing $CO_2$ mineral storage and, therefore, stands as one of the major concerns of the present thesis. In this spirit, we first investigate the modeling and numerical simulation of $CO_2$ mineral trapping mechanisms within the pore space of a porous medium.

To achieve this, we have devised a novel model for calcite crystallization that hinges on a two-step chemical process. This process first accounts for the nucleation of precipitates within the pore space and then nuclei aggregation at the pore interface, ultimately facilitating crystal growth. In the model, we integrate a deterministic Transition State Theory (TST) formulation to describe the initial nucleation step with a probabilistic model, which represents the aggregation step. The latter includes a non-uniform probability of attachment rate to the pore interface, depending on local mineral volume fraction and adsorption frequencies (see Sect 2.7.2 page 47 in Chapter 2). This attachment probability, therefore, hinges on a volumic formulation of the surface crystal growth in preferential areas (adapted from a validated surface model, see Sect. 2.7.2 page 47).

The reactive model is subsequently integrated into a semi-Lagrangian framework that employs a micro-continuum Darcy-Brinkman Stokes (DBS) formulation for the hydrodynamics, hence the need for volumic modeling.

Reactive flow modeling of calcite crystallization at the pore scale is subsequently performed according to this model in order to quantify the macro-properties changes on the upscaled macro-porosity $\phi$ and the permeability $\kappa_0$ introduced in equations (1.1) and (1.2) page 4. We identify pore-clogging effects within the pore-scale geometry and establish its impact on the macro-scale properties (see Figure 2.9 page 53 in Chapter 2). In particular, we demonstrate the significant effect of crystal aggregation — or nuclei adsorption to the mineral surface — on the reactive patterns and highlight that merely considering the transport and nucleation rates is not sufficient to characterize pore-clogging (see Figure 2.10 page 54 in Chapter 2). In this sense, we propose a new characterization of the overall crystallization regimes based on three dimensionless numbers, which makes it possible to account for the nuclei adsorption rates in the different regime characterization (see Sect. 2.7.3 page 50 in Chapter 2).

A numerical formulation of hybrid grid-particle methods has been adapted from the dissolution set of PDEs to the nucleation and crystallization (see Sect. 2.7.2 page 47), involving the modeling of preferential areas for surface crystal growth. The related space-variable diffusion operator has been formulated under a particle-based approach, namely the Particle-Strength-Exchange (PSE) scheme, detailed in Sect. 2.5 page 32.

Finally, we enhance the existing HySoP library [112] (Hybrid Simulation with Particles), which is an efficient HPC framework for modeling reactive hydrodynamics using semi-Lagrangian methods across hybrid hardware setups. Specifically, our efforts are directed toward implementing heterogeneous diffusion operators on GPU accelerators, employing the Open Computing Language (OpenCL) standard and the Particle-Strength-Exchange method (see Sect. 2.5.3 page 35 and 2.6.3 page 42 in Chapter 2). This results in an implementation of reactive flows that encompasses both Central Processing Unit (CPU) and GPU devices. Furthermore, such improvement makes it possible to account for spatially varying diffusion in the porous medium in the hybrid two-scale formalism, namely the Darcy-Brinkman Stokes model, based on the micro-continuum description of the sample. In this sense, this enables better control of the diffusion of the chemical species within the porous matrix $\Omega_S$, under some stability constraints identified in Sect. 2.5.4 page 37 of Chapter 2.

The numerical improvements developed in the present thesis are validated and applied to address $CO_2$ mineral trapping under the form of calcite crystallization within 3D pore scale geometries arising from $\mu$CT images (see Sect 2.7 page 44 in Chapter 2).

### 1.3.2 Robust Artificial Intelligence methodology for Uncertainty Quantification in BPINNs

A second major concern hinges on ensuring the reliability of the pore-scale modeling of $CO_2$ mineral storage and quantifying the inherent uncertainties of the macro-scale properties evolution. To achieve this, the present thesis aims to provide mathematical formulations of Deep Learning methodologies and enhance their reliability by incorporating robust uncertainty quantification assessment to avoid using Artificial Intelligence tools as merely "black boxes".

We investigate this concern within the framework of Bayesian Physics-Informed Neural Networks (BPINNs) and address the actual issue of appropriately setting the weight parameters in the context of multi-objective Bayesian Inference problems, as introduced in Sect. 1.2.4 page 13. In particular, we develop in Chapter 4 a deep-learning alternative that robustly accounts for the multitask considerations which is crucial when considering coupled physics-based and data-driven inference.

In this sense, we propose a novel strategy for the BPINNs that relies on an adaptive and automatic weighting of the target posterior distribution based on an Inverse Dirichlet control of the weights, which leverages gradient variance information of the different tasks (see Sect. 4.4.1 page 105 in Chapter 4). This results in an alternative Markov Chain Monte Carlo (MCMC) sampler that we have named Adaptively Weighted Hamiltonian Monte Carlo (AW-HMC), detailed on Al-

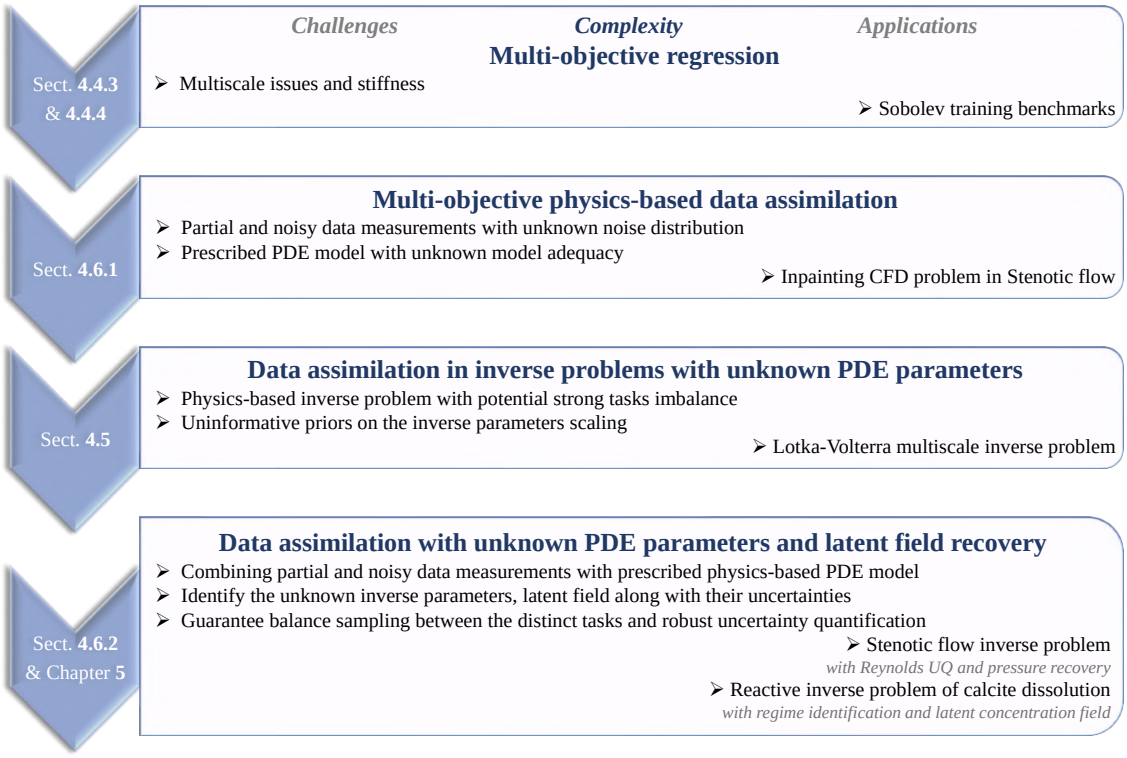


**Figure 1.6: Hierarchic complexity of the data-assimilation problems handled by our novel sampling strategy.** The main challenges corresponding to each problem are presented on the left, along with the different sections and chapters that address them throughout this thesis. And, their related applications are briefly described on the right.

gorithm 1 page 108. It concentrates its sampling on the Pareto front exploration after the adaptive procedure and avoids imbalanced conditions between the different tasks. It also benefits from enhanced convergence and stability compared to conventional samplers and reduces sampling bias by avoiding manual tuning of critical weighting parameters. Furthermore, this guarantees reasonable computational costs compared to the recent alternative of Psaros *et al.* that requires the pre-training of a Generative Adversarial Neural Network (GAN) with a large number of additional parameters. On the contrary, our approach keeps a similar efficiency as the standard Hamiltonian Monte Carlo (HMC) sampler since it merely relies on the gradient information of the distinct tasks, and therefore goes in the direction of the energy sobriety of deep learning approaches.

This new alternative also demonstrated efficiency in managing the scaling sensitivity of the different terms either to noise distributions or multi-scale issues. In fact, the adjusted weights bring intrinsic information on the distinct task uncertainties. This improves the reliability of the noise-related and model adequacy estimates as the uncertainties are quantified with minimal a-priori assumptions on their scaling. From an overall AI perspective, this thesis focuses on developing a robust adaptive weighting strategy to address complex real-world Bayesian inference within the BPINNs framework.

We incorporate this novel alternative in PyTorch by performing an extensive reformulation of the Hamiltorch library so that it now accounts for the multitask formulation of the target posterior distribution. We subsequently implement the AW-HMC sampler within this improved framework and, therefore, benefit from its original flexibility to compare with other sampling strategies and address Bayesian inference on CPU or GPU devices.

Finally, our novel sampling strategy demonstrates outstanding performances on several levels of complexity. This covers applications ranging from data-fitting predictions based on sparse measurements, physics-based data-assimilation problems, data-assimilation in inverse problems with unknown PDE model parameters, and data-assimilation in inverse problems with unknown parameters and latent fields (see Figure 1.6). Indeed, this adaptive weighting sampling presents the ability to effectively address multiscale and multitask inverse problems, to couple uncertainty

quantification with physical priors, and to handle sparse noisy data. It also showed effectiveness in addressing stiff dynamics problems including latent field reconstruction and deriving unbiased uncertainty information from the measurement data (see Sect. 4.6.2 page 129 in Chapter 4 and Chapter 5). Taken together, the AW-HMC sampler enhances BPINNs robustness and offers a promising alternative as an overall data-assimilation strategy. This makes it possible to extend its applications to more complex inference problems and achieve reliable Bayesian inference in multitask inverse problems.

### 1.3.3 Reliability estimates: the macro-scale permeability

Ensuring reliable changes in the petrophysical properties, namely the macro-porosity $\phi$ and permeability $\kappa_0$, hinges on correctly estimating the micro-scale evolutions due to $CO_2$ geochemical interactions with the porous environment. We investigate that changes in the macro-scale properties, observed through DNS of reactive flows at the pore-scale, result from meaningful geochemical interactions rather than intrinsic uncertainties. This aims to query the reliability of the DNS given the uncertainties arising from the X-ray $\mu$CT imaging process, along with discrepancies in the estimations of kinetic parameters and reaction rates.

Consequently, we firstly address the macro-scale permeability deviations resulting from $\mu$CT limitations, namely uncertainties related to the unresolved morphological features and the pore interface location, as introduced in Sect. 1.1.3 page 4. This is achieved in Chapter 3 through an upscaling direct approach based on a slip-length formalism that models both the unseen roughness effects and the approximation in the interface position.

While the idea of using slip formalism has been extensively studied to theoretically approximate surface roughness, we propose two strategies to investigate in practice the permeability deviations on real rock geometries (see Sect. 3.3.1 page 60 in Chapter 3). The first one directly aims to solve for a Stokes flow in the pore space with Navier boundary conditions characterized by a prescribed slip length at the fluid/solid interface. The second one theoretically establishes the permeability deviation as a correction of the permeability $\kappa_0$ by slip-correction terms of first and second order, arising from the solution of Stokes-like closure problems at successive orders. These successive problems are determined by a two-scale asymptotic expansion analysis and involve non-homogeneous Dirichlet boundary conditions involving a prescribed slip (see Sect. 3.4 page 65 in Chapter 3).

However, such formalism requires a proper estimation of meaningful slip coefficients which are related to the $\mu$CT uncertainties, and an effective management of the slip boundary condition at the pore interface. The first point is addressed in Sect. 3.6.1 page 74 by modeling the effects, within a voxel, of periodic roughness patterns of different shapes on the slip length values. The second point, however, needs to develop a numerical solver for Stokes that properly handles slip boundary conditions. While the Darcy-Brinkman Stokes formulation of the hydrodynamics accounts for flow penetration within the porous matrix and therefore intrinsically introduces a residual slip, this approach is unsuitable to study Stokes flow with a prescribed slip (see Sect. 3.5.1 page 69 in Chapter 3). Similarly to penalization techniques, the Darcy-Brinkman Stokes (DBS) model indeed generates a transition layer depending on the micro-porosity that makes it difficult to properly manage the slip at the interface. Hence, we develop an in-house code, based on a Generalized Minimal Residual Method (GMRES) solver, to address Stokes flow with slip and demonstrate that this ensures a robust control of the boundary conditions (see Sect. 3.5.2 page 70 in Chapter 3). In this sense, one makes sure that the permeability deviations computed are representative of slip-length values characterizing the $\mu$CT uncertainties.

This numerical code is validated and applied to quantify uncertainty ranges on the permeability $\kappa_0$ of several 3D porous samples, for which we compare the first-order linear and full permeability deviations (see Sect. 3.6 page 74 in Chapter 3). We emphasize, in Sect. 3.7 page 87, the significant relevance of the second-order deviation in explaining the apparent macroscopic effects on permeability in rock geometries arising from $\mu$CT images. Finally, we identify a dimensionless ratio depending on the relative permeability deviation and the specific area, which is likely to serve as a representative criterion for the porous samples. Overall, this provides a numerical framework to

investigate permeability uncertainties and query its significant evolution along a reactive process.

### 1.3.4 Reliability estimates: porosity fields and reactive parameters

Beyond the morphological aspects described in the previous section, this thesis targets data assimilation and field reconstruction to provide an accurate local description of porous materials by observing their dissolution through dynamical $\mu$CT experiments. The objective is to explore the morphological uncertainties that stem from X-ray $\mu$CT limitations and to quantify the subresolved micro-porosity within the initial porous medium by incorporating information derived from the dynamical process (see Chapter 5). This guarantees reliable quantification of the micro-porosity changes during the geochemical transformation of calcite dissolution.

In addition to the morphological uncertainty assessment on the micro-porosity field $\varepsilon$ at the pore scale, this aims to characterize the experimental reaction rates and dissolution regimes by identifying the proper dimensionless numbers through an inverse problem approach (see Sect. 5.4.3 page 143 in Chapter 5). Therefore, we derive uncertainty ranges on the kinetic parameters by combining prescribed PDE models and dissolution experiments, which afterward renders reliable the calibration of the reaction rates for the direct numerical simulations. This also avoids using DNS reactive parameters merely estimated from laboratory experiments, which may not be representative of the pore scale dynamics and are subject to wide discrepancies.

Considering standard variational data assimilation approaches on such reactive flow problems would be challenging, mainly due to the computational cost and complexity hinging on the direct numerical simulation of these phenomena. In this sense, relying on a robust AI methodology to achieve data assimilation and inverse problems coupling complex and non-linear physics-based PDE with noisy $\mu$CT dissolution images is a worthwhile alternative.

Consequently, we exploit the efficient data assimilation framework developed in Chapter 4 to address reactive inverse problems integrating uncertainty quantification. We investigate a multitask formulation of calcite dissolution inverse problems and establish a new methodology of sequential reinforcement approach that successively incorporates additional PDE constraints into the data assimilation workflow (see Sect. 5.5.2 page 146 in Chapter 5). Besides, we highlight computational efficiency related to suitable formulations of complex and non-linear differential operators, especially when considering heterogeneous diffusion within the porous matrix (see Sect. 5.5.3 page 149 in Chapter 5). We apply this methodology to 1D+Time and 2D+Time calcite dissolution problems based on synthetic $\mu$CT images encompassing varying porosity levels. This demonstrates successful uncertainty quantification on the kinetic parameters and the estimation of the micro-porosity field (see Sect. 5.6 page 151 and 5.7 page 159 in Chapter 5). The later uncertainties on the field $\varepsilon$ can subsequently translate into distributions on the macro-porosity $\phi$ at Darcy's scale.

Compared to machine learning alternatives in geosciences, the main novelty of this work lies in the robust assessment of uncertainties related to unresolved morphological features and mineral reactivity by integrating physics-based models with data-driven techniques. In this sense, this would provide deeper insights into the relationship between experimental data and mathematical modeling theory, significantly enhancing the confidence in DNS approaches for $CO_2$ mineral storage modeling.

## 1.4 Manuscript outline

The manuscript is organized into six chapters as follows:

Chapter 2 establishes the DNS framework and mathematical models for investigating reactive flows at the pore scale in complex geometries arising from X-ray $\mu$CT experiments. In particular, we describe the hybrid micro-continuum DBS reactive model and the semi-Lagrangian methodology along with the improvements addressed in this thesis. We subsequently present our two-step crystallization model and apply it in the context of $CO_2$ mineral trapping in real rock geometries.

We investigate macro-properties alterations, different precipitation regimes, and pore-clogging effects.

The rest of the manuscript focuses on the reliability concerns of pore-scale modeling of reactive flows. We address the macro-scale permeability deviations, quantification of the uncertainties on the sub-resolved micro-porosity field, and robust calibration of the kinetic parameters along with their uncertainty ranges.

Chapter 3 is dedicated to characterizing the reliability of the macro-scale permeability subject to unresolved morphological features and the approximated location of the pore interface. We develop the upscaling approach based on slip-length formalism and present its practical use in 3D complex geometries arising from $\mu$CT images.

In Chapter 4, we develop our novel data assimilation framework which relies on the automatic sampling of weighted multi-objective problems, arising from the coupling of physics-based PDE systems with data-driven approaches. This results in a robust deep learning methodology for uncertainty quantification within the BPINNs that is extensively validated on several benchmarks and test cases of different complexities.

In Chapter 5, this novel framework serves as a basis to address Bayesian Inference in reactive inverse problems of calcite dissolution. We target data assimilation and field reconstruction of the potentially sub-resolved micro-porosity through the observation of the dynamical dissolution of synthetic calcite cores. We estimate reliability ranges on the dimensionless numbers characterizing the dissolution regime (including the chemical kinetic coefficients and molecular diffusion) along with local uncertainties on the micro-porosity field.

Chapter 6 recalls the various outcomes of the current thesis and presents several perspectives and possibilities for, *inter alia*, improving the present DNS methodology and broadening the applications of our data assimilation framework within the context of $CO_2$ mineral storage.

Different highlights or questions addressed in every chapter are recalled in their respective *Context and positioning* sections.

CHAPTER 2

# Direct Numerical Simulation of reactive flows at the pore-scale for $CO_2$ mineral storage into carbonate porous media

## Contents



## 2.1 Motivation

Studying reactive flows in porous media is essential to manage the geochemical effects arising from $CO_2$ capture and storage in natural underground reservoirs. While long-term predictions are commonly modeled at the field scale [81], pore-scale approaches meanwhile provide insights into local geochemical interactions between the injected $CO_2$ and the aquifer structure [232]. Through mathematical homogenization of the sub-micrometer porous medium and appropriate modeling, one can simulate the reactive processes that occur at the pore scale and predict their impact on the macro-scale properties [11, 12]. Geochemical processes are critical components for understanding the mineral trapping mechanisms and local evolving interfaces within the porous environment.

In this sense, investigating the impact of such reactive processes provides insight into reservoir safety submitted to chemical interactions that may compromise the aquifer structure. Pore-scale modeling of reactive flow hence appears as a complementary mean to field scale studies wherein homogenization theory bridges the gap between these scales.

In this context, several geochemical mechanisms play a critical role in the $CO_2$ sequestration process and mainly involve precipitation, crystallization, and dissolution phenomena. On one side, carbonate precipitation and crystallization ensure efficient capture of the injected $CO_2$ in the form of minerals such as calcite, aragonite, or dolomite: this is referred to as mineral trapping, which informs about the storage capacities of the reservoir. These processes significantly impact the flow within the porous sample at the pore scale, leading to restructuring of the flow path and morphological changes that alter, *inter alia*, the pore size distribution and the roughness of the interface due to partial or complete clogging of pore throats. Such alterations at the micro-scale subsequently alter the estimation of the macro-scale properties, namely the porosity and permeability, and thereby require investigations to ensure wise management of the underground reservoir structures. On the other side, the reverse chemical process can also occur, resulting in carbonate mineral dissolution due to an acidification of the aqueous solution. This may compromise not only the efficiency of the trapping mechanisms, leading to an increase of both porosity and permeability, but also the integrity of the reservoir cap rock, and is, therefore, of great interest to prevent acute leakage issues. In this sense, one needs reliable estimations of the macro-properties changes due to these overall geochemical processes at the pore scale, to manage their impact on the reservoir scale modeling of $CO_2$ storage. This can be achieved through, first, efficient DNS of reactive flows at the pore-scale and, subsequently, by embedding uncertainty concerns on the quantification of the petrophysical properties. In the present chapter, we address the first point with a focus on precipitation and crystallization modeling for $CO_2$ mineral storage into carbonate porous media.

## 2.2 Context and positioning

Pore-scale investigation of reactive geochemical systems has garnered interest over the past decades based on imaging processes and laboratory experiments [200, 218, 273], numerical simulations [232, 280], and a combination thereof [204, 220]. In this sense, image-based DNS coupling $\mu$CT characterization of a porous sample REV with efficient scientific computing and numerical method appears as a promising tool to query the impact of reactive processes on real rock geometries. While some pore-scale modeling approaches consider conceptual simplification of the pore structure [169, 198], we account throughout this thesis for the complex 3D morphology of the porous medium. The latter can subsequently be incorporated into mesh-based or grid-based methods, as presented in Sect. 1.2.1 from Chapter 1, or eventually combined with particle methods. Indeed, Lagrangian and particle methods exhibit significant advantages to model transport-dominant regimes, and therefore, hybrid formalisms coupling grid-based approaches with particles present an interesting alternative to purely Eulerian or Lagrangian models [41, 71, 88]. The current chapter relies on such a semi-Lagrangian approach, which handles a Lagrangian description of the chemistry with underlying grid methods for the hydrodynamic, based on the superficial velocity formalism introduced in the 1980s by Quintard and Whitaker [250]. The latter makes it possible to account for the involvement of the porous matrix in the overall flow process through a micro-continuum description of the medium. In this sense, one considers an intermediate state between the full resolution of each individual solid grain and the completely averaged continuum representation of the porous media at Darcy's scale. This establishes two-scale models that are widely used in hydrodynamics pore-scale modeling and $\mu$CT image-based DNS [204, 227, 279].

The present semi-Lagrangian formalism has been successfully employed in the context of carbonate dissolution at the pore scale [113] and extensively benchmarked against state-of-the-art numerical alternatives [204]. In this chapter, we rely on this existing numerical model to build some improvements, particularly in the management of highly heterogeneous diffusion arising from Archie's law in the two-scale description of the medium. We first demonstrate the relevant use of particle-based approaches in the approximation of Archie's law term that accounts for a

reduced diffusion of the chemical species in the porous matrix. We subsequently incorporate such a particle formulation within the numerical framework through a dedicated implementation for HPC on hybrid architectures, coupling CPU and GPU devices.

The other contributions of this chapter lie in the modeling aspects of $CO_2$ mineral trapping under the form of calcite crystal aggregates at the pore scale. Precipitation kinetics of calcite have been historically studied since the 1970s from the experimental and theoretical sides [77, 156, 245], and this has commonly established Transition State Theory (TST) as an efficient and straightforward way of predicting mineral reaction rate. Indeed, the deterministic TST is currently one of the most widely used models in reactive transport codes and DNS [206, 219, 222, 282]. However, several doubts have risen in the research community about using such a deterministic approach for predicting crystal growth rates. In particular, comparison with experimentally determined growth rates has highlighted a wide range of discrepancies, querying the reliability of the TST model for overall crystallization processes [131, 240]. Meanwhile, probabilistic approaches, which find their origins in classical nucleation theory and the probabilistic nature of the precipitation and crystal growth mechanisms, have been developed [194, 223, 320]. These models make it possible to incorporate, *inter alia*, the effects of induction time characterizing the onset of the nucleation, the ionic affinities of the growing sites, and attachment frequencies of the ionic species involved in the reaction. Such attachment frequencies are, especially, significant for modeling surface adsorption and crystal aggregation that largely hinges on the surrounding porous structure in the sense that kinks or corners, for instance, are experimentally identified as preferential growing sites. However, such a geometrical dependency of the crystal aggregation is commonly neglected in most models, which makes it difficult to predict the spatial distribution of the new crystals.

Therefore, we developed a two-step crystallization process wherein nuclei generation relies on a deterministic TST model before considering the probabilistic mineral aggregation — crystal growth — into the pore interface. The latter accounts for adsorption frequencies of the precipitate to the growth sites, which is weighted by a non-uniform probability of attachment rate depending on local mineral volume fraction. In this sense, we incorporate local geometrical dependency at the pore scale in the overall crystallization model, which is crucial to ensure reliable prediction of pore clogging. We subsequently use this model for calcite crystallization into a carbonate porous medium, arising from $\mu$CT observations, and investigate both the impact on the macro-scale properties evolution and the effects of several dominant regimes on the precipitation and crystal growth patterns. In this sense, we propose a characterization of the crystallization regime based on three distinct dimensionless numbers, including, for the first time, the effects of nuclei adsorption — or crystal aggregation — in this regime characterization. We demonstrate that the first nucleation process and the crystal aggregation through surface adsorption play a critical role in the pore-clogging and precipitation patterns.

Overall, the main contributions of this chapter can be summarized as follows:

1. A two-step crystallization model is developed, accounting for preferential areas of surface crystal growth through a probabilistic nuclei aggregation rate.
2. Using three dedicated dimensionless numbers improves the usual classification of precipitation/crystallization regimes. Different reactive patterns are identified, eventually leading to pore-clogging.
3. We adapt and improve the hybrid Semi-Lagrangian method from dissolution to precipitation/crystallization processes, integrating a PSE formulation of the spatially varying diffusion operator. A GPU implementation is provided within the Hybrid Simulation with Particles (HySoP) numerical framework.
4. We monitor the macro-scale properties evolution resulting from $CO_2$ mineral trapping, modeled by calcite precipitation and crystallization at the same time.

The chapter is organized as follows: In Sect. 2.3, we present the pore scale hydrodynamics model and describe the governing equations of reactive transport and diffusion based on the two-scale representation of a heterogeneous porous medium. Sect. 2.4 explains the semi-Lagrangian

formalism on which we rely for the DNS of CO2 mineral storage, along with the splitting operator strategy that efficiently combines with such a hybrid grid-particle approach. In Sect. 2.5, we establish the particle-based approximation of the heterogeneous diffusion arising from Archie's law and query the stability concerns of this term in complex pore-scale geometries. Sect. 2.6 is dedicated to the HPC numerical framework and the implementation of the previous particle formulation for GPU devices along with its validation and performance analyses. Finally, in Sect. 2.7 we develop our new crystallization model and apply it to DNS of $CO_2$ mineral trapping into carbonate porous media. The evolution of the macro-scale properties and the effects of crystallization regimes on the clogging is especially investigated in Sect. 2.7.3. Sect. 2.8 concludes this analysis and highlights future challenges regarding uncertainty quantification for application to $CO_2$ mineral storage.

## 2.3 Reactive hydrodynamics at the pore scale

The present section focuses on the modeling of reactive hydrodynamics in the context of $CO_2$ mineral storage and presents the mathematical model used to simulate reactive processes at the pore scale. We first introduce the so-called Darcy-Brinkman-Stokes formulation for microfluidic flows based on superficial velocity formalism. We subsequently incorporate transport-reaction-diffusion equations modeling the geochemical interactions between the different species involved. Finally, we present an alternative formulation in velocity-vorticity for the hydrodynamics equation, which ensures the fluid incompressibility condition.

### 2.3.1 Darcy-Brinkman-Stokes formulation at the pore scale: a superficial velocity formalism

We introduce a spatial domain $\Omega \subset \mathbb{R}^n$, $n = 1, 2, 3$ which corresponds to the porous medium described at its pore scale. This sample description involves a pure fluid region $\Omega_F$, also called void-space and assumed to be a smooth connected open set, and a surrounding solid matrix $\Omega_S$ itself considered as a porous region. This region is seen as complementing the full domain $\Omega$, which in practice represents the computational box of the numerical simulations such that $\Omega_F = \Omega \setminus \overline{\Omega}_S$, and the internal fluid/solid interface is denoted $\Sigma$. We denote the computational domain boundary by $\partial\Omega$ and use $\Gamma_F = \partial\Omega \cap \Omega_F$ and $\Gamma_S = \partial\Omega \cap \Omega_S$ to refer to the fluid and solid parts of the computational domain boundary, respectively, such that $\partial\Omega = \Gamma_F \cup \Gamma_S$ (*e.g.* see Figure 1.1 in Chapter 1 or Figure 3.1 in Chapter 3).

The boundary conditions at the inlet and outlet faces, typically for a cubic computational domain $\Omega = ]0, l[^3$ but not exclusively, either impose a prescribed flow rate $\overline{u}$ on the velocity or satisfy periodic boundary conditions for a prescribed driving force $f$. The boundary conditions on the other lateral faces are systematically periodic since rock samples are commonly constrained in an impermeable solid casing when $\mu$CT experiments are conducted. In this sense, it ensures a consistent numerical representation of the sample compared to the experiments. This also guarantees $\mathcal{C}^\infty$ regularity on the boundary even if the domain exhibit corners, since the problem can be formalized by considering the equivalence relationship with the quotient space $\Omega \equiv \mathcal{Q}/G$ where $\mathcal{Q} = \mathbb{R}^2 \times ]0, l[$ and $G = l\mathbb{Z}^2 \times \{0\}$ (*e.g.* see [261] for detailed configurations of acceptable domains).

From the $\mu$CT images, we can also characterize the static pore-space structure, corresponding to the sample's initial state before any geochemical interactions. In this sense, we denote by $\varepsilon = \varepsilon_f = 1 - \varepsilon_s$ the micro-porosity field defined on $\Omega$, given $\varepsilon_f$ and $\varepsilon_s$ respectively the volume fractions of void and solid according to usual notations [279]. This defines a micro continuum description of the porous medium such that $\varepsilon = 1$ in the pure fluid region $\Omega_F$ and takes a small value in the surrounding matrix $\Omega_S$. In fact, the local micro-porosity $\varepsilon$ is assumed to have a strictly positive lower bound $\varepsilon(x, t) \geqslant \varepsilon_0 > 0$ for all $(x, t)$ in the spatiotemporal domain $\Omega \times [0, T_f]$ for a final real-time $T_f > 0$ in the reactive process. This lower bound $\varepsilon_0$ characterizes the residual porosity of the porous matrix, potentially unresolved due to X-ray $\mu$CT imaging limitations as introduced in Sect. 1.1.3 of Chapter 1 (see also Figure 1.1). In practice, we assume throughout

this chapter $\varepsilon_0 = 5\%$. Considerations on the estimation of this residual porosity bound will, however, be investigated in Chapter 5 in the context of uncertainty quantification and reliability of the pore-scale models. This micro-continuum formulation at the pore scale relies on a two-scale representation of the sample characterized by its micro-porosity field $\varepsilon$.

Such a two-scale description of the local heterogeneities in the carbonate rocks is appropriate to simulate the pore-scale physics and establish the governing flow and transport equations in each distinct region. Indeed, although the hydrodynamic of a viscous flow in a pure fluid region is commonly quantified through the Navier-Stokes equation, we can formulate the problem on the whole domain $\Omega$ based on the two-scale micro continuum description of the medium. We, therefore, consider the model on the superficial velocity $u$ introduced and derived rigorously by Quintard and Whitaker in the late 80s [250] and commonly used until nowadays [159, 204, 279, 321]:

$$\varepsilon^{-1}\frac{\partial \rho u}{\partial t} + \varepsilon^{-1}\mathrm{div}(\varepsilon^{-1}\rho u \otimes u) - \varepsilon^{-1}\mathrm{div}(2\mu D(u)) + \mu^* K_\varepsilon^{-1} u = f - \nabla p \tag{2.1}$$

along with the divergence-free condition $\mathrm{div}\, u := \nabla \cdot u = 0$. It is noticeable that this incompressibility condition should be changed when considering evolving porous structures to account for density variations, especially in the context of fast dissolution or nucleation [280]. Indeed, this only depicts that crystal nucleation within a liquid volume, for instance, drastically increases the density and induces divergence effects in its neighborhood. Nevertheless, the divergence-free condition can be assumed to remain if the characteristic time of fluid/solid interface changes is way larger than the hydrodynamics time scale [279], which is the case for our study. In equation (2.1), the notation $D(u)$ refers the shear-rate tensor $D(u) = (\nabla u + \nabla u^T)/2$, $\mu$ is the dynamic viscosity, $p$ is the volumic pressure, $f$ the volumic driving force and $\rho$ the fluid density. The related viscosity $\mu^*$ usually coincides with the fluid viscosity $\mu$ but may be different in order to account for viscous deviations.

The quantities $\rho$, $\mu$, $\mu^*$ and $f$ are assumed to be constant. The quantities $\varepsilon$, $\rho$, $\mu$ and $p$ are scalar fields, $u$, its rotational $\omega = \nabla \times u$, $f$ and $\nabla p$ are vector fields, while $D(u)$ and $K_\varepsilon$ are matrices.

The permeability $K_\varepsilon$ refers to the micro-scale permeability and depends on the local micro-porosity field $\varepsilon$. In fact, the permeability of the micro-porous domain is modeled by the empirical Kozeny-Carman relationship [67, 68, 147]:

$$K_\varepsilon^{-1} = \kappa_b^{-1}\frac{(1-\varepsilon)^2}{\varepsilon^3} \tag{2.2}$$

where $\kappa_b$ is the bulk permeability, which can be taken as a coarse estimation of the reference macro-scale permeability $\kappa_0$. For instance, Soulaine *et al.* [279] estimated that four orders of magnitude below the permeability are required for $\kappa_b$ to ensure adherent boundary conditions at the pore interface. In this chapter, we consider both $K_\varepsilon$, $\kappa_b$ and $\kappa_0$ as scalars, meaning we restrict ourselves to the isotropic case although this formalism can be extended to anisotropic porous media. The superficial velocity formulation (2.1) defines a two-scale model that can be solved on the overall domain $\Omega$ — using, for instance, penalization principles — and retrieves the usual Navier-Stokes equation in the pure fluid region $\Omega_F$ (since $K_\varepsilon^{-1} = 0$ for $\varepsilon = 1$). Depending on the flow regime hypothesis, one can also encounter simplified versions of equation (2.1) wherein some terms can be neglected. In the context of pore-scale simulations, in particular, the inertial effects become negligible compared to viscous forces due to low Reynolds number, denoted $\mathrm{Re}$. The latter is a characteristic dimensionless number defined as:

$$\mathrm{Re} = \rho \overline{u} L/\mu, \tag{2.3}$$

where $\overline{u}$ and $L$ are respectively the characteristic velocity and length of the sample. The characteristic length $L$ can be related to average pore throat diameters and, therefore, we typically fall within the assumption $\mathrm{Re} \ll 1$ throughout this chapter.

At low Reynolds numbers and for highly viscous Darcian flows, equation (2.1) hence reduces to the following DBS model:

$$-\mathrm{div}(2\mu D(u)) + \mu\kappa_b^{-1}\frac{(1-\varepsilon)^2}{\varepsilon^2}u = \varepsilon(f - \nabla p), \quad \text{in} \quad \Omega \tag{2.4}$$

where $\mu^* = \mu$ for sake of readability. In the present work, we consider this DBS equation (2.4), which is adequate in the flow regime hypothesis of low Reynolds number representative in pore-scale modeling. The DBS equation based on the superficial velocity is an efficient formalism to model the hydrodynamic in multi-scale porous media, and account for heterogeneous porosity levels.

### 2.3.2 Reactive flow model: general formulation

The DBS flow model (2.4) needs to be complemented by transport-reaction-diffusion equations of the different species involved in the geochemical processes. These equations are derived from the mass balance of the chemical species [279], and can be written under the form:

$$\frac{\partial \varepsilon \widetilde{C}_k}{\partial t} + \mathrm{div}(u\widetilde{C}_k) - \mathrm{div}\left(\alpha_k(\varepsilon)\varepsilon\nabla\widetilde{C}_k\right) = \dot{m}_k/M_k, \tag{2.5}$$

where $\widetilde{C}_k = \rho_f \overline{\omega}_{f,k}/M_k$ is a concentration per unit of fluid with $M_k$ the molar mass and $\dot{m}_k$ the rate of mass transfer for the $k^{\text{th}}$ species. We here follow the notations introduced by Quintard and Whitaker in [250], and afterward used by Soulaine and al. in [279], where $\rho_f$ is the fluid density and $\overline{\omega}_{f,k}$ is the mass fraction of the $k^{\text{th}}$ component averaged on the fluid phase. The term $\alpha_k(\varepsilon)$ is a space-variable effective diffusion coefficient and accounts for a reduced diffusion in the surrounding porous matrix due to the tortuosity effect, which is usually quantified using Archie's law [29]:

$$\alpha_k(\varepsilon) = D_{m,k}\varepsilon^{\eta}. \tag{2.6}$$

In this empirical relationship, $\eta$ refers to the tortuosity index and $D_{m,k}$ to the molecular diffusion of the considered species [311]. We finally introduce $C_k = \varepsilon\widetilde{C}_k$, so that the equation (2.5) is written:

$$\frac{\partial C_k}{\partial t} + \mathrm{div}(\varepsilon^{-1}uC_k) - \mathrm{div}\left(D_{m,k}\varepsilon^{1+\eta}\nabla(\varepsilon^{-1}C_k)\right) = R_k(\mathbf{C}), \tag{2.7}$$

which is no more than a superficial modeling of the chemistry, that is to say $C_k$ is the amount of moles per unit of volume while $\widetilde{C}_k$ is the amount of moles per unit of fluid volume. The notation $R_k(\mathbf{C})$ refers to a function (without differential operators) that models the rate contribution of the chemical reactions for the $k^{\text{th}}$ component, where we denote by $\mathbf{C} \in \mathbb{R}^{N_s}$ the vector of the concentrations $C_k$ of all the $N_s$ chemical species. The $k^{\text{th}}$ rate contribution $R_k(\mathbf{C})$ is, practically, the balance of kinetics of all reactions involving the $k^{\text{th}}$ species. The sign of individual reaction rates lies in the nature of the species $k$ considered, either positive for a chemical product or negative for a reactant.

The model (2.7) is the formalism that we retain for the aqueous species in the liquid phase. In particular, this model highlights a superficial gradient operator denoted $\nabla^{\varepsilon} := \varepsilon\nabla\varepsilon^{-1}$ involved in the heterogeneous diffusion arising from the Archie's law. One should notice that the superficial gradient can become highly sensitive at the mineral boundary, mainly due to jumps in the porosity levels on either side of the interface, and thus will require special considerations to adequately manage evolving medium under reactive processes.

Concerning the solid phase of concentration $C_{(s)}$ (*e.g.* the $k^{\text{th}}$ component in vector $\mathbf{C}$), which we assume contains only one chemical species of molar volume $\upsilon$, it is not subject to transport or diffusion, so that

$$\frac{\partial C_{(s)}}{\partial t} = R_k(\mathbf{C}). \tag{2.8}$$

This solid concentration is subsequently linked to the micro-porosity $\varepsilon$ by the relation $C_{(s)} = (1-\varepsilon)/\upsilon$, so one gets

$$\frac{\partial \varepsilon}{\partial t} = -\upsilon R_k(\mathbf{C}). \tag{2.9}$$

In the case of a typical reaction involving a unique solid $X_{(s)}$ of molar volume $\upsilon$, and two aqueous species Y and Z in the liquid phase, with their respective positive stoechiometric

coefficients $\chi_i$ and following, for instance, the general chemical reaction:

$$\chi_1 \, \mathrm{X}_{(\mathrm{s})} + \chi_2 \, \mathrm{Y} \rightleftharpoons \chi_3 \, \mathrm{Z}, \tag{2.10}$$

we define the vector of concentrations $\mathbf{C} := (C_1, C_2, C_3)^T = \big([\mathrm{X}_{(\mathrm{s})}], [\mathrm{Y}], [\mathrm{Z}]\big)^T \in \mathbb{R}^3$. Since there is only one reaction, one gets a unique kinetic balance written as $R_i(\mathbf{C}) = \pm\chi_i R(\mathbf{C})$, with $R(\mathbf{C})$ the kinetic rate. By default, we assume a positive sign for the solid species, so that one follows the convention $R(\mathbf{C}) < 0$ for the forward reaction corresponding to the solid $\mathrm{X}_{(\mathrm{s})}$ dissolution (see Sect. 5.3.1 from Chapter 5), while $R(\mathbf{C}) > 0$ for the reverse reaction (*e.g.* precipitation and crystallization processes whose models are detailed in Sect. 2.7). The sign for the aqueous species subsequently depends on its interaction with the solid $\mathrm{X}_{(\mathrm{s})}$: we get a plus sign for species Y, which is either consumed or produced in the same way as the solid, and a minus sign for species Z, which behaves oppositely. The reaction rate $R(\mathbf{C})$ can involve many concentrations, specific areas, chemical activities, equilibrium constants, etc. (see Sect. 2.7 for practical examples and further details).

Along with its boundary and initial conditions, the model for reaction (2.10) defines a set of partial differential equations modeling reactive flows at the pore scale:

$$\begin{cases} -\mathrm{div}(2\mu D(u)) + \mu\kappa_b^{-1}\dfrac{(1-\varepsilon)^2}{\varepsilon^2}u = \varepsilon(f - \nabla p), & \text{in } \Omega\times]0,T_f[ \\ \dfrac{\partial C_1}{\partial t} = \chi_1 \, R(\mathbf{C}), & \text{in } \Omega\times]0,T_f[ \\ \dfrac{\partial C_2}{\partial t} + \mathrm{div}(\varepsilon^{-1}uC_2) - \mathrm{div}\left(D_{m,2}\varepsilon^{1+\eta}\nabla(\varepsilon^{-1}C_2)\right) = \chi_2 R(\mathbf{C}), & \text{in } \Omega\times]0,T_f[ \\ \dfrac{\partial C_3}{\partial t} + \mathrm{div}(\varepsilon^{-1}uC_3) - \mathrm{div}\left(D_{m,3}\varepsilon^{1+\eta}\nabla(\varepsilon^{-1}C_3)\right) = -\chi_3 R(\mathbf{C}), & \text{in } \Omega\times]0,T_f[ \\ \varepsilon = 1 - \upsilon C_1, & \text{in } \Omega\times]0,T_f[ \\ \text{+ adequate boundary and initial conditions, along with } \mathrm{div}\, u = 0 \end{cases} \tag{2.11}$$

which is strongly coupled, since $u$ and $\mathbf{C}$ depend on each other by means of the micro-porosity changes $\varepsilon$ during the chemical process. It is also possible to straightforwardly substitute $C_1$ with $\varepsilon$ in this system (2.11). Finally, one can notice that the reactive system (2.11) is valid on the whole domain $\Omega$, whether the local state is fluid or not. In the pure fluid region, this system indeed converges toward a Stokes hydrodynamic model coupled with a standard transport-diffusion equation. Mathematical modeling of reactive hydrodynamics at the pore-scale can be expressed under the general form of the PDE system (2.11) coupling DBS with transport-diffusion-reaction equations.

One can notice that $\varepsilon \leqslant 1$ by definition (the 5th equation of (2.11)) as long as the system remains physically admissible — with positive concentrations — which is guaranteed by a meaningful reaction rate $R(\mathbf{C})$. Moreover, if $\varepsilon$ evolves too close to 0, the reactants no longer reach the residual fluid space located in the porous matrix — with minimal porosity $\varepsilon_0 > 0$ — due to tortuosity effects, so the reaction rate $R(\mathbf{C})$ is supposed to stop by reaching an equilibrium. These properties are satisfied for all the reactions considered in the present thesis, for example, in the crystallization or dissolution reaction rates given by the relations (2.71) page 49, or (5.3) page 139. Consequently, the micro-porosity $\varepsilon$ remains in the range $[\varepsilon_0, 1]$ which provides a well-posed Darcy-Brinkman-Stokes equation for the flow (the 1st equation of (2.11)).

This can be extended naturally to systems of reactions involving as many aqueous species in the liquid phase as needed, and involving potentially several solid — in this case the porosity is a linear combination of solid species. In the present thesis, we mainly focus on carbonate porous media and thereby target chemical reactions such as dissolution or precipitation of calcite. Indeed, investigating heterogeneous mineral structures with more complex interactions like dolomitization [183], where dissolved calcite is replaced by dolomite crystals in contact with magnesium-rich water, would require integrating a more efficient numerical library dedicated to chemistry within the computational framework. Specific reaction terms will be detailed, case-by-case, in

the different chemical processes throughout the thesis. Most of the configurations studied in this thesis involve solid calcite — or calcium carbonate — whose concentration is denoted $C_{\mathrm{CaCO_3}(s)}$ or $[\mathrm{CaCO_3}]$, and whose molar volume is given by $\upsilon = 36.93\mathrm{e}{-3}\,\mathrm{L.mol}^{-1}$.

### 2.3.3 A velocity-vorticity formulation

Two distinct approaches are successfully used in the literature to solve numerically the DBS equation (2.4), namely the velocity-pressure or velocity-vorticity formulations [135, 154, 204, 242]. The latter, inherited from vortex methods [72, 92, 110, 130] introduces the vorticity field $\omega$ which is intrinsically related to the fluid velocity $u$ through the relation:

$$\omega = \nabla \times u. \tag{2.12}$$

Several advantages arise when considering the velocity-vorticity formulation that regards the PDE unknowns $(u, \omega)$ and can be interpreted as describing the local spinning motions generated by the flow constraints. First of all, one can benefit from the velocity projection on divergence-free fields, and thereby analytically ensures the incompressibility condition $\mathrm{div}\, u = 0$. Secondly, this formalism can be effectively coupled with splitting strategies that sequentially separate the resolution of distinct physical phenomena, such as convection and diffusion (see Sect. 2.4.3). Finally, this also makes it possible to eliminate the pressure unknown from the momentum equation by applying the curl operator on the DBS equation, which reads as follows:

$$-\mu\Delta\omega \;+\; \mu\kappa_b^{-1}\nabla\times\left(\frac{(1-\varepsilon)^2}{\varepsilon^2}u\right) = \nabla\varepsilon\times(f-\nabla p) \tag{2.13}$$

given the assumption $\nabla \times f = 0$. Developing the curl of the Kozeny-Carman term, one gets the following expression:

$$\nabla\times\left(\frac{(1-\varepsilon)^2}{\varepsilon^2}u\right) = \frac{(1-\varepsilon)^2}{\varepsilon^2}\omega + 2(\varepsilon-1)\varepsilon^{-3}\nabla\varepsilon\times u \tag{2.14}$$

which, in practice, exhibits terms that become dominant compared to $\nabla\varepsilon\times(f-\nabla p)$. In this sense, the right-hand side in the vorticity formulation of the DBS equation (2.13) is usually neglected (*e.g.* see [113, 204]).

Equation (2.13) is then supplemented with an equation that retrieves the velocity field from the related vorticity, and results in the relation:

$$-\Delta u = \nabla \times \omega \tag{2.15}$$

based on the incompressibility condition. In practice, the previous Poisson equation (2.15) is not straightforwardly considered, and one relies on an alternative using a stream function $\psi : \Omega \subset \mathbb{R}^3 \to \mathbb{R}^3$ (a vector potential) solution of:

$$\begin{cases} -\Delta\psi = \omega, \quad \text{in} \quad \Omega \\ + \text{ boundary conditions such that } \mathrm{div}\,\psi = 0 \text{ on } \partial\Omega. \end{cases} \tag{2.16}$$

The condition $\mathrm{div}\,\psi = 0$ on $\partial\Omega$ is essential to ensure the overall incompressibility condition of the stream function on $\Omega$ and thereby identify $u = \nabla \times \psi$. This requires satisfying appropriate boundary conditions, namely the following combination of homogeneous Dirichlet/Neumann conditions for a computational cubic domain $\Omega = ]x_{\min}, x_{\max}[\times]y_{\min}, y_{\max}[\times]z_{\min}, z_{\max}[$:

$$\begin{cases} x = x_{\min} \text{ or } x = x_{\max} & : \psi_y = \psi_z = \dfrac{\partial\psi_x}{\partial n} = 0, \\ y = y_{\min} \text{ or } y = y_{\max} & : \psi_x = \psi_z = \dfrac{\partial\psi_y}{\partial n} = 0, \\ z = z_{\min} \text{ or } z = z_{\max} & : \psi_x = \psi_y = \dfrac{\partial\psi_z}{\partial n} = 0. \end{cases} \tag{2.17}$$

Such boundary conditions ensure $(\nabla \times \psi) \cdot n = 0$, $\operatorname{div} \psi = 0$ and $\psi \times n = 0$ at the same time, where $n$ is the normal field at the interface, and consequently lead to a zero average velocity field lifted by a prescribed flow rate $\overline{u}$ oriented in the flow direction. Indeed, given $u = \overline{u} + \nabla \times \psi$, one gets:

$$< u >_{\Omega} = \frac{1}{|\Omega|} \int_{\Omega} u \, \mathrm{d}v = \overline{u} + \frac{1}{|\Omega|} \int_{\partial\Omega} \psi \times n \, \mathrm{d}s = \overline{u}, \tag{2.18}$$

which replaces the setting of the driving force $f$ by a prescribed flow rate, managed through the lifted vector $\overline{u}$.

Finally, using the stream function $\psi$, one analytically ensures the divergence-free condition on the velocity as $\operatorname{div} u = \operatorname{div} (\nabla \times \psi) = 0$. Overall, the velocity-vorticity formulation (2.13) of the DBS equation is subsequently coupled with the transport-reaction-diffusion PDE system developed in Sect. 2.3.2 to model reactive hydrodynamics at the pore-scale. Detailed models for applications to the calcite dissolution or precipitation/crystallization processes can be encountered respectively in Sect. 5.3.1 from Chapter 5 and in Sect. 2.7.

## 2.4 A Semi-Lagrangian approach

The present thesis relies on a semi-Lagrangian numerical method, mixing Eulerian and Lagrangian formalism, to tackle dynamically evolving porous media due to reactive micrometric processes. Such a semi-Lagrangian approach has been successfully used for simulations of calcite dissolution at the pore scale [113] and extensively benchmarked against state-of-the-art numerical alternatives [204].

This section is dedicated to presenting this hybrid formalism, which is subsequently improved to account for the heterogeneous diffusion of the chemical reactants through the porous matrix. In the following, we also extend this approach to the modeling of precipitation and crystallization in the context of $CO_2$ mineral storage.

### 2.4.1 A hybrid grid-particle framework

A Lagrangian formalism consists of describing the flow motion through the observation along time of a large number of fluid particles, with their attached intrinsic properties and spatially varying positions [57, 93]. Each particle is then tracked throughout the evolving mechanism (transport, diffusion, ...) to measure variations in the main properties (velocity, concentration, ...). On the contrary, from the Eulerian point of view, the previous property changes are characterized on a predetermined spatial grid along the dynamical process.

The particle formulation is especially well-suited for transport-dominant phenomena as it avoids the explicit discretization of convective terms and alleviates the consideration of their related stability constraints — namely the Courant–Friedrichs–Lewy (CFL) conditions which constrains the time step for a given spatial discretization. The lack of regularity in the particle distributions throughout the dynamic process is, however, a recurring problem of Lagrangian methods. Indeed, as the particle positions move according to the flow field gradients, accumulation or scarcity issues in the particle repartition commonly occur. This, thereby, requires periodic remeshing steps to avoid this problem and not to lose information: namely, one proceeds two successive interpolations from the disorganized particle structure to a regular grid and subsequently from the grid to the new particle distribution [72, 91, 189].

This is particularly suitable for hybrid approaches, wherein dedicated solvers can be straightforwardly implemented in the Eulerian context before performing the remeshing step. This also allows a representation of the Quantity of Interest (QoI) on the grid, which can be coupled with domain decomposition or mesh adaptation methods. Hybrid grid-particle formalism has, thereby, garnered considerable interest in addressing multiple complex phenomena in CFD and geosciences [41, 71, 73, 88]. Besides, incorporating high-order and compact support interpolation kernels makes it possible to reduce the overall computational complexity of the remeshing steps

while keeping accurate predictions of the numerical solution. The choice of the interpolation kernels is, however, important to ensure a robust numerical method and guarantee properties such as mass conservation and sign-preservation of the interpolated quantities [189]. Improvements of the interpolation kernels, especially for applications to dissolution processes at the pore scale, have been investigated by Etancelin *et al.* in [113]. Such improvements focused on sign preservation and accurate high-order interpolation through a correction step of the potential over-diffusive effects resulting from the remeshing step. This provides a well-established hybrid grid-particle framework that can robustly address pore-scale reactive flows.

In the present work, we aim to benefit from the main advantages of both approaches to model reactive hydrodynamics at the pore scale. We will, thereby, use a Lagrangian description for the chemical equations — including the heterogeneous diffusion operator and reactant transport — with an underlying regular grid for solving the DBS equation in its velocity-vorticity formulation.

### 2.4.2 Reactive dynamical system with particles

In this section, we present the Lagrangian formulation dedicated to the resolution of the reactive dynamical system (2.11) detailed in Sect. 2.3.2, and more specifically to the transport-reaction-diffusion equation (2.7).

We define a set of $N_p$ fluid particles covering the computational domain $\Omega$ and characterize as triplets $(C_{k,i},\, x_{k,i},\, v_{k,i})$ of species concentrations $C_{k,i}$, positions $x_{k,i} \in \Omega$ and volumes $v_{k,i}$, where $i$ and $k$ respectively refers to the particle and species indexes. This mathematically introduces the particle description, denoted $C_k^h$, of the concentration fields $C_k$ that reads as follows:

$$C_k^h(t) = \sum_{i=1}^{N_p} C_{k,i}(t)\, v_{k,i}(t)\, \delta_{x_{k,i}}(t) \tag{2.19}$$

which only depends on time $t$, and where $\delta$ refers to the Dirac function. The Lagrangian formulation of equation (2.7) can then be written using the particle description (2.19):

$$\begin{cases} \dfrac{\mathrm{d}C_{k,i}}{\mathrm{d}t} = R_k(\mathbf{C}_i(t)) + \left[\mathrm{div}(\alpha_k(\varepsilon)\nabla^\varepsilon C_k)\right]_{x_{k,i}(t)} \\ \dfrac{\mathrm{d}x_{k,i}}{\mathrm{d}t} = \left[\varepsilon^{-1}u\right]_{x_{k,i}(t)} \\ \dfrac{\mathrm{d}v_{k,i}}{\mathrm{d}t} = 0 \end{cases} \tag{2.20}$$

given the incompressibility condition $\mathrm{div}\, u = 0$ and the notations introduced in Sect. 2.3.2. This results in a dynamical system over the particles whose positions are controlled by the field $\varepsilon^{-1}u$, and volumes remain constant under divergence-free conditions. The main advantage of such a Lagrangian formulation (2.20) is that the transport term $\mathrm{div}(\varepsilon^{-1}uC_k)$ vanishes along with its stability condition and, thereby, the method presents the ability to use arbitrary large time steps. This is, especially, of great interest when the CFL condition on the transport term induces a stronger constraint on the time step compared to the diffusion stability condition.

The velocity field $u$ in (2.20) arises from the solution of the DBS equation which is solved on an underlying Cartesian grid and coupled with the Lagrangian formulation of the chemical PDE system. Regarding such a strong coupling between these equations, one needs to interpolate on the grid the particle description of the solid chemical species — namely $C^h_{\mathrm{CaCO_3}(s)}$ — which is related to the micro-porosity field $\varepsilon$ and consequently involved in the DBS model. Similarly, the velocity field subsequently needs to be interpolated on the particles to solve the Lagrangian set of chemical equations. This requires, as introduced in the previous Sect. 2.4.1, convolution with high-order remeshing kernels with compact supports (*e.g.* see [113, 189]). The dynamical system (2.20) is finally integrated using standard numerical methods for Ordinary Differential Equation (ODE), such as explicit Runge-Kutta, while the diffusion term $\mathrm{div}(\alpha_k(\varepsilon)\nabla^\varepsilon C_k)$ is approximated through the PSE method, detailed in Sect. 2.5.

In the present thesis, we incorporate in the semi-Lagrangian workflow the consideration of robustly estimating Archie's law term through such a particle-based PSE method. In this sense, we make it possible to fully address the superficial gradient $\nabla^{\varepsilon}$ approximation with heterogeneous diffusion throughout the porous matrix (see Sect. 2.5.3).

### 2.4.3 Splitting operator strategy

The semi-Lagrangian formalism introduced in the previous Sect. 2.4.1 and 2.4.2 intrinsically relies on splitting strategies. Time-splitting methods, also known as fractional time-step algorithms, arise in many fields of computational science related to physics-based models and have been developed by Chorin in the 1970s [76] in the context of vortex methods for the Navier-Stokes equation. Such methods have been widely investigated afterward to separate the resolution of distinct physical phenomena and render more efficient algorithms [40, 91, 110, 115]. Indeed, one of the main advantages of splitting strategies is one can use different approaches for the distinct parts of the overall model, namely either a Lagrangian or Eulerian formulation. This also straightforwardly extends to the choice of the numerical solver available for each component, allowing the use of the most efficient, accurate, and robust schemes independently.

The first natural splitting arising in workflow, thereby, lies in the semi-Lagrangian formalism itself, wherein we do not consider solving the overall PDE system at once. We rather separate the transport-diffusion-reaction dynamics in its Lagrangian formulation from the pore-scale hydrodynamic resolved on the underlying Cartesian grid. The hydrodynamic part, composed of the DBS equation in the velocity-vorticity formulation, is also solved through a time-splitting method. In this sense, we approximate the solution of (2.13) by the limit in time of the evolution equation

$$\frac{\partial \omega}{\partial t} - \mu \Delta \omega \; + \; \mu \kappa_b^{-1} \nabla \times \left( \frac{(1-\varepsilon)^2}{\varepsilon^2} u \right) = 0, \tag{2.21}$$

together with $\omega = \nabla \times u$, using a three-step operator splitting strategy coupled with a fixed-point algorithm. This means that considering a sequence $(u_m, \omega_m)$ of velocity-vorticity we aim to successively perform, over a time interval $[t_m, t_{m+1}]$ with $t_m = m\delta t$, Brinkman penalization, diffusion, and projection on divergence-free fields. The latter is achieved through the reconstruction of the velocity field $u$ based on the stream function $\psi$ (see Sect. 2.3.3). In practice, these three steps are specifically defined as:

- The Brinkman iteration given by the ordinary differential equation $\dfrac{\partial u}{\partial t} + \mu\lambda(\varepsilon)(u + \overline{u}) = 0$ with prescribed flow rate $\overline{u}$ and $\lambda(\varepsilon) := \kappa_b^{-1}(1-\varepsilon)^2\varepsilon^{-2}$, whose exact solution after a $\delta t$ is generated by
$$\Lambda(u) := e^{-\mu\lambda(\varepsilon)\delta t}(u + \overline{u}) - \overline{u}$$
- The vorticity diffusion iteration, $\dfrac{\partial \omega}{\partial t} - \mu\Delta\omega = 0$, solved using an implicit Euler scheme given by the operator
$$\mathcal{D}_{\omega}(u) := \left[ I - \mu\delta t \nabla \right]^{-1} (\nabla \times u)$$
- The projection step $\Pi(\zeta) = \nabla \times \left( (-\Delta^{-1})\zeta \right)$ which takes as $\zeta$ the right-hand side of the Poisson equation $-\Delta\psi = \zeta$ satisfying the boundary conditions (2.17), and followed by $u = \nabla \times \psi$.

Overall, this leads to the full iteration of the Brinkman-Diffusion-Projection splitting $\Pi \circ \mathcal{D}_{\omega} \circ \Lambda$ over a time step $[t_m, t_{m+1}]$, which reads as follows:

$$u_{m+1} = \Pi \circ \mathcal{D}_{\omega} \circ \Lambda(u_m) \tag{2.22}$$

and whose consistency has been theoretically discussed in [135]. One should notice that this projection step is not a projection by pressure gradient correction (*e.g.* see [73]), but an operator

that takes the vorticity field $\omega$ and retrieves a divergence-free velocity field whose mean velocity is zero. The final velocity field is subsequently given by

$$u = \overline{u} + \lim_{m \to \infty} u_m \tag{2.23}$$

whose average is $\overline{u}$ and satisfies the Kozeny-Carman relation inside the solid region.

From a numerical perspective, we consider the exact treatment of the Brinkman term, fourth-order finite difference scheme for the discrete curl operator, and Fast Fourier Transform (FFT) solvers for the vorticity diffusion and stream function recovery. Using FFT avoids matrix assembly procedure and, therefore, consists of efficient solvers in terms of computational time and memory storage requirements. Besides, the complexity of such algorithm scales as $\mathcal{O}(N_p \log(N_p))$, where $N_p$ is recalled to refer to the number of particles. A stopping criterion on this fixed point algorithm is also defined based on the relative residual norm on the velocity, which manages the convergence of the pore-scale hydrodynamics toward a stationary state.

The updated velocity $u_{m+1}$ is subsequently interpolated from the grid to the particles and used for solving the Lagrangian reactive system, which is split into convective/remeshing and diffusive/reactive steps. Regarding the convection, the particle trajectories are pushed to the next step through a directional advection, given the field $\varepsilon^{-1}u$ according to the Lagrangian formulation (2.20), and are then remeshed to avoid stagnation issues (see Sect. 2.4.1). The purpose of such a directional splitting is to reduce the dimensionality of the overall advection problem by considering several one-dimensional equations [90, 189]. The particle remeshing is also addressed using directional treatment of the multidimensional convolution. This means that within a time step $[t_m, t_{m+1}]$, the joint step of advection/remeshing of the particles is successively performed by alternating the spatial directions [111, 143]. This presents the advantage of significantly improving the computational efficiency of the method and allows the use of high-order remeshing kernels with large stencils while maintaining a minimal cost compared to multidimensional cases. This is also well-suited to parallel implementation on GPU architecture. The dimensional splitting is addressed, in practice, by a second-order Strang formula [288] and coupled with a second-order Runge-Kutta for time integration. The diffusion/reaction step is finally solved by means of a second-order explicit Runge-Kutta scheme along with PSE approximation of the heterogeneous diffusion operator. Once the Lagrangian formulation of the chemistry has been fully updated and remeshed on the underlying grid, one starts pushing the DBS hydrodynamics to the next sequential step of these temporal iterations.

Such an operator splitting strategy, in the context of a semi-Lagrangian approach, has been applied to the modeling of dissolution processes on a 2D synthetic calcite core and validated against state-of-the-art alternatives and experiments [204]. This has also been used in [113] on real porous media structures at the pore scale to investigate the dissolution of 3D carbonate rocks arising from $\mu$CT scans. Nonetheless, these previous works assumed that the superficial gradient $\nabla^{\varepsilon}$ involved in the heterogeneous diffusion could be approximated by the gradient operator, and subsequently addressed this Archie's law term with standard finite differences schemes. In Sect. 2.5, we intend to alleviate this assumption and, therefore, improve the semi-Lagrangian method by incorporating in the workflow a PSE approximation of the heterogeneous diffusion.

## 2.5 Particle-Strength-Exchange method and Archie's law approximation

This section concerns the theoretical aspects of the PSE method that finds its essence in estimating diffusion in a Lagrangian context with meshless and scattered particle structures. Since the original article from Degond and MasGallic [101] in 1989, the PSE approach has appeared as an efficient numerical method for solving convection-diffusion problems with particles [268] and has been successfully used in vortex methods [92, 243].

Several reviews have also extended its application to the Eulerian context, with structured grids, but also to hybrid grid-particles formalism while enhancing the accuracy of the original

method by replacing continuous integration with discrete one [47, 88, 246, 267]. These novel PSE approaches, therefore, enable us to efficiently evaluate the heterogeneous diffusion operator arising from Archie's law in a Semi-Lagragian context. In the following, we briefly review the general principles of this original method along with an overview of its successive improvements using discretization corrections. We finally demonstrate the relevant use of the PSE approach to approximate Archie's law term and account for a reduced diffusion in the porous matrix of the porous medium.

### 2.5.1 Classical PSE formulation

The PSE method consists in the approximation of a diffusion operator $\mathrm{div}(\mathbf{L}\nabla f)(x)$ with $x \in \Omega \subset \mathbb{R}^n$ and $\mathbf{L}$ a positive symmetric matrix, accounting for heterogeneous diffusion for instance. The main idea is then to approximate the diffusion by an integral operator, more suitable for particle methods:

$$Q^\xi \cdot f(x) = \int_\Omega \sigma^\xi(x,y)\big(f(y) - f(x)\big)dy \tag{2.24}$$

where the kernel $\sigma^\xi$ is supposed to be symmetric and satisfies some moment conditions, detailed thereafter. In the Lagrangian formulation, a particle approximation of the function $f$, denoted $f^h$, is also introduced based on the particle triplet $(f_i,\, x_i,\, v_i)$, such that:

$$f^h = \sum_{i=1}^{N_p} f_i\, v_i\, \delta_{x_i} \quad \text{where} \quad f_i = f(x_i) \tag{2.25}$$

where $x_i$ and $v_i$ are respectively the particle positions and volumes, while $\delta_{x_i}$ refers to the Dirac measure at position $x_i$. With such a $N_p$-particle representation of the function $f$, a discrete version of the operator $Q^\xi$ is obtained by using the particles as quadrature points where $h$ refers to the characteristic distance between particles. This results in the following quadrature expression, called Particle-Strength-Exchanges:

$$Q^\xi \cdot f^h(x_k) = \sum_{x_l \in \mathcal{S}} \sigma^\xi(x_k, x_l)\, \big(f_l - f_k\big)\, v_l. \tag{2.26}$$

where $\mathcal{S} := supp(\sigma^\xi)$ refers to the set of points in the support of the kernel function $\sigma^\xi$.

The PSE scheme is then completely determined once the kernel $\sigma^\xi$ is defined and exhibits its relation with the diffusion matrix $\mathbf{L}$. The original approach from Degond and MasGallic [101] suggests the following kernel choice

$$\sigma^\xi(x,y) = \frac{1}{\xi^2} \sum_{i,j=1}^{n} M_{ij}(x,y)\psi_{ij}^\xi(y-x), \tag{2.27}$$

where

$$\psi_{ij}^\xi(x) = \frac{1}{\xi^n}\psi_{ij}\left(\frac{x}{\xi}\right)$$

is a matrix cutoff function with $\psi_{ij}$ symmetric and even, and $\mathbf{M} = (M_{ij}(x,y))$ a symmetric matrix to be determined. These hypotheses are of great interest as they guarantee the conservation property of the operator $Q^\xi$ based on symmetric exchanges. We then introduce the matrix $\mathbf{m}(x) := \mathbf{M}(x,x)$ and the moments of the cutoff functions $\psi_{ij}$ given by:

$$Z_{ij}^\alpha = \int \psi_{ij}(x)x^\alpha dx, \tag{2.28}$$

for any $i, j$ and multi-index $\alpha$. It has been proved by Degond and Mas-Gallic that if some moment conditions are satisfied, namely the hypotheses (i) and (ii), we obtain the following convergence result [101]:

**Property 1** *We assume that there exists an integer $r \geq 2$ such that :*
*(i) $Z_{ij}^{\alpha} = 0$ for $1 \leqslant |\alpha| \leqslant r+1$ and $|\alpha| \neq 2$*
*(ii) for any integer k,l in $[1,n]$, we have $\sum_{i,j=1}^{n} m_{ij}(x) Z_{ij}^{e_k+e_l} = 2L_{kl}(x)$.*
*In addition of the previous hypotheses on matrices $\mathbf{M}$, $\mathbf{m}$ and $\psi$, we assume the following regularities $\mathbf{M} \in W^{r+1,\infty}(\mathbb{R}^n \times \mathbb{R}^n)$, $\mathbf{m} \in W^{r+1,\infty}(\mathbb{R}^n)$ and $(1+|x|^{r+2})\psi(x) \in \mathrm{L}^1(\mathbb{R}^n)$. There exists a positive constant $C = C(\mathbf{M}, \psi)$ such that for any function $f \in W^{r+2,\infty}(\mathbb{R}^n)$*

$$\|\mathrm{div}(L\nabla f) - Q^{\xi} \cdot f\|_{0,\infty} \leqslant C\xi^r \|f\|_{r+2,\infty}. \tag{2.29}$$

Several matrix cutoff functions have been investigated in [101] but we mainly focus on the most suitable for practical use, which reads as:

$$\psi_{ij} = x_i x_j \theta(x) \tag{2.30}$$

with $\theta$ a smooth spherically symmetric function with fast decreasing, also called the stencil generator. Finally, one needs to define the second moments' matrix of $\theta$, denoted $\mathbf{A} = (a_{kl})$, and given by

$$a_{kl} = \int x_k^2 x_l^2 \theta(x) dx, \qquad k,l \in [1,n]. \tag{2.31}$$

In this case, one gets the existence of a matrix $\mathbf{m}(x)$ such that the hypotheses (i) and (ii) of Property 1 are satisfied if and only if $\mathbf{A}$ is an invertible symmetric matrix and, for any k,l $k \neq l$, we have $a_{k,l} \neq 0$. The matrix $\mathbf{m}(x)$ is then defined by (see Lemma 1 in [101]):

$$m_{kl}(x) = a_{kl}^{-1} L_{kl}(x), \quad \text{for} \quad k,l \in [1,n],\ k \neq l \tag{2.32}$$

$$\sum_{i=1}^{n} a_{ki} m_{ii}(x) = 2L_{kk}(x), \quad \text{for} \quad k \in [1,n] \tag{2.33}$$

which is a fundamental result of the original PSE article. In 3D applications, for instance, one can compute the matrix $\mathbf{A}$ coefficients using spherical coordinates to obtain $a_{kk} = 3\gamma$ and $a_{kl} = \gamma$, if $k \neq l$, with $\gamma$ expressed by:

$$\gamma = \frac{4\pi}{15} \int_0^{\infty} \widetilde{\theta}(r) r^6 dr \tag{2.34}$$

where the spherically symmetric function $\theta$ is written $\theta(x) = \widetilde{\theta}(|x|)$. Solving the problem given by equations (2.32) and (2.33) then explicitly provides

$$m_{kl} = \gamma^{-1} L_{kl}, \quad \text{if } k \neq l, \quad \text{and} \quad m_{kk} = \gamma^{-1} L_{kk} - \frac{\gamma^{-1}}{5} Tr(\mathbf{L}), \tag{2.35}$$

which also writes

$$\mathbf{m} = \gamma^{-1}\mathbf{L} - \frac{\gamma^{-1}}{5} Tr(\mathbf{L}) \mathbf{Id}_3. \tag{2.36}$$

When the conditions (2.32) and (2.33) are satisfied and in the case of a kernel defined with a spherical-symmetric function $\theta$ such as in (2.30), the method provides at least second order approximation of the diffusion operator (see Property 1) which is suitable for any particle distribution in a Lagrangian context. One should notice that in practice the method is limited to second-order convergence for positive kernel $\sigma^{\xi}$ (*e.g.* see [87, 101]).

Finally, to make the approximation operational, it remains to define the relation between $\mathbf{M}$, $\mathbf{m}$, $\mathbf{L}$, and $\theta$. A usual approach is to consider the matrix $\mathbf{M}$ under the forms:

$$\mathbf{M}(x,y) = \mathbf{m}\left(\frac{x+y}{2}\right) \quad \text{or} \quad \mathbf{M}(x,y) = \frac{1}{2}\Big(\mathbf{m}(x) + \mathbf{m}(y)\Big), \tag{2.37}$$

and for $\psi$ given by (2.30), one gets the following kernel formula:

$$\sigma^{\xi}(x,y) = \frac{1}{\xi^{n+4}} \theta\left(\frac{y-x}{\xi}\right) \mathbf{M}(x,y) : (x-y)^{\otimes 2}. \tag{2.38}$$

This entirely specifies the numerical scheme by combining the equations (2.26), (2.38), and (2.36). This original formalism is based on continuous integration of the second moments of $\theta$ through the equation (2.34) and is second order consistent in the sense $\mathcal{O}[(h/\xi)^2]$.

### 2.5.2 Discrete renormalized PSE scheme

The previous second-order consistency, however, raises concerns about the practical implementation of the original PSE formulation. This arises from the strong relationship between the inter-particle spacing $h$ and the width $\xi$ of the kernel $\sigma^\xi$, which commonly implies choosing the ratio $h/\xi$ to be constant. Otherwise, small kernel sizes require a large number of particles to guarantee the method's consistency, and a small number of particles alternatively leads to large stencils for the diffusion kernel. Neither option is affordable from a computational efficiency perspective and, therefore, induces a strong constraint on the choice of the ratio $h/\xi$.

Alternatives relaxing this constraint result in replacing the continuous moment integration with discrete moment conditions, which is referred to as discretization correction of the PSE scheme. The latter has been successfully developed for several state-of-the-art applications including mesh-free scenarios with arbitrary particle distributions, uniform Cartesian grids, and also in hybrid formulations involving both an underlying grid along with the particles [47, 55, 267, 342]. In particular, such a discrete renormalized version of the PSE appears to adequately combine with a semi-Lagrangian formulation, ensuring low computational cost and equivalent accuracy compared to a pure Lagrangian approach. Indeed, this can benefit from the advantages of using the Cartesian underlying grid through the redistribution of the particles with remeshing kernels. In this sense, we focus in the following on a discrete correction formulation which holds both in the Eulerian and Lagrangian context.

The consistency of the original PSE scheme can be improved to $\mathcal{O}(h^2)$ by using discrete integration when particles are distributed over a uniform grid [246]. The main idea is to replace (2.31) by the matrix of discrete second-order moments, which subsequently leads to a distinct evaluation of the matrix $\mathbf{m}$. One introduces the following coefficients using discrete integration:

$$\gamma_1 = \sum_{x\in\mathbb{J}} x_k^4 \theta(x) h^3, \quad k \in [1,3] \tag{2.39}$$

$$\gamma_2 = \sum_{x\in\mathbb{J}} x_k^2 x_l^2 \theta(x) h^3, \quad k,l \in [1,3] \tag{2.40}$$

for $\mathbb{J} \subset h\mathbb{Z}^3$ a three-dimensional lattice, including at least one neighborhood of the current mesh point. One then gets similar equations as (2.32) and (2.33) with respect to the coefficients $\gamma_1$ and $\gamma_2$, resulting in the characterization of $\mathbf{m}$. We introduce the matrix $\mathbf{H} = H_{ij}$ given by

$$H_{ij} = \left( \frac{\gamma_1^2 - \gamma_1\gamma_2 - 6\gamma_2^2}{\gamma_2(\gamma_1^2 + \gamma_1\gamma_2 + 2\gamma_2^2)} \right) (1 - \delta_{ij}) L_{ij}$$

where $\delta_{ij}$ is the Kronecker symbol, such that the matrix $\mathbf{H}$ is zero when $\mathbf{L}$ is diagonal or when $\gamma_1 = 3\gamma_2$. We thus obtain a discrete renormalization of the matrix $\mathbf{m}$ which reads as follows:

$$\mathbf{m} = \frac{2(\gamma_1 + 2\gamma_2)}{\gamma_1^2 + \gamma_1\gamma_2 - 2\gamma_2^2} \mathbf{L} \; - \; \frac{2\gamma_2}{\gamma_1^2 + \gamma_1\gamma_2 - 2\gamma_2^2} \mathrm{Tr}(\mathbf{L}) \mathbf{Id_3} \; + \; \mathbf{H} \tag{2.41}$$

and replaces the equation (2.36) in the original PSE version. Finally, this formulation with discrete integration is completely defined through the formula (2.38). This also leads to a better accuracy since this scheme is consistent in $h^2$ whereas the classical PSE method has a convergence in the sense that the error is of order $(h/\xi)^2$. In this sense, this alleviates the considerations of properly choosing the kernel width $\xi$ and therefore makes it possible to consider a $\xi$-neighborhood of the current particles, previously redistributed on the Cartesian grid of mesh size $h$ through remeshing (in practice, we have $\xi \in h\mathbb{N}^*$). In the next section, we will use the present formalism to evaluate the heterogeneous diffusion operator arising from Archie's law within the semi-Lagrangian context introduced in Sect. 2.4.

### 2.5.3 PSE scheme for an Archie's law of index $\eta$

While the discrete renormalization of PSE method can be assimilated to a Finite Differences (FD) stencil on a uniform Cartesian grid and satisfies the same order of accuracy as standard FD

schemes, one can query the motivation for using this seemingly complex approach. First of all, behind appearances, this method is easy to implement and not computationally expensive in the context of uniformly distributed grids. In 3D applications, for instance, one can summarize the PSE discrete formulation as follows

$$Q^{\xi}\cdot f^{h}(x_k)=\frac{1}{\xi^7}\sum_{l\sim k}\frac{f_l-f_k}{1+|\frac{x_l-x_k}{\xi}|^p}\left[\sum_{i,j=1}^{3}M_{ij}(x_k,x_l)(x_l-x_k)_i(x_l-x_k)_j\right]v_l \tag{2.42}$$

with the spherically symmetric function $\theta$ taken as:

$$\theta(x)=\frac{1}{1+|x|^p}, \tag{2.43}$$

where $|\,.\,|$ is the Euclidean norm in $\mathbb{R}^3$. The formula (2.42) basically involves all the contributions of the mesh points of index $l$ in the $\xi$-neighborhood of the current mesh point $x_k$, representing namely 26 neighbors in 3D for $\xi = h$ compared to merely 6 neighbors with standard crossed FD scheme. In practice, $\xi$ is taken equal to $h$ or $2h$, and the numerical results presented in this thesis are given with $p = 10$ along with the matrix $\mathbf{M}$ taken under the form $\mathbf{M}(x,y) = \big(\mathbf{m}(x) + \mathbf{m}(y)\big)/2$.

Besides, we also aim to estimate Archie's law term of tortuosity index $\eta$ through this PSE formalism. When considering the heterogeneous diffusion operator

$$\mathcal{D}_i(\varepsilon,C) := \mathrm{div}\left(\varepsilon^{1+\eta}\nabla(\varepsilon^{-1}C)\right) \tag{2.44}$$

involved in the PDE system (2.11), one gets a particular expression for the matrix $\mathbf{L}$ which reads $\mathbf{L} = \varepsilon^{1+\eta}\,\mathbf{I}_3$ with $\mathbf{I}_3$ the identity matrix in $\mathbb{R}^3$. This accounts for the spatially varying coefficient $\varepsilon^{1+\eta}$ of the diffusion operator even if the matrix $\mathbf{L}$ is diagonal. In this case, we end up with a diagonal matrix $\mathbf{m}$, and denoting $c_0$ and $c_1$ respectively the coefficients:

$$c_0=\frac{2(\gamma_1+2\gamma_2)}{\gamma_1^2+\gamma_1\gamma_2-2\gamma_2^2}\quad\text{and}\quad c_1=\frac{2\gamma_2}{\gamma_1^2+\gamma_1\gamma_2-2\gamma_2^2} \tag{2.45}$$

which only depend on the choice of the function $\theta$ defined in (2.43), we obtain the contributions of each diagonal term of $\mathbf{m}$ through $m_{ii} = c_0 L_{ii} - c_1\mathrm{Tr}(\mathbf{L})$ from (2.41). This implies that the matrix $\mathbf{M}$ is also diagonal with its coefficient expressed by

$$M_{ii}(x_k,x_l)=\frac{(c_0-3c_1)}{2}\Big(\varepsilon^{1+\eta}(x_k)+\varepsilon^{1+\eta}(x_l)\Big). \tag{2.46}$$

Overall, the discrete renormalization of the PSE scheme approximating the Archie's law diffusion operator (2.44) reads as follows:

$$Q^{\xi}\cdot f^{h}(x_k)=\frac{1}{\xi^7}\sum_{l\sim k}\frac{f_l-f_k}{1+|\frac{x_l-x_k}{\xi}|^p}\frac{(c_0-3c_1)}{2}\Big(\varepsilon^{1+\eta}(x_k)+\varepsilon^{1+\eta}(x_l)\Big)|x_l-x_k|^2v_l \tag{2.47}$$

where $|\,.\,|$ is the Euclidean norm in $\mathbb{R}^3$ and $f_\bullet := \varepsilon^{-1}(x_\bullet)C(x_\bullet)$. The overall formula (2.47) accounts for the heterogeneous diffusion and ensures the accurate management of the chemical reactant penetration, given by its concentration field $C$, within the porous matrix. Indeed, one of the main advantages of the PSE scheme is that it includes all the lattice neighborhoods in the computation of the heterogenous diffusion, unlike crossed FD. Finally, this guarantees the conservation of the reactant exchanges between the fluid portion and the porous matrix due to the symmetry hypotheses on $\mathbf{M}$ and the matrix cutoff function $\psi_{ij}$ when defining the PSE scheme (see Sect. 2.5.1). Taken together, this motivates the use of the discrete renormalization of PSE method to robustly address the approximation of Archie's law of tortuosity index $\eta$.

### 2.5.4 Stability analysis of the Archie's law term with superficial gradient

Considering the heterogeneous diffusion of the chemical species with superficial gradient $\nabla^\varepsilon$ formalism, however, leads to additional stability concerns that need to be investigated. In this section, we focus on the necessary conditions of stability of the diffusion equation arising from Archie's law. To do so, we proceed in stability analysis of the usual FD discrete operators of the following evolution equation:

$$\frac{\partial C}{\partial t} - D_m \mathrm{div}\left(\varepsilon^{1+\eta}\nabla(\varepsilon^{-1}C)\right) = 0 \tag{2.48}$$

on a restricted spatiotemporal domain $\Omega \times [0, T_f]$ with $\Omega \subset \mathbb{R}$ for sake of readability. Extension of the present work to multi-dimensional spatial domains $\Omega$ should be explored in the future with PSE approximation of the heterogeneous diffusion term.

First, we introduce a spatiotemporal grid $(x_k, t_n)$ with $x_k = k\delta x$, $k \in [0, N_x]$ and $t_n = n\delta t$, $n \in [0, N_t]$ and define the discrete approximation $C^n(x_k) := C(x_k, t_n)$ of the concentration field $C$. Considering a forward Euler-Explicit scheme, the discrete formulation of equation (2.48) subsequently reads as:

$$C^{n+1}(x_k) = C^n(x_k) + \delta t D_m \mathrm{div}_h\left(\varepsilon^{1+\eta}(x_k)\nabla_h(\varepsilon^{-1}(x_k)C^n(x_k))\right) = 0, \tag{2.49}$$

where the subscript $h$ defers to discrete operators. One should notice that, in the previous equation, the micro-porosity field $\varepsilon$ is merely regarded as spatially dependent since a diffusion/reaction splitting is also considered in practice. In this sense, we do not account for the micro-porosity variations over time when diffusing the chemical species concentration in equation (2.48). We define $Y^n := \varepsilon^{-1}C^n$ and divide by $\varepsilon$ the equation (2.49) to study the stability analysis of the equivalent problem:

$$Y^{n+1}(x_k) = Y^n(x_k) + \delta t D_m \varepsilon^{-1}(x_k)\mathrm{div}_h\left(\varepsilon^{1+\eta}(x_k)\nabla_h Y^n(x_k)\right) = 0. \tag{2.50}$$

We subsequently introduce the following notations, dedicated to the present section:

$$x_k^+ = x_k + \delta x/2 \quad \text{and} \quad x_k^- = x_k - \delta x/2$$
$$x_k^{++} = x_k + \delta x \quad \text{and} \quad x_k^{--} = x_k - \delta x$$

along with $\lambda = D_m \delta t/\delta x^2$, such that the spatial discretization considered explicitly reads:

$$\begin{aligned} Y^{n+1}(x_k) &= Y^n(x_k) + \delta t(\delta x)^{-1} D_m \varepsilon^{-1}(x_k)\Big[\varepsilon^{1+\eta}(x_k^+)\nabla_h Y^n(x_k^+) - \varepsilon^{1+\eta}(x_k^-)\nabla_h Y^n(x_k^-)\Big] \\ &= Y^n(x_k) + \lambda\varepsilon^{-1}(x_k)\Big[\varepsilon^{1+\eta}(x_k^+)\big(Y^n(x_k^{++}) - Y^n(x_k)\big)\Big] \\ &\quad - \lambda\varepsilon^{-1}(x_k)\Big[\varepsilon^{1+\eta}(x_k^-)\big(Y^n(x_k) - Y^n(x_k^{--})\big)\Big]. \end{aligned} \tag{2.51}$$

Finally, we set $Y^n(x_k) := \gamma^n e^{\mathbf{i}\,\xi k\,\delta x}$ — with $\mathbf{i}$ the complex number — and use the Fourier method to determine the amplification factor $\gamma$ of the discrete scheme (2.51), such that

$$Y^{n+1}(x_k) = \gamma Y^n(x_k). \tag{2.52}$$

Denoting by $\Theta := \cos(\xi\delta x)$, one obtains:

$$\gamma = 1 + \lambda\varepsilon^{-1}(x_k)\Big[(\Theta - 1)\big(\varepsilon^{1+\eta}(x_k^+) + \varepsilon^{1+\eta}(x_k^-)\big) + \mathbf{i}\sin(\xi\delta x)\big(\varepsilon^{1+\eta}(x_k^+) - \varepsilon^{1+\eta}(x_k^-)\big)\Big] \tag{2.53}$$

for which requiring $|\gamma|^2 \leqslant 1$, with $|\cdot|$ the complex number modulus, ensures the stability of the numerical scheme. In our case, this condition eventually writes $|\gamma|^2 = 1 - f(\Theta) \leqslant 1$ with $f(\Theta)$ defined by:

$$f(\Theta) = (1 - \Theta)\left[2\alpha_1 - \alpha_1^2 - \alpha_2^2 + \Theta(\alpha_1^2 - \alpha_2^2)\right] \tag{2.54}$$

where $\alpha_1 := \lambda\varepsilon^{-1}(x_k)\big(\varepsilon^{1+\eta}(x_k^+) + \varepsilon^{1+\eta}(x_k^-)\big)$ and $\alpha_2 := \lambda\varepsilon^{-1}(x_k)\big(\varepsilon^{1+\eta}(x_k^+) - \varepsilon^{1+\eta}(x_k^-)\big)$.

Considering a general form of the function $f$ given by $f(\Theta) = (1-\Theta)\,[c_1 + \Theta c_2]$, the necessary conditions for the stability satisfy the constraints $c_2 > 0$ and $c_1/c_2 \geqslant 1$ — with the resulting implication $c_1 \geqslant 0$. These conditions subsequently provide $\alpha_1^2 > \alpha_2^2$ (for $c_2 > 0$) along with $2\alpha_1 - \alpha_1^2 - \alpha_2^2 \geqslant 0$ (for $c_1 \geqslant 0$) which can be combined to obtain $\alpha_2^2 \leqslant \alpha_1$, while $c_1/c_2 \geqslant 1$ straighforwardly provides $\alpha_1 \geqslant 1$. Overall, the two stability conditions related to the equation (2.48) with heterogeneous diffusion are:

$$1) \quad \alpha_1 \leqslant 1 \qquad \text{and} \qquad 2) \quad \alpha_2^2 \leqslant \alpha_1. \tag{2.55}$$

Finally, these conditions can be expressed in terms of the spatial variations of the micro-porosity field $\varepsilon$ such that:

$$\begin{aligned} &1) \quad \lambda\varepsilon^{-1}(x_k)\big(\varepsilon^{1+\eta}(x_k^+) + \varepsilon^{1+\eta}(x_k^-)\big) \leqslant 1, \\ &2) \quad \lambda \leqslant \frac{\varepsilon(x_k)\big(\varepsilon^{1+\eta}(x_k^+) + \varepsilon^{1+\eta}(x_k^-)\big)}{\big(\varepsilon^{1+\eta}(x_k^+) - \varepsilon^{1+\eta}(x_k^-)\big)^2}, \quad \text{if} \quad \alpha_2 \neq 0. \end{aligned} \tag{2.56}$$

Assuming, in the spirit of the PSE formalism, the following averaged combinations of the micro-porosity in the grid points:

$$\begin{aligned} \varepsilon^{1+\eta}(x_k^+) &= \frac{1}{2}\big(\varepsilon^{1+\eta}(x_k^{++}) + \varepsilon^{1+\eta}(x_k)\big) \\ \text{and } \varepsilon^{1+\eta}(x_k^-) &= \frac{1}{2}\big(\varepsilon^{1+\eta}(x_k^{--}) + \varepsilon^{1+\eta}(x_k)\big), \end{aligned} \tag{2.57}$$

the second stability condition from (2.56) can, especially, be written on the grid points such that:

$$2b) \quad \lambda \leqslant 2\varepsilon(x_k)\frac{\varepsilon^{1+\eta}(x_k^{++}) + \varepsilon^{1+\eta}(x_k^{--}) + 2\varepsilon^{1+\eta}(x_k)}{\big(\varepsilon^{1+\eta}(x_k^{++}) - \varepsilon^{1+\eta}(x_k^{--})\big)^2}. \tag{2.58}$$

This analysis highlights several stability constraints depending on the distinct domain areas and the micro-porosity values. In particular, when $\varepsilon$ is constant — for instance when considering the diffusion in the fluid of the chemical species — the first condition 1) is sufficient to guarantee the stability of the numerical scheme. In the fluid domain, we recover as expected the usual CFL condition of a diffusion operator $\lambda \leqslant 1/2$, while in the porous matrix, we obtain the condition $\lambda \leqslant 1/2\varepsilon^\eta$ for $\varepsilon$ constant, that is already satisfied due to the necessary condition arising in the fluid region, since $\lambda \leqslant 1/2 \leqslant 1/2\varepsilon^\eta$.

At the pore interface, however, the numerical stability is constrained by the second condition 2b) and depends on the micro-porosity jump and the tortuosity index $\eta$, which leads to a more restrictive constraint on the time step $\delta t$. For instance, the worst configuration occurs when $x_k$ is in the first layer of solid whose porosity is denoted $\varepsilon_s$. That is, $x_k$ and one of its neighbors are in the porous matrix and the other neighbor is in the fluid, in a 1D configuration. Let us denote $[\varepsilon^{1+\eta}] = 1 - \varepsilon_s^{1+\eta}$ the jump of $\varepsilon^{1+\eta}$ at the interface. The condition 2b) then reduces to:

$$\lambda \leqslant 2\varepsilon_s \frac{4 - 3[\varepsilon^{1+\eta}]}{[\varepsilon^{1+\eta}]^2}. \tag{2.59}$$

The strongest constraint occurs asymptotically when $\varepsilon_s \to 0$, that is to say $[\varepsilon^{1+\eta}] \to 1$, so that the effective constraint is

$$\lambda \leqslant 2\varepsilon_s. \tag{2.60}$$

In practice, for a $5\%$ porous solid matrix, this condition is $\lambda \leqslant 0.1$ which is a bit more constrained than condition $\lambda \leqslant 0.5$ : this is not orders of magnitude different, but requires a time step reduction.

The stability constraints presented in this section show more restrictive constraints arising from the consideration of heterogeneous diffusion of the chemical species within the porous matrix. Therefore, we account for these constraints in the numerical simulation, using the stability conditions 1) and 2) developed here. The stability analysis of the general case for multi-dimensional PSE methods in the context of such heterogeneous diffusion models will be investigated in the future.

## 2.6 High-Performance-Computing framework

One of the major constraints when dealing with a semi-Lagrangian formulation lies in the ability of the computational framework to handle an overall hybrid approach in terms of grid-particle formalism, numerical methods, multi-grid resolutions, and hardware devices. Indeed, Cottet *et al.* suggested in [89] a semi-Lagrangian method coupled with hybrid grid resolutions to address a multi-scale transport problem of a passive scalar. The scalar is, indeed, discretized on a sub-grid compared to the velocity and vorticity fields and enables the accurate prediction of the small-scale effects. Finally, considering hybrid computing methodologies makes it possible to distribute the distinct parts of an overall problem to different types of hardware architectures. This formalism, therefore, exploits the advantages of each method individually according to the characteristics of the problem.

Nonetheless, implementing such a hybrid approach requires a highly flexible computational framework that gathers a wide range of numerical methods and, therefore, benefits from their intrinsic strengths. One also needs libraries incorporating effective parallel computing tools and able to address, *inter alia*, hybrid CPU-GPU programming. In this section, we present the HPC framework considered to address the DNS of pore-scale reactive flows for $CO_2$ mineral trapping into carbonate rocks.

### 2.6.1 The HySoP library

HySoP is a high-performance computing platform [112], jointly developed at LMAP (Laboratoire de Mathématiques et de leurs Applications, UMR 5142 CNRS, UPPA), LJK (Laboratoire Jean Kuntzmann, Alpes-Grenoble University, UMR 5224 CNRS), and M2N (Laboratoire Modélisation mathématique et numérique, Conservatoire National des Arts et Métiers – CNAM, Paris, EA 7340 CNRS). The library, originally developed to address flow simulations based on remeshed particle methods, was initiated by the work of Etancelin in 2014 [111] and has been successfully extended to a larger scope of HPC applications. This includes the investigation of passive control of flows around a hemisphere that targets drag reduction by introducing a porous coating at the body surface [202], but also sediment flow simulations subject to instabilities [143].

The overall library relies on a Python interface incorporating the object-oriented programming paradigm that provides a flexible framework for both code development and usage. Several numerical solvers can, however, be directly implemented in other compiled languages including Fortran, C or C++, and OpenCL — which is a C++ library that provides high-level interfaces for programming multi-architectures, in the same way as Compute Unified Device Architecture (CUDA). Interface wrappers, such as **f2py** for instance, enable the integration of external dependencies arising from these compiled backends. A dynamical library gathering all the Fortran dependencies is also generated allowing access to efficient Fortran libraries implementing the FFT solver — used in the DBS fixed-point algorithm for instance (see Sect. 2.4.3). Python is particularly suitable as an interface with the compiled languages and, therefore, enables the use of several computing backends.

Another key point in the library design lies in its semantic decomposition into several levels of abstraction that separate the abstract concepts — such as problems, operators, variables, and domains — from the resolution methods. In this sense, the highest level of abstraction allows the user to manipulate objects that closely resemble mathematical concepts, regardless of the architecture or discrete models. The lower levels of abstraction, on the contrary, address the concerns of variable discretization, resolution algorithms, method implementations, data storage aspects, etc. The advantage of such decomposition is that there is a strong cohesion between each level of abstraction but a weak coupling in the sense that various implementation methods can coexist to ensure higher flexibility of the overall code. For instance, the available implementations for a diffusion solver are FFT in Fortran, Python, and OpenCL, while the abstract concept of diffusion operator exists independently of these implementations. This makes it particularly convenient and flexible to investigate several combinations of numerical methods from the user side, but also to develop efficiently new features from the developer's perspective.

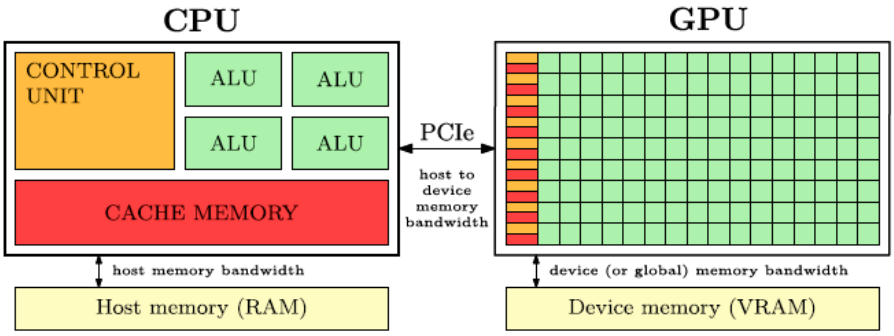


**Figure 2.1: Comparison between a multi-core CPU and GPU architecture [143].**

The entire code is, therefore, structured around the operator-splitting strategy that defines the different operators involved in a problem (at a high level of abstraction), and afterward, enables the discretization of these operators, which are solved using the most appropriate numerical method (at a lower level of abstraction). The overall problem is, afterward, described through an acyclic graph that formalizes the operator interactions in the splitting formulation (*e.g.* see [111, 113, 143]).

From the code development perspective, one has to deal with the lower levels of abstraction, which means defining the operator class and methods with their inherited properties regarding the object-oriented programming concept. The operator backends are also implemented in parallel as, for instance, a Python and OpenCL backend of a given operator can coexist at the same time. At this stage, one encounters, *inter alia*, the operator discretization including ghost-point management (especially useful for parallelization based on domain decomposition), memory request policy with temporary buffer requirements, and memory order (C-contiguous or Fortran-contiguous). In the OpenCL context, the compute backend of the operator can also drive memory exchanges between the several hardware architectures (see Sect. 2.6.2). Finally, HySoP also integrates numerous unit tests whose purpose is to provide a validation of the class or operator implementations with respect to analytic expressions or other implementations. These unit tests can be performed after the library installation, and are useful to check whether the continuous integration of additional classes within the platform does not disrupt the existing ones.

Overall, HySoP is a highly flexible HPC framework well-suited for solving algorithms based on operator splitting strategy, and semi-Lagrangian formalism. On top of that, the library handles high-order remeshing methods including directional splitting, as introduced in Sect. 2.4.3, that can be supported on GPU devices using OpenCL standard.

### 2.6.2 A hybrid CPU-GPU computational framework

The library also offers the possibility to deal with parallelism on hybrid architectures, including various computing devices such as CPU and GPU. In addition to its high flexibility developed in Sect. 2.6.1, HySoP holds promise as an effective computational framework able to handle an overall hybrid approach. This resulted from successive developments of the original library, which have rendered possible the integration of OpenCL standard and the implementation on hardware accelerators [90, 143, 287]. This was also made possible by the emergence, in the 2000s, of the so-called General-Purpose computing on Graphics Processing Units (GPGPU) concept, which integrates the GPU as a CPU processing partner targeting accelerated performances.

First of all, one needs to understand the main characteristics of a hybrid architecture providing multiple computing devices, along with the differences between the CPU and GPU. A GPU device allows a very high speed of elementary and independent tasks that are carried out in parallel by the numerous computing units, namely the Arithmetic Logical Unit (ALU) in Figure 2.1. While a GPU device presents a much larger number of cores than a CPU, the available memory on a GPU is usually smaller and gathered between several ALU, which puts forward the motivation to use hybrid architecture. Indeed, the CPU processors benefit on the contrary from access to the overall system memory, also called the host memory directly accessible from the host proces-

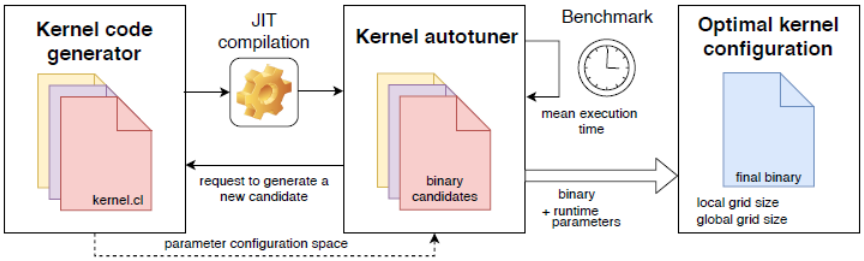


**Figure 2.2: Micro-benchmarking strategy on OpenCL kernels [143].**

sor. Memory exchanges between the host CPU processor and the OpenCL devices are achieved through a Peripheral Component Interconnect Express (PCIe) connection, which can lead to some latency due to sending back-and-forth computational data. The efficient management of such data exchanges is an intrinsic part of the overall performance analysis in hybrid computing frameworks.

Direct GPU programming requires specific languages and among the most widely developed are CUDA and OpenCL [107, 165, 300]. Currently, the latter is mainly used within the HySoP platform: first, it benefits from an open-source version of the standard even if optimized implementations are developed for specific devices (NVIDIA, Intel, ...), and also presents higher portability across a variety of hardware. Indeed, OpenCL not only handles GPU programming but also presents the advantage of supporting more heterogeneous devices, including multi-core processors. Such a standard makes it possible to consider several levels of parallelism, namely tasks and data parallelization.

Overall performance can largely vary across the different OpenCL platforms such that optimal kernels need to be tuned depending on the target device, where a kernel here commonly refers to a function executed on an OpenCL device. Optimizing the kernel parameters is, however, a challenging problem and widely dependent on the hardware architecture [106]. In this sense, a major improvement of the HySoP platform was to integrate automatic code generation and performance auto-tuning in the OpenCL backends of the GPU targeted operators [143]. This involves a micro-benchmarking strategy performed at the code runtime, which provides the best kernel parameters according to the target OpenCL device and, thereby, ensures optimal use of the available resources. Such an auto-tuning process principle is illustrated in Figure 2.2 and guarantees performance-portability and flexibility of the HySoP library. Once the kernel optimal parameters are determined, one gets compiled OpenCL sources generated at the runtime, also called Just-in-time compilation (JIT), through a code generation framework. Several methods can be used to address code generation, among them Abstract Syntax Trees (AST) which is mostly used to generate and vectorize code based on symbolic expressions (see Sect. 2.6.3).

Finally, data parallelization on distributed architectures is also handled within the HySoP library through domain decomposition, which splits the overall domain into multiple sub-grids distributed to several processes [85]. Communication patterns between each process, and consequently each sub-domain, are ensured via Message Passing Interface (MPI) and ghost layers data exchanges. The latter is particularly useful for stencil-based numerical methods such as finite differences or discrete renormalized PSE that require evaluation on the neighbors' vertices. In this sense, the sub-domain boundaries are extended with these additional ghost layers, whose number depends on the stencil requirements.

The numerical simulations presented in Sect. 2.7.3 are conducted on the Pyrene Cluster at the UPPA and benefit from the ability of the HySoP library to handle hybrid architecture. The GPU accelerators available are 2 NVIDIA Tesla P100 graphic cards, whose memory bandwidth for host-to-device and device-to-host exchanges relies on a PCIe of 16Gb/s, and device memory is estimated at around 16GB. The simulations are performed using a single GPU node, and we also account for data parallelization based on MPI domain decomposition involving four processes.

### 2.6.3 OpenCL implementation of the PSE for heterogeneous diffusion

One of the objectives of this thesis consists in the improvement of the semi-Lagrangian method presented in Sect. 2.4 to account for the heterogeneous diffusion of the chemical reactants through a porous matrix in the context of reactive flow processes. In this section, we thus address the implementation within the HySoP platform of the discrete renormalized version of the PSE algorithm, as introduced in Sect. 2.5.2. This aims to provide an efficient approximation for Archie's law in the context of $CO_2$ mineral storage and, more broadly, to develop an overall DiffusionPSE class in HySoP that could be extended to other applications. A GPU targeted version of the method is developed with the OpenCL standard to benefit from the hybrid architecture of the computational framework, as introduced in Sect. 2.4.1. The latter is validated against a reference CPU implementation based on the Python host backend, along with a unit test to guarantee the proper continuous integration of this additional numerical method in HySoP.

The implementation process is, therefore, decomposed into several steps: a Python operator was first integrated into the host backend, involving the lower levels of abstraction of the library. One needs to develop the operator class that will be common to both Python and OpenCL implementations and, therefore, defines the main attributes of the operator independently of the compute backend. These common attributes include the input and output fields — which are the concentration fields $C_k$ and the micro-porosity $\varepsilon$ when considering the Lagrangian equation (2.20) —, the diffusion matrix $\mathbf{L}$, the support of the kernel $\sigma^{\xi}$, the space steps in each direction and the coefficients $(c_0, c_1)$ of the matrix $\mathbf{m}$ introduced in equation (2.45). Indeed, as the latter matrix coefficients mainly depend on the choice of the function $\theta$ (see Sect. 2.5.3), they can be regarded as constant in the different implementations of the operator.

Concerning the Python backend, the class is inherited from the parent class HostOperator and the main concerns are the ghost-point management and the implementation of the Python method, which contains the proper execution of the PSE scheme. First, the number of ghost points in each direction is constrained by the kernel support attribute — providing the minimal number of ghost points required — and is processed individually for each field through the HySoP automatic ghost-point management. This takes into account that only the input and diffusion matrix fields will require ghost points, in this particular case, and also makes it possible to update their numbers with respect to boundary conditions or domain decomposition constraints. The implementation of the diffusion operator along with a PSE approximation is performed using a stencil data structure — similar to finite differences schemes — along with Python slices depending on the kernel support and indexing the local neighbors of the current mesh point. This can afterward be coupled with a second-order Runge-Kutta scheme to address the overall diffusion problem.

For the OpenCL backend, and as introduced in Sect. 2.6.2, we focus on the code generation technique which relies on symbolic representations of the operator variables and expressions. This offers the possibility to efficiently generate stencil schemes on GPU devices based on elementwise operations, allowing their distribution over the elements of the OpenCL index space. In this sense, the OpenCL kernel consists of an instruction sequence, grouped in a list of symbolic expressions, that will be executed on subdivisions of the compute resolution through data parallelism. Memory coherency between the OpenCL index space and the host grid resolution is maintained thanks to the pyOpenCL package, thus rendering communication easier between the discrete fields on the host process and the OpenCL multidimensional buffers. This is especially significant because structured data is not necessarily arranged in the same manner on the host and devices.

The approach developed in [111] and [143] when dealing with OpenCL stencil schemes, in remeshing kernels implementation for instance, was to use a directional splitting to only treat one-dimensional stencils in each spatial direction successively. This choice was relevant in the sense that, for the remeshing formula, the n-dimensional case can be treated as a tensor product of one-dimensional kernels. For the PSE method with spherically symmetric function $\theta$, given by formula (2.43), the directional splitting is, however, not suitable. Indeed, this would require a tensorial PSE formulation that allows the splitting in efficient one-dimensional stencils, which is not the case with the present formulation. We, therefore, use a prototype of a three-dimensional stencil which is inherited from the stencil generator class and goes through the overall $\xi$-neighborhood in

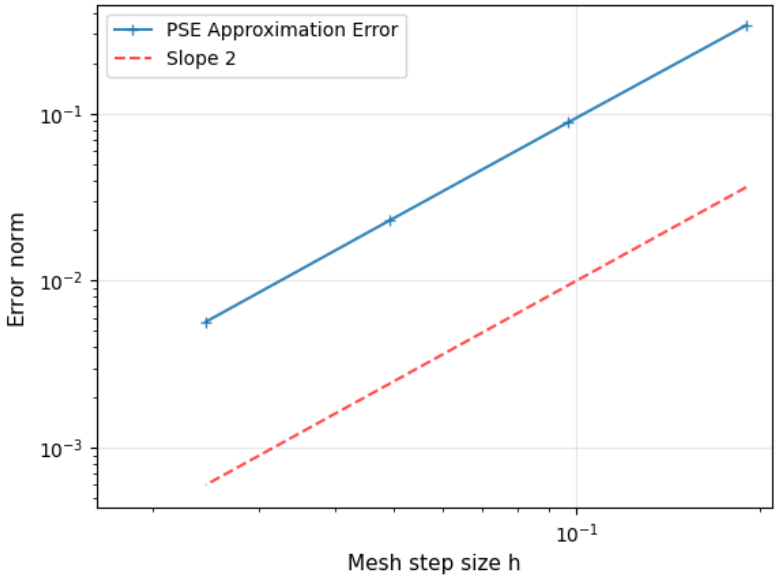


**Figure 2.3: Mesh convergence analysis of the OpenCL implementation of the PSE method:** Error norm $\|\mathrm{Err}\|_{\mathrm{RMS}}$ with respect to the mesh step size $h$ for heterogeneous diffusion operator with a spatially varying diffusion matrix $\mathbf{L}$. The convergence analysis is performed for mesh resolutions going from $32^3$ to $256^3$.

the PSE formulation (2.42).

A first unit test is developed to validate the Python backend implementation of the PSE operator using an analytic expression. We consider the approximation of a diffusion operator $\mathrm{div}(\mathbf{L}\nabla f)$ on a domain $\Omega \subset \mathbb{R}^3$ with a spatially varying diffusion matrix

$$\mathbf{L}(x, y, z) = (1 + \cos^2(x))\mathbf{I}_3$$

and a function $f$ given by $f(x, y, z) = \sin(x)\sin(y)\sin(z)$. This ensures three-periodic boundary conditions on the domain $\Omega = ]-\pi;\pi[^3$. Direct computation of the exact solution provides

$$\mathrm{div}(\mathbf{L}\nabla f)(x, y, z) = -3f(x, y, z) - 5\cos^2(x)f(x, y, z)$$

and a mesh convergence analysis is performed, studying the error norm against the mesh step $h$, for mesh resolutions going from $32^3$ to $256^3$. Introducing the discrete error vector Err, defined for each point $X_k \in \mathbb{R}^3$ of the grid by

$$\mathrm{Err}_k := \mathrm{div}(\mathbf{L}\nabla f)(X_k) - Q^{\xi} \cdot f^h(X_k),$$

we compute for each mesh resolution the Root Mean Square (RMS) norm $\|\mathrm{Err}\|_{\mathrm{RMS}}$ inherited from the functional $\mathbb{L}^2$-norm on $\Omega$. The value of $Q^{\xi} \cdot f^h$ is defined on every particles by formulae (2.26) or (2.42), despite the fact that $f^h$ is a measure function, that is to say a combination of Dirac functions.

As theoretically expected in Sect. 2.5, we retrieve a second-order convergence curve presented in Figure 2.3. Finally, the unit test was completed to include the validation of the OpenCL implementation. In this case, the test is performed with respect to the Python backend reference. These kinds of unit tests are conducted for small mesh resolutions since they consist of short checks performed right after the HySoP install. It does not break down if: first, the Python implementation provides an error norm $\|\mathrm{Err}\|_{\mathrm{RMS}}$ less than a given tolerance, and then if the OpenCL implementation provides an error norm — compared to the reference version in Python — less than a given tolerance, for the discrete $\ell^\infty$-norm.

The OpenCL operator performances have also been investigated on this unit test, measuring the computational time of the diffusion operator approximation for several mesh refinements of the 3D computational domain $\Omega$. The measured times include kernel execution on GPU but do not

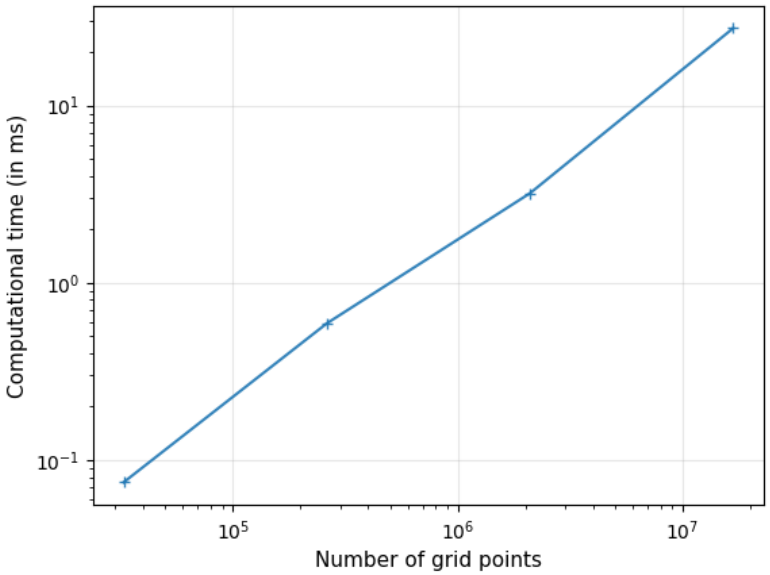


**Figure 2.4: Computational time analysis of the OpenCL implementation of the PSE method:** The analysis is performed for mesh resolutions going from $32^3$ to $256^3$, for heterogeneous diffusion operator with a spatially varying diffusion matrix $\mathbf{L}$. All the measured times are expressed in milliseconds (ms) and averaged over several evaluations of the PSE operator.

account for the communication latency due to data exchanges between the host process and the GPU devices. The results are presented in Figure 2.4 and highlight a complexity in $\mathcal{O}(N)$, with $N$ the total number of grid points. Such a linear complexity is also characteristic of the particle remeshing and Lagrangian advection steps in the general algorithm.

Overall, we benefit from the capacities of the HySoP library to generate efficient and accelerated elementwise PSE operators based on symbolic and code generation approaches. The OpenCL backend of the DiffusionPSE class, can subsequently approximate an overall diffusion-reaction problem with spatially varying diffusion coefficients, coupling the previous PSE implementation with second-order Runge-Kutta numerical schemes. This makes it possible to address the Lagrangian formulation of the chemistry, given by equation (2.20), globally on the GPU devices. Indeed, in the operator splitting strategy developed in Sect. 2.4.3, the advection/remeshing step can already be handled on GPU due to efficient directional splitting implemented within the HySoP platform. In this sense, the DBS equation in its velocity-vorticity formulation is solved in an Eulerian context through a fixed-point algorithm implemented on the host CPU while the chemical convection-diffusion-reaction equations are fully implemented on GPU devices in their Lagrangian formulation.

## 2.7 Precipitation and crystallization modeling for $CO_2$ mineral storage at the pore-scale

$CO_2$ mineral storage in natural underground reservoirs, such as saline aquifers, involves competing geochemical phenomena occurring at a large variety of scales. Among them, mineral dissolution and precipitation play crucial roles. On one side, studying the dissolution of native carbonate species, already present in the aquifers, provides insight into potential leakage issues and queries the reservoir safety. On the other side, $CO_2$ trapping under the form of carbonate precipitates and crystals informs on the storage capacities of the reservoir. These geochemical processes also induce changes in the macro-scale properties of the subsurface material, including permeability and porosity evolutions, that need to be investigated to ensure sustainable management of the reservoir structures.

In this section, we develop mathematical models for calcite precipitation and crystallization at the pore scale, with special considerations on the reaction rate expressions arising in the PDE

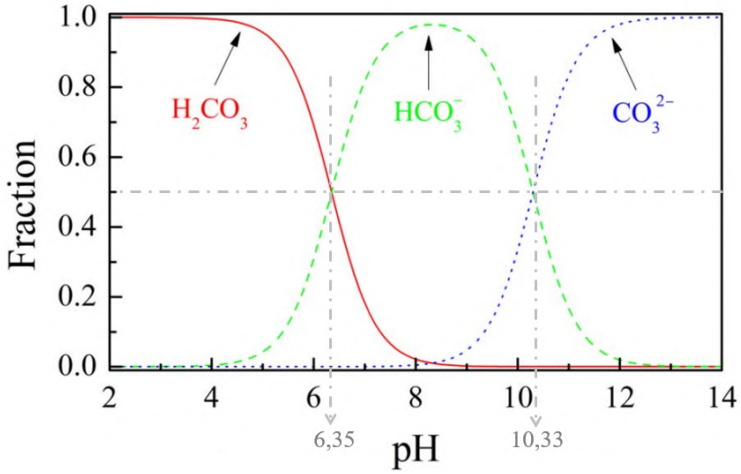


**Figure 2.5: Distribution diagram of aqueous carbonate species against pH solution [53, 304].** Species distributions are represented as a fraction of total dissolved carbonate. The grey dotted lines highlight the transition pH of the chemical equilibria from equation (2.61).

system (2.11). Numerical simulations are performed within the HySoP platform along with PSE treatment of the heterogeneous diffusion on accelerated GPU devices and address porous sample arising from X-ray $\mu$CT observations. This enables the investigations of macro-scale property changes along the $CO_2$ mineral trapping on real 3D rock geometries, which is an important component in the overall study of $CO_2$ storage.

### 2.7.1 The Transition State Theory: from Dissolution to Precipitation Modeling

Dissolution of the injected $CO_2$ in the aqueous phase of deep underground reservoirs will affect the pH of the formation water through the following series of chemical reactions:

$$CO_2\,(g) \rightleftharpoons CO_2\,(aq) \tag{2.61a}$$

$$H_2O + CO_2\,(aq) \rightleftharpoons H_2CO_3 \tag{2.61b}$$

$$H_2CO_3 \rightleftharpoons H^+ + HCO_3{}^- \tag{2.61c}$$

$$HCO_3{}^- \rightleftharpoons H^+ + CO_3{}^{2-}. \tag{2.61d}$$

Indeed, once the $CO_2$ has dissolved into water and established a first equilibrium under the form of the weak acid $H_2CO_3$, the $H_2CO_3$ species dissociates successively to bicarbonate $HCO_3{}^-$ and carbonate $CO_3{}^{2-}$ ions as the pH increases. These chemical reactions are pH-dependent, and the distribution evolutions of all these carbonate species are displayed in Figure 2.5 against the pH of the solution. In alkaline media, the chemical reactions (2.61c) and (2.61d) can, therefore, join together to read as follows:

$$H_2CO_3 + 2\,OH^- \rightleftharpoons CO_3{}^{2-} + 2\,H_2O \tag{2.62}$$

such that carbonate ions are the main carbonate species present in the solution. Such transformations in the ionic species composition of the aquifer water will considerably impact the original mineral structure through chemical rock-water interactions such as carbonate dissolution and precipitation.

Historically, the dissolution and precipitation kinetics of calcite in the context of $CO_2$ injection have been studied since the 1970s, both from the experimental and theoretical sides. Plummer *et al.* investigated the influence of several parameters on the forward reaction rates of calcite dissolution under far-from-equilibrium conditions [245]. Among these parameters, one finds the partial pressure of $CO_2$ denoted $P_{CO_2}$, the hydrogen ions activities denoted $a_{H^+}$ — directly related to the pH — and the temperature. Their experimental work was subsequently extended by Chou *et*

*al.* in 1989 using a fluidized bed reactor to compare the dissolution kinetics mechanisms between various carbonate minerals — involving *inter alia* calcite, aragonite, and dolomite — at 25°C [77]. One should notice that these experiments were conducted under laboratory conditions in terms of pressures and temperatures, in opposition to the current abilities of *in situ* experiments to manage realistic reservoir conditions [20, 317]. Nonetheless, these experimental studies have highlighted three kinetic mechanisms occurring simultaneously in the process of calcite dissolution due to $CO_2$ injection. Such mechanisms are given by the following chemical reactions:

$$\mathrm{CaCO_3\,(s) + H^+ \overset{K_1}{\rightleftharpoons} Ca^{2+} + HCO_3^-} \tag{2.63a}$$

$$\mathrm{CaCO_3\,(s) + H_2CO_3 \overset{K_2}{\rightleftharpoons} Ca^{2+} + 2\,HCO_3^-} \tag{2.63b}$$

$$\mathrm{CaCO_3\,(s) \underset{K_{-3}}{\overset{K_3}{\rightleftharpoons}} Ca^{2+} + CO_3^{2-}} \tag{2.63c}$$

where the notations $K_i$, $i = 1...3$ refer to forward reaction rate constants, depending on the temperature [61, 245, 244], and $K_{-3}$ is the backward reaction rate corresponding to the reverse calcite precipitation process in equation (2.63c). They experimentally identified both the forward and backward reaction rates and established the validity of kinetic models for carbonate dissolution and precipitation in comparison to thermodynamics theoretical considerations.

Meanwhile, mineral reaction rates were, indeed, theoretically investigated by Lasaga in 1981 [156] using the Transition State Theory (TST), originally formulated by Erying in 1935 [114]. Since then, this formalism has successfully been extended [1, 157, 285] and widely accepted in current kinetic geochemical models [113, 206, 282]. In this context, the reaction rates are commonly expressed as the product of far-from-equilibrium terms, involving the activities of the chemical species in solution, with an affinity term written as a function of the Gibbs free energy change $\Delta G$ for close to the equilibrium conditions. Considering the chemical model of calcite dissolution (2.63) suggested by Plummer *et al.* [245] and Chou *et al.* [77] and the vector of concentrations $\mathbf{C}$, the reaction rate arising from TST writes:

$$R(\mathbf{C}) = A_s(K_1 a_{\mathrm{H^+}} + K_2 a_{\mathrm{H_2CO_3}} + K_3)\left(\frac{a_{\mathrm{Ca^{2+}}}\, a_{\mathrm{CO_3^{2-}}}}{K_{\mathrm{eq}}} - 1\right) \tag{2.64}$$

where $K_{\mathrm{eq}}$ is the equilibrium constant of the reaction, also called the solubility product, $A_s$ is the reactive surface area of the mineral — in $\mathrm{m}^{-1}$. The notations $a_\bullet = \gamma_\bullet C_\bullet$ refer to the dimensionless species activities with $\gamma_\bullet$ and $C_\bullet$, respectively, their activity coefficients and molar concentrations — whose unit is $\mathrm{mol.m}^{-3}$. It follows that the micro-porosity changes reads as:

$$\frac{\partial \varepsilon}{\partial t} = -\upsilon R(\mathbf{C}), \tag{2.65}$$

given equation (2.8) from Sect. 2.3.2 and the relation $C_{\mathrm{CaCO_3}(s)} = (1-\varepsilon)/\upsilon$. Denoting by $Q = a_{\mathrm{Ca^{2+}}}\, a_{\mathrm{CO_3^{2-}}}$ the ion activity product, one obtains the following relation between $Q$ and the Gibbs energy change [1, 157]:

$$\Delta G = RT \ln\left(\frac{Q}{K_{\mathrm{eq}}}\right) \tag{2.66}$$

with $T$ the temperature in Kelvin K, and $R$ the universal gas constant in $\mathrm{J.mol^{-1}.K^{-1}}$. The sign of the reaction term $R(\mathbf{C})$ in (2.64) is driven by the sign of $\ln\left(Q/K_{\mathrm{eq}}\right)$ that is negative for dissolution and positive for precipitation, which is consistent with the convention from Sect. 2.3.2.

From now on, we focus on the concern of calcite precipitation and crystallization resulting from $CO_2$ injection based on the series of homogeneous reactions (2.61) along with the mineral-solute interaction given by equation (2.63c). In practice, we enforce a pH greater than 10.33 such that the carbonate ions $CO_3^{2-}$ are the predominant species (see Figure 2.5). This enables the restriction of the overall set of chemical reactions (2.61) to merely consider the equation (2.63c) in the sense that we assume the intermediate reactions as instantaneous and conservative — without

loss of quantity of matter. Such an assumption is acceptable, in practice, since fluid-mineral reaction rates are usually slower than intra-aqueous reaction rates. Therefore, the initial concentration of carbonate ions, denoted $C_{\mathrm{CO_3}^{2-}}(x, t=0)$ for $(x,t) \in \Omega \times [0, T_f]$ following the notations introduced in Sect. 2.3, is directly related to the partial pressure of injected $CO_2$ by means of the Henry law. The latter states, at a constant temperature, the relation between the amount of dissolved gas in a solute and its partial pressure based on Henry's law constant denoted $K_H$, which depends on the gas and temperature, such that for the $CO_2$ at 25°C one gets:

$$C_{\mathrm{CO_2(aq)}} = \frac{P_{\mathrm{CO_2}}}{K_H} \simeq C_{\mathrm{CO_3}^{2-}}(x, t=0) \tag{2.67}$$

where $K_H = 29.41\,\mathrm{L.atm.mol^{-1}}$. Considering such an alkaline medium — with pH $> 10.33$ — also results in the treatment of the chemical reaction (2.63c) as completely irreversible which corresponds to far-from-equilibrium conditions modelling the calcite precipitation chemical reaction:

$$\mathrm{Ca^{2+}} + \mathrm{CO_3^{2-}} \xrightarrow{\mathrm{K_{-3}}} \mathrm{CaCO_3\,(p)} \tag{2.68}$$

where the subscript $p$ here refers to the precipitate form of the calcite product. In this case, the rate constants $K_1 = K_2 = 0$ in (2.64) and the affinity term dependent on the Gibbs energy satisfies the condition $\ln\left(Q/K_{\mathrm{eq}}\right) \gg 0$ — corresponding to a supersaturated solution — so that we obtain an overall reaction rate for the calcite precipitation which reads as:

$$R_{\mathrm{prec}}(\mathbf{C}) = K_{-3}\, A_s\, a_{\mathrm{Ca^{2+}}}\, a_{\mathrm{CO_3^{2-}}} \tag{2.69}$$

where $K_{-3} = K_3/K_{\mathrm{eq}}$, which theoretically results from the TST law in equation (2.64) and has been experimentally validated, *inter alia*, by Chou *et al.* in [77].

Therefore, in the following, we rely on the kinetic formulation of the mineral precipitation given by equation (2.69), considering the rate laws determined by laboratory experiments [77] and normalized by the reactive surface area of the mineral $A_s$ [245]. As the geometry evolves, the micro-porosity $\varepsilon$ and the reactive specific area $A_s$, associated with the porous structure, also change. These evolutions are taken into account in the reaction rates management and the hydrodynamic modeling of the reactive process (see the overall PDE system (2.11) in Sect. 2.3.2). The calcite precipitation reaction is subsequently supplemented with a crystallization model which is elaborated in the next Sect. 2.7.2.

### 2.7.2 Crystal growth modeling: a two-step process

Crystal growth kinetics involves complex mechanisms occurring simultaneously and depending, *inter alia*, on the concentration of the constituent ions in the solute, but also on attachment frequencies of the ions or precipitates to lattice growth sites [216, 320]. Indeed, the growth rate is first controlled by advection and diffusion of the $\mathrm{Ca^{2+}}$ and $\mathrm{CO_3^{2-}}$ ions to the crystal surface coupled with a surface adsorption process that largely hinges on the crystal lattice shape. For instance, the growth of crystal aggregates is more likely to occur near kinks or corners [216, 334]. Mineral heterogeneity of the pore interface is also an important factor that influences the crystal growth location and morphology, providing preferential sites [174]. This first process is commonly called primary heterogeneous nucleation, for which the crystallization reaction is catalyzed by the solid surface of the porous medium. In the absence of solid interface, crystal clusters can also form spontaneously in the solute, which is known as primary homogeneous nucleation and is closely related to the supersaturation state of the solution in order to initiate the nucleation — namely satisfying the condition $\ln\left(Q/K_{\mathrm{eq}}\right) \gg 0$. Finally, secondary nucleation occurs in the presence of existing crystals and is more likely to generate large crystal aggregates at the mineral surface. Overall, calcite crystallization results from a combination of all these previous phenomena.

In this section, we consider a two-step crystallization process wherein calcite precipitates, also referred to as nuclei and denoted $\mathrm{CaCO_3(p)}$, are first generated within the solute during the so-called nucleation stage according to the chemical equation (2.68). These precipitates are

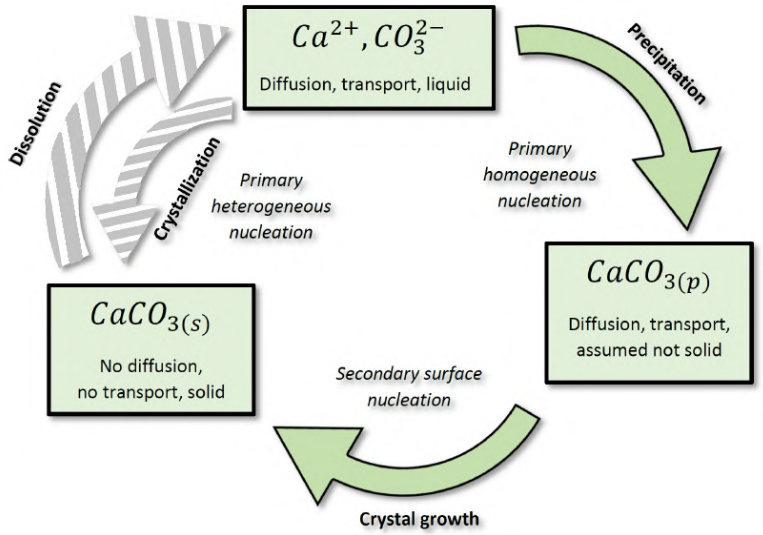


**Figure 2.6: Overall reactive diagram of the reversible chemical equation (2.63c) and two-step calcite crystallization process.** This diagram represents the chemical interactions between the different ionic species ($Ca^{2+}$ and $CO_3^{2-}$), the calcium carbonate precipitate $CaCO_3$(p) and mineral crystal $CaCO_3$(s) and accounts for both dissolution, precipitation crystal growth processes. In the numerical applications (see Sect. 2.7.3), we mainly address the green part of this diagram that highlights the two-step modeling of the calcite crystallization process.

subsequently aggregated at the mineral surface through adsorption phenomena during the crystal growth step. This sequential crystallization process is described in Figure 2.6, where the notation $\mathrm{CaCO_3(s)}$ stands for the calcite crystal. In the applications developed in Sect. 2.7.3, we consider that the solid matrix of the 3D porous sample has a similar carbonate nature to the calcite crystal generated, though rock mineral heterogeneities can be integrated into the numerical framework as prospects. From now on, we refer to precipitation as the primary homogeneous nucleation and we investigate the surface attachment of the calcite precipitate, $\mathrm{CaCO_3(p)}$, based on an autocatalytic process to model calcite crystal growth, referred to as the secondary surface nucleation in Figure 2.6. In the reaction scheme from Figure 2.6, we account for the precipitate diffusion and advection until the solid boundary where it leads to crystal growth through adsorption phenomena. Besides, we neglect the direct crystallization process induced by the solute diffusion to the solid matrix and the so-called primary heterogeneous nucleation.

In the literature, two distinct approaches are mainly developed when considering precipitation and crystal growth modeling altogether. The former can be regarded as "deterministic models" relying on the TST modeling developed in Sect. 2.7.1. Noiriel *et al.*, for instance, investigated the effects of pore-scale precipitation on permeability through a combination of X-ray $\mu$CT experiments and "deterministic" modeling [219, 222]. They also derived crystal growth rates directly from the $\mu$CT through an imaging comparison between the beginning and end of the precipitation experiment. In this case, only two $\mu$CT scans were performed, and therefore, the process should be understood as distinct from 4D $\mu$CT experiments incorporating time dynamics. Such experimental identification of crystal growth rates can, however, be prone to intrinsic imaging limitations introduced in Sect. 1.1.3 from Chapter 1 and result in wide discrepancies in the reaction rate estimations. Nonetheless, their results showed satisfactory agreement between the experiments and numerical experiments for precipitation processes into fractures [219]. Alternative modeling approaches lie in the probabilistic nature of nucleation or crystal growth and are referred to as "probabilistic models" [118, 194, 223]. Wolthers *et al.*, for instance, developed a probabilistic approach for calcite crystal growth based on the nature of the kink sites depending on their ionic affinities and attachment frequencies of the constituent ions [320]. Estimations of such adsorption frequency ranges can also be found in the literature [79, 215]. Finally, while it is commonly

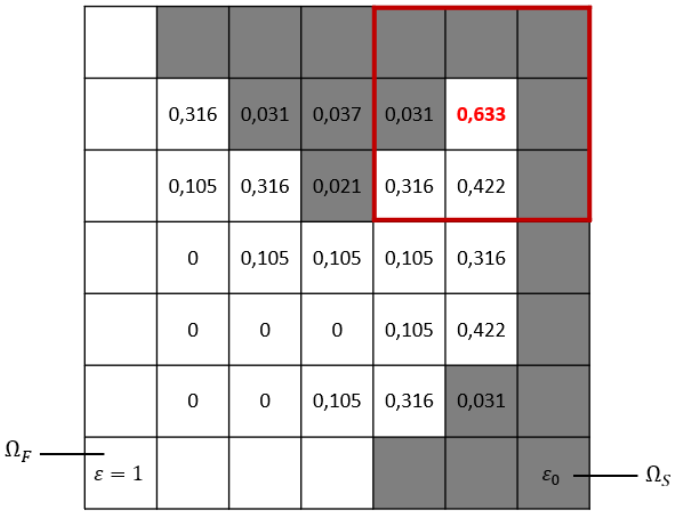


**Figure 2.7: Impact of the probability of attachment rate $P_{\text{ad}}$ for crystal growth modeling.** Synthetic representation of a porous medium, at the voxel size, with a residual micro-porosity in the porous matrix $\Omega_S$ estimated to $\varepsilon_0 = 5\%$. The probability values are computed based on equation (2.70) and include the one-neighborhood — *e.g.* the red square — of the current mesh point — marked by the red value.

established experimentally that crystal growth occurs preferentially at kinks and corners of the surface lattice, few models incorporate the geometrical dependency of the crystal aggregation in the reaction rates [310].

In the present thesis, we propose a new approach coupling a deterministic model for the precipitation, which directly depends on the supersaturation ratio following the TST formalism, and a probabilistic formulation of the crystal growth process. The latter accounts for the adsorption frequencies of the precipitate to the growth sites with a coefficient, quantifying the physical probability of attachment rate, denoted $P_{\text{ad}}$, which relies on a locally averaged mineral volume fraction. This makes it possible to include the geometrical dependency in the crystal growth reaction rate through the relation

$$P_{\text{ad}} = (1 - \overline{\varepsilon})\varepsilon, \tag{2.70}$$

where $\overline{\varepsilon}$ is the micro-porosity average on the one-neighborhood of the current point. If we denote by $W_h = \mathbb{1}_{[-h,h]}/2h$ the averaging kernel over $[-h, h]$, then $\overline{\varepsilon} = \varepsilon * W_h^{\otimes 3}$ so that $(1 - \overline{\varepsilon})\varepsilon$ is enhanced in the layer close to the fluid/solid interface and depending on the solid proportion in the neighborhood (see Figure 2.7). This is a convolution-based formulation appropriate for a crystallization process and inspired by the gradient-based technique from [182] and [279] that locates the first layer on the solid side and is suitable for dissolution processes. In practice, the local averaging kernel $W_h$ is approximated by its pointwise discretization $\widetilde{W}_h = (\delta_{-h}+\delta_0+\delta_h)/3$.

The resulting probability values are represented in Figure 2.7 for a synthetic example, where the residual micro-porosity in $\Omega_S$ is estimated to $\varepsilon_0 = 5\%$. In this formalism, one obtains the crystal growth reaction rate, which is expressed as:

$$R_{\text{crys}}(\mathbf{C}) = K_c\, C_{\text{CaCO}_{3(\text{p})}}(1 - \overline{\varepsilon})\varepsilon \tag{2.71}$$

with $K_c$ the adsorption frequency — in $\text{s}^{-1}$. The adsorption coefficient $K_c$ can have several meanings, based either on surface or volume balance. It can be a front velocity (in $\text{m.s}^{-1}$) times a specific area (in $\text{m}^{-1}$), or a volume production rate of crystal (in $\text{m}^3\text{.s}^{-1}$) per unit of volume (in $\text{m}^3$). Depending on the formulation, the coefficient $P_{ad}$ has to be normalized accordingly. In order to keep a general formulation, the present study will focus on the impact of the term $K_c(1 - \overline{\varepsilon})\varepsilon$, so that the possible normalization of $P_{ad}$ is hold by the coefficient $K_c$. Moreover, we can see *a posteriori* on Figure 2.7 that coefficient $P_{ad}$ is in the range 0.3–0.7, which is close to unity, hence does not require a strong normalization. If needed, such a normalization can be done using the method given in section 2.2 of [279].

Finally, we define the vector of concentrations $\mathbf{C} = \left(C_{\mathrm{CaCO_3(s)}}, C_{\mathrm{CaCO_3(p)}}, C_{\mathrm{CO_3^{2-}}}, C_{\mathrm{Ca^{2+}}}\right)$ and consider the reactions rates $R_{\text{prec}}(\mathbf{C})$ and $R_{\text{crys}}(\mathbf{C})$ respectively given by formula (2.69) and (2.71). Overall, the calcite crystallization modeled as a two-step process of precipitation and crystal growth, according to the reaction scheme from Figure 2.6, writes:

$$
\begin{cases}
-\mathrm{div}(2\mu D(u)) + \mu\kappa_b^{-1}\dfrac{(1-\varepsilon)^2}{\varepsilon^2}u = \varepsilon(f - \nabla p), & \text{in } \Omega\times]0,T_f[ \\
\dfrac{\partial C_{\mathrm{CO_3^{2-}}}}{\partial t} + \mathrm{div}\big(F(C_{\mathrm{CO_3^{2-}}})\big) = -R_{\text{prec}}(\mathbf{C}), & \text{in } \Omega\times]0,T_f[ \\
\dfrac{\partial C_{\mathrm{Ca^{2+}}}}{\partial t} + \mathrm{div}\big(F(C_{\mathrm{Ca^{2+}}})\big) = -R_{\text{prec}}(\mathbf{C}), & \text{in } \Omega\times]0,T_f[ \\
\dfrac{\partial C_{\mathrm{CaCO_3(p)}}}{\partial t} + \mathrm{div}\big(F(C_{\mathrm{CaCO_3(p)}})\big) = R_{\text{prec}}(\mathbf{C}) - R_{\text{crys}}(\mathbf{C}), & \text{in } \Omega\times]0,T_f[ \\
\dfrac{\partial C_{\mathrm{CaCO_3(s)}}}{\partial t} = R_{\text{crys}}(\mathbf{C}), & \text{in } \Omega\times]0,T_f[ \\
\varepsilon = 1 - \upsilon C_{\mathrm{CaCO_3(s)}}, & \text{in } \Omega\times]0,T_f[ \\
\text{+ adequate boundary and initial conditions, along with } \mathrm{div}\, u = 0
\end{cases}
\tag{2.72}
$$

where $F(C_\bullet) = \varepsilon^{-1}uC_\bullet - \alpha_\bullet(\varepsilon)\nabla^\varepsilon C_\bullet$ is the advective and diffusive flux given the notations from Sect. 2.3.2. The reactive hydrodynamic model (2.72) ensures that part of the precipitate, generated in the solute through homogeneous nucleation, is transferred to the mineral surface by adsorption. One should notice that in this model the precipitate $C_{\mathrm{CaCO_3(p)}}$ is both advected and diffused. Such diffusion enables to account for the interaction of the precipitates with potential unresolved roughness or features in the porous matrix $\Omega_S$.

In the next Sect. 2.7.3, we apply this two-step crystallization model to DNS of $CO_2$ mineral trapping into a real rock geometry at the pore-scale. We investigate the morphological changes in the porous matrix structure, the clogging of pore throats, and the evolution of the macro-scale properties, namely the porosity and permeability.

### 2.7.3 DNS of $CO_2$ mineral trapping into calcite

The present section focuses on the effects of calcite crystallization on changes in the pore geometry, macro-properties, and flow at the pore scale in the context of $CO_2$ mineral trapping. We consider a pore-scale geometry obtained by microtomography measurements from Sheppard and Prodanovic in 2015 and freely available on the Digital Rocks data portal, which includes *inter alia* $\mu$CT datasets of limestone, glass bead pack, and Castlegate sandstone [272]. The numerical simulations are performed on the Castlegate geometry at a resolution of $128^3$ with a voxel size of $5.6\mu$m, which represents a numerical sub-sample of about $L = 0.7168$mm. We assume, as previously introduced in Sect. 2.7.2, that the porous matrix is of identical mineral nature as the crystal generated along the reactive process and, thereby, consider that the sub-sample is composed of calcite. While including mineral heterogeneities as perspectives, we here hypothesize the homogeneity of the mineral structure within the sample. Finally, the specific area is numerically estimated for this sample to get, at the initial state, $A_s = 8300\mathrm{m}^{-1}$, and is afterward updated along the reactive process.

Numerical simulations are performed under atmospheric conditions in terms of pressure and temperature and rely on the experimental identification of the reaction rate constants, arising from the literature [77]. We consider isothermal conditions with a temperature of $T = 25$°C and an injection of $CO_2$ with a partial pressure of $P_{CO_2} = 3.15\mathrm{e}{-2}\,\mathrm{bar} = 2.96\mathrm{e}{-2}\,\mathrm{atm}$ — which is about 100 times greater than the partial pressure of $CO_2$ in the atmosphere. Given Henry's law constant for the $CO_2$ at 25°C, and under the assumption of a highly alkaline medium — with pH $> 10.33$ — we estimate from equation (2.67) that the initial concentration of carbonate ions is given by $C_{\mathrm{CO_3^{2-}}}(x, t=0) = 1\mathrm{e}{-3}\,\mathrm{mol.L}^{-1}$.

The calcium initial concentration is subsequently determined based on the equilibrium constant $K_{\text{eq}} = 10^{-8.48}$ [77, 244] to ensure a far-from-equilibrium precipitation regime given by the supersaturation condition $Q \gg K_{\text{eq}}$. In this sense, we assume that the medium pore space is initially filled with a saturated solution wherein the initial concentration of calcium ions is $C_{\text{Ca}^{2+}}(x, t = 0) = 1\text{e}{-1}\,\text{mol.L}^{-1}$. Therefore, in our case, the saturation in calcium ions $\text{Ca}^{2+}$ initially present in the domain is not a limiting factor of the precipitation reaction, and we consider a continuous calcium injection that maintains the supersaturation constraint. Actually, in order to maintain this supersaturation, we will assume that the concentration in $\text{Ca}^{2+}$ remains constant at its initial value. Comparable initial conditions and assumptions have been employed in investigating dissolution experiments by Maes *et al.* [188], wherein the sample core was initially flooded with a brine solution that had previously reached equilibrium with supercritical $CO_2$.

Regarding the reaction rate constant for the precipitation, we rely on the experimental identification from Chou *et al.* [77] such that:

$$K_{-3} = \frac{K_3}{K_{\text{eq}}} = \frac{6.6e-7}{10^{-8.48}} = 199\,\text{mol.m}^{-2}.\text{s}^{-1}$$

while adsorption frequencies $K_c$ commonly encountered in the literature range from 1e3 to $1\text{e}8\,\text{s}^{-1}$ [79, 215, 310, 320]. In practice, we set for the numerical simulations $K_c = 1\text{e}3\,\text{s}^{-1}$, the molecular diffusion $D_m = 1\text{e}{-9}\,\text{m}^2.\text{s}^{-1}$ for all the species and the prescribed flow rate $\overline{u} = 1e-3\,\text{m.s}^{-1}$.

Investigating the different precipitation patterns and regimes relies on the definition of well-established characteristic dimensionless numbers, namely the Peclet and (second or catalytic) Damköhler numbers respectively denoted $\text{Pe}$ and $\text{Da}_{\text{II}}$ [219, 279, 284]. However, in the context of the joint precipitation and crystal growth modeling, we define two distinct Damköhler numbers characterizing each process and respectively denoted $\text{Da}_{\text{II}}^{\text{prec}}$ and $\text{Da}_{\text{II}}^{\text{crys}}$. These dimensionless numbers are subsequently defined as:

$$\text{Pe} = \frac{\overline{u}L}{D_m},\ \text{Da}_{\text{II}}^{\text{prec}} = \frac{K_{-3}\gamma_{\text{CO}_3{}^{2-}}A_sL^2}{D_m}\ \text{and}\ \text{Da}_{\text{II}}^{\text{crys}} = \frac{K_cL^2}{D_m} \tag{2.73}$$

where $\overline{u}$ and $L$ are respectively the characteristic velocity and length of the sample, and the activity coefficient of the carbonate ions is $\gamma_{\text{CO}_3{}^{2-}} = 1\text{e}{-3}\,\text{m}^3.\text{mol}^{-1}$. The characteristic length $L$ can be related to pore size [284], though it is commonly set as $L = \sqrt{\kappa_0}$ provided an experimental or numerical estimation of $\kappa_0$ [279]. The latter alternative is applied here, with an estimation of $\kappa_0 = 2\text{e}{-11}\,\text{m}^2$ for the porous sample considered.

Therefore, the first crystallization regime we investigate is characterized by the following dimensionless numbers $\text{Pe} = 4.47$, $\text{Da}_{\text{II}}^{\text{prec}} = 33.034$ and $\text{Da}_{\text{II}}^{\text{crys}} = 20$. Precipitation and crystallization of calcite lead to a significant decrease in the macro-scale permeability and porosity, resulting from flow path disruptions at the micro-scale through partial or complete clogging of pore throats. This can also affect the roughness of the mineral interface and the pore-size distribution of the sample and, thereby, contribute to influencing the sample hydrodynamics properties. In particular, we observe these effects at the pore scale in Figure 2.8 along the reactive process and for several physical times $t$ going from 2h45 to $T_f = 6\text{h}56$. On the right side of Figure 2.8, we depict partial views of the porous sample's morphology, illustrating the changes in pore structure over the reaction time, along with the micro-porosity field $\varepsilon$ within the porous matrix $\Omega_S$. On the left side, we represent along a slice in the main flow direction (taken at $z = -0.0168\text{mm}$), the local variations on the micro-porosity with respect to the initial state — before the reaction process — given by $\varepsilon(t) - \varepsilon(0)$. Initially, we notice that higher micro-porosity variations are more likely localized at the mineral interfaces but also near thin pore throats. These variations subsequently lead to pore-clogging and reorganization of the main flow pathway (see Figure 2.8c). In Figure 2.9b, we investigate the effects of such micro-scale changes on the evolution of the petrophysical properties at the macro-scale, namely the porosity $\phi$ and permeability $\kappa_0$ defined in equations (1.1) and (1.2) from Chapter 1. The results are consistent with the expected decrease along the $CO_2$ mineral trapping process but also highlight sharp permeability drops, which characterize the

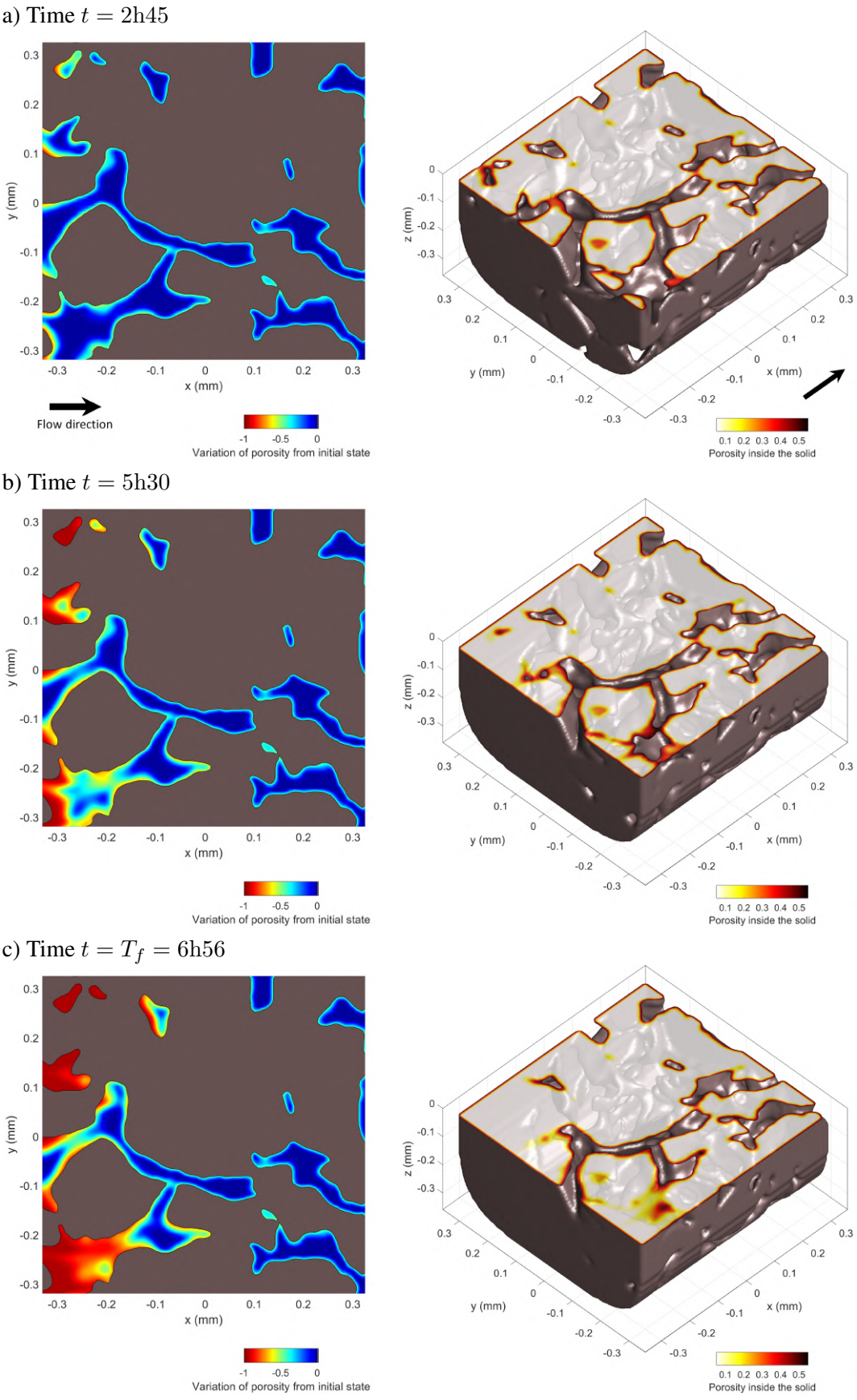


**Figure 2.8: Time evolution of the sample geometry and micro-porosity at the pore scale, illustrating pore-clogging effects.** Slice at $z = -0.0168$ of the porosity variations $\varepsilon(t) - \varepsilon(0)$ in the fluid region of the pore space for various times $t$, on the left (dark color displays the initial solid matrix). Partial view of the pore space structure as an isosurface of $\varepsilon(t)$ for several times $t$, sliced with the micro-porosity values inside the porous matrix, on the right.

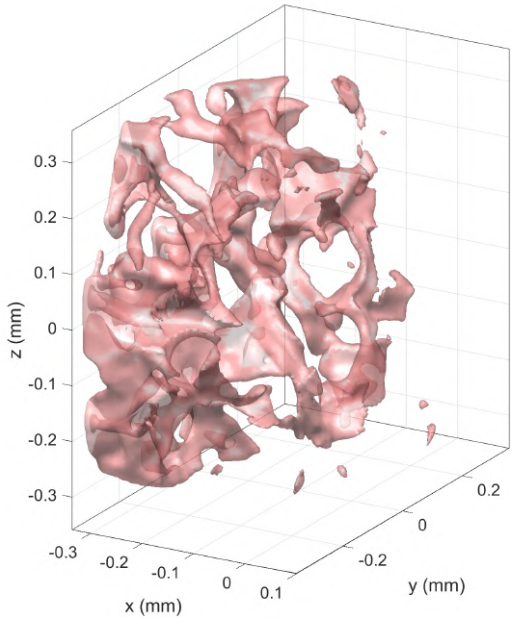


a) Micro-porosity evolution

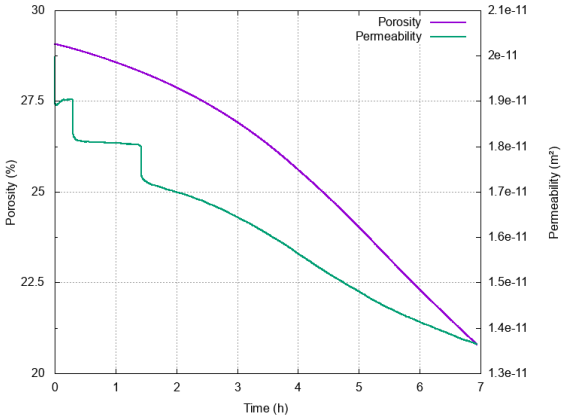


b) Macro-scale porosity $\phi$ and permeability $\kappa_0$

**Figure 2.9: Evolution of the sample properties along the reactive process:** a) Micro-porosity evolution represented by an isosurface of the porosity variation $\varepsilon(T_f) - \varepsilon(0)$ at half of its maximum value. Results after nearly 7h of precipitation and crystal growth, illustrating a non-uniform compact regime following the natural ramification of the sample. b) Evolution of the macro-scale properties, porosity $\phi$ and permeability $\kappa_0$, along the two-step crystallization process from Figure 2.6.

pore-clogging phenomena. Finally, in order to identify more clearly the crystallization pattern in this particular regime, we display in Figure 2.9a an isosurface of the micro-porosity variation between the final and initial times. This illustrates that micro-scale variations occur preferentially in a compact and non-uniform manner in the first inlet part of the domain while following the individual ramifications in the pore structure.

We subsequently investigate the impact of different dominant regimes on the overall two-step crystallization process. To do so, we consider both transport dominant cases with $\mathrm{Pe} = 4.47 > 1$ and diffusion dominant cases with $\mathrm{Pe} = 0.447 < 1$, coupled with two different crystal growth regimes characterized by $\mathrm{Da}_{\mathrm{II}}^{\mathrm{crys}} = 2$ and $\mathrm{Da}_{\mathrm{II}}^{\mathrm{crys}} = 20$. One should notice that the effect of precipitation Damköhler $\mathrm{Da}_{\mathrm{II}}^{\mathrm{prec}}$ changes are not analyzed since this number, characterizing the first homogeneous nucleation regime, is a limiting factor of the crystallization process from Figure 2.6. In this sense, we assume in all the previous cases that $\mathrm{Da}_{\mathrm{II}}^{\mathrm{crys}} < \mathrm{Da}_{\mathrm{II}}^{\mathrm{prec}}$ which guarantees a supersaturation state suitable to the development of crystal aggregates on the mineral surface.

To the best of our knowledge, considering that the crystallization regime can be driven by three distinct dimensionless numbers is one of the contributions of the present thesis. Indeed, most of the regime diagrams presented in the literature mainly characterize precipitation patterns according to the $\mathrm{Pe}$ and $\mathrm{Da}_{\mathrm{II}}^{\mathrm{prec}}$ dimensionless numbers, which implies neglecting the effects of nuclei adsorption at the mineral surface in the different regime configurations [297, 327]. However, our results indicate that both homogeneous calcite nucleation (the precipitation step in Figure 2.6) and growth stages are important in the development of precipitation and crystallization patterns. In particular, we establish that the crystal growth Damköhler number $\mathrm{Da}_{\mathrm{II}}^{\mathrm{crys}}$ has a non-negligible impact on precipitation pattern and porosity variations along the reactive process, regardless of the other dimensionless numbers $\mathrm{Pe}$ and $\mathrm{Da}_{\mathrm{II}}^{\mathrm{prec}}$ commonly investigated. Indeed, Figures 2.10b and 2.10d highlight two distinct crystallization regimes at similar $\mathrm{Pe}$ and $\mathrm{Da}_{\mathrm{II}}^{\mathrm{prec}}$, but with a ten times smaller adsorption frequency $K_c$ in Figure 2.10b which impact the $\mathrm{Da}_{\mathrm{II}}^{\mathrm{crys}}$. Figure 2.10b shows that, for a small adsorption frequency $K_c$, the calcite precipitate is uniformly generated and advected along the main flow path direction (due to the transport dominant regime with $\mathrm{Pe} > 1$) while the micro-porosity changes are minimal. This illustrates that the main flow path is main-

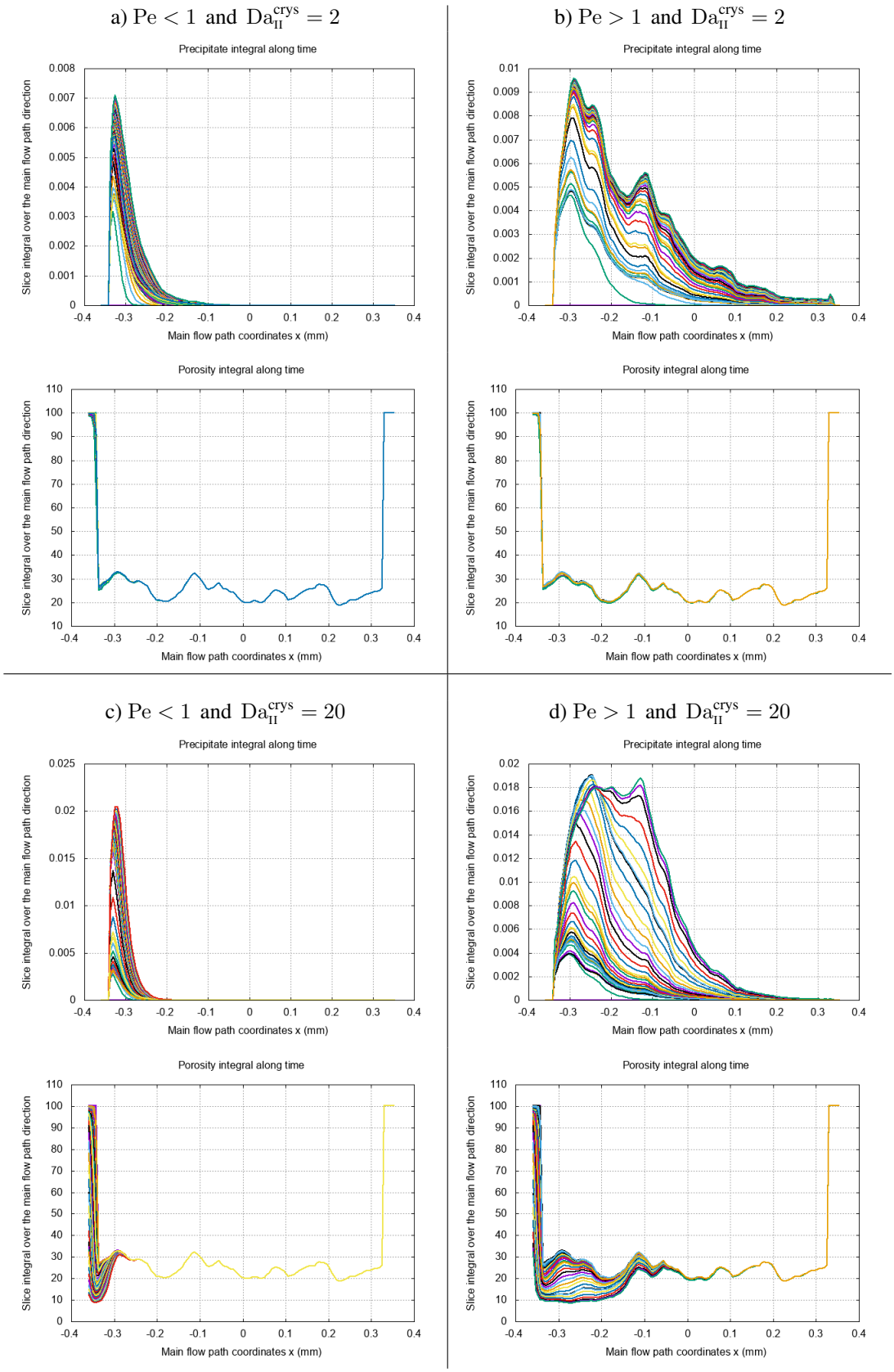


**Figure 2.10: Impact of the different crystallization regimes, with respect to the dimensionless numbers** Pe **and** $\mathrm{Da}_{\mathrm{II}}^{\mathrm{crys}}$**, on the precipitate patterns and porosity changes along time.** Slice integrals of the precipitates and macro-porosity — computed over 2D YZ directional slices — plotted with respect to the main flow path direction coordinates x (in millimeters mm) and where each curve represents a distinct time in the reactive process.

tained since few calcite nuclei aggregate to the mineral surface. By increasing the adsorption frequency in Figure 2.10d, the precipitate formation concentrates on the inlet of the domain and is less subject to advection, while the micro-porosity changes become significant. On one side, this highlights pore-clogging that prevents further transport of the calcite nuclei. On the other side, we also notice a backward increase in calcite precipitates that accumulate behind the clogging after some time. The same analysis holds for Figure 2.10a and 2.10c, except we consider a diffusion dominant regime with $\mathrm{Pe} < 1$, which means that the precipitate transport is reduced so that the nuclei formation and micro-porosity changes are even more constrained to the inlet boundary of the domain. The results presented in Figure 2.8 and 2.9 correspond to the crystallization regime identified by $\mathrm{Pe} > 1$ and $\mathrm{Da}_{\mathrm{II}}^{\mathrm{crys}} = 20$ in Figure 2.10d. In this sense, this confirms that the permeability drops observed in Figure 2.9b are characteristics of pore-clogging effects.

## 2.8 Concluding remarks and toward Uncertainty Quantification

The current chapter focused on developing an efficient DNS framework to address reactive flows at the pore scale in the context of $CO_2$ mineral storage. Indeed, the injected $CO_2$ will interact with the aquifer structure and eventually lead to mineral trapping in the form of calcite precipitates and crystals. These processes are interesting to study at the pore scale to ensure a comprehensive analysis of the local rock-fluid interactions and evolving pore structures. This can subsequently translate into meaningful estimations of the macro-scale properties changes and measure the impact of the geochemical processes on the natural underground reservoirs. In particular, precipitation and crystallization lead to a significant reduction in the macro-scale permeability and porosity, which result from partial or complete pore clogging and thus from a reorganization of the flow path at the micro-scale.

In this chapter, we present a reactive hydrodynamic model that consistently couples a Lagrangian formulation for the reaction equations with a grid-based approach for the flow using the DBS equation with the superficial velocity formalism. This semi-Lagrangian method is addressed through a splitting operator strategy coupled with high-order remeshing steps for grid-particle interpolations. This efficiently incorporates into the hybrid numerical framework HySoP and results in a CPU-GPU implementation of the method. From this perspective, one of the main contributions of this chapter is to incorporate in this existing workflow a robust estimation of the heterogeneous diffusion operator arising from Archie's law term in the reactive system. This is achieved through a particle-based method, namely a discrete renormalized PSE scheme, that makes it possible to fully address the superficial gradient approximation under some stability constraints.

From a conceptual perspective, we developed a new crystallization model that efficiently combines a classical deterministic TST approach of the nucleation process with a probabilistic view of the crystal aggregation to the pore surface. This enables us to account for spatial and geometrical dependency in the crystal growth modeling through a probabilistic attachment rate depending on local mineral volume fraction. In this sense, we integrate the modeling of preferential growing sites that largely hinge on the surrounding pore arrangement. To the best of our knowledge, such considerations are here accounted for the first time to model crystallization processes in complex 3D geometries at the pore scale. Investigating probabilistic attachment rates based on the surrounding pore structure also ensures reliable prediction of pore-clogging at the pore scale. Finally, we demonstrate that the proper characterization of crystallization regimes both depends on the nucleation process and crystal aggregation. Indeed, we exhibit that the two commonly considered dimensionless numbers, $\mathrm{Pe}$ and $\mathrm{Da}_{\mathrm{II}}^{\mathrm{prec}}$, are not sufficient to explain clogging effects and precipitation patterns. A novelty of the present manuscript is, therefore, that the crystallization regimes are characterized by three dimensionless numbers that include the effects of nuclei adsorption to the pore surface.

At the same time, this chapter also demonstrated strong implications in the overall reactive system of several parameters that can be subject to a wide range of discrepancies. In particular, morphological features and kinetic parameters, such as the micro-porosity $\varepsilon$, specific area $A_s$, rate constants $K_i$, and adsorption frequencies $K_c$, have a significant impact on the reaction rates and

the dynamical patterns. Experimental determination of these parameters can range over several orders of magnitude (*e.g.* the adsorption frequencies) and result in highly different regimes that drastically affect the estimation of the macro-scale properties. As mentioned above, the adsorption frequencies $K_c$ commonly found in the literature range from $1e3$ to $1e8\,s^{-1}$ [79, 215, 310, 320].

Considerable uncertainties are, therefore, associated with the reaction rate estimates [190, 205]. In this sense, one needs to account for these uncertainties to ensure a reliable calibration of the morphological and kinetic parameters to match with laboratory experiments. This also aims to guarantee trustable macro-property changes due to the geochemical process of $CO_2$ mineral storage. The rest of the manuscript addresses such uncertainty quantification concerns. In order to investigate such estimations under the perspective of inverse problems and uncertainty analysis, Chapter 4 develops a methodological framework, and Chapter 5 applies it to calcite dissolution for uncertainty quantification on the micro-porosity field $\varepsilon$ and kinetic parameters. Future work will focus on the crystallization/precipitation process with this methodology. Uncertainty assessment on the macro-scale permeability deviation is developed in the next Chapter 3.

CHAPTER 3

# Reliability in the computation of absolute permeability

Contents



## 3.1 Motivation

Ensuring reliable calibration of model parameters in Direct Numerical Simulation (DNS) of reactive flows is crucial to provide suitable evolution of the macro-scale properties due to geochemical processes. Indeed, it is commonly established that discrepancies in the permeability estimates, for instance, will strongly affect the flow and overall behavior of the aquifer for $CO_2$ storage assessment. In this sense, detailed reservoir characterization, especially in terms of permeability and porosity distributions, is required for proper DNS of $CO_2$ storage at the macro-scale. The availability of such data is, however, generally restricted in the literature, time-consuming, and difficult to obtain from laboratory measurements [212]. Uncertainty quantification assessment of the reservoir spatial heterogeneities has thus garnered increasing interest over the past decades. The effects of these uncertainties at the reservoir scale can be achieved, *inter alia*, through sensitivity analysis of the (relative or absolute) permeability distribution in the aquifer structure. This aims to study and characterize potential leakage issues resulting from permeability discrepancies

in highly heterogeneous aquifers or to assess reservoir performances submitted to these uncertainties [138, 195].

Meanwhile, spatial variations in microscopic morphology at the pore scale also have a considerable influence on the upscaled permeability [27, 278]. This consequently raises concerns about quantifying reliable permeability ranges resulting from pore-scale imaging techniques, such as X-ray microtomography (X-ray $\mu$CT). Zhao *et al.* [339], for instance, parametrized the randomness of reconstructed pore space through Karhunen-Loève expansions and evaluated the permeability response to this variability in the micro-pore structures. Sub-resolved pores are, indeed, one of the X-ray $\mu$CT imaging issues that can induce significant bias in the petrophysical properties estimations. Several methods can though overcome this challenge by accounting for the effects of under-resolved morphological characteristics. This ranges from downsampling [109] and deep learning approaches providing super-resolved segmented $\mu$CT images [16] to uncertainty estimates. We focus on the latter approach since permeability distributions obtained by uncertainty quantification could, afterward, be efficiently transferred at the field scale for sensitivity analyses in reservoir simulations. Investigating the impact of pore-scale morphological bias and how microscopic uncertainties propagate to the petrophysical properties is a fundamental topic necessary to ensure reliable management of $CO_2$ storage at the macro-scale. This is, however, still a challenging task that raises concerns in the research community.

This chapter describes how the upscaled absolute permeability is impacted by slip effects at the fluid/solid interface, in the context of single-phase flow at the pore scale. While this effect is well quantified in microchannels or simple geometries, the present study focuses on its average effect in real rock matrix geometries, by means of high-resolution X-ray microtomography. Due to the inherently finite resolution of the technique, uncertainties exist on the true position of the fluid/solid interface and its morphological features below the image resolution, namely the unseen roughness. We demonstrate that both these morphological uncertainties can be interpreted as a slip condition, and consequently focus on how a characteristic slip length can impact the computed absolute permeability. To that extent, we provide an estimation of meaningful bounds on the slip coefficient estimations which makes it possible to quantify permeability deviations submitted to pore-scale imaging limitations. In this chapter, uncertainty assessment mainly relies on an upscaling approach of the sub-resolved features, and two strategies are employed to quantify the permeability deviations: the full deviation based on slip boundary conditions, and the theoretically established deviations from asymptotic analysis. Three high-definition 3D geometries are used as practical examples of the methodology and as a baseline for comparison of the two permeability deviation ranges. Results are discussed in terms of relative deviation versus specific surface area and lead to quantities of interest involving the linear deviation of permeability. We eventually confirm apparent macroscopic effects arising from the second-order deviation on the permeability in real rock geometries.

Two of these geometries were acquired by $\mu$CT scans performed at the DMEX Center for X-ray Imaging at UPPA (UAR 3360 CNRS), by Professor Peter Moonen. Part of the work presented in this chapter has been published in Transport in Porous Media with Prof. Peter Moonen and Prof. Philippe Poncet [238].

## 3.2 Context and positioning

According to Encyclopædia Britannica, permeability is "the capacity of a porous material for transmitting fluid; it is expressed as the velocity with which a fluid of specified viscosity, under the influence of a given pressure, passes through a sample having a certain cross-section and thickness" [45]. This deceivingly simple definition hides a complex reality at the pore scale, even when only a single-phase fluid is involved. In particular, this hinges on correctly characterizing the complex 3D morphology of real porous media whose local heterogeneities can spread over multiple length scales [153].

Advances in X-ray $\mu$CT makes it possible to non-destructively determine the inner morphology of the porous samples considered, characterizing by distinct grey levels the local X-ray atten-

uation of the medium (see Sect. 1.1.3 in Chapter 1). As the attenuation is material-dependent, the pore space can easily be separated from the surrounding matrix through a segmentation process. The resulting dataset subsequently combines with pore-scale numerical models [211, 264, 318].

Pore-scale models of flow and transport roughly fall into one of two broad categories: a) Direct Numerical Simulations and b) Pore Network models (PNM) [198] (see Sect. 1.2.1 in Chapter 1). At low Reynolds numbers, both solve the same fundamental governing equations, although in the first DNS case, the true geometry of the porous medium is employed. On the contrary, in PNM the actual pore space is regarded as a simplified structure with a number of pores interlinked by flow channels (see Figure 1.4 in Chapter 1). Consequently, DNS based on Stokes and Navier-Stokes equations promises to be more precise, at the cost of being computationally more expensive. On the other hand, PNM models based on Hagen-Poiseuille formula are highly efficient, and their way of conceptualizing the true geometry offers a mental framework for transposing the conclusions of fundamental research on idealized flow channels, into real rock geometries. Combining high-resolution X-ray $\mu$CT scans and advanced DNS approaches offers the opportunity to study the evolving petrophysical characteristic under geochemical processes.

However, as introduced in Sect. 1.1.3, limitations exist in the X-ray $\mu$CT imaging process that may affect the medium effective properties computation, independently of the numerical method choice. In this chapter, we focus on the morphological uncertainties arising from these imaging limitations, namely the presence of unresolved features and the approximation in the location of the pore space walls induced by blurred interfaces (*e.g.* see Figure 1.3 in Chapter 1).

In particular, we address the question of the reliability of the permeability value induced by these morphological uncertainties, both mathematically translating into models of slip flows. The unseen roughness of a channel wall and the exact position of that wall — and hence the channel dimensions — will generally be visible only in an approximate sense on an X-ray $\mu$CT scan of a Representative Elementary Volume (REV) of the material. This is not to say that sufficient resolution cannot be obtained, but rather that real pore media covering a wide range of pore scales generally requires a compromise between the volume being investigated and the scan resolution. The former has to be large enough to be representative, whereas the latter has to be small enough to observe enough details.

The present chapter consequently focuses on quantifying the uncertainty of the computed permeability by providing a range of possible values instead of a single value and accounting for the deviation between the true morphology of the pore space and the assumed one. We focus on absolute permeability, which means that we consider the single-phase flow of a Newtonian fluid through the pore space in an impermeable rock matrix. We will employ a slip length formalism and use the variation in slip length as a way to represent the uncertainty of the geometry. While slip formalism has been intensively studied [95, 229] and developed for porous media [158, 160], we focus on its practical aspects and use for real three-dimensional rock geometries.

The main contributions of this work are summarized below:

1. We quantify uncertainty on the absolute macro-scale permeability by means of a slip length formalism on $\mu$CT scans of porous samples.
2. The first-order linear and second-order deviations on the permeability are established asymptotically and compared to the full deviation based on Navier boundary conditions.
3. The ratio between the relative linear deviation and the specific area is defined as a non-dimensional quantity of interest, likely providing a representativeness criterion of the porous samples.
4. We show that the second-order deviation is meaningful to explain the apparent permeability macroscopic effects.
5. We provide a numerical framework to investigate, in 3D complex porous geometries, the uncertainty ranges on the permeability due to X-ray $\mu$CT imaging limitations, wherein we define the absolute permeability in terms of intervals instead of explicit values.

The remainder of the chapter is organized as follows: In Sect. 3.3, we introduce the slip formalism for upscaling unresolved features and exhibit the two methods considered to get the

permeability ranges. The governing equations, namely the stationary 3D Stokes equation in the pore space involving the slip condition, are defined in Sect. 3.3.2, along with the construction of the tangent and normal fields on the fluid/solid interface. The numerical method developed for solving efficiently the Stokes system with slip boundary conditions is detailed in Sect. 3.5 and validated in Sect. 3.5.3 on a cylindrical synthetic geometry, including a convergence study and a global analysis of the absolute permeability deviation. In Sect. 3.4, the focus is given on establishing the first-order linear deviation by means of a two-scale asymptotic development. Sect. 3.6 first provide insight on the choice of a representative slip length value $\beta$ based mainly on the voxel size and adjusted to account for the unresolved solid fraction or the biased interface location. We finally investigate several types of real porous rock with very different pore structures, briefly presented in Sect. 3.3.3. The samples considered for this study are an unconsolidated Sandpack, and two types of sandstone: a Bentheimer sandstone and Castlegate outcrop sandstone. A discussion on the relative deviation for representative samples, and non-dimensional quantities of interest introduce Sect. 3.7. We also compare the permeability range resulting from the full deviation and the theoretically established linear deviation and exhibit non-linear effects on the apparent macroscale permeability. Sect. 3.7.2, thereby, concludes our analysis by considering the second-order deviation on the Castlegate sandstone.

## 3.3 Upscaling unresolved features with slip formalism

This section motivates the use of slip length formalism for upscaling the unresolved morphological features arising from X-ray $\mu$CT limitations. This aims to provide a mathematical framework for managing uncertainties on the upscaled absolute permeability.

### 3.3.1 Slip modeling and permeability uncertainties

In an isolated flow channel, fluid flow encounters a resistance caused by viscous shear stresses which are dependent, among many things, on the roughness of the channel material. The permeability of the channel wall itself also plays a role [58, 204, 289], with more permeable walls increasing the slip velocity on the porous wall. Furthermore, chemical effects and hydrophobic properties may also cause slip [162, 269], as well as trapped gas or liquid along the pore walls [46], clearly quantified for fully wetting films [99]. Although these situations involve slip conditions illustrating physical processes, the idea of using a slip-length formalism to describe flow over a rough surface has also been investigated for years. Slip modeling hence is available for both physical applications and formal upscaling of sub-resolved pore features.

Historically, the relation between roughness and slip length had been proposed by Navier as early as 1823 [213] and established via computation by Achdou *et al.* [2]. Nowadays, for an ideal impermeable rock matrix whose pore space is filled with a Newtonian fluid, the linear formulation of the slip, based on the Stokes equations with no-slip-through $u \cdot n = 0$ at the solid boundary, is quite conventional [162, 163, 229]. In particular, its tangential components are inherited from the relation

$$u - \beta D(u)n = 0 \tag{3.1}$$

where $D(u) = (\nabla u + \nabla u^T)/2$ is the shear-rate tensor, that is to say, the symmetric part of the velocity gradient, $n$ is the unit vector field normal to the fluid/solid interface and directed toward the fluid region, and $\beta$ is the slip length. The hydrophobic and/or slip length reported in literature ranges typically from 200nm [78] to 700nm for multi-phase flows [46] and even 950nm [140]. Slip lengths in the range $500 - 860$nm have also been observed on a mica/water interface with a roughness of 15nm [162].

Meanwhile, many researchers since Navier have attempted to elucidate the precise relationship between permeability and roughness. Numerical studies have focused on various, mostly periodic, roughness patterns such as trenches (ridges, transverse or not) [43, 97, 163], pillars [98, 140] or holes [333]. This highlighted that for a given kind of pattern, the pitch and the liquid-solid contact area are the two most important parameters for determining the slip length, *i.e.* the extrapolated

distance relative to the surface where the tangential velocity component vanishes [164]. Degruyter *et al.* [102] showed that the permeability of laminar and turbulent gas escape during the ascent of rhyolitic magma in volcanic conduits depends on the - unresolved - surface roughness. Similarly, Noiriel *et al.* [222] found that permeability changes are linked to changes in pore surface roughness, induced by calcite precipitation. As the surface roughness itself was difficult to observe directly, they use the ratio between the surface areas before and after calcite precipitation as a proxy and rely on thresholding coupled with erosion–dilatation to separate the different materials and define the surface area [221]. Permeability deviations resulting from under-resolved roughness are intrinsically related to slip modeling and can thus be investigated through upscaling approaches.

Overall, the uncertainties on the geometrical features of pore space, whether it is unresolved roughness or approximate pore wall position, can be modeled using a slip length. When both uncertainties occur simultaneously, as is generally the case, Daly and Roose [96] showed by means of homogenization that the surface roughness is the key property of the micro-scale geometry which determines the hydraulic conductivity at the macro-scale. Consequently, we intend to study the morphological uncertainties arising from X-ray $\mu$CT and quantify its impact on the absolute permeability deviations for single-phase flow using slip modeling.

The present method provides permeability ranges according to two strategies based on the following formalism. Firstly, we estimate the reference absolute permeability $\kappa_0$ by solving numerically the Stokes problem (3.4) — introduced in the next Sect. 3.3.2 — with adherent boundary conditions. We then evaluate the permeability deviation $\kappa_\beta$ using the slip interface condition (3.1) with a meaningful characteristic slip length. Such a choice of a value for a maximum slip length is developed in Sect. 3.6.1, and leads to the confidence interval $\delta K := [\kappa_0, \kappa_\beta]$ for the computed permeability. We naturally call this first uncertainty estimation the *raw permeability deviation* or the *full permeability deviation*.

Furthermore, another method to evaluate such an uncertainty interval is to consider the linear momentum $L_0$ of $\kappa_\beta$ for a given porous material of permeability $\kappa_0$. This is introduced in the linear expansion of the permeability $\kappa_\beta$, given by:

$$\kappa_\beta = \kappa_0 + \beta L_0 + \mathcal{O}(\beta^2). \tag{3.2}$$

The range of permeability then writes $\delta K := [\kappa_0, \kappa_0 + \beta L_0]$, which is denoted as the *linear permeability deviation*. This approach is especially convenient when one needs to change the value of $\beta$ or apply a different coefficient of security to it. Although it could be possible to estimate $L_0$ numerically by its approximation $(\kappa_\beta - \kappa_0)/\beta$, this method can be unreliable due to strong noise in the estimation of $\kappa_\beta$ with respect to $\beta$, inducing non-linear effects (*e.g.* see Figure 3.11 for the Castlegate sandstone in Sect. 3.6.3). The latter approach can be clarified by considering Poisson's equation on the 1D domain $[0, l]$ of length $l$ with a constant driving force $f$, an adherent condition in $l$ and a slip condition $u - \beta u' = 0$ in 0. In this toy example, we readily find $\kappa_0 = l^2/12$, its linear deviation $L_0 = l/4$, and a remainder scaling as $\beta^2$.

More generally, our aim is to provide from a representative slip value $\beta$ the two uncertainty ranges

$$\delta K = [\kappa_0, \kappa_\beta] \quad \text{or} \quad \delta K = [\kappa_0, \kappa_0 + \beta L_0] \tag{3.3}$$

for the absolute macro-scale permeability, instead of a single value $\kappa_0$ whose confidence level is often questionable [105]. Each of our practical study cases is performed with a single meaningful slip length value $\beta$ since any other deviation induced by a different slip length can be resolved by extrapolation, especially with the linear expansion feature. We formally establish in Sect. 3.4 the asymptotic analysis method for determining the linear deviation $L_0$.

### 3.3.2 Governing equations

We introduce a computational domain $\Omega$ divided into a solid part $\Omega_S$, representing the solid matrix of the porous medium, and a fluid part $\Omega_F = \Omega \setminus \overline{\Omega_S}$, corresponding to the pore space (Figure 3.1). The latter is assumed to be a smooth connected open set. In practice, real rock geometries can

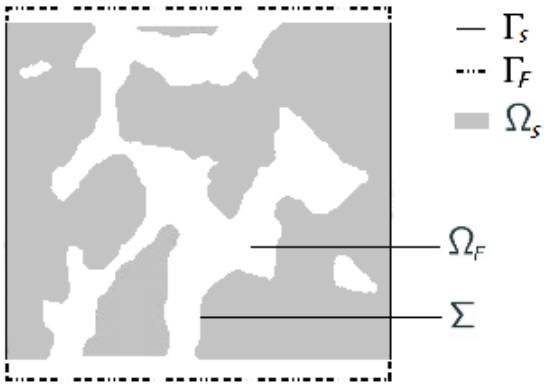


**Figure 3.1: General representation of the computational domain $\Omega$.** The notations are introduced in Sect. 3.3.2. The geometry is laterally constrained by a solid layer, the top and bottom surfaces by a fluid layer to be able to impose periodic boundary conditions on $\partial\Omega = \Gamma_S \cup \Gamma_F$ in the three spatial directions. The image shows some apparently unconnected pores. This is because it presents a 2D slice through the 3D connected pore network. In practice, the full 3D geometry is considered.

present unconnected pores, yet they do not contribute to the flow. The preceding hypothesis, therefore, remains valid and avoids computing a (zero) velocity field in the unconnected pores. We denote the computational domain boundary by $\partial\Omega$ and use $\Gamma_F = \partial\Omega \cap \Omega_F$ and $\Gamma_S = \partial\Omega \cap \Omega_S$ to refer to the fluid and solid parts of the computational domain boundary, respectively, such that $\partial\Omega = \Gamma_F \cup \Gamma_S$. The internal fluid/solid continuous interface is defined by $\Sigma = \partial\Omega_F \setminus \Gamma_F$. The inward normal vector $n$ at each point of the pore interface is oriented towards the fluid part of the sample and is well-defined, assuming sufficient regularity on $\Omega_F$. This condition is satisfied if the voxel sizes are sufficiently small in comparison to the pore dimensions.

In this chapter, we focus on the reliable numerical simulation of microfluidic slip flows in three-dimensional porous rocks. For typical fluids and given the small dimensions of pore throats (micrometer scale or less), we are dealing with very low Reynolds number flows. In this flow regime, the dynamic momentum conservation law for the fluid phase, known as the Navier-Stokes equation, simplifies to the quasi-stationary Stokes equation. On the other hand, the fluid/solid interface featuring unresolved surface roughness can be elegantly modeled by a smooth interface with a slip boundary condition [229]. This formal approach, however, requires an accurate description of the boundary conditions at the fluid/solid interface, relying for instance on a two-domain formulation, as introduced in Sect. 1.2.1 in Chapter 1.

We, therefore, consider the following three-dimensional incompressible Stokes equation in the fluid domain $\Omega_F$, subjected to a downward pointing force field $f$, with a slip boundary condition at the interface $\Sigma$:

$$\begin{cases} -\mu\Delta u + \nabla p = f, & \text{in} \quad \Omega_F \\ \operatorname{div} u = 0, & \text{in} \quad \Omega_F \\ u - \beta T D(u) n = 0, & \text{on} \quad \Sigma \\ u \text{ and } p \text{ periodic} & \text{on} \quad \Gamma_F \end{cases} \tag{3.4}$$

with $u$ the fluid pore-scale velocity, $p$ the pressure, $T = I - n \otimes n$ the projection operator on the tangential components, $\mu$ the dynamic viscosity assumed to be constant, and $\beta > 0$ the slip coefficient. We impose three-dimensional periodic boundary conditions on $\partial\Omega$ since rock samples are typically constrained in a solid casing with a fluid layer on top and bottom when permeability tests are conducted (see Figure 3.1). Provided the considered volume is sufficiently large to be representative, the lateral solid boundaries do not impact the results. The boundary conditions at the pore interface $\Sigma$ are split according to the normal and tangential parts of the velocity and ensure, respectively, the impermeability of the interface and the slip along the tangential directions. In literature, two formulations can be found for the slip condition on the tangential velocity components: using either the velocity gradient whose formalism was detailed in [2] and [54], or the Navier condition involving the shear tensor, as considered in (3.4).

After segmentation of the $\mu$CT data, a binary dataset is obtained, with 1 for the solid phase and 0 for the liquid phase, that can mathematically be described by the function $\chi_S$. This separates the pore space from the surrounding matrix for each voxel and defines the pore interface on a computational grid directly based on the $\mu$CT scans. In this sense, the cells of the computational domain coincide with the voxels of the images. In order to express the slip in equation (3.4), we then define the normal field $n$ from the characteristic function of the solid phase $\chi_S$. In fact, the normal vector computation at the interface relies on the convolution principle with a Gaussian kernel chosen as

$$\mathcal{G}_\sigma(X) = e^{-(X\cdot X)/2\sigma^2} \tag{3.5}$$

with $(X \cdot X)$ the usual scalar product on $\mathbb{R}^3$ and a given standard deviation $\sigma = h$ or $2h$, where $h$ is the computation grid step. An approximation of the inward unit normal $n$ — oriented toward the fluid domain $\Omega_F$ — is then given by

$$n_{|\Sigma} \simeq -\frac{\nabla(\chi_s * \mathcal{G}_\sigma)}{\|\nabla(\chi_s * \mathcal{G}_\sigma)\|}. \tag{3.6}$$

with $\nabla(\chi_s * \mathcal{G}_\sigma) = \chi_s * \nabla\mathcal{G}_\sigma$. Assuming that $\Omega_s$ bounded, we indeed have $\chi_s \in \mathrm{L}^1(\mathbb{R}^3)$ and on the other hand, $\mathcal{G}_\sigma \in \mathcal{C}^\infty(\mathbb{R}^3)$ with all its partial derivatives of order one which are bounded. Theoretically, $\chi_s * \nabla\mathcal{G}_\sigma$ is thus $\mathcal{C}^1(\mathbb{R}^3)$ and the normal vector is well-defined at each point of the interface $\Sigma$.

We also introduce $\tau_k,\ k \in \{1, 2\}$ the tangential vectors to set the Robin/Navier boundary condition on the tangential velocity components. These vectors are computed such that $(n, \tau_1, \tau_2)$ is a direct orthonormal basis locally on the interface, meaning that if $n \times e_k \neq 0$ with $e_k \in (\vec{e_x}, \vec{e_y}, \vec{e_z})$ a generator, we get:

$$\tau_1 = \frac{e_k \times n}{\|e_k \times n\|} \quad \text{and} \quad \tau_2 = n \times \tau_1, \tag{3.7}$$

where $(\vec{e_x}, \vec{e_y}, \vec{e_z})$ are the $\mathbb{R}^3$ usual canonical basis vectors. These normal and tangential fields are used to define the projection operator $T = I - n \otimes n$ in the system (3.4), which is equivalent to $Tu = -n \times n \times u$ with $n$ variable in space along the fluid/solid interface. It is noticeable that the slip condition $u - \beta TD(u)n = 0$ in (3.4) expresses the tangential slip

$$u \cdot \tau_k = \beta(D(u)n) \cdot \tau_k$$

on the two tangential directions of the fluid/solid interface $\Sigma$ (for $k = 1, 2$), and at the same time one obtains the no-slip-through condition

$$u \cdot n - \beta(TD(u)n) \cdot n = u \cdot n = 0$$

on the normal direction.

Furthermore, we consider a dimensionless formulation of the Stokes system (3.4) using the non-dimensional spatial variables $X^* = X/L$ referred to as relative coordinates, where $X = (x, y, z)$ are the absolute coordinates and $L$ is a characteristic length linked to the physical scale of the problem. The dimensionless Stokes problem is thus written:

$$\begin{cases} -\Delta u^* + \nabla p^* = f^*, & \text{in} \quad \Omega_F \\ \text{div } u^* = 0, & \text{in} \quad \Omega_F \\ u^* - \beta^* TD(u^*)n = 0, & \text{on} \quad \Sigma \\ u^* \text{ and } p^* \text{ periodic} & \text{on} \quad \Gamma_F \end{cases} \tag{3.8}$$

where $u^* = u/U$ depends on the characteristic velocity $U$, $p^* = Lp/\mu U$, $f^* = fL^2/\mu U$ and $\beta^* = \beta/L$.

The macro-scale permeability tensors $K^* \in \mathcal{M}_{3,3}(\mathbb{R})$ are then determined from the dimensionless pore-scale simulations through homogenization by:

$$\phi < u^* >_{\Omega_F} = K^* < f^* >_{\Omega_F} \tag{3.9}$$

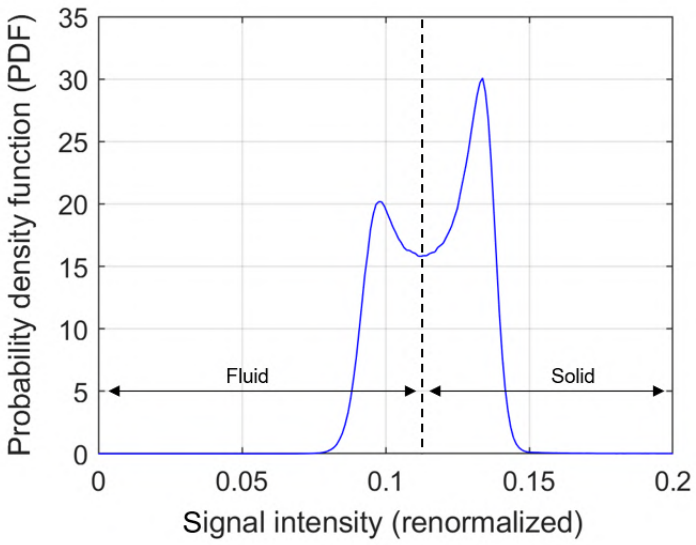


**Figure 3.2: Probability density function of the grey levels in the raw $\mu$CT image of the Sandpack sample:** the dashed line provides the segmentation threshold between the pore space and the solid matrix. The signal is normalized so that the image sensor values range from 0 to 1 for the maximum measurable intensity.

where $< . >_{\Omega_F}$ represents the average in the fluid domain, $\phi$ the sample porosity, and $\phi < u^* >_{\Omega_F}$ are the so-called superficial velocities [250] corresponding to their respective Stokes problems: the velocity $u^*$ can be obtained by adherent ($\beta = 0$) or slip ($\beta > 0$) boundary conditions at the fluid/solid interface. The definition (3.10) involves the source term $f^*$ of the equation (3.8), for which $\nabla p^*$ has zero mean value due to the periodic boundary conditions. An alternative definition of the permeability could be $\phi < u^* >_{\Omega_F} = K^* < -\Delta u^* >_{\Omega_F}$, but most of the works in the literature consider the driving force. If the driving force is included in the pressure with shearing-sheet or hydrostatic Dirichlet boundary conditions, then the permeability can be expressed by $\phi < u^* >_{\Omega_F} = K^* < \nabla p^* >_{\Omega_F}$.

The porosity is numerically estimated by taking $N_F/N_V$ with $N_F$ the number of grid points such that $\chi_s = 0$ in the reference computational domain $\Omega$ and $N_V$ the total number of mesh points in the sample, excluding the casing.

In this work, we focus on the permeability estimate in the main flow direction, namely we consider an isotropic permeability case $K^* = \kappa^* I$, and we can thus estimate $\kappa^*$ induced by a vertical driving force $f_z$ based on the vertical velocity component $u_z$:

$$\kappa^* = \frac{\phi < u_z >_{\Omega_F}}{< f_z >_{\Omega_F}}, \tag{3.10}$$

yielding to $\kappa_0^*$ or $\kappa_\beta^*$. This is compatible with the solid casing constraint on the lateral domain boundaries. The permeability estimations are obtained using such a dimensionless formulation and the absolute permeabilities are then computed based on the dimensional relation $\kappa_\bullet = L^2 \kappa_\bullet^*$. From this point forward on, we will work on the non-dimensional problem but the star notation will be omitted for the sake of readability.

### 3.3.3 Test cases for validation and sample geometries

Several porous sample geometries are considered to quantify the permeability uncertainties in Sect. 3.6. The geometries considered are of different natures, each having its own interest and objective. First, a single-pore corresponding to a cylindrical test case is studied. As an analytical solution exists for this particular geometry, this offers an interesting opportunity for validation of the numerical method developed in Sect. 3.5.3. Next, three real geometries are considered: a Bentheimer sandstone (in Sect. 3.6.2), a Castlegate sandstone (in Sect. 3.6.3) and a Sandpack (in

Sect. 3.6.4). All three datasets are obtained by X-ray tomography and are of comparable quality. Two of them were acquired at the DMEX Center for X-ray Imaging at UPPA (UAR 3360 CNRS), namely the Bentheimer and Sandpack samples, while the Castlegate is freely available in the Digital Rocks data portal [272].

The primary objective of these test cases is to illustrate the model performance on a range of real samples featuring different morphological characteristics. The key difference between both sandstone samples lies in the average pore size, which is much larger for the Bentheimer than for the Castlegate. Besides, the Sandpack has the advantage to present a pore space that is topologically very different from both sandstones along with a much higher porosity. Both aspects are interesting to study for comparisons on permeability deviations and enable verifying the robustness of the model for different flow configurations.

Apart from the morphological differences, the selected samples also present differences in terms of representativeness. In particular, the considered volume of the Bentheimer sandstone was intentionally selected smaller than the REV. On the contrary, both other material geometries were representative: *e.g.* with $512$ cells in each direction and a voxel size of $5.6\mu$m for the Castlegate. In addition to the first objective, we aim to investigate whether the analyzed sample volume must have a representative size and to which extent this impacts the permeability deviations.

The X-ray $\mu$CT imaging technique is used to characterize the morphologies of each porous medium in 3D at the micron scale. This technique relies on the material-specific attenuation of an X-ray beam when traversing a sample. By probing the sample from different angles and, each time, recording the intensity of the transferred beam, one can spatially reconstruct the regions with higher and lower attenuation. These results are represented under the form of a three-dimensional tensor containing the local attenuation coefficients, whereby each tensor entry corresponds to a voxel, *i.e.* a three-dimensional pixel having a given lateral dimension. In a greyscale tomographic scan, the minimum signal then corresponds to the least attenuating areas, namely the pore space, while the maximum signal refers to the most attenuating areas characterizing the solid matrix. At the DMEX center for X-ray imaging, one disposes of two tomographs, a Bruker Skyscan 1172 and a Zeiss Xradia Versa 510, respectively used to obtain the Bentheimer and the Sandpack dataset (source: https://imagingcenter.univ-pau.fr).

The X-ray dataset of the Bentheimer rock has a physical voxel size of around $2.2\mu$m and consists of $1000$ images of $1000 \times 1000$ voxels. The numerical sample studied in Sect. 3.6.2 is extracted from this experimental dataset and the simulations are performed at a resolution of $256$ cells in each direction. The numerical sample has thus a physical size of about $L = 0.56$mm constrained in an impermeable casing. The 3D Sandpack dataset itself is based on $3201$ independent X-ray images of a $0.768$mm sample, acquired over an angular range of $360°$ with a $24s$ exposure time per image. The reconstructed geometry has a voxel size of around $1.5\mu$m and results in a grid-based dataset sizing $512$ cells in each direction, which is used in the application Sect. 3.6.4.

The datasets used were filtered and segmented prior to being used as input for the model. The filtration was done with an edge-preserving 3x3 median filter and aimed to reduce the image noise while avoiding smoothing the interfaces. The segmentation into phases was based on thresholding, where the threshold corresponds to the local minimum of the (normalized) histogram of the dataset. This is illustrated in Figure 3.2 for the Sandpack sample. More sophisticated image processing techniques exist, but in the scope of this chapter, we favored a minimalist approach to data processing to demonstrate that this is sufficient for the proposed model.

## 3.4 Linear deviation of permeability and asymptotic expansion

The first approach to quantify the uncertainty on the permeability is (i) to estimate the permeability to no-slip flow $\kappa_0$, and then (ii) to impose a small slip length $\beta$ — compared to the domain size — and estimate the resulting permeability $\kappa_\beta$. The permeability interval $\delta K = [\kappa_0, \kappa_\beta]$ can be used directly as a first type of confidence range whether the value taken as the slip length is considered realistic. The second type of confidence range relies on the linear deviation which can be approximated as $L_0 \simeq (\kappa_\beta - \kappa_0)/\beta$, provided that the slip length is sufficiently small in order

to avoid the noise in the evaluation of $\kappa_\beta$.

The aim of this section is to show that linear deviation can also be computed accurately in a straightforward fashion by solving a Stokes equation with non-homogeneous Dirichlet boundary conditions. To do so, we focus on the asymptotic development of the solution to the Stokes equation subject to a Navier boundary condition, with $\beta$ a small parameter compared to the image size, so as to obtain

$$\kappa_\beta = \kappa_0 + \beta L_0 + \beta^2 R(\beta) \tag{3.11}$$

with a bounded remainder $R(\beta)$. This results in an estimation of the uncertainty interval $\delta K = [\kappa_0, \kappa_0 + \beta L_0]$ for the absolute permeability subject to a possible slip length $\beta$.

### 3.4.1 Asymptotic expansion problem setup and notations

To simplify the readability, we will set the problem in the fluid part $\Omega_F$ with the no-slip-through condition on its boundary $\Sigma$ and slip one on the tangential components. This gives the following equations:

$$-\Delta u_\beta + \nabla p_\beta = f, \quad \text{in} \quad \Omega_F \tag{3.12a}$$

$$\operatorname{div} u_\beta = 0, \quad \text{in} \quad \Omega_F \tag{3.12b}$$

$$Tu_\beta - \beta TD(u_\beta)\cdot n = 0, \quad \text{on} \quad \Sigma \tag{3.12c}$$

$$u_\beta \cdot n = 0, \quad \text{on} \quad \Sigma. \tag{3.12d}$$

The goal of the asymptotic expansion is to provide a formal development of $u_\beta$ and $p_\beta$ with respect to the slip length $\beta$. So, we need to consider a second-order asymptotic expansion given by

$$u_\beta = U^0 + \beta U^1 + \beta^2 r_\beta \tag{3.13}$$

for the velocity and

$$p_\beta = P^0 + \beta P^1 + \beta^2 q_\beta \tag{3.14}$$

for the pressure, where the profiles $U^j$ and $P^j$ are obtained from Stokes problems at successive orders, and $r_\beta$, $q_\beta$ designate the respective remainders.

To characterize these profiles, we first introduce $\varphi : \Omega_F \to \mathbb{R}^+$ the Euclidean distance to the boundary $\varphi(x) = \operatorname{dist}(x, \Sigma)$. Assuming sufficient regularity on $\Omega_F$, typically a smooth bounded open set, $\varphi$ is smooth in the neighborhood $\omega \subset \Omega_F$ of $\Sigma$. In addition, it can be shown using differential geometry tools that $\forall x \in \omega$, $\|\nabla\varphi\| = 1$ and $\forall x \in \Sigma$, $\nabla\varphi(x) = n(x)$, where we recall that $n$ is the inward unit normal at the interface, oriented towards the fluid region. We can also extend $n$ by setting $n(x) = \nabla\varphi(x)$. As a formal step, we look for the velocity and the pressure in the usual form of a two-scale asymptotic expansion [9, 65]:

$$u_\beta(x) \simeq \sum_{j\geq 0} \beta^j U^j\left(x, \frac{\varphi(x)}{\beta}\right), \quad \text{with } U^j(x,z) = \overline{U}^j(x) + \widetilde{U}^j(x,z) \tag{3.15a}$$

$$p_\beta(x) \simeq \sum_{j\geq 0} \beta^j P^j\left(x, \frac{\varphi(x)}{\beta}\right), \quad \text{with } P^j(x,z) = \overline{P}^j(x) + \widetilde{P}^j(x,z) \tag{3.15b}$$

where the boundary layer terms $\widetilde{U}^j$ and $\widetilde{P}^j$ and their derivatives must tend to 0 when $z \to +\infty$ and the interior terms $\overline{U}^j$ and $\overline{P}^j$ depend only on $x$, that is at the limit of $U^j$ and $P^j$ when $z \to +\infty$. We plug the asymptotic expansions (3.15a) and (3.15b) in the system of equations (3.12) and formally assume that $x$ and $z$ are independent to identify the powers of $\beta$ and thereafter characterize the profiles $U^j$ and $P^j$, for $j = 0$ and 1.

In order to differentiate the main operators involved, we introduce a generic function $\psi$, whose values belong to $\mathbb{R}^3$ and $\mathbb{R}$ for the velocity and pressure profiles respectively, defined by $\psi(x) = \Psi\left(x, \frac{\varphi(x)}{\beta}\right)$. Simple calculations of the first derivatives provide for $x \in \mathbb{R}^3$:

$$\frac{\partial\psi}{\partial x_j}(x) = \frac{\partial\Psi}{\partial x_j}\left(x, \frac{\varphi(x)}{\beta}\right) + \frac{1}{\beta}\frac{\partial\Psi}{\partial z}\left(x, \frac{\varphi(x)}{\beta}\right)\frac{\partial\varphi}{\partial x_j}(x) \tag{3.16}$$

which can be written using standard notations as

$$\nabla\psi = \beta^{-1}\nabla\varphi\,\partial_z\Psi + \nabla\Psi. \tag{3.17}$$

In the same way, we can obtain the other operators as follows:

$$\Delta\psi = \beta^{-2}\|\nabla\varphi\|^2\,\partial_{zz}\Psi + \beta^{-1}\left(2\nabla\varphi\cdot\nabla\partial_z\Psi + \Delta\varphi\,\partial_z\Psi\right) + \Delta\Psi \tag{3.18}$$

$$\operatorname{div}\psi = \beta^{-1}\nabla\varphi\cdot\partial_z\Psi + \operatorname{div}\Psi \tag{3.19}$$

$$D(\psi)\cdot n = \beta^{-1}\frac{1}{2}\left(\partial_z\Psi + (\partial_z\Psi\cdot n)n\right) + D(\Psi)\cdot n, \quad \text{on } \Sigma. \tag{3.20}$$

### 3.4.2 Stokes problems at successive orders

Along with the notations introduced in the previous Sect. 3.4.1, we identify the terms with the same power in $\beta$ for each equation of (3.12). We thereby characterize the Stokes problems at successive orders satisfied by the profiles $U^j$ and $P^j$.

We first consider (3.12a). At order $\beta^{-2}$, it holds that $-\partial_{zz}U^0(x,z) = -\partial_{zz}\widetilde{U}^0(x,z) = 0$ with the assumption that $\widetilde{U}^0(x,z) \to 0$ when $z \to +\infty$. Thus we get $\widetilde{U}^0 = 0$ in $\Omega_F \times \mathbb{R}^+$ and

$$U^0(x,z) = \overline{U}^0(x). \tag{3.21}$$

At order $\beta^{-1}$ and considering directly that $\widetilde{U}^0 = 0$, we infer that

$$-\partial_{zz}U^1(x,z) + \nabla\varphi\,\partial_z P^0(x,z) = 0. \tag{3.22}$$

At order $\beta^0$, we find that $-\Delta U^0 - 2\nabla\varphi\cdot\nabla\partial_z U^1 - \Delta\varphi\,\partial_z U^1 - \partial_{zz}U^2 + \nabla P^0 + \nabla\varphi\,\partial_z P^1 = f$, hence taking the limit $z \to +\infty$ and based on the assumption that tilda terms and all their derivatives tend to 0 when $z$ tends to $+\infty$, we recover the Stokes equation

$$-\Delta U^0 + \nabla P^0 = f, \quad \text{in } \Omega_F \tag{3.23}$$

and by taking the difference with the previous, we also have

$$-\partial_{zz}U^2 - 2\nabla\varphi\cdot\nabla\partial_z U^1 - \Delta\varphi\,\partial_z U^1 + \nabla\varphi\,\partial_z P^1 = 0. \tag{3.24}$$

The latter can be generalized at any order $k \geq 1$ given the following set of equations

$$-\Delta U^k + \nabla P^k = 0, \tag{3.25}$$

$$-\partial_{zz}U^{k+2} - 2\nabla\varphi\cdot\nabla\partial_z U^{k+1} - \Delta\varphi\,\partial_z U^{k+1} + \nabla\varphi\,\partial_z P^{k+1} = 0. \tag{3.26}$$

For equation (3.12b) at order $\beta^0$, we get $\operatorname{div}U^0 + \nabla\varphi\cdot\partial_z U^1 = 0$, noting that the term in $\beta^{-1}$ involving only $\widetilde{U}^0$ vanishes with (3.21). Taking the limit $z$ tends to $+\infty$, we infer the two relations: $\operatorname{div}U^0 = 0$ in $\Omega_F$ first and then, $\nabla\varphi\cdot\partial_z U^1 = 0$. For the latter, we take $\nabla\varphi = n$ and assume that $\widetilde{U}^1(x,z) \to 0$ when $z \to +\infty$ to obtain $\widetilde{U}^1\cdot n = 0$ in $\Omega_F \times \mathbb{R}^+$. We can easily generalize and thus the divergence-free condition provides the following set of equations for $k \geq 0$:

$$\operatorname{div}U^k = 0, \quad \text{in } \Omega_F \tag{3.27}$$

$$\widetilde{U}^{k+1}\cdot n = 0. \tag{3.28}$$

For equation (3.12d), we directly obtain $U^k\cdot n = 0$ on $\Sigma$ for $k \geq 0$ and (3.12c) at order $\beta^0$ provides $U^0 + \frac{1}{2}\left(\partial_z U^0 + (\partial_z U^0\cdot n)n\right) = 0$ which according to (3.21) reduces to

$$U^0(x,0) = \overline{U}^0(x) = 0, \quad \text{for } x \in \Sigma. \tag{3.29}$$

Finally, at any order $k \geq 1$ we can obtain:

$$U^k(x,0) + \frac{1}{2}\left(\partial_z U^k(x,0) + (\partial_z U^k(x,0)\cdot n)n\right) = D(U^{k-1})\cdot n, \quad \text{for } x \in \Sigma. \tag{3.30}$$

At this step, we are able to characterize the profiles $U^j$ and $P^j$. We have already obtained from equations (3.23), (3.27), (3.29) that $(U^0, P^0)$ satisfy a no-slip Stokes problem with $U^0(x,z) = \overline{U}^0(x)$ and $P^0(x,z) = \overline{P}^0(x)$ for any $z$. This implies that the profiles $(U^0, P^0)$ do not depend on $z$ and hence reduce to one space variable.

Then, the tangential component of (3.22) reduces to $-\partial_{zz} T(U^1) = 0$ (as a reminder $T$ is the projection operator on the tangential components as defined in Sect. 3.3.2). Hence, in the same way as before, we obtain $T(\widetilde{U}^1) = 0$. Combined with (3.28) for $k = 0$ we have $\widetilde{U}^1 = 0$ in $\Omega_F \times \mathbb{R}^+$ (since the tangential and normal parts are both equal to 0). On the normal part of (3.22), there remains $\nabla\varphi\, \partial_z P^0 = 0$ which gives, since $\widetilde{P}^0(x,z) = 0$ for any $z$, $\widetilde{P}^0 = 0$ and thus $P^0(x,z) = \overline{P}^0(x)$, as introduced before. Furthermore, equation (3.24) can now reduce to $-\partial_{zz} U^2 + \nabla\varphi\, \partial_z P^1 = 0$ which resembles equation (3.22), so we can check in the same way that $\widetilde{P}^1 = 0$.

Taking $k = 1$ in equations (3.25), (3.27) and (3.30), we obtain profiles $(U^1, P^1)$ that satisfy a Stokes problem with slip: there exist functions $\overline{U}^1$ and $\overline{P}^1$ such as $U^1(x,z) = \overline{U}^1(x)$ and $P^1(x,z) = \overline{P}^1(x)$. This implies that the profiles $(U^1, P^1)$ also reduce to one variable of space and do not depend on $z$.

Assuming sufficient regularity on $\Omega_F$, supposed to be simply connected, and regularity of the source function $f$, the Stokes problems respectively satisfied by the profiles $(U^0, P^0)$ and $(U^1, P^1)$ admit unique weak solutions, up to additive constants for $P^0$ and $P^1$. They also satisfy regularity results not developed here. We refer *inter alia* to the De Rahm theorem and to usual elliptic regularity theorems for the existence, uniqueness, and regularity demonstrations of such variational problems (*e.g.* see Sect. 4 in [19] and Sect. 3 in [10]). Finally, one would also have to characterize the remainders $r_\beta$ and $q_\beta$ and provide higher order estimations, so that the first-order asymptotic expansion can be strictly justified.

### 3.4.3 Linear deviation results summary

Overall, we have considered the second order asymptotic expansion of the solution to the Stokes problem (3.12), with $u_\beta = U^0 + \beta U^1 + \beta^2 r_\beta$ and $p_\beta = P^0 + \beta P^1 + \beta^2 q_\beta$. We have found that the profiles $U^j$ and $P^j$ are characterized by the results from Sect. 3.4.2. The functions $(U^0, P^0)$ hence satisfy the dimensionless no-slip Stokes problem written as follows

$$\begin{cases} -\Delta U^0 + \nabla P^0 = f, & \text{in} \quad \Omega_F \\ \operatorname{div} U^0 = 0, & \text{in} \quad \Omega_F \\ U^0 = 0, & \text{on} \quad \Sigma \end{cases} \tag{3.31}$$

and the profiles $(U^1, P^1)$ satisfy the following Stokes problem:

$$\begin{cases} -\Delta U^1 + \nabla P^1 = 0, & \text{in} \quad \Omega_F \\ \operatorname{div} U^1 = 0, & \text{in} \quad \Omega_F \\ T\, U^1 = T\, D(U^0) \cdot n, & \text{on} \quad \Sigma \\ U^1 \cdot n = 0, & \text{on} \quad \Sigma. \end{cases} \tag{3.32}$$

Finally, we obtain the dimensionless absolute permeability and its linear deviation by the first order Taylor development (3.11) of (3.10), *i.e.*

$$\kappa_0 = \frac{\phi < U_z^0 >_{\Omega_F}}{< f_z >_{\Omega_F}} \tag{3.33}$$

and

$$L_0 = \frac{\phi < U_z^1 >_{\Omega_F}}{< f_z >_{\Omega_F}} \tag{3.34}$$

where $U^1$ is the solution of (3.32) involving non-homogeneous Dirichlet boundary conditions, *i.e.* a prescribed slip velocity. Similarly, we obtain $R(\beta) \propto < r_\beta >_{\Omega_F}$. One can recover the dimensional permeability and its first order deviation respectively by $\kappa_0 L^2$ and $L_0 L$.

## 3.5 Numerical method

Quantifying the permeability uncertainty ranges, whether it arises from the global or linear deviation, requires accurately solving Stokes problems in complex 3D geometries with adherent or slip boundary conditions. In particular, when considering the linear deviation, one needs to evaluate the solution of coupled closure problems at successive orders to compute the slip correction terms. We, therefore, require an efficient numerical method that reliably manages the interface boundary conditions. In this section, we present the methodology used within the thesis and first validate it on an analytical test case.

### 3.5.1 Boundary layer issues prevent effective management of slip

Many numerical methods exist to solve the Stokes equation in a domain with complex morphology, including *inter alia* mesh-based and grid-based approaches (see Sect. 1.2.1 in Chapter 1 for an overview). Mesh-based methods include conventional finite elements [6, 34], finite volumes [64, 206, 235], Lattice Boltzmann (LBM) [204], Arbitrary-Lagrangian-Eulerian (ALE) [281] or Boundary Element methods [38, 175, 247]. Grid-based methods involve discrete operators on structured grids such as finite differences, staggered [209] or not [135], spectral methods [230], or finite volume [279] and LBM [145] on structured meshes. For successive evaluations of differential operators — typically gradient and divergence — grid-based methods can either use a collocation formulation or staggered grids. While the latter can allow a gain in accuracy, the use of collocated grids easily aligns the computational points to the experimental datasets. Optimized grid-based methods can also be coupled to other methods dedicated to the flow features to be investigated: transport based on particle methods [36, 73] (*e.g.* see Sect. 2.4.2 in Chapter 2), anisotropic diffusion for space-variable medium [113, 261], phase-field description of multi-phase flows [159, 280] and its upscaling [158, 252], complex fluid and rheology [261], etc.

Furthermore, a common way to deal with flow modeling around obstacles or flowing inside a complex geometry, especially the solid matrix of a porous medium, lies in penalized methods [25, 73, 135]. The latter avoids specific meshing constraints, such as separated meshes for the solid and fluid parts or mesh refinement at the interface as illustrated in Figure 1.4a, by considering the problem in the overall domain $\Omega$. In particular, the Brinkman term used for the reactive flow formulation in Chapter 2 acts as a penalization of the solid domain related to the micro-porosity field $\varepsilon$ through the Kozeny-Carman relationship (2.2). In the porous matrix, where the porosity field value decreases until the residual lower bound, $\varepsilon \ll 1$ becomes a small penalization parameter, which disappears in the pore space (see Sect. 2.3.1 of Chapter 2).

Penalization, however, gives rise to transition layer — scaling as $\sqrt{\varepsilon}$ for a penalization in $1/\varepsilon$ — at the solid/liquid interface that has been widely studied theoretically using asymptotic expansions [26, 65, 66]. Such a transition layer introduces a residual slip, due to the penalization, possibly used to model flow onto a porous domain or roughness [95, 279]. However, this is unsuitable to study Stokes flows with prescribed slip boundary conditions. Indeed, penalization controls the slopes only inside the solid region, but discontinuity of slopes of velocity at the fluid/solid interface forbids satisfying the Navier boundary condition on the fluid side. Furthermore, the slope in this boundary layer is $\mathcal{O}(\sqrt{\varepsilon})$ while we need a quantitative setting of this coefficient in order to quantify the impact of roughness and wall positioning on the macroscopic estimates. One thus needs to evaluate the shift induced by the penalization at the interface to compare it to the effective slip length, implicitly leading to constraints on the slip value $\beta$. In the context of the present chapter, the Darcy-Brinkman-Stokes formalism hence presents a major disadvantage and prevents effective management of the slip boundary condition. In this sense, we will not rely on the numerical method presented in Chapter 2 but rather developed an alternative that mitigates such boundary layer issues.

### 3.5.2 A GMRES grid-based approach with fluid/solid interface description

In the present work, we consider a grid-based approximation of the stationary Stokes problem, with the velocity and pressure fields as unknowns, using the restarted GMRES to solve the linear system inherited from centered and one-sided finite difference schemes. In this formalism, detailed hereafter, we encode and satisfy the Navier or Dirichlet boundary condition at the fluid/solid interface, the Stokes equation in the fluid region, and a trivial identity inside the solid region, since these points are not connected to the fluid and interface set of grid points. This makes it possible to alleviate the boundary layer issues from penalization approaches, introduced in Sect. 3.5.1, and ensures proper management of the slip boundary conditions.

#### Review of the GMRES method

In the following, we briefly review the general principles of the GMRES method, originally developed in 1986 by Saad and Schultz [260]. GMRES is an iterative method that aims at solving a non-symmetric system of linear equations $A\xi = b$, with $A \in \mathbb{R}^{N\times N}$ a non-symmetric square matrix and $b \in \mathbb{R}^N$. The method approximates the solution by a vector in a Krylov subspace with a minimal residual. We define the Krylov subspace of order m related to this problem with respect to the initial residual $r_0$ by

$$\mathcal{K}_m(A, r_0) = \text{Span}\left\{r_0, Ar_0, ..., A^{m-1}r_0\right\}$$

where $r_0 = b - A\xi_0$ and $\xi_0 \in \mathbb{R}^N$ is the initial iterate.

The GMRES algorithm provides an approximate solution that minimizes, at every time step, the Euclidean norm denoted by $\|.\|$ of the residual vector. The next iterate $\xi_k$ is sought in the form $\xi_k = \xi_0 + q_k$ where $q_k \in \mathcal{K}_k(A, r_0)$ is the solution of the least squares problem:

$$\min_{q\in\mathcal{K}_k(A,r_0)} \|b - A(\xi_0 + q)\| = \min_{q\in\mathcal{K}_k(A,r_0)} \|r_0 - Aq\|. \tag{3.35}$$

First, the modified Gram-Schmidt Arnoldi algorithm is applied to build an orthonormal basis $\{v_1, ..., v_k\}$ for the Krylov subspace $\mathcal{K}_k(A, r_0)$. It provides the following relationship:

$$AV_k = V_{k+1}\overline{H}_k, \tag{3.36}$$

where $\overline{H}_k \in \mathbb{R}^{(k+1)\times k}$ is an upper Hessenberg matrix whose only non-zero entries are the $h_{ij}$ elements generated by the Arnoldi process, and $V_{k+1} \in \mathbb{R}^{N\times(k+1)}$ is an orthogonal matrix whose columns are the orthonormal basis $\{v_1, ..., v_{k+1}\}$. Using this relation, it has been shown in [260] that by setting $q = V_k y$, the solution of the problem (3.35) is given by $\xi_k = \xi_0 + V_k y_k$, with $y_k$ the solution of

$$\min_{y\in\mathbb{R}^k} \left\| \|r_o\| e_1 - \overline{H}_k y\right\|, \tag{3.37}$$

where $e_1$ is the first canonical vector of $\mathbb{R}^{k+1}$. The above problem is generally solved using a (Givens) $QR$ decomposition of the Hessenberg matrix. The iterative process carries on until a convergence criterion is reached, usually related to the residual norm.

Among the main convergence results of the GMRES method, we reiterate the following proposition from [260]:

**Property 2** *Let A be diagonalizable such that $A = XDX^{-1}$ and we denote $P_m$ the space of all polynomials of degree $\leq m$ and $\sigma$ the spectrum of A. Then, the residual norm provided at the $m^{th}$ step of GMRES satisfies*

$$\|r_{m+1}\| \leq \|X\| \|X^{-1}\| \varepsilon^{(m)} \|r_0\|, \tag{3.38}$$

*with* $\varepsilon^{(m)} = \min_{p\in P_m, p(0)=1} \max_{\lambda_i\in\sigma} |p(\lambda_i)|$.

Regarding memory requirements, the cost of the method rises as the Krylov subspace grows, so in practice restarted methods are used to reduce the storage and orthogonalization costs. This

means that the algorithm is restarted every $m$ step, with $m$ a fixed integer that sets the Krylov subspace size, where the initial guess chosen for the restart is the final previous one, obtained by minimizing the residual norm. This can be regarded as a preconditioning that speed up the convergence. The convergence of the restarted GMRES(m) algorithm is also proven when A is a positive real with an error bound derived from the above proposition. However, this result is not consistent when A is not positive real, in which case the following theorem has been proven:

**Property 3** *Assuming that there are $\nu$ eigenvalues $\lambda_1, \lambda_2, ..., \lambda_\nu$ of A with non-positive real parts. Let the other eigenvalues be enclosed in a circle centered on $C$ with $C > 0$ and with a radius $R$ where $C > R$. Then,*

$$\varepsilon^{(m)} \leq \left(\frac{R}{C}\right)^{m-\nu} \max_{j=\nu+1,N} \prod_{i=1}^{\nu} \frac{|\lambda_i - \lambda_j|}{|\lambda_i|} \leq \left(\frac{D}{d}\right)^{\nu} \left(\frac{R}{C}\right)^{m-\nu} \tag{3.39}$$

*with $D = \max_{i=1,\nu;\ j=\nu+1,N} |\lambda_i - \lambda_j|$ and $d = \min_{i=1,\nu} |\lambda_i|$.*

In any case, the convergence is closely linked to the condition number of $X$ and the eigenvalue distribution: in particular, extremely small eigenvalues slow down the convergence.

### Implementation choices

We introduce a uniform Cartesian grid, with a mesh step $h$, and a resolution of $N_x$, $N_y$, and $N_z$ points in each direction respectively. We also use a renumbering index to convert from 3D numbering, with respect to the indices $(i, j, k)$, to 1D labeling of the mesh points indexed by $l = i + N_x(j + N_y k)$. As stated before, the raw datasets are segmented to obtain the characteristic function $\chi_S$ on the Cartesian grid points. We then construct a discrete version of the continuous interface $\Sigma$, which is only visible in an approximated way due to the uncertainties of the pore wall position and unseen roughness. To do so, we identify the mesh points $X_{ijk} := (x_i, y_j, z_k) \in \mathbb{R}^3$ which lie in the solid matrix $\Omega_S$ and have at least one neighbor in the pore domain. We denote this discrete set as the first solid layer $\Sigma_S$, such that

$$\Sigma_S = \left\{ (i,j,k) \in \Omega_S \text{ such that } \exists (i_n, j_n, k_n) \in \mathcal{B}^f_{||.||_\infty}((i,j,k),1) \text{ with } \chi_s(X_{i_n j_n k_n}) = 0 \right\} \tag{3.40}$$

and impose the pore interface boundary conditions on this interface layer. As the computational grid is aligned with the $\mu$CT images — up to the dimensioning factor $L$ (see Sect. 3.3.2) — one gets an effectively close link between the two versions $\Sigma$ and $\Sigma_S$ of the interface.

At this point, we detail the implementation procedure of the linear system solving the Stokes problem (3.4) with a GMRES-based method. Let us define the unknowns vector $\xi \in \mathbb{R}^{4N}$, with $N = N_x N_y N_z$ the total number of mesh points, such that $\xi = (u_x, u_y, u_z, p)^T$. Then, depending on the mesh point identification, we define the numerical product function $A\xi$, from $\mathbb{R}^{4N}$ to $\mathbb{R}^{4N}$, representing the discretization of equation (3.4) extended by 0 for both the velocity and the pressure fields inside the solid domain. This is given as follows:

$$A\xi(X_{ijk}) = \begin{cases} -\Delta_h u(X_{ijk}) + \nabla_h p(X_{ijk}), & if\ \chi_s(X_{ijk}) = 0, \\ \mathrm{div}_h\ u(X_{ijk}), & (\iff X_{ijk} \in \Omega_F) \\ u(X_{ijk}) \cdot \tau_1(X_{ijk}) - \beta D_h(u) n(X_{ijk}) \cdot \tau_1(X_{ijk}), & if\ X_{ijk} \in \Sigma_S \\ u(X_{ijk}) \cdot \tau_2(X_{ijk}) - \beta D_h(u) n(X_{ijk}) \cdot \tau_2(X_{ijk}), & \\ u(X_{ijk}) \cdot n(X_{ijk}), & \\ \mathrm{div}_h\ u(X_{ijk}), & \\ u(X_{ijk}), & if\ \chi_s(X_{ijk}) = 1, \\ p(X_{ijk}), & (\iff X_{ijk} \in \Omega_S) \end{cases} \tag{3.41}$$

where the subscript $h$ denotes the usual discrete operators defined below. The evaluation of the differential operators, including Laplacian, divergence and gradient, is performed using straightforward finite difference schemes of order two. The formalism used in this study lies in the fact

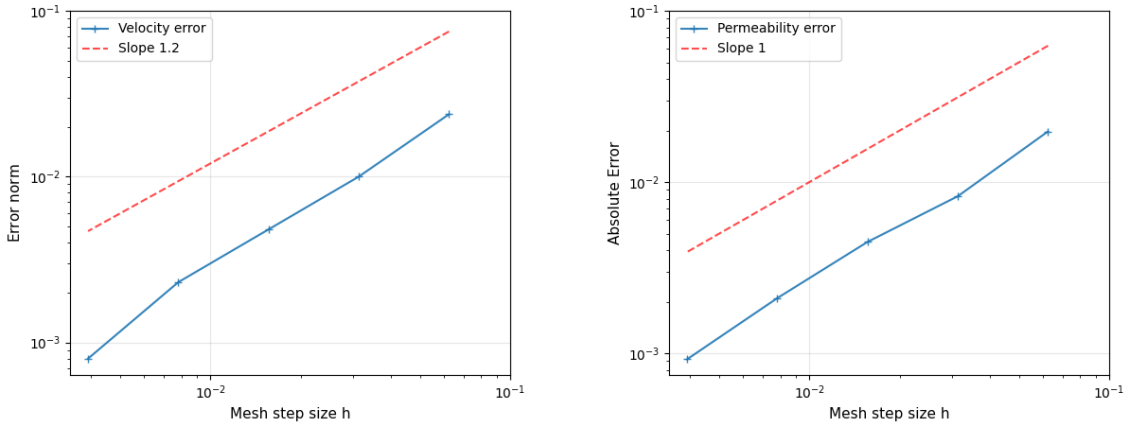


a) Error on velocity b) Error on permeability

**Figure 3.3: Mesh convergence analysis in a cylindrical geometry for $\beta = 0.1$:** a) Velocity error in RMS norm with respect to the grid size $h$ for 32 to 512 cells in the lateral directions. b) Absolute permeability error with respect to the grid size $h$, given the theoretical permeability (3.45).

that the solid and fluid domains are disconnected and can be considered as two independent parts in the linear system. We are, therefore, interested in decoupling the problem between the solid on the one hand, and the fluid/interface parts on the other hand, such that the computational size of the problem could be reduced to just the latter. Consequently, we use centered schemes in the whole fluid part, even for the interface neighbors, and non-centered schemes in the normal direction on the first solid layer $\Sigma_S$. Concerning the right-hand-side of the problem, and denoting by $(f_x, f_y, f_z) \in \mathbb{R}^{3N}$ the components of the driving force $f$ in the Stokes problem, we have the following expressions for $b$:

$$b(X_{ijk}) = \begin{cases} (f_x, f_y, f_z, 0), & if\ \chi_s(X_{ijk}) = 0, \\ (0,\ 0,\ 0,\ 0), & \text{otherwise} \end{cases} \tag{3.42}$$

noting that the last components of the vector $b$ ensure the incompressibility condition, on the fluid and first solid layer parts. On the solid domain, this also imposes a zero value for both the velocity field and the pressure. Moreover, this method presents the advantage of algebraically ensuring the divergence-free condition.

We use the restarted GMRES approach to solve the linear system $A\xi = b$ introduced above. In this study, the stopping criterion for the GMRES convergence is given with respect to the relative residual norm at the iterate $\xi_k$ such that

$$\|r_k\| = \frac{\|b - A\xi_k\|}{\|b - A\xi_0\|} < \varepsilon_{\text{tol}} \tag{3.43}$$

for a given tolerance $\varepsilon_{\text{tol}}$, but it also includes a maximum number of iterations for the restarted algorithm. Furthermore, we do not use an assembly procedure for the matrix $A$ but rather focus on the implementation of a matrix-vector product function. From a numerical point of view, we use a Fortran subroutine for the GMRES restarted method and a C implementation of the main program including the definition of the matrix-vector product function computing $A\xi$, with $A$ the matrix representing the Stokes problem and $\xi$ the main unknowns vector, which contains the velocity and pressure fields. This makes it possible to reduce the operating costs related to the full or sparse matrix assembly procedure.

### 3.5.3 Validation on a cylindrical domain with analytical solution

In this section, we first perform convergence analysis by studying the Stokes flow in a vertical cylinder of radius $R$, with slip boundary conditions along the lateral boundary. The goal is to

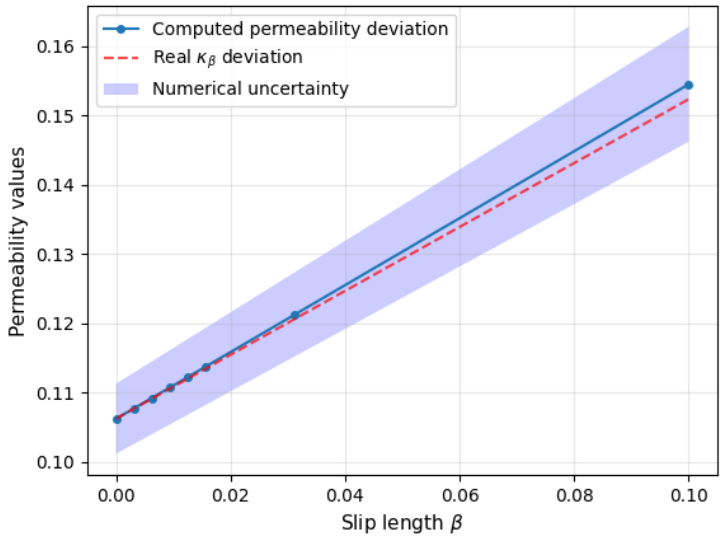


**Figure 3.4: Permeability deviation (non-dimensional) with respect to $\beta$ for the cylindrical domain:** we set a grid of 64 cells in each direction and compare the real deviations $\kappa_\beta$ — given by equation (3.45) — with the computed permeability deviations. A theoretical slope of $R/2$ is expected for the permeability deviation. The error bounds represent the numerical uncertainty on the computed permeability deviations.

validate the numerical method presented in this work and detailed in Sect. 3.5.2, and at the same time exhibit the features of a pore with simple geometry.

The exact solution of the velocity profile is analytically computed and depends on $\beta$ through the relation:

$$u(r,\theta,z) = \frac{(R^2 - r^2)}{4\mu} f + \beta \frac{fR}{2\mu}, \tag{3.44}$$

given in cylindrical coordinates with $f = -\vec{e_z}$, which means we consider a downward pointing force. Given the permeability estimation (3.10) derived from Darcy's law, one also gets the analytical expression for the dimensionless permeability as a function of $\beta$, which reads as:

$$\kappa_\beta = \frac{R^2}{8} + \beta \frac{R}{2}. \tag{3.45}$$

The analytical permeability (3.45) is computed by regarding the cylinder as the whole porous domain, meaning we assume here that $\phi = 1$. In this case, the linear deviation is exact and the development of $\kappa_\beta$ contains no remainder after the first order term. The full permeability deviation $\kappa_\beta$ corresponds to $\kappa_0 + \beta L_0$, with $L_0 = R/2$, and hence this first test case provides a single confidence interval $\delta K$. One should notice that, for homogenization purposes, we can also consider a cylindrical pore in a domain of a given size $l$. The domain porosity is then given by $\phi = \pi R^2/l^2$, and all the analysis performed in the case $\phi = 1$ can be straightforwardly extended.

The computational domain is the unit box $[-1,1]^3$ and the cylindrical geometry is defined by all the grid points whose distance from the vertical axis is smaller than 0.9, which statistically corresponds to a cylinder of radius $R = 0.922$ — the solid being strictly outside, this gives an effective radius larger than 0.9. In the present work, we are dealing with two different diagnostics: on the one hand, we set $\beta = 0.1$ and investigate mesh convergence for the velocity errors in RMS norm and the permeability estimates. On the other hand, we monitor the permeability deviation with respect to $\beta$ for a given mesh resolution. The convergence diagnostics, presented in Figure 3.3, are performed with a Krylov space size set to $m = 50$, a given tolerance of $\varepsilon_{\text{tol}} = 1\text{e}{-6}$ and up to a resolution of 512 cells, except in the main flow direction where we set 32 cells. In fact, since both the analytic and numerical solutions are invariant with respect to the vertical axis, we consider only a thin layer of the cylindrical domain for this validation study — without loss of generality — and thereby we limit the memory requirements to below 8GB of RAM.

We observe a convergence order in $\mathcal{O}(h^{1.2})$ for the velocity, given $h$ the mesh step. This is slightly smaller than in the adherent pore interface case — wherein the convergence is of or-

der $\mathcal{O}(h^{1.5})$ — since slip boundary conditions tend to disrupt the GMRES convergence. Moreover, this convergence is lower than the order two finite difference schemes used in the numerical method, mainly because of the cramming effect on this cylindrical test case. Concerning the permeability estimate, we get an order one convergence with respect to the mesh resolution with an error on the permeability of $1.9\%$ for the coarsest resolution grid and $0.09\%$ for the finest one. We also verify that the permeability deviation due to slip boundary conditions is not merely related to the numerical errors. To do so, we represent in Figure 3.4 the permeability evolution as a function of $\beta$, with the slip coefficient taking values between $0$ and $0.1$. We recover a linear deviation on the permeability close to the theoretical slope of $L_0 = R/2$ confirming the robustness of the implementation, while the numerical uncertainty related to the cramming effect — *i.e.* to the difference between the effective radius $R$ and the theoretical one — provide larger error bounds (see Figure 3.4).

Another meaningful investigation that was performed on this validation case is the monitoring of the boundary condition at the interface: it is satisfied with an error of $1\mathrm{e}{-3}$ even for the coarsest considered grid, which means that the slip boundary condition is properly controlled with the present method. This observation highlights the ability of this direct approach to robustly deal with slip flows.

## 3.6 Absolute permeability deviation analysis on real geometries of porous rocks

This section is dedicated to applications on the real porous sample geometries introduced in Sect. 3.3.3. We quantify the full permeability deviation interval $\delta K = [\kappa_0, \kappa_\beta]$ based on meaningful slip length values $\beta$, accounting for morphological imaging bias on the $\mu$CT scans.

### 3.6.1 Slip value estimation and link to multi-scale modeling

Estimating the slip length values, which appropriately represent the uncertainties associated with the $\mu$CT imaging process, is crucial for quantifying permeability deviations on rock geometries. In order to carry out possible slip lengths and exhibit their bounds, we consider periodic roughness patterns — as introduced by Achdou, Pironneau, and Valentin in [2] — in a computational box of size $h^3$ representing one voxel. The periodic sinusoidal geometry has a mean height $\delta$, an amplitude $\gamma$ and a pitch $L$ such that

$$\varphi(x, y) = \delta + \frac{\gamma}{2} \sin(2\pi x/L) \sin(2\pi y/L). \tag{3.46}$$

The solid portion of the cell is then defined as the domain below the graph of the function $\varphi$ (that is to say the point $(x, y, z)$ such that $z < \varphi(x, y)$), and the fluid portion is located above its graph. This formalism makes it possible to estimate properly the slip length bounds resulting from unresolved morphological features within the voxel, whether it is unseen roughness or mineral interface approximation.

The usual approach when modeling a roughness or its homogenization is to set a Navier/Robin boundary condition that quantifies the slip at a given height relative to the top, mean line, or bottom of the roughness pattern [54]. This leads to the relation (3.1) on the tangential velocity introduced previously:

$$u - \beta D(u)n = 0 \quad \text{on } \Gamma \tag{3.47}$$

where $\Gamma$ is the smooth — or flat — reference surface on which a model of roughness effect is used or a homogenization of the roughness pattern is performed. After averaging along the crosswise directions in this reference voxel, the above equation writes $u(\zeta) - \beta u'(\zeta) = 0$, which merely depends on the roughness pattern height.

A practical example of surface roughness from [140] is displayed in Figure 3.5, for which one observes that the pitch and amplitude can be easily determined from microscopy imaging. The related slip length can also be computed from such realistic roughness patterns based on the

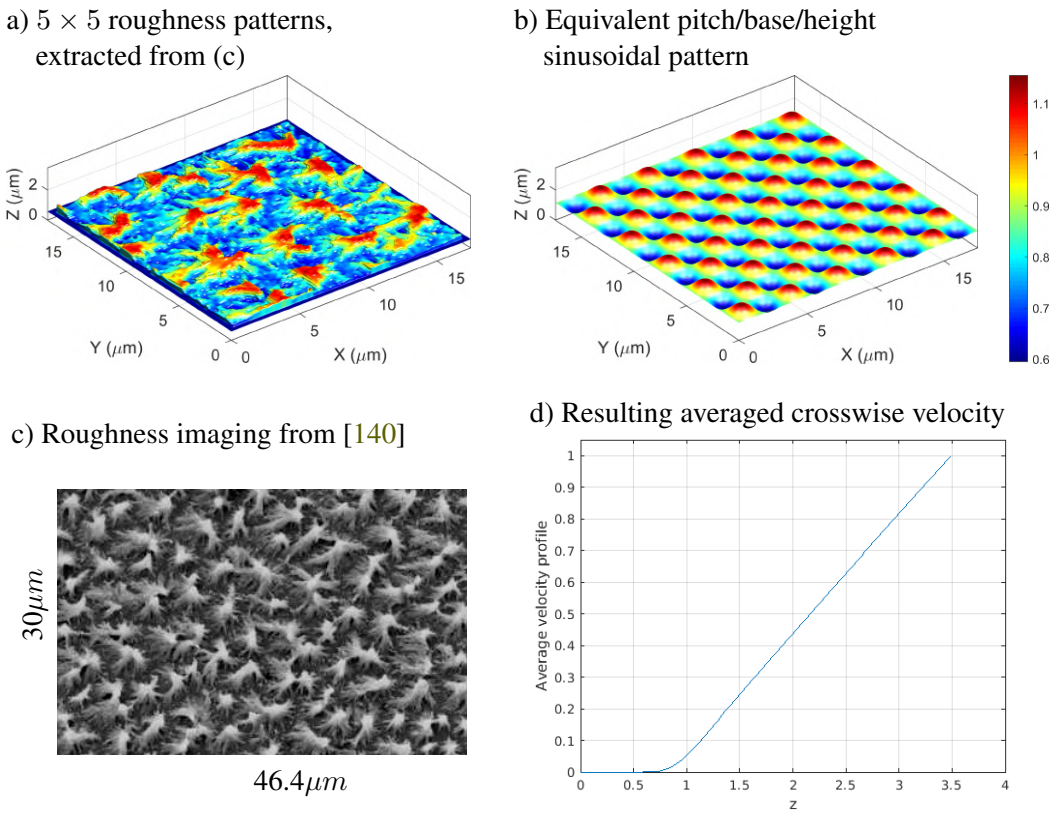


**Figure 3.5: Slip induced by realistic surface roughness:** Roughness geometry from [140] exhibiting an amplitude of $\gamma = 0.56\mu m$ and a pitch $L = 3.5\mu m$. The domain is adjusted so that its height and its related variable $z$ agree with the pitch and the ratio solid/volume is $0.25$.

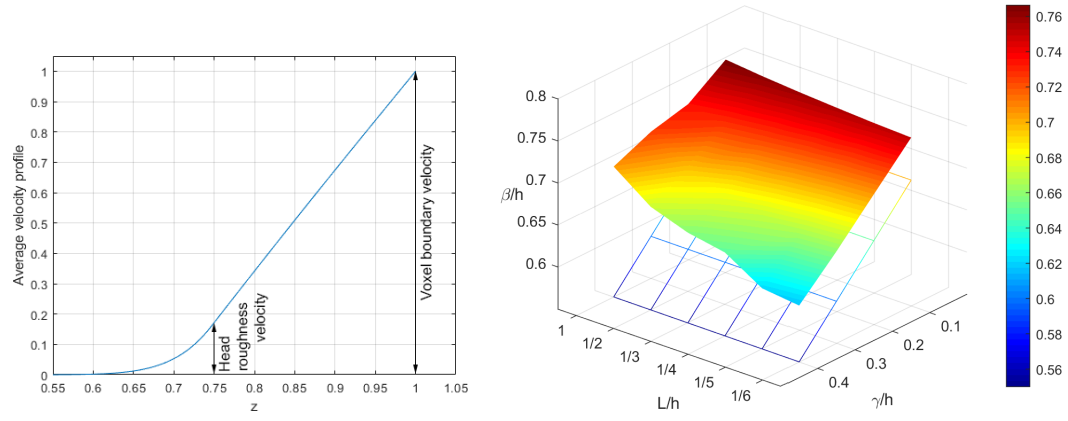


a) Averaged velocity profile

b) Slip length induced by a 2D sinus roughness pattern

**Figure 3.6: Slip length bounds estimation on periodic roughness patterns at the voxel size:** a) Average velocity profile along the crosswise directions plotted with respect to the z-axis in non-dimensional coordinates, for a roughness (3.46) with $\gamma/h = 0.5$, $L/h = 1/6$ and $\delta/h = 0.5$. The slip coefficient is about $\beta/h = 0.306$ when using a definition based on the box boundary velocity, and $\beta/h = 0.046$ when based on the roughness head velocity. b) Evaluation of the slip coefficients with respect to the roughness amplitude and pitch for a low X-ray absorption level, corresponding to a light grey voxel with unresolved micro-porosity and $\delta/h = 0.25$. Comparison to the flat case with no roughness. The slip coefficient estimation ranges from $\beta/h = 0.617$ to $\beta/h = 0.766$.

averaged velocity along the crosswise directions (see Figure 3.5d). In Figure 3.6a, we can see that the reference height $\zeta$ — or equivalently the position of the surface $\Gamma$ — can be chosen very closely to the effective rough surface. Actually, the head of the roughness pattern is usually considered in nano-fluidics experiments to describe this effective surface. In our case, we choose to consider the edge of the voxel as a meaningful boundary condition for the neighboring voxel. Despite a difference in use between a slip at the roughness head, intrinsic to the surface, and a slip at the voxel edge, pertinent in image processing and related to the voxel size, there is only one concept and definition of the slip condition and slip length.

However, whatever the choice of the reference velocity on this surface, as long as it is chosen above the solid, we can see in Figure 3.6a that the velocity gradient remains constant in the fluid part, which is quite a conventional result [99]. Consequently, the slip velocity based on the voxel size is proportional to the slip based on the head of the roughness pattern obtained by microscopy or nano/micro-fluidics experiments. Such experiments can therefore evaluate slip lengths depending on the typology of the roughness pattern for applications on porous sample geometries. Moreover, according to different studies involving ridges or trenches [43, 163], pillars [98] and holes [333], or carbon nanotube coatings [140], for a given kind of pattern, the pitch and the solid fraction are the two most important parameters for determining slip lengths [164].

A direct consequence of the proportionality of the slip velocity is a shift in the slip length: an intrinsic slip length $\beta_{exp}$ at the top of the rough surface evaluated at 50% of the voxel width (at position $h/2$), results in an effective slip at the voxel boundary equal to

$$\beta \simeq \beta_{exp} + h/2 \tag{3.48}$$

since $u(h) = \beta u'(h) = u(h/2) + hu'(h/2)/2 = \beta_{exp}u'(h/2) + hu'(h/2)/2 \simeq \beta u'(h/2)$ due to $u'(h) \simeq u'(h/2)$ (*e.g.* see Figure 3.6a).

At a quantification level, Figure 3.6b presents the slip lengths for a range of roughness amplitudes $0.1 \leqslant \gamma/h \leqslant 0.4$ and a range of pitches $1/6 \leqslant L/h \leqslant 1$. The mean solid position is set at $\delta/h = 0.25$, corresponding to a light grey voxel due to its low absorption, which characterizes unresolved micro-porosity features. Numerically, we used the GMRES method, detailed in Sect. 3.5.2, with a Krylov subspace size $m = 20$, a given tolerance of $\varepsilon_{\text{tol}} = 1\text{e}{-4}$ and a grid resolution of 64 cells in each direction, leading to a residual error of $5\text{e}{-5}$. In such a situation, the maximum slip length value tends to $\beta/h = 0.766$, but in most cases, the slip length belongs to the range $\beta/h \simeq 0.6 - 0.7$.

Beyond these estimations based on a case study of roughness, the hydrophobic and/or slip length reported in the literature for multi-phase flows conventionally ranges from 200nm [78] to 700nm and even 950nm [140]. For a mica/water interface with a roughness of 15nm, slip lengths in the range of $500 - 860$nm have been observed [162]. Moreover, Yao *et al.* [332] report roughness heights up to 400nm, for quartz sand, observed using optical interferometry. We note that Krinsley [148] reports different roughness patterns for quartz grains, depending on their depositional environment (aqueous, high energy beach, desert, hill, fjord). The resolution $h$ of the samples considered in the present study ranges from $1.5\mu$m for the Sandpack and $2.2\mu$m for the Bentheimer sandstone to $5.6\mu$m for the Castlegate sandstone. For fine resolutions, choosing a slip length of $\beta/h$ in the range $0.5 - 0.8$ is then coherent for both the under-resolved roughness and the blur of fluid/solid interface, especially when the blur is limited to one voxel. It is nevertheless possible to consider larger slip lengths to quantify the uncertainty induced by wider blurred layers. Within the applications presented in the following sections, we mainly consider slip lengths of $\beta/h = 0.5$ and $0.76$.

### 3.6.2 Flow inside a Bentheimer sample

This section is dedicated to an initial application on a real porous rock: the Bentheimer sandstone sampled at a resolution of $256^3$, corresponding to a physical size of $L = 0.56$mm with $2.2\mu$m wide voxels, whose acquisition details are provided in Sect. 3.3.3.

We are first interested in analyzing the memory storage requirements in order to identify the Krylov subspace size we can afford in practice, using the numerical method detailed in Sect. 3.5.2.

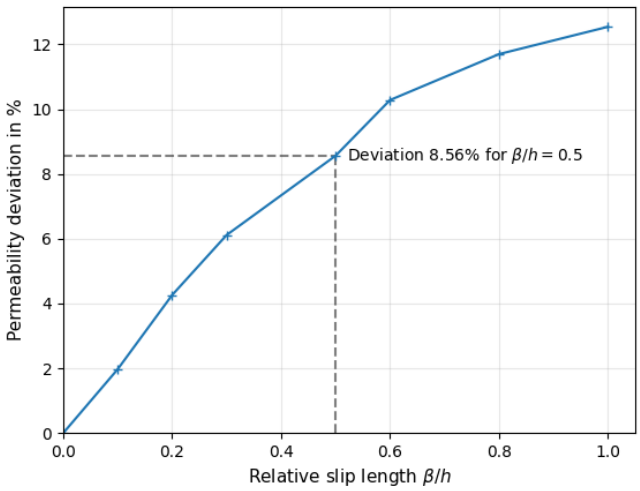


**Figure 3.7: Permeability deviation on the Bentheimer geometry:** permeability deviation values are computed through relation (3.49) and plotted with respect to the different slip coefficients related to the voxel size $h = 2.2\mu$m. For $\beta/h = 0.5$, the permeability deviation is about $8.56\%$.

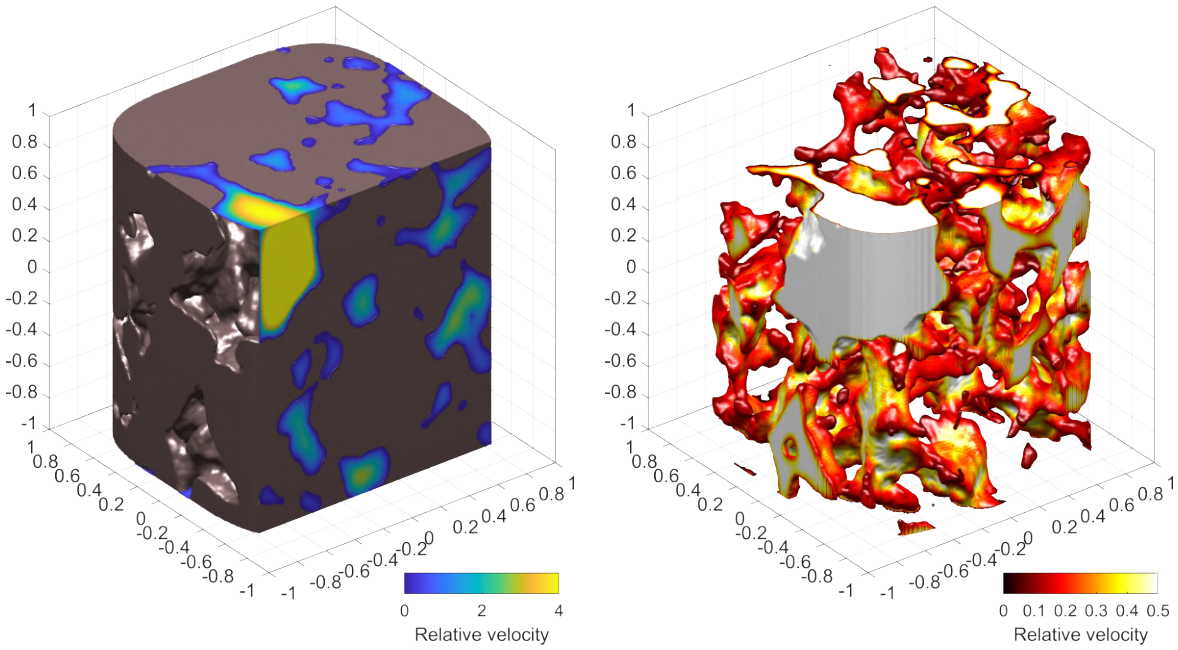


**Figure 3.8: Bentheimer geometry with a slip coefficient of $\beta/\mathrm{h} = 0.5$:** Relative velocities in the fluid domain (to the left) and at the fluid/solid interface (to the right). Resolution of $256$ cells per direction. The grey part represents the solid matrix constrained in an impermeable solid casing.

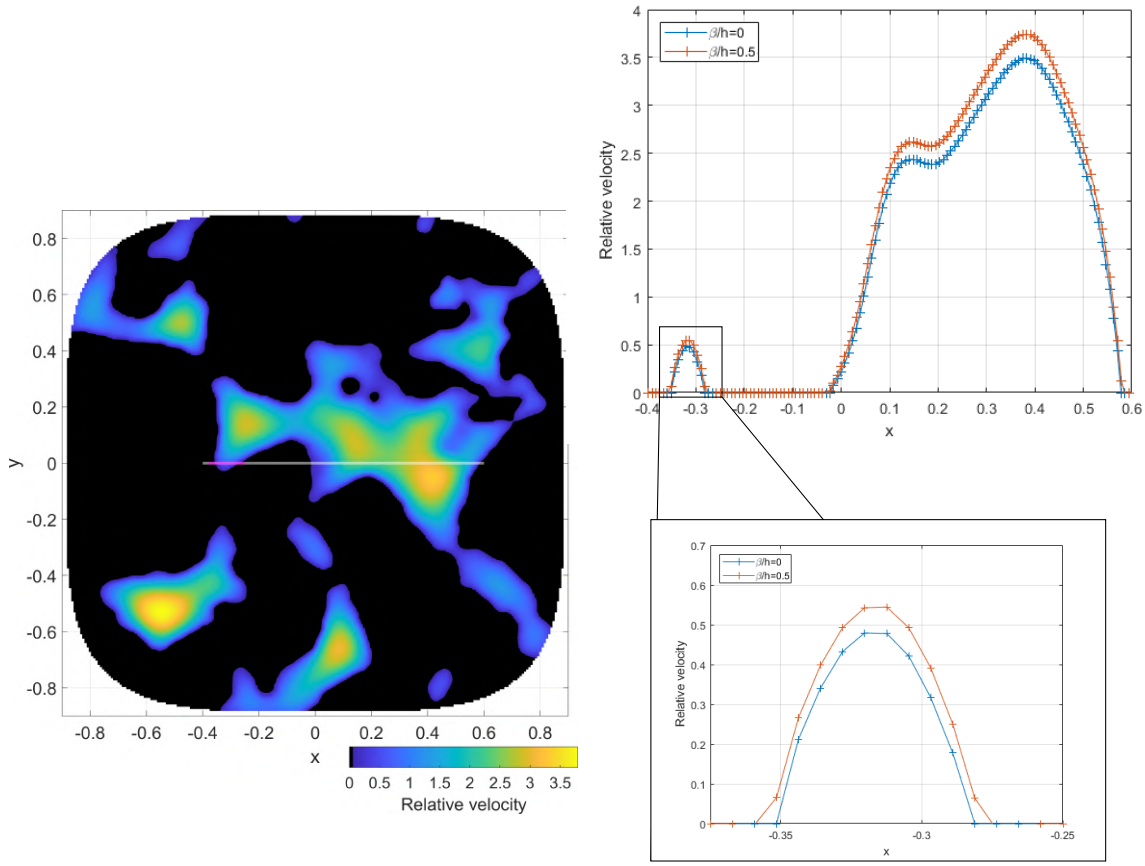


**Figure 3.9: Relative velocities in the main flow direction and on a sectional profile (taken at $y = 0$ and $z = -0.5$ in relative coordinates) on the Bentheimer geometry:** comparison between the adherent and slip boundary conditions for $\beta/h = 0.5$. The $z = -0.5$ slice for a slip length of $\beta/h = 0.5$ is displayed on the left image. The white and magenta lines respectively show the cut, at relative coordinate $y = 0$, for the whole and zoomed curves on the right.

The memory cost mainly depends both on the grid resolution and the Krylov subspace size, so we will present it as a function of the total number of mesh points $N$ and the Krylov size $m$. Five tables, mainly, are used to call the Fortran GMRES(m) subroutine: a table to store the unknowns, one for the result of the matrix-vector product function, one for the right-hand-side and which are all of size $4N$. Additionally, one needs a vector of size $4N(m+1)$ to store the orthonormal basis $\{v_1, ..., v_{k+1}\}$ of the Krylov subspace obtained by Arnoldi's process and finally one table of size $N$ to identify each mesh point with respect to its nature — either solid, fluid or first layer. Then, the GMRES algorithm itself requires the storage of the Hessenberg matrix of size $(m+1)m$ (defined in Sect. 3.5.2) and four additional tables (three of size $m$ and one of size $m+1$) for solving the least squares problem (3.37). This leads to a total storage space of $14N+4N(m+1)+(m+1)^2+3m$.

The simulations are then performed using 16GB of RAM, such that the Krylov space is set to $m = 20$. However, it must be noted that the Krylov subspace size has an effect on the convergence rate. This highlights the difficulty in choosing an appropriate value of $m$, especially when the system size grows. Therefore, in the next section, we propose a strategy for improving convergence in high-resolution simulations.

As the physical parameters, the dynamic viscosity is set to $\mu = 1\mathrm{e}{-3}\ \mathrm{N.m^{-2}.s}$ and the driving force to $f = 5000\mathrm{N.m^{-3}}$. To study the impact of the under-resolved roughness on the permeability, the slip coefficient range is taken between 0 and $h$ with a particular interest in $\beta/h = 0.5$ which helps provide an upper bound for the permeability deviation when the X-ray absorption level is estimated to one half.

The permeability with an adherent pore interface denoted $\kappa_0$, is taken as a reference for the computation of the relative deviation of absolute permeability, given by

$$\frac{|\kappa_\beta - \kappa_0|}{\kappa_0} \tag{3.49}$$

where $\kappa_\beta$ is the permeability with slip boundary condition on the pore interface. In the adherent case, after 100 iterations we obtained a dimensional permeability of $2.87\mathrm{e}{-11}\mathrm{m}^2$, noticing that the usual values obtained from experimental measurements for this type of porous medium are around $1\mathrm{e}{-12}\mathrm{m}^2$, and this actual Bentheimer sample at a representative scale has been measured at 2-3$\mu\mathrm{m}^2$ [22]. The difference is not necessarily significant, as the numerical porosity of the sample considered is about $\phi = 28.75\%$, while typical values for the Bentheimer sandstone are rather around $24\%$ [338]. Finally, the pore interface represents about $7.18\%$ of the sample geometry, excluding the solid casing. In order to provide a physical characterization of the pore interface, we introduce the specific area of the porous medium defined as the ratio of the pore interfacial surface area per unit volume, expressed in $\mathrm{m}^{-1}$. This quantity is numerically estimated and provides a specific area of about $A_s = 25027\mathrm{m}^{-1}$.

The relative residual norms quantifying the convergence of the numerical method, and the permeability changes with respect to the iterations are displayed in Figures 3.10a and 3.10b, on which we compare $\beta/h = 0$ for $\beta/h = 0.5$. For the latter, the relative residual norm and the permeability estimation scale respectively around $1\mathrm{e}{-2}$ and $3.11\mathrm{e}{-11}\mathrm{m}^2$ which represents a permeability deviation of $8.56\%$ for such a slip coefficient. This deviation increases to about $12\%$, as illustrated in Figure 3.7 by the full permeability deviation analysis performed with slip coefficients between 0 and $h$. Both the 3D sample geometry and the final relative velocity field with slip pore interface, in the case $\beta/h = 0.5$, are shown in Figure 3.8.

This example highlights that even a small slip coefficient induces a significant permeability deviation since the pore boundary condition induced by an invisible roughness leads to a different evaluation of the flow rate, as illustrated in Figure 3.9. Actually, we present a sectional profile of the relative velocities in the main flow direction for adherent and slip boundary conditions with $\beta/h = 0.5$ (see Figure 3.9, on the right). The related 2D pore slice and the exact 1D segments for the main profile and its zoomed version are also displayed on the left in Figure 3.9. It remains that one should carefully consider this uncertainty on the permeability estimate to provide a permeability range thanks to a tomographic dataset rather than a single value, especially when the absorption level does not enable us to precisely capture the pore interface roughness.

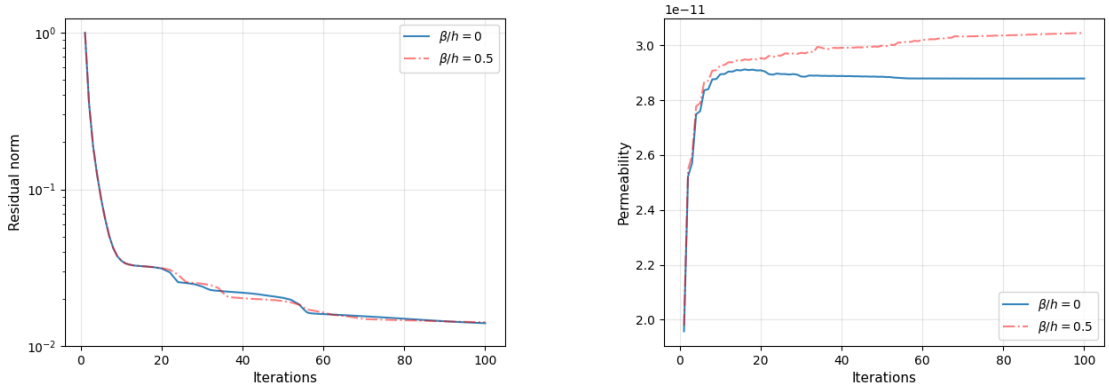


a) Relative residual norm b) Permeability evolution

**Figure 3.10: Convergence analysis on the Bentheimer geometry for adherent and slip boundary conditions:** a) Relative residual norm quantifying the convergence of the GMRES numerical method. b) Evolution of the permeability estimation with respect to the iterations of the numerical method.

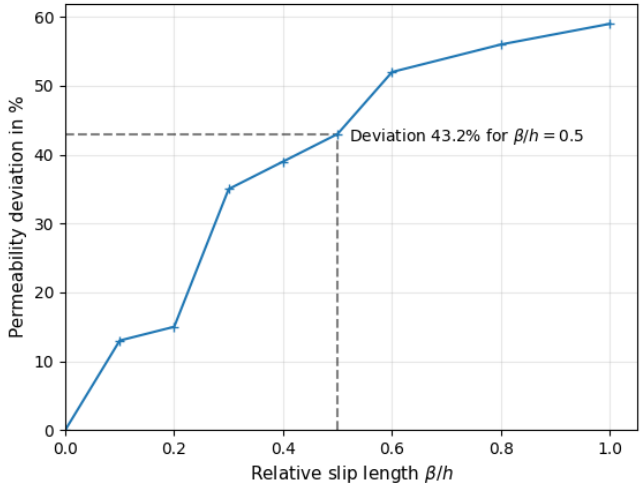


**Figure 3.11: Permeability deviation on the Castlegate sandstone sample for the coarse grid:** deviations are plotted with respect to the slip coefficients for a resolution of 256 cells per direction. The reference permeability $\kappa_0$ is given by $2.09\text{e}{-11}\text{m}^2$.

### 3.6.3 High-resolution flow inside a Castlegate sample

The second real geometry considered is a highly porous Castlegate rock whose numerical porosity is estimated to be $\phi = 25.10\%$. This sandstone outcrop was sampled in southeastern Utah, USA [272]. The numerical sample is extracted from the experimental X-ray dataset — accessible in the Digital Rocks data portal — using a physical voxel size of $5.6\mu$m and has a physical size of $L = 2.8$mm. This Castlegate sandstone is segmented between fluid and solid points on a $512^3$ grid: the pore interface, characterized by the grid points among the solid ones which are in contact with fluid points, denoted $\Sigma_S$, represents about $12.63\%$ of the sample geometry without the casing. Finally, the specific area is also numerically estimated for this sample to get $A_s = 15678\text{m}^{-1}$.

In such high-resolution simulations on a fine grid, the Krylov subspace size is clearly limited regarding memory storage, and consequently, the convergence slows down in comparison with a lower-resolution grid. We thus use preconditioning to obtain convergence results that are reasonable for well-resolved real geometries.

Regarding the sample geometry that contains various small pores, we consider the preconditioning on a grid twice as coarse, with a grid size of 256 cells per direction. The process consists

a) Rock matrix and in-pore velocity, no-slip ($\beta/h = 0$)

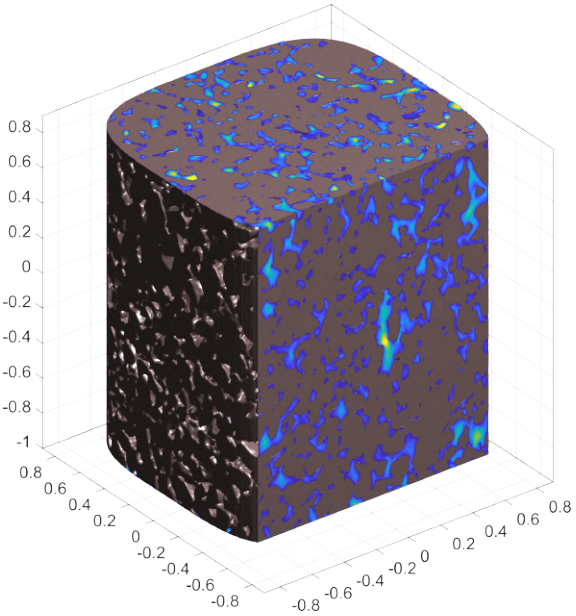

b) Rock matrix and in-pore velocity, slip length $\beta/h = 0.76$

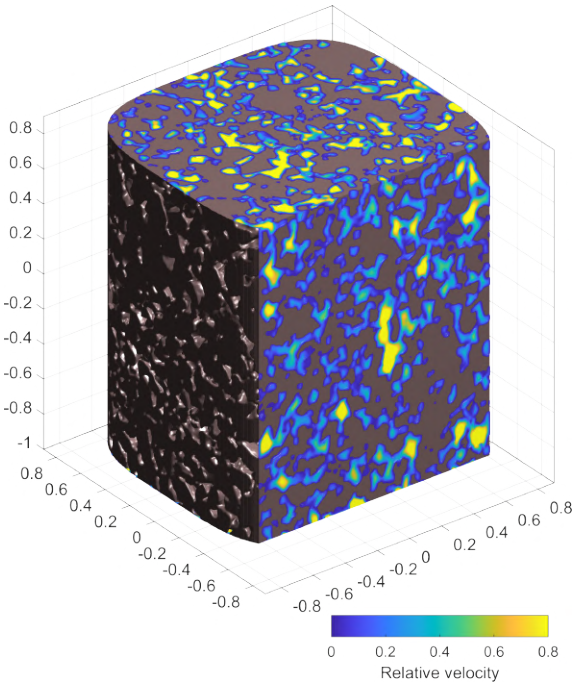


c) Interpolated slip at interface, slip length $\beta/h = 0.76$

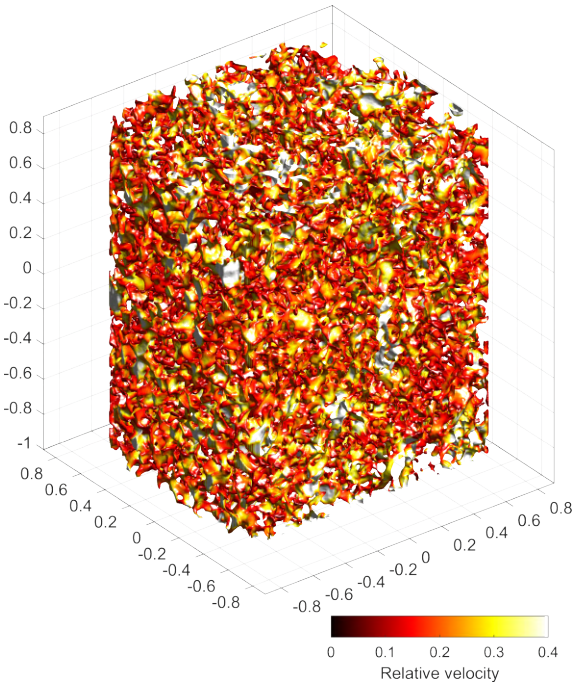


**Figure 3.12: Flow in the Castlegate geometry for the fine resolution** ($512^3$)**:** a) With adherent boundary condition, and b) slip coefficient $\beta/h = 0.76$ corresponding to the light-grey case with low X-ray absorption (see Sect. 3.6.1). c) Interpolated slip at fluid/solid interface. Flow pictures are colored by the norm of relative velocity with the same scale (0-0.8), with respect to relative coordinates (from -1 to 1).

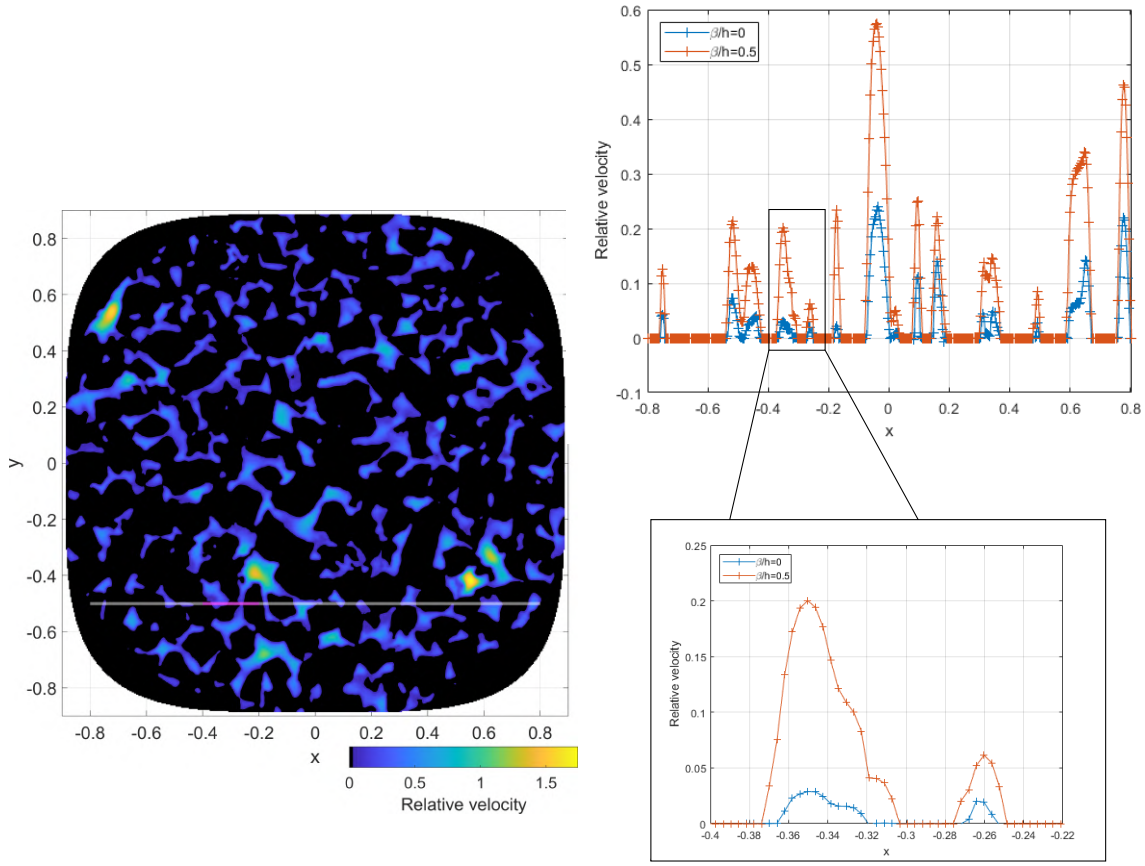


**Figure 3.13: Relative velocities in the main flow direction and on a sectional profile (taken as $z = 0$ and $y = -0.5$ in relative coordinates) on the Castlegate geometry:** comparison between adherent and slip boundary conditions for $\beta/h = 0.5$ for the fine resolution ($512^3$). The slice $z = 0$ for a slip length $\beta/h = 0.5$ is displayed on the left-hand image. The white and magenta lines show the respective locations of the cuts, at relative coordinate $y = 0$, for the whole and zoomed curves on the right.

in computing the velocity and pressure fields on the coarser grid, with a Krylov size that ensures proper convergence results for the residual norm. Indeed, we reach a relative residual of around $1\mathrm{e}{-4}$ after 100 iterations for a 56GB RAM simulation with a Krylov size of $m = 100$, which speeds up dramatically the global simulation.

We then perform an interpolation of these fields to obtain their approximation on the finer grid using an interpolation kernel such that the interpolated pressure and velocity fields are taken as initial guesses for the computation on the whole grid. We use tilde notations when dealing with the refined grid variables and fields, so we denote the interpolated velocity and pressure by $\widetilde{u}$ and $\widetilde{p}$, respectively. We also respectively introduce $\widetilde{x}_q$ and $x_p$ in $\mathbb{R}^3$ as the space variables on the refined and coarse grids. Afterward, the interpolated velocity is computed using the convolution:

$$\widetilde{u}(\widetilde{x}_q) = (u * {M'_4}^h)(\widetilde{x}_q) = \int_{\mathbb{R}^3} u(x){M'_4}^h(\widetilde{x}_q - x)dx = \sum_{p\in S} u_p {M'_4}^h(\widetilde{x}_q - x_p)v_p \tag{3.50}$$

where $S = \{p \text{ such that } \widetilde{x}_q - x_p \in supp({M'_4}^h)\}$ and $v_p$ the volume element of the coarse grid. Moreover, ${M'_4}^h$ is defined with respect to the classical 1D interpolation kernel $M'_4$

$$M'_4(x) = \begin{cases} (3x^3 - 5x^2 + 2)/2 & if\ 0 \leqslant x \leqslant 1 \\ (2-x)^2(1-x)/2 & if\ 1 \leqslant x \leqslant 2 \\ 0 & if\ x \geq 2 \end{cases} \tag{3.51}$$

and is written as the following tensor product, with $h$ referring to the coarse grid mesh step:

$${M'_4}^h(x) = \frac{1}{h^3} {M'_4}^{\otimes 3}\left(\frac{x}{h}\right). \tag{3.52}$$

For the physical parameters, we take $\mu = 1\mathrm{e}{-3}\ \mathrm{N.m^{-2}.s}$ for the dynamic viscosity and $f = 2000\mathrm{N.m^{-3}}$ for the driving force. The full permeability deviation analysis, as displayed in Figure 3.11, with a slip coefficient between 0 and $h$, is performed on the coarse grid with the 256 resolution per direction. For high-resolution simulations, we only consider two main slip coefficient values: $\beta/h = 0.5$ and $\beta/h = 0.76$ previously justified in Sect. 3.6.1. The reference permeability on the adherent pore interface, obtained through the preconditioning process detailed before, is about $\kappa_0 = 1.59\mathrm{e}{-11}\mathrm{m}^2$ after 200 iterations. The Krylov subspace size is set to $m = 50$ on the thinner grid such that this permeability estimate is provided with a relative residual norm of less than $1\mathrm{e}{-6}$. In this case, both the evolution of the relative residual norms and the permeability changes with respect to the number of iterations are presented in Figures 3.14a and 3.14b respectively, on which we compare the adherent case with slip pore boundary by taking $\beta/h = 0.5$. Figure 3.12 also shows the final relative velocity field at the full resolution, obtained in the adherent and slip pore boundary cases.

By considering a slip coefficient of $\beta/h = 0.5$, we reach after the preconditioning process a final relative residual norm of around $1\mathrm{e}{-5}$, which is larger than for the adherent case. This can be explained by the fact that slip boundary conditions tend to disrupt the convergence since the slip may induce a lack of coercivity in the variational formulation. The permeability evolution scales at about $2.57\mathrm{e}{-11}\mathrm{m}^2$ which represents a permeability deviation of $61.63\%$ compared to the adherent case.

Finally, a slip coefficient of $\beta/h = 0.76$, corresponding to light grey voxels, provides a permeability of $3.05\mathrm{e}{-11}\mathrm{m}^2$ with a final relative residual norm of $1\mathrm{e}{-5}$. It represents a permeability deviation of $91.82\%$ which means that $\kappa_\beta$ is nearly twice the reference permeability $\kappa_0$ for such a slip coefficient. We note that we get substantially higher permeability deviations on the Castlegate sandstone sample compared to the Bentheimer sample. This can be explained by a higher proportional pore interface: the pore interface represents $7.18\%$ on the Bentheimer and $12.63\%$ on the Castlegate. In fact, since the Castlegate geometry presents a large variety of small pores, the slip boundary conditions on the pore interface more significantly impact the velocity and thereby the permeability. In that regard, Figure 3.13 shows the relative velocities, for $\beta/h = 0$ and $0.5$, on a sectional profile taken as $z = 0$ and $y = -0.5$ in relative coordinates. On the left, we also represent the related 2D pore slice and the exact 1D segment where the velocity profiles and their zoomed versions are represented — to the right.

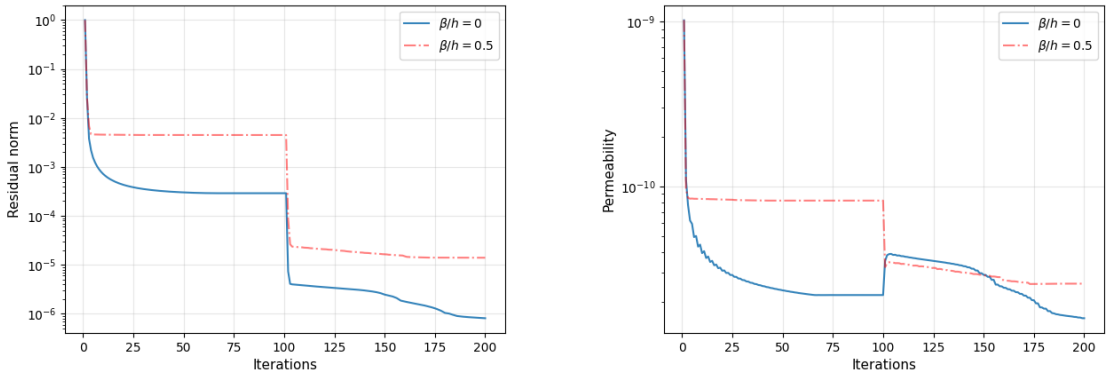


a) Relative residual norm

b) Permeability evolution

**Figure 3.14: Convergence analysis on the Castlegate sandstone sample for adherent and slip boundary conditions up to the fine resolution** $(512^3)$**:** a) Relative residual norm quantifying the convergence of the GMRES numerical method. b) Evolution of the permeability estimation with respect to the iterations of the numerical method. Preconditioning on the coarse grid with a resolution of 256 cells per direction is performed until the 100th iteration, while the final iterations address the global high-resolution grid.

### 3.6.4 High-resolution flow inside a Sandpack sample

The numerical study of the Sandpack considered in this last test case involves a grid resolution of 512 cells in each direction so that the numerical sample extracted from the X-ray dataset has a physical length of $L = 0.768$mm with $1.5\mu$m wide voxels. The acquisition details concerning this sample are provided in Sect. 3.3.3. Porosity and specific area are computed, respectively, at $\phi = 45.43\%$ and $A_s = 93174\text{m}^{-1}$. In this case, the pore interface represents about $20.04\%$ of the grid points that model the sample geometry.

As described in the previous Sect. 3.6.3, preconditioning starts on a twice coarser grid with a Krylov space size of $m = 100$, followed by $M_4'$ interpolation and computations on the refined grid with $m = 50$. The physical parameters involving the dynamic viscosity and the driving force are taken as in Sect. 3.6.3.

The reference permeability on the adherent pore interface is about $\kappa_0 = 1.02\text{e}{-11}\text{m}^2$ after 200 iterations, obtained with a relative residual norm around $1\text{e}{-6}$. In Figures 3.17a and 3.17b we compare both the evolution along the preconditioning process of the relative residual norm and the permeability for $\beta/h = 0, 0.5$ and $0.76$. The permeability reaches $2.48\text{e}{-11}\text{m}^2$ and $2.98\text{e}{-11}\text{m}^2$, respectively, for these two slip coefficient values. This means that on such geometries the permeability deviations are even greater than in the previous applications and scale at about $143\%$ and $192\%$.

As for the previous samples, Figure 3.15 shows the 3D geometry at full resolution with the final velocity fields obtained in the adherent and slip pore boundary cases. Moreover, a 2D pore slice, taken in the main flow direction, is also illustrated on the left-hand side of Figure 3.16 to characterize the sectional profiles presented on the right. It shows the impact of the slip boundary condition on the flow rate, in the particular case $\beta/h = 0.5$.

Furthermore, we verify in this case that the permeability variation does not reflect the residual errors of the numerical scheme: Figure 3.17a shows that the relative residual is the same for the two slip lengths $\beta/h = 0.5$ and $0.76$. Overall, our methodology shows large permeability deviations due to slip boundary conditions that account for the unresolved features of the $\mu$CT imaging technique. These deviations, thereby, need to be considered when investigating the impact of geochemical processes of $CO_2$ storage in underground natural reservoirs. One should provide reliable evolutions of the upscaled petrophysical properties arising from dynamical effects rather than measuring uncertainties related to imaging morphological bias.

a) Rock matrix and in-pore velocity, no-slip ($\beta/h = 0$)

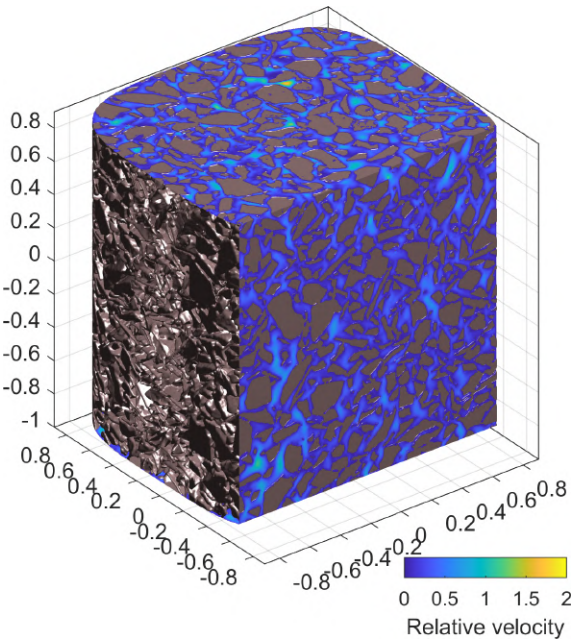


b) Rock matrix and in-pore velocity, slip length $\beta/h = 0.76$

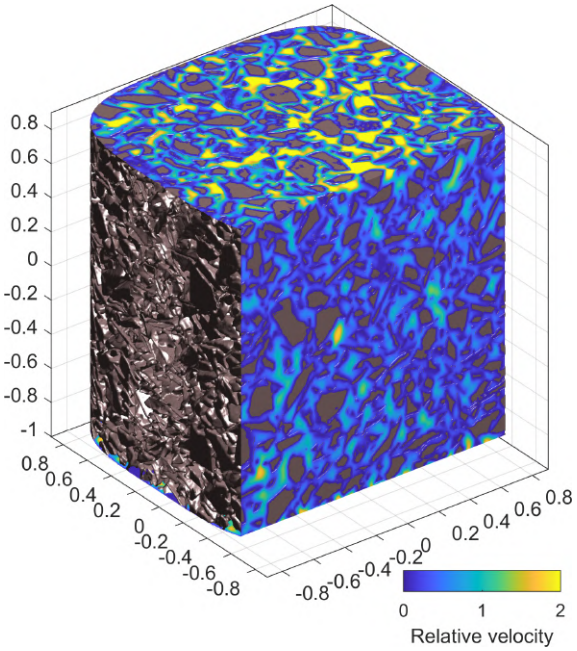


c) Interpolated slip at interface, slip length $\beta/h = 0.76$

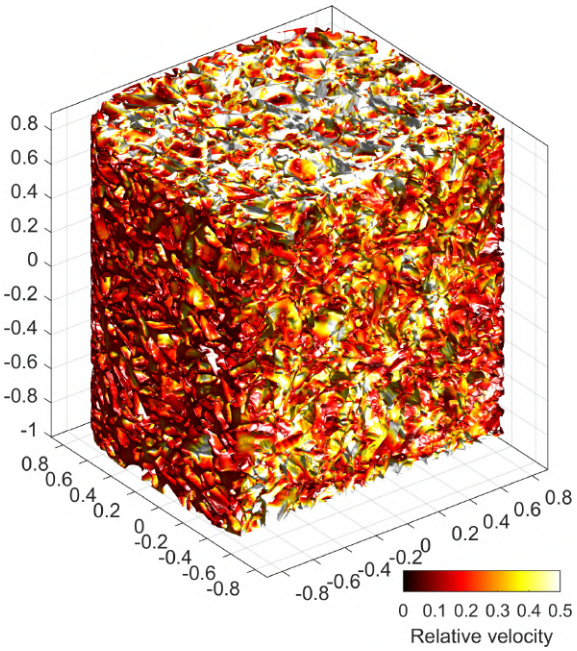


**Figure 3.15: Flow in the compact Sandpack geometry for the fine resolution** ($512^3$)**:** a) With adherent boundary condition, and b) slip coefficient $\beta/h = 0.76$. c) Interpolated slip at pore boundaries. We use the same color legend as for Figure 3.12.

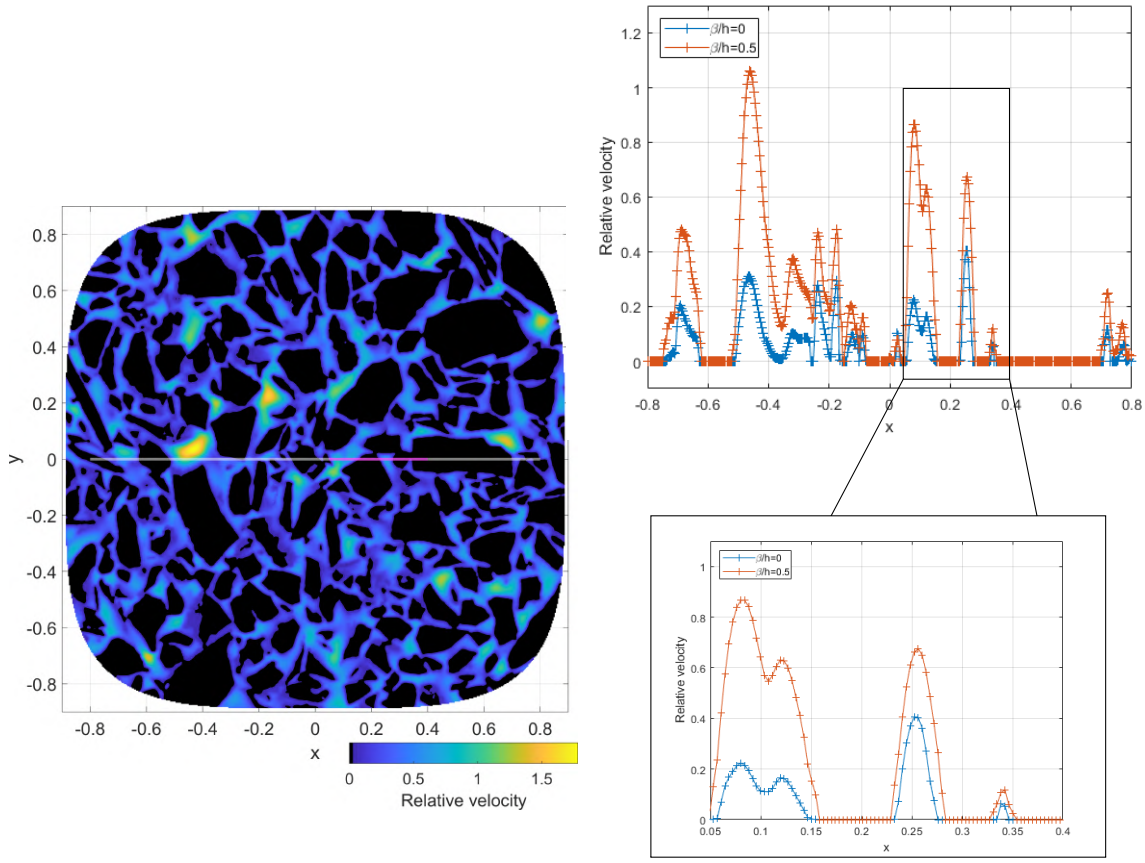


**Figure 3.16: Relative velocities in the main flow direction and through a sectional profile (taken at $z = -0.75$ and $y = 0$ in relative coordinates) on the Sandpack geometry:** comparison between the adherent and slip boundary conditions for $\beta/h = 0.5$. The slice $z = -0.75$ for a slip length $\beta/h = 0.5$ is displayed on the left-hand image. The white and magenta lines show the location, respectively, of the cuts for the whole and zoomed curves of the velocity profiles on the right.

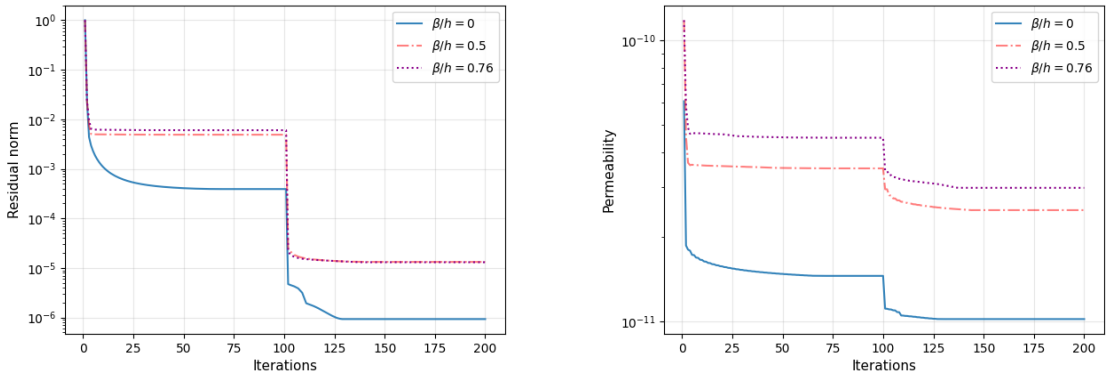


a) Relative residual norm b) Permeability evolution

**Figure 3.17: Convergence analysis on the Sandpack sample for adherent and slip boundary conditions up to the fine resolution ($512^3$):** a) Relative residual norm quantifying the convergence of the GMRES numerical method. b) Evolution of the permeability estimation with respect to the iterations of the numerical method. Preconditioning on the coarse grid with a resolution of 256 cells per direction is performed until the 100th iteration, while the final iterations address the global high-resolution grid. Comparisons are performed for $\beta/h = 0$, 0.5 and 0.76.

## 3.7 Toward the second order deviation of the permeability

In addition to the full permeability deviation analysis performed throughout the application Sect. 3.6, we also investigate the impact of the linear deviation on the real porous sample geometries. We use the methodology developed in Sect. 3.5 to solve the Stokes closure problems at successive orders resulting from the two-scale asymptotic expansion (see equations (3.31) and (3.32) in Sect. 3.4.3). The apparent permeability is thereby regarded as the combination of the intrinsic permeability $\kappa_0$ and the slip-correction first order term $L_0$ according to equation (3.11). The related permeability ranges $\delta K = [\kappa_0, \kappa_\beta]$ and $[\kappa_0, \kappa_0 + \beta L_0]$ are then compared and analyzed for each geometry.

### 3.7.1 First-order linear deviation on real geometries: results summary

Table 3.2 summarizes the results obtained for both the raw deviations and the linear deviations for all considered samples from Sect. 3.6. The permeability ranges account for the sample resolution, its permeability, and its geometry at the pore scale. The main features of each sample are described in Table 3.1.

Overall, we observe the permeability deviations using the raw values — namely the full deviation based on the PDE system (3.8) — and the values based on the linear momentum resulting from the asymptotic development are consistent. However, when performing the permeability deviation analysis for several slip length values, we notice small non-linear effects (*e.g.* see in Figures 3.4 and 3.11). These non-linear effects can also be observed in Table 3.2, where the linear deviations are usually underestimated compared to the global permeability uncertainty ranges. This suggests that macroscopic effects, especially on the upscaled permeability, may arise from higher-order developments of the asymptotic expansion which involve additional slip-correction terms. While this statement has already been pointed out in several studies on analytical test cases and synthetic geometries [158, 161], we also show that this impacts the apparent permeability estimation for real applications. This motivates the investigation of the second-order deviation, developed in the subsequent Sect. 3.7.2, to confirm such macroscopic effects resulting from higher-order correction terms.

Furthermore, to compare the permeability deviations based on the pore structure of the distinct samples, we compute a dimensionless ratio from the slip-independent relative deviations and the specific area $A_s$ that both have the same units ($\mathrm{mm}^{-1}$). This provides respectively the following dimensionless ratios for the full and linear deviations:

$$\frac{\kappa_\beta - \kappa_0}{\kappa_0 \beta A_s} \quad \text{and} \quad \frac{L_0}{\kappa_0 A_s} \tag{3.53}$$

which are displayed in Table 3.3 for the different samples. This dimensionless number is theoretically equal to 2 for the cylinder and could be of great interest since it appears to be independent through the homogenization process in this theoretical case. One should also notice that when considering a foam structure with a cylindrical pore surrounded by a solid domain of size $l$, this dimensionless ratio writes $2l^2/\pi R^2$. In fact, in this case, the porosity and specific area are respectively given by $\phi = \pi R^2/l^2$ and $A_s = 2\pi R/l^2$. This gives insight into how the pore space structure impacts this dimensionless ratio, as a smaller pore radius $R$ will enhance the slip deviation effect.

In this sense, it also appears that the Bentheimer sandstone, which is of size $256^3$ and too coarse to be a representative sample, has dimensionless ratios given by the expressions in (3.53) around 2-3 which is close to the cylindrical case (see Table 3.3). On the contrary, representative samples of their media, namely the Castlegate sandstone and the Sandpack, have ratios in the range 12-17, even though their porosity values are highly different. This dimensionless number may thereby appear to provide a criterion for representative porous samples. Future work will investigate whether or not sandstones with porosities in the range of 20-25% correlate with a universal dimensionless ratio and whether this is related to sample representativity.

| Sample | Computed porosity $\phi$ | Grain size | Charact. length $\sqrt{\kappa_0}$ | Sample width | Sample resolution | Sample volume |
|---|---|---|---|---|---|---|
| Unit | — | $\mu$m | mm | $\mu$m | — | $\mathrm{mm}^3$ |
| Bentheimer | 28.75% | 200-330 | 5.3 | 563 | $256^3$ | 0.131 |
| Castlegate | 25.1% | $\simeq$150 | 4.0 | 2867 | $512^3$ | 17.30 |
| Sandpack | 45.4% | $\simeq$50 | 3.2 | 768 | $512^3$ | 0.332 |

**Table 3.1: Rock and numerical sample features.** Orders of magnitude of grain size are taken from [22, 234] and [135]. The sample volume excludes the digital cell surrounding the rock matrix.

| Sample | Slip length $\beta$ | No-slip permeability $\kappa_0$ | Full deviation | | Linear deviation | |
|---|---|---|---|---|---|---|
| | | | Relative deviation $(\kappa_\beta - \kappa_0)/\kappa_0$ | Permeability range $[\kappa_0, \kappa_\beta]$ | Relative deviation $\beta L_0/\kappa_0$ | Permeability range $[\kappa_0, \kappa_0+\beta L_0]$ |
| Unit | $\mu$m | $\mu\mathrm{m}^2$ | — | $\mu\mathrm{m}^2$ | — | $\mu\mathrm{m}^2$ |
| Cylinder | — | $R^2/8$ | $4\beta/R$ | $[\kappa_0, \kappa_0+\beta R/2]$ | $\beta 4/R$ | $[\kappa_0, \kappa_0+\beta R/2]$ |
| Bentheimer | 1.1 | 28.7 | 8.56% | [28.7, 31.1] | 6.97% | [28.7, 30.7] |
| Castlegate | 4.26 | 15.9 | 91.82% | [15.9, 30.5] | 79.25% | [15.9, 28.5] |
| Sandpack | 1.14 | 10.2 | 192.15% | [10.2, 29.8] | 179.22% | [10.2, 28.4] |

**Table 3.2: Summary of absolute permeability ranges obtained for the three samples and the ideal cylindrical pore:** results are both presented in terms of the full deviation and linear deviation models. The results for the Castlegate and Sandpack samples are provided for the finest resolution of $512^3$.

### 3.7.2 Second order deviation: the Castlegate example

To quantify the non-linear effects observed in the previous Sect. 3.7.1, we consider the generalization of the Stokes-like closure problems up to the second-order profile to account for additional slip-correction terms. We thereby extend the two-scale asymptotic expansion developed in Sect. 3.4 such that the formal developments of $u_\beta$ and $p_\beta$ writes:

$$u_\beta = \sum_{j=0}^{2} \beta^j U^j + \beta^3 r_\beta \quad \text{and} \quad p_\beta = \sum_{j=0}^{2} \beta^j P^j + \beta^3 q_\beta \tag{3.54}$$

following the notations previously introduced. This enables us to address the second-order slip momentum, denoted $L_1$, given the following Taylor development of (3.10):

$$\kappa_\beta = \kappa_0 + \beta L_0 + \frac{\beta^2}{2} L_1 + \mathcal{O}(\beta^3) \tag{3.55}$$

and afterward provides the second-order deviation on the permeability. Similarly to the analysis of Sect. 3.4, we obtain that the profiles $(U^2, P^2)$ satisfy a Stokes problem with an intrinsic slip-flow correction resulting from non-homogeneous Dirichlet boundary conditions, written as follows:

$$\begin{cases} -\Delta U^2 + \nabla P^2 = 0, & \text{in} \quad \Omega_F \\ \operatorname{div} U^2 = 0, & \text{in} \quad \Omega_F \\ T\,U^2 = T\,D(U^1)\cdot n, & \text{on} \quad \Sigma \\ U^2 \cdot n = 0, & \text{on} \quad \Sigma. \end{cases} \tag{3.56}$$

Accounting for the second-order deviation on the permeability, therefore, requires solving successively the Stokes problems (3.31), (3.32) and (3.56) that respectively identify the intrinsic permeability $\kappa_0$, its first-order linear deviation $L_0$ and the second-order momentum $L_1$. The latter is given by the following relation:

$$L_1 = \frac{\phi < U_z^2 >_{\Omega_F}}{< f_z >_{\Omega_F}} \tag{3.57}$$

| Sample | Computed porosity $\phi$ | Specific area $A_s$ | Relative deviation $K'/\kappa_0$ | Dimensionless ratio $K'/\kappa_0 A_s$ | Relative linear deviation $L_0/\kappa_0$ | Dimensionless ratio $L_0/\kappa_0 A_s$ |
|---|---|---|---|---|---|---|
| Unit | — | $\mathrm{mm}^{-1}$ | $\mathrm{mm}^{-1}$ | — | $\mathrm{mm}^{-1}$ | — |
| Cylinder | 100 % | $2/R$ | $4/R$ | 2 | $4/R$ | 2 |
| Bentheimer | 28.75% | 25 | 78 | 3.1 | 63.7 | 2.5 |
| Castlegate | 25.1% | 15.7 | 215.5 | 13.7 | 186 | 11.9 |
| Sandpack | 45.4% | 93 | 1 684 | 18.1 | 1 561 | 16.8 |

**Table 3.3: Dimensionless ratios characterization for the several samples and ideal cylindrical pore:** Comparison of relative deviations with respect to specific areas for the different samples. We use the notation $K' = (\kappa_\beta - \kappa_0)/\beta$. The relative deviations are slip-independent.

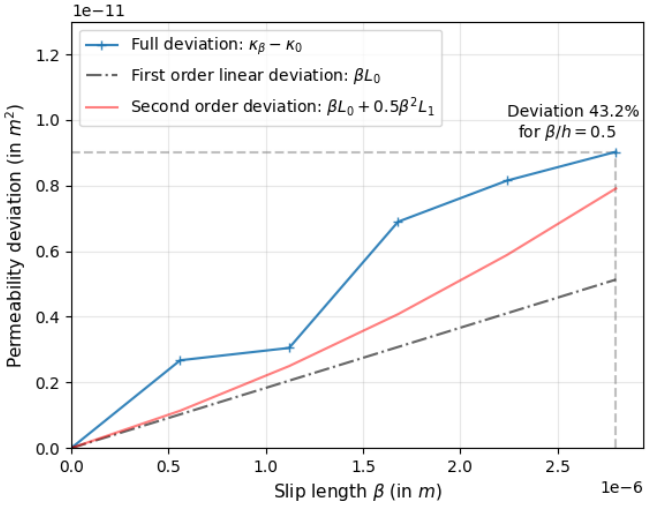


**Figure 3.18: Comparison between full, first-order, and second-order permeability deviations on the Castlegate sandstone sample:** absolute deviations (in $\mathrm{m}^2$) plotted with respect to the slip coefficients (in m) on the coarse grid with a resolution of 256 cells per direction. The analysis is performed for slip length values between $\beta/h = 0$ and 0.5. Data for the full permeability deviations result from Figure 3.11 in Sect. 3.6.3.

such that the second-order permeability range writes

$$\delta K = \left[\kappa_0, \kappa_0 + \beta L_0 + \frac{\beta^2}{2} L_1\right]. \tag{3.58}$$

The analysis is performed on the Castlegate sample, on the coarse grid with a resolution of $256^3$, to compare with the full permeability deviation from Figure 3.11 and requires using fourth-order finite difference stencils. In this case, we obtain a reference permeability $\kappa_0 = 2.09\mathrm{e}{-11}\mathrm{m}^2$, a linear deviation $L_0 = 1.8338\mathrm{e}{-6}\mathrm{m}$ and a second-order momentum $L_1 = 0.708364$. We represent in Figure 3.18 the comparison between the full deviation — obtained from Sect. 3.6.3 — the first and second-order permeability deviations with respect to the slip length. Overall, this confirms the macroscopic effects resulting from the non-linear correction of the apparent permeability and shows that the second-order deviation improves the uncertainty estimation resulting from the first-order linear approximation. Accounting for the second-order slip correction term, indeed, results in a relative permeability deviation of $37.7\%$ compared to the $43.2\%$ for the global deviation and $24.57\%$ for the linear deviation. This validates for applications to porous samples what was anticipated in [158] for simplified 2D geometries and confirms the importance of properly considering slip effects at the macro-scale, especially on the absolute permeability deviation.

## 3.8 Concluding remarks

Pore-scale modeling and numerical simulations of flow in porous media are commonly based on sample datasets obtained through X-ray micro-tomography. Imaging limitations, however, exist in this process. The finite resolution of these tomographic scans, for instance, leads to an uncertainty on the position and morphology of the pore interfaces, which subsequently impacts the estimation of the effective petrophysical properties of the porous medium. Unresolved morphological features also play a role in the flow within the sample, while these effects are difficult to incorporate in the workflow and thereby generate uncertainties. The current chapter attempts to assess the impact of such imaging artifacts on the computed permeability of the medium.

To do so, we relied on a slip length formalism [54, 163], whose idea is closely related to homogenization principles. It aims to approximate the actual surface roughness or its position subject to uncertainty by a smooth interface supplemented with slip boundary conditions. The underlying Stokes problem with Robin/Navier boundary condition is then solved using a restarted GMRES method that ensures precise monitoring of the velocity at the pore interface, after which the permeability tensor is obtained by Darcy's law. Two approaches are proposed to evaluate the absolute permeability ranges, namely the full deviation based on slip boundary conditions and the theoretically established deviations from asymptotic analysis. The latter regards the permeability deviation induced by morphological uncertainties as the combination of the reference permeability $\kappa_0$ and slip-correction terms of first and second-order, arising from the solutions of Stokes-like closure problems at successive order. This reformulation of the global deviation hence requires solving a classical Stokes problem with adherent interfaces, followed by coupled problems with non-homogeneous Dirichlet boundary conditions involving a prescribed slip that depends on the immediate lower-order profile.

We compared the full permeability deviation interval $\delta K = [\kappa_0, \kappa_\beta]$ and its first-order approximation $\delta K = [\kappa_0, \kappa_0 + \beta L_0]$ on sample geometries with different morphological characteristics and heterogeneous porosity distributions. We also estimated meaningful slip length values $\beta$ that adequately represent the $\mu$CT imaging uncertainties. We showed that considering $\beta$ proportional to the voxel size $h$ is relevant to characterize the not fully resolved solid fraction within a voxel or the biased interface location.

For the porous samples considered in this chapter, we observed that within the range $\beta/h < 1$, both the full deviation and the linear deviation provided comparable results. Some non-linear effects, however, appear as soon as $\beta$ nears the voxel size. At this point, the global permeability deviation and its estimation based on the first-order linear deviation begin to differ. Slip-correction terms beyond the first-order linear deviation are thus considered to capture these non-linear effects on the apparent macro-scale permeability. This resulted in the development of the second-order deviation on the Castlegate sandstone with $\delta K = [\kappa_0, \kappa_0 + \beta L_0 + \beta^2 L_1/2]$, and we showed the importance of considering such higher-order slip-correction terms in porous media applications.

Absolute permeability analysis on real porous rock applications highlighted that geometrical uncertainties induce a significant deviation, which can lead to discrepancies of twice the reference permeability. It must be noted that the permeability deviation is sensitive to the structure of the pore space and its effect increases for geometries with a large proportion of small pores. We also provided dimensionless ratios quantifying the relative permeability deviations versus the specific area to provide a geometrical-independent characterization of the permeability uncertainties. Representative samples have been shown to exhibit similar ratios in the range of $12 - 17$, even though their morphological characteristics were highly different. On the contrary, the non-representative Bentheimer sample presented a dimensionless ratio close to the theoretical value obtained for the single cylindrical pore.

Overall, one must be careful with the permeability estimation in which the geometrical uncertainty should be rendered by a range of permeability resulting from tomographic measurements. In this sense, this chapter provided a numerical and mathematical framework to investigate the uncertainty ranges on the permeability in 3D complex porous geometries. This makes it possible to understand how pore-scale morphological bias, arising from $\mu$CT imaging, propagates to upscaled permeability uncertainties. We can, thereby, provide reliable quantification of the macro-

properties changes based on geochemical processes and ensure that these variations are not merely biased due to imaging limitations. These results were obtained for a few samples covering a diverse distribution of morphological features and exhibited interesting characteristics that would be interesting to investigate in the future. Another prospect could be to extend the approach developed in this chapter to multi-phase flows at low Reynolds regimes to monitor the relative permeability deviations of each phase.

CHAPTER 4

# Multitask Bayesian Physics-Informed Neural Networks for multiscale forward and inverse problems

**Contents**



## 4.1 Motivation

In Chapter 3, we demonstrated that uncertainty assessment on the macro-scale absolute permeability can be addressed through upscaling principles of the sub-resolved features resulting from X-ray $\mu$CT images. This makes it possible to characterize the impact of imaging morphological biases on the macro-scale properties and, subsequently, ensures reliable quantification of the permeability evolution. Nonetheless, upscaling approaches do not straightforwardly provide insight into the sub-resolved porosity but rather consider the morphological biases as averaged properties. In this sense, we do not capture the micro-porosity field uncertainties. This, however, presents a great interest for field-scale sensitivity analyses as this can provide a range of macro-porosity distributions in reservoir simulations. Thus, quantifying the macro-porosity deviations due to these local uncertainties on the microscopic features remains challenging and requires developing other alternatives.

Machine learning, for instance, offers an interesting framework to investigate the unresolved features through image treatment analysis of the $\mu$CT scans. Efforts have been directed toward developing deep learning methodologies such as Convolutional Neural Networks (CNN)

and Generative Adversarial Neural Networks (GAN) that provide super-resolved segmented images [16, 330]. Meanwhile, differential imaging techniques based on comparisons between several enhanced contrast scans [172] or statistical studies based on $\mu$CT histograms [341] have also garnered interest. Nonetheless, these approaches present the main disadvantage of solely considering the imaging dataset to address an overall data assimilation problem.

On the contrary, the following two chapters aim to develop a robust data assimilation method incorporating both physic-based principles through PDE models and $\mu$CT imaging data. The motivation is to compensate for their respective limitations by finding a proper balance between experiments and physical principles. This should provide reliable insights into the uncertainty quantification issues related to reactive pore-scale modeling. In the sequel, we mainly focus on the methodological development of such an alternative for reliable data assimilation, while Chapter 5 will address the porous media application for inverse problems in pore-scale imaging.

This chapter presents a novel methodology for automatic and adaptive weighting of Bayesian Physics-Informed Neural Networks (BPINNs), and we demonstrate that this makes it possible to robustly address multi-objective and multiscale AI problems. We intend to develop a reliable framework for data assimilation that merges Uncertainty Quantification (UQ), physics-informed PDE models, and data-driven methods. BPINNs, in particular, have recently emerged as a popular framework combining the constraints of UQ and PDE. The relative weights of the BPINN target distribution terms are directly related to the inherent uncertainty in the respective learning tasks. Yet, these weights are usually manually set a-priori, which can lead to pathological behavior, stability concerns, and to conflicts between tasks which are obstacles that have deterred the use of BPINNs for inverse problems with multiscale dynamics.

The present weighting strategy automatically tunes the weights by considering the multitask nature of target posterior distribution. We show that this remedies the failure modes of BPINNs and provides an efficient exploration of the optimal Pareto front. This leads to better convergence and stability of BPINN training while reducing sampling bias. The determined weights moreover carry information about task uncertainties, reflecting noise levels in the data and adequacy of the PDE model. We demonstrate the effectiveness of the present methodology on an extensive Sobolev training benchmark wherein this solves stiffness and instability issues altogether while comparing to analytically $\varepsilon$-optimal baseline. We further perform validation on a multiscale Lokta-Volterra inverse problem. We eventually apply this framework to an inpainting task and an inverse problem, involving latent field recovery for incompressible flow in complex geometries.

This research topic has led to a three-month doctoral mobility at the Max Planck Institute of Molecular Cell Biology and Genetics (MPI-CBG) in Dresden (Germany), where I have been hosted in the MOSAIC Group, headed by Professor Ivo F. Sbalzarini. I have enhanced my understanding of data-driven and deep-learning methodologies, which align with the MOSAIC Group's expertise, and initiated a collaboration to develop such a robust data assimilation framework with UQ. This has resulted in a joint publication in the Journal of Computational Physics with Prof. Ivo F. Sbalzarini, Dr. Suryanarayana Maddu, and Prof. Philippe Poncet [237].

## 4.2 Context and positioning

Direct numerical simulation relies on appropriate mathematical models, derived from physical principles, to conceptualize real-world behavior and provide an understanding of complex phenomena. Experimental data are mainly used for parameter identification and a-posteriori model validation. However, a wide range of real-world applications are characterized by the absence of predictive physical models, notably in the life sciences. Data-driven inference of physical models has therefore emerged as a complementary approach in those applications [185]. The same is true for applications that rely on data assimilation and inverse modeling, for example in geosciences. This has established data-driven models as complementary means to theory-driven models in scientific applications.

Depending on the amount of data available, several data-driven modeling strategies can be chosen. An overview of the state of the art in data-driven modeling, as well as of the remaining chal-

lenges, has recently been published [103] with applications focusing on porous media research. It covers methods ranging from model inference using sparse regression [60, 117, 184, 265], where the symbolic structure of a Partial Differential Equation model is inferred from the data, to equation-free forecasting models based on extrapolation of observed dynamics [186, 231, 307]. Therefore, model inference methods are available for both physics-based and equation-free scenarios.

A popular framework combining both scenarios are Physics-Informed Neural Networks (PINNs) [254]. They integrate potentially sparse and noisy data with physical principles, such as conservation laws, expressed as mathematical equations. These equations regularize the neural network while the network weights $\theta \in \mathbb{R}^d$ and unknown equation coefficients $\mathcal{P}_{\text{inv}} \in \mathbb{R}^p$ are inferred from data. This has enabled the use of PINNs as surrogate models, for example in fluid mechanics [226, 290]. Overall, PINNs provide an effective alternative to purely data-driven methods, since a lack of high-fidelity data can be compensated by physical regularization [176, 199].

Despite their effectiveness and versatility, PINNs can be difficult to use correctly, as they are prone to a range of training instabilities. This is because their training amounts to a weighted multi-objective optimization problem for the joint set of parameters $\Theta = \{\theta, \mathcal{P}_{\text{inv}}\}$,

$$\widehat{\Theta} = \arg\min_{\Theta} \sum_{k=0}^{K} \lambda_k \mathcal{L}_k(\Theta), \tag{4.1}$$

where each term $\mathcal{L}_k(\Theta)$ of the loss function corresponds to a distinct inference task. For typical PINNs, these tasks include: data fitting, PDE residual minimization, boundary and initial condition matching, and additional physical constraints such as divergence-freeness of the learned field. Such a combination of measurement and physical constraints, usually encountered in the PINN formulation, readily results in multi-objective problems with tens of different tasks. Proper training of this multitask learning problem hinges on correctly setting the loss term weights $\lambda_k$ [187]. An unsuitable choice of weights can lead to biased optimization [253], vanishing task-specific gradients [80, 270], or catastrophic forgetting [187]. Automatically optimizing the loss weights is crucial and not straightforward, especially if the multi-objective problem is highly nonlinear and suffers from multiscale issues.

The problem of how to tune the loss weights of a PINN is widely known and several potential solutions have been developed to balance the objectives [75, 187, 312, 313]. This offers criteria to impartially optimize the different tasks and provide a good exploration of the optimal Pareto front [258]. While it improves reliability by reducing optimization bias, several open questions remain regarding the confidence in the predictions, noise estimates, and model adequacy [199, 127, 329]. These questions motivate a need for uncertainty quantification to ensure trustworthy inference, extending PINNs to Bayesian inference in the form of Bayesian Physics-Informed Neural Networks [173, 328]. How to adapt successful PINN weighting strategies to BPINNs and integrate them with UQ, however, is still an open problem.

BPINNs benefit from the combined advantages of neural network structures in building parameterized surrogate models based on physical principles and Bayesian inference standards in estimating target distribution. They enable integration of UQ by providing posterior distribution estimates of the predictions — also known as Bayesian Model Averages [319] — based on Markov Chain Monte Carlo (MCMC) sampling. One of the most popular MCMC schemes for BPINNs is Hamiltonian Monte Carlo (HMC), which provides a particularly efficient sampler for high-dimensional inference problems with smooth (physical) dynamics [48]. Although HMC has been shown to be more efficient for BPINNs, its formulation implies potential energy that is closely related to the cost function of the PINN. The multi-objective loss of a PINN directly translates to multi-potential energy and thus to a weighted multitask posterior distribution for BPINN sampling. Sampling from such a target posterior distribution resulting from dozens of distinct tasks, which may be conflicting or involve different scales, is not straightforward. Unsuitable weights can even prevent the sampler from identifying the mode neighborhood in the parameter space that maximizes the overall posterior density. Therefore, it suffers from the same difficulties as a PINN

to avoid bias in the sampling and provide an efficient exploration of the Pareto front, characterizing the region of the highest posterior probability.

This often causes HMC to not correctly explore the Pareto front neighborhood during BPINN training. Efficient exploration of a high-dimensional Pareto front remains challenging for multitask and multiscale learning problems incorporating UQ and has not yet been addressed in the Bayesian case. The challenge arises because each term of the multi-potential energy is weighted within the Bayesian framework by parameters that relate to scaling, noise magnitude, and ultimately the inherent uncertainties in the different learning tasks [80]. While these weights are recognized as critical parameters in the sampling procedure, they are mostly hand-tuned [173, 199, 207], introducing hidden priors when the true uncertainties are not known. Not relying on such a-priori manual calibration of the posterior distribution becomes critical when considering multitask inference problems with potential nonlinear and multiscale effects. In such cases, appropriately setting these parameters is neither easy nor computationally efficient and can lead to either a biased estimation of the uncertainties or a considerable waste of energy in ineffective tuning. Properly optimizing these weights is therefore essential to ensure that HMC samples from the posterior distribution around the Pareto front. This is not only required for robust BPINN training but also for enhanced reliability of the UQ estimates, not subject to biased priors.

In order to robustly handle multitask UQ inference in BPINNs, the open questions addressed in this chapter are:

1. How can we automatically adjust the weights in BPINNs to efficiently explore the Pareto front and avoid bias in the UQ inference?
2. How can we manage sensitivity to the noise distributions (homo- or hetero-scedastic) and their amplitude, without imposing hidden priors, to ensure reliable uncertainties estimates?

We intend to provide a reliable framework to address multitask Bayesian inference problems, with potential multiscale effects, stiffness, or competing tasks, such that we do not rely on a-priori hand-tuning or biased calibration of the posterior distribution. We aim to automatically and adaptively build the weighted posterior distribution that concentrates on the region of highest posterior probability, localized in the Pareto front neighborhood. The main novelty is here to address the problem of appropriate weighting in multitask inference problems from the posterior distribution perspective, which becomes crucial when dealing with physics-based inference. On the contrary, related state-of-the-art adaptive methods regard the problem from the adaptation of some hyperparameters (*e.g.* the leapfrog parameters in the No-U-Turn sampler [132]) or the adaptation of the momentum based on local geometrical information (*e.g.* Riemann Hamiltonian Monte Carlo [123]). Other strategies aim to speed up the Bayesian inversion and reduce the computational cost of evaluating the forward model itself, with some adaptations based on multi-fidelity surrogate models either computed through polynomial chaos expansion [325] or neural network proxies [326]. These adaptations are usually performed through online and local refinement of the surrogate models using only a few simulations from the high-fidelity model. However, all these adaptive methods do not consider the case where we face multi-objective problems with potentially conflicting tasks or multiscale issues.

In this chapter, we start by characterizing potential BPINN failure modes, which are particularly prevalent for multiscale or multitask inverse problems. We then propose a modified HMC sampler, called Adaptively Weighted Hamiltonian Monte Carlo (AW-HMC), which avoids the problem by balancing gradient variances during sampling. We show that this leads to a weighted posterior distribution that is well suited to exploring the Pareto front neighborhood, since it concentrates on the region of highest posterior probability by leveraging gradient information of the different tasks during the adaptation procedure. Our benchmarks show that this strategy reduces sampling bias and enhances the BPINN robustness. In particular, our method improves the stability along the leapfrog steps during training, since it ensures optimal integration and frees the sampling from excessive time step decrease. Moreover, it is able to automatically adjust the potential energy weights and with them, the uncertainties according to the sensitivity to noise of each term and their different scaling. This considerably improves the reliability of the UQ by reducing

the need for hyperparameter tuning, including the prior distributions, and reducing the need for prior knowledge of noise levels or appropriate task scaling. We show that this improves BPINNs with respect to both the convergence rate and the computational cost. Moreover, we introduce a new metric for the quality of the prediction, quantifying the convergence rate during the marginalization step. We finally demonstrate that our proposed approach enables the use of BPINNs in multiscale and multitask Bayesian inference over complex real-world problems with sparse and noisy data. Therefore, we establish the present AW-HMC method for the BPINNs as an efficient data assimilation framework incorporating robust uncertainty quantification.

The main contributions of this chapter can be summarized as follows:

1. Automatic and adaptive weighting of BPINNs enables their use for multitask and multiscale inverse problems in the Bayesian context. This avoids manual tuning of noise and model adequacy hyper-parameters when facing unknown priors.
2. We prevent BPINNs training failure mode and improve the formulation robustness by providing unbiased uncertainty quantifications, independently of the noise level in the data.
3. We develop a computational cost-free method, ensuring automatic task balancing, by straightforwardly leveraging gradient information of the different tasks within the BPINNs.
4. A new metric, namely the Bayesian Model Average Cumulative Error (BMA-CE), is introduced and used to quantify the convergence of individual tasks in the AW-HMC method.

The chapter is organized as follows: In Sect. 4.3, we review the general principles of BPINNs with a focus on the HMC sampler and characterize their failure mode in Sobolev training. Sect. 4.4 describes the proposed adaptive weighting strategy for UQ using BPINNs. We validate this strategy in a benchmark with a known analytical solution in Sect. 4.4.3 and 4.4.4. We then demonstrate the effectiveness of the proposed AW-HMC algorithm on a Lotka-Volterra inverse problem in Sect. 4.5, focusing on a multiscale inference of dynamical parameters. We then illustrate the use of AW-HMC in a real-world problem from fluid dynamics in Sect. 4.6. This particularly demonstrates, in Sect. 4.6.1, successful inpainting of incompressible stenotic blood flow from sparse and noisy data, highlighting UQ estimates consistent with the noise level and noise sensitivity. Finally, Sect. 4.6.2 considers an inverse flow problem in a complex geometry, where we infer both the flow regime and the latent pressure field from partial velocity measurements. Sect. 4.7 provides a summary of our results and highlights future challenges for real-world data assimilation inferences in porous media research.

## 4.3 From Uncertainty Quantification to Bayesian Physics-Informed Neural Networks: concepts and limitations

Real-world applications of data-driven or black-box surrogate models remain a challenging task. Predictions often need to combine prior physical knowledge, whose reliability can be questioned, with sparse and noisy data exhibiting measurement uncertainties. These real-world problems also suffer from non-linearity [173], scaling [84], and stiffness [139] issues that can considerably impact the efficiency of the usual methodologies. This needs the development of data-driven modeling strategies that robustly address these issues.

At the same time, the need to build upon Bayesian inference raises the question in the research community of ensuring trustable intervals in the estimations. This is important for quantifying uncertainties on both the underlying physical model and the measurement data, although it may be challenging in the context of stiff, multiscale, or multi-fidelity problems. Therefore, embedding UQ in the previous data-driven methodologies is essential to effectively manage real-world applications.

### 4.3.1 HMC-BPINN concepts and principles

The growing popularity of Bayesian Physics-Informed Neural Networks [171, 173, 207, 328] offers the opportunity to incorporate uncertainty quantification into PINNs standards, and benefit

from their predictive power. It features an interesting Bayesian framework that claims to handle real-world sparse and noisy data and, as well, it bestows reliability on the models together with the predictions.

The basic idea behind a BPINN is to consider each unknown, namely the neural network and inverse parameters, $\Theta$, as random variables with specific distributions instead of single parameters as for a PINN. The different sampling strategies all aim to explore the posterior distribution of $\Theta$

$$P(\Theta|\mathcal{D},\mathcal{M}) \propto P(\mathcal{D}|\Theta)P(\mathcal{M}|\Theta)P(\Theta) \tag{4.2}$$

given some measurement data $\mathcal{D}$ and a presumed model $\mathcal{M}$, rather than looking for the best approximation satisfying the optimization problem (4.1). The posterior distribution expression (4.2) is obtained from Bayes theorem and basically involves a data-fitting likelihood term $P(\mathcal{D}|\Theta)$ evaluating the distance to the experimental data, a PDE-likelihood term $P(\mathcal{M}|\Theta)$ characterizing the potential modeling discrepancies and a joint prior distribution $P(\Theta)$. These specific terms are detailed, case-by-case, in the applications, along with the different sections. Through a marginalization process, the posterior distribution (4.2) on the parameters $\Theta$ then transfers into a posterior distribution of the predictions, also called a predictive Bayesian Model Average (BMA) distribution (*e.g.* see [319]):

$$\underbrace{P(y|x,\mathcal{D},\mathcal{M})}_{\text{predictive BMA distribution}} = \int \underbrace{P(y|x,\Theta)}_{\text{prediction for }\Theta} \underbrace{P(\Theta|\mathcal{D},\mathcal{M})}_{\text{posterior}} \mathrm{d}\Theta \tag{4.3}$$

where $x$ and $y$ respectively refer to the input (*e.g.* spatial and temporal points) and output (*e.g.* field prediction) of the neural network. In this equation, the different predictions arising from all the $\Theta$ parameters sampling (4.2) are weighted by their posterior probability and averaged to provide an intrinsic UQ of the BPINN output. Overall, BPINNs introduce a Bayesian marginalization of the parameters $\Theta$ which forms a predictive distribution (4.3) of the QoI, namely the learned fields and inverse parameters.

Different approaches were developed for Bayesian inference in deep neural networks including Variational Inference [177, 322] and Markov Chain Monte Carlo methods. In fact, the later can efficiently combine with surrogate models based on deep learning approaches and, therefore, significantly speed up the sampling from the posterior distribution. A particular MCMC sampler based on Hamiltonian dynamics — the Hamiltonian Monte Carlo — has drawn increasing attention due to its ability to handle high-dimensional inference problems by taking into account the geometric properties of the posterior distribution. Betancourt explained the efficiency of HMC through a conceptual comprehension of the method [48] and theoretically demonstrated the ergodicity and convergence of the chain [50, 178]. From a numerical perspective, Yang *et al.* [328] highlighted the out-performance of BPINNs-HMC formulation on forward and inverse problems compared to its Variational Inference declination. This has established HMC as a highly effective MCMC scheme for the BPINNs, both theoretically and numerically and, therefore, as an efficient data-assimilation alternative coupling physics-based with data-driven approaches, and incorporating intrinsic uncertainty quantification.

In the following, we briefly review the basic principles of the classical BPINNs-HMC and point out their limitations, especially in the case of multi-objective and multiscale problems.

The idea of HMC is to introduce a fictive particle of successive positions and momenta $(\Theta, r)$ which follows the Hamiltonian dynamics on the frictionless negative log posterior (NLP) geometry. This requires the auxiliary variable $r$ to immerse the sampling of (4.2) into the exploration of a joint probability distribution $\pi(\Theta, r)$ in the phase space

$$\pi(\Theta, r) \sim \mathrm{e}^{-H(\Theta,r)}. \tag{4.4}$$

The latter is related to a conservative system whose the Hamiltonian energy, denoted $H(\Theta, r)$, is the sum of a potential energy $U(\Theta)$ which characterize the problem formulation and a kinetic energy $K(r)$ accounting for stochastic momentum perturbations. This relies on the particular decomposition of the Hamiltonian, where the potential and kinetic energies are chosen such that

$$\pi(\Theta, r) \propto P(\Theta|\mathcal{D},\mathcal{M})\mathcal{N}(r|0,\mathbf{M}) \tag{4.5}$$

where the momentum follows a centered multivariate Gaussian distribution, with a covariance — or mass — matrix $\mathbf{M}$ often scaled identity. The Hamiltonian of the system is thus given by

$$H(\Theta, r) = U(\Theta) + \frac{1}{2} r^T \mathbf{M}^{-1} r \tag{4.6}$$

where the potential energy directly relates to the target posterior distribution. Indeed, the potential energy definition relies on a Bayesian probabilistic formulation of the problem such that it depends on the posterior distribution (4.2) by the relation $U(\Theta) = -\ln P(\Theta|\mathcal{D}, \mathcal{M})$, which results in a multi-potential energy as detailed in the following Sect. 4.3.2. Along with this Euclidean-Gaussian assumption for the kinetic energy, this ensures that the marginal distribution of $\Theta$ provides immediate samples of the target posterior distribution

$$P(\Theta|\mathcal{D}, \mathcal{M}) \sim \mathrm{e}^{-U(\theta)} \tag{4.7}$$

since an efficient exploration of the joint distribution $\pi(\Theta, r)$ directly projects to an efficient exploration of the target distribution, as described by Betancourt [48]. The HMC sampling process alternates between deterministic steps, where we solve for the path of a frictionless particle given the Hamiltonian dynamical system

$$\begin{cases} \mathrm{d}\Theta = \mathbf{M}^{-1} r \, \mathrm{d}t \\ \mathrm{d}r = -\nabla U(\Theta) \, \mathrm{d}t, \end{cases} \tag{4.8}$$

and stochastic steps through kinetic energy perturbations, where the momentum is sampled according to the previously introduced Gaussian distribution. As Hamilton's equation (4.8) theoretically preserves the total energy of the system, each deterministic step is then constrained to a specific energy level while the stochastic steps enable us to diffuse across the energy level set for efficient exploration in the phase space. This theoretical conservation of the energy level set during the deterministic steps requires numerical schemes that ensure energy conservation.

A symplectic integrator is thus commonly used to numerically solve for the Hamiltonian dynamics (4.8): the Störmer-Verlet also known as the leapfrog method. However, these integrators are not completely free of discretization errors that may disrupt, in practice, the Hamiltonian conservation through the deterministic iterations. Hence, a correction step is finally added in the process to reduce the bias induced by these discretization errors in the numerical integration: this results in a Metropolis-Hasting criterion based on the Hamiltonian transition. This acceptance criterion tends to preserve energy by rejecting samples that lead to divergent probability transition. The exploration of the deterministic trajectories though remains sensitive to two specific hyperparameters managing the integration time: the step size $\delta t$ and the number of iterations $L$ used in the leapfrog method. Tuning these parameters can be challenging, especially if the posterior distribution presents pathological or high curvature regions [48], yielding instability, under-performance, and poor validity of the MCMC estimators. Despite the use of numerical schemes that preserve the Hamiltonian properties, a conventional HMC-BPINN can be confronted with pathological discrepancies.

To counteract these divergence effects, efforts have been put into developing strategies to either adaptively set the trajectory length $L$ [133] while preserving detailed balance condition or use standard adaptive MCMC approaches to adjust the step size $\delta t$ on the fly [49]. In this regard, one of the most popular adaptive strategies is the No-U-Turn Sampler (NUTS) from Hoffmann and Gelman [132]. Nonetheless, these divergent trajectories indicate significant bias in the MCMC estimation even if such adaptive methods may offer an alternative to overcome them. This raises the question of the validity of this adaptation when facing multi-potential energy terms that lead to significantly different geometrical behaviors or different scaling in the posterior distribution. In fact, the adaptive strategy mostly tunes the leapfrog parameters so that the most sensitive term respects the energy conservation, which may result in poorly-chosen hyper-parameters for the other potential energy terms, and then the whole posterior distribution. This reflects the limitations of such adaptive strategies that rely on adjusting the leapfrog hyperparameters.

When these divergent pathologies become prevalent, another approach suggested by Betancourt [48] is to regularize the target distribution, which can become strenuous in real-world applications and lead to additional tuning. Nevertheless, it offers a great opportunity to investigate the impact of each learning task on the overall behavior of the target distribution and paves the way for novel adaptive weighting strategies.

In the next sections, we focus particularly on the challenges arising from real-world multitasks and multiscale paradigms. We show that present BPINN methods result in major failures in these cases and we identify the main pathologies using powerful diagnostics based on these divergent probability transitions.

### 4.3.2 The multi-objective problem paradigm

As for the issue of the multi-objective optimization problem in a PINN, sampling of the target posterior distribution (4.2) arising from a direct or inverse problem requires the use of a multi-potential energy term $U(\Theta)$. Furthermore, in real-world applications, we have to deal with sparse and noisy measurements whose fidelity can also cover different scales: this is the case of multi-fidelity problems with multi-source data [176, 199].

For sake of generality, we introduce a spatio-temporal domain $Q = \Omega \times \mathcal{T}$ with $\Omega \subset \mathbb{R}^n$, $n = 1, 2, 3$ and we assume a PDE system in the following form:

$$\begin{cases} \mathcal{F}(u(t,x),\ \mathcal{P}_{\text{inv}}) &= 0, \qquad (t,x) \in Q \\ \mathcal{H}(u(t,x),\ \mathcal{P}_{\text{inv}}) &= 0, \qquad (t,x) \in Q \\ \mathcal{B}(u(t,x),\ \mathcal{P}_{\text{inv}}) &= 0, \qquad (t,x) \in Q^{\partial} := \partial\Omega \times \mathcal{T} \\ \mathcal{I}(u(t,x),\ \mathcal{P}_{\text{inv}}) &= 0, \qquad (t,x) \in Q^{I} := \Omega \times \mathcal{T}_0 \end{cases} \tag{4.9}$$

where $u$ is the principal unknown, $\mathcal{F}$ the main differential equation (*e.g.* the Navier-Stokes equation), $\mathcal{H}$ an additional constraint (*e.g.* incompressibility condition), $\mathcal{B}$ and $\mathcal{I}$ the boundary and initial conditions respectively, and $\mathcal{P}_{\text{inv}}$ the PDE model parameters, either known or inferred. Some partial measurements of the solution field $u$ may also be available in a subset $Q^u \subset Q$. Such a continuous description of the spatio-temporal domain is then discretized to enable the selection of the training dataset, which is used in BPINNs sampling.

We first define the dataset $\mathcal{D}$ of training data, as a subset of $\overline{Q}$, which is decomposed into $\mathcal{D} = \mathcal{D}^Q \cup \mathcal{D}^{\partial} \cup \mathcal{D}^I \cup \mathcal{D}^u$ and includes scattered and noisy measurements sampled in their respective sets $Q$, $Q^{\partial}$, $Q^I$, and $Q^u$. Regarding data corruption, we consider independent Gaussian noise for the sparse observations on $u$, such that $\mathcal{D}^u$ is defined as

$$\mathcal{D}^u = \{(t_i, x_i) \in Q^u, \quad i = 1...N^u \quad \text{with} \quad u_i := u(t_i, x_i) + \xi_u(t_i, x_i)\} \tag{4.10}$$

where the noise $\xi_u \sim \mathcal{N}(0, \sigma_u^2 I)$ and the standard deviation $\sigma_u$ might be estimated from the sensor fidelity, if accessible. The neural network component of the BPINN then provides a surrogate model of $u$ denoted $u_\Theta$ for each sample of the parameters $\Theta = \{\theta, \mathcal{P}_{\text{inv}}\}$, whose prior distribution is referred to as $P(\Theta)$. The latter takes into account both the priors on the neural network parameters $\theta$, which are assumed to be centered and independent Gaussian distributions, and the priors on the model parameters $\mathcal{P}_{\text{inv}}$, so that $P(\Theta) = P(\theta)P(\mathcal{P}_{\text{inv}})$ under the independence condition. In the case of a forward problem, where the PDE model parameters are prescribed, the prior distribution reduces to $P(\theta)$. When some measurements of the unknown are available, meaning $\mathcal{D}^u$ is not an empty set, which is the case in inverse or inpainting problems, then the surrogate model $u_\Theta$ should satisfy a data-fitting likelihood term in the Bayesian framework. This consists in quantifying, over the set $\mathcal{D}^u$, the fit between the neural network prediction and the training data defined by:

$$P(\mathcal{D}^u|\Theta) \propto \prod_{i=1}^{N^u} \exp\left(\frac{-\left(u_\Theta(t_i, x_i) - u_i\right)^2}{2\sigma_u^2}\right). \tag{4.11}$$

Similarly, the boundary conditions of the model output are imposed on the set $\mathcal{D}^{\partial}$

$$\mathcal{D}^{\partial} = \left\{(t_i, x_i) \in Q^{\partial} \quad i = 1...N^{\partial} \quad \text{with} \quad \mathcal{B}(u_i) := \mathcal{B}(u(t_i, x_i)) + \xi_b(t_i, x_i)\right\} \tag{4.12}$$

by satisfying the following boundary-likelihood term

$$P(\mathcal{D}^{\partial}|\Theta) \propto \prod_{i=1}^{N^{\partial}} \exp\left(\frac{-\left(\mathcal{B}(u_\Theta(t_i,x_i)) - \mathcal{B}(u_i)\right)^2}{2\sigma_b^2}\right). \tag{4.13}$$

The noise sensitivity on the boundary condition term is also characterized by independent Gaussian distributions in the sense that $\xi_b \sim \mathcal{N}(0,\sigma_b^2 I)$ where the standard deviation $\sigma_b$ needs to be estimated. Such a distinction between $\xi_u$ and $\xi_b$ is prescribed since there is no guarantee that the data corruption is uniform: in fact, the measurement distribution variances can differ locally when facing heteroscedastic noise. This is the case in geosciences, where data-driven modeling based on X-Ray microtomography images require special attention on this boundary noise estimation $\xi_b$. This is mainly due to the artifact limitations (*e.g.* partial volume effect, edge-enhancement) that tend to enhance the blurring effects at the material interface and therefore impact the quantification of the medium effective properties, such as the permeability and micro-porosity [16, 238]. The same holds for the initial condition with potentially a different sensitivity $\xi_i$. In a BPINN, the previous data-fitting terms are complemented with physical principles that regularize the neural network predictions, given the PDE system (4.9).

Concerning the PDE-likelihood term, the $\mathcal{D}^Q$ dataset is defined as the training points on which we force the PDE and the additional physical constraint to be satisfied by the surrogate modeling:

$$\begin{aligned}\mathcal{D}^Q = \big\{(t_i,x_i) \in Q, \quad i = 1...N^Q \quad \text{with} \quad \mathcal{F}(u_\Theta(t_i,x_i)) = \xi_f(t_i,x_i)\\ \text{and} \quad \mathcal{H}(u_\Theta(t_i,x_i)) = \xi_h(t_i,x_i)\big\}\end{aligned} \tag{4.14}$$

with $\xi_f$ and $\xi_h$ standing for the model uncertainty in both equations, which are usually unknown and can easily lead to physical model misspecification. According to these notations, a forward problem consists in $\mathcal{D}^u = \varnothing$ and $\mathcal{P}_{\text{inv}}$ is known to perform a direct prediction of the field $u_\Theta$ on $Q$ based only on the PDE physical assumptions. On the contrary, an inverse problem aims to infer $\mathcal{P}_{\text{inv}}$ using together the PDE model with the partial and noisy information $\mathcal{D}^u$ of the predictive field $u$. Finally, an inpainting problem relies on these partial measurements to complement and recover some missing information on the predictive field, in addition to the PDE-based priors.

Finally, the target posterior distribution of $\Theta$, given by equation (4.2), is decomposed according to the Bayes rule, into a sequence of multitask likelihood terms — involving data-fitting and PDE likelihood — and the priors:

$$P(\Theta|\mathcal{D},\mathcal{M}) \propto P(\mathcal{D}^u|\Theta)P(\mathcal{D}^{\partial}|\Theta)P(\mathcal{D}^I|\Theta)P(\mathcal{D}^Q,\mathcal{F}|\Theta)P(\mathcal{D}^Q,\mathcal{H}|\Theta)P(\theta)P(\mathcal{P}_{\text{inv}}) \tag{4.15}$$

which results, for the HMC sampler, in the multi-potential energy

$$\begin{aligned}U(\Theta) = &\frac{\|u_\Theta - u\|^2_{\mathcal{D}^u}}{2\sigma_u^2} + \frac{\|\mathcal{B}(u_\Theta) - \mathcal{B}(u)\|^2_{\mathcal{D}^{\partial}}}{2\sigma_b^2} + \frac{\|\mathcal{I}(u_\Theta) - \mathcal{I}(u)\|^2_{\mathcal{D}^I}}{2\sigma_i^2}\\ &+ \frac{\|\mathcal{F}(u_\Theta)\|^2_{\mathcal{D}^Q}}{2\sigma_f^2} + \frac{\|\mathcal{H}(u_\Theta)\|^2_{\mathcal{D}^Q}}{2\sigma_h^2} + \frac{\|\theta\|^2_{\mathbb{R}^d}}{2\sigma_\theta^2} + \frac{\|\mathcal{P}_{\text{inv}} - \mu_{\mathcal{P}}\|^2_{\mathbb{R}^p}}{2\sigma_{\mathcal{P}}^2}\end{aligned} \tag{4.16}$$

according to equation (4.7). The notation $\|\cdot\|$ refers to either the RMS norm — inherited from the functional $\mathbb{L}^2$-norm on the open set $Q$ — for the log-likelihood terms or to the usual Euclidean norm for the log-prior terms. In addition, the multi-potential (4.16) is written here, in a general framework, based on the prior assumptions $P(\theta) \sim \mathcal{N}(0,\sigma_\theta^2 I_d)$ and $P(\mathcal{P}_{\text{inv}}) \sim \mathcal{N}(\mu_{\mathcal{P}},\sigma_{\mathcal{P}}^2 I_p)$. We note that the log-prior term on $\theta$ can be regarded as a $\mathbb{L}^2$-regularization in the equivalent constrained optimization problem. Nonetheless, suitable selection of these prior distributions — hence appropriate tuning of the parameters $\sigma_\theta$, $\mu_{\mathcal{P}}$, and $\sigma_{\mathcal{P}}$ — is usually not straightforward and is time-consuming. Overall, equation (4.16) highlights that, even in a simple problem setup, a BPINN may face a potential energy term that closely resembles a weighted multi-objective loss appearing in a PINN. This multi-potential energy results, according to equation (4.7), in a multitask weighted posterior distribution for which an appropriate adaptive weighting strategy is critical.

Therefore, the main challenge is to sample near the Pareto-optimal solution such that the BPINNs provide efficient and reliable prediction and UQ. Otherwise, the risk is that the samples obtained gravitate around a local minimum, corresponding to one of the multi-potential terms at the cost of the others. The present work focuses on how to estimate a well-fitted weighted posterior distribution that concentrates on the region of the highest posterior probability. The latter, localized in the Pareto front neighborhood, should ensure balanced conditions for all the different terms in equation (4.16) and therefore provide robust Bayesian inference for multitask problems with multiscale or multi-objective issues. Effectively dealing with multitask Bayesian inference problems is a distinct concern from capturing multi-modal distributions. In this chapter, we intend to address the first issue, while the second one is out of consideration. This comes from the observation that the HMC formulation, which serves as a basis of the present work, is prone to struggle with multi-mode scenarios while having excellent performances in sampling single-mode distributions. The main reason is that HMC relies on local gradient information that may ignore other isolated modes [191]. Efficiently sampling from multi-modal distributions requires other samplers. These alternatives include, for instance, Variational Hybrid Monte Carlo [292], wormhole Hamiltonian Monte Carlo [155], and augmented Markov Chain Monte Carlo with normalizing flow methods for adapting the proposal distribution (transition kernels) during sampling [122], but this is beyond the scope of this work. A way to handle likely multi-modal distributions with the HMC sampler is to consider different initializations of the neural network parameters or inverse parameters in order to incorporate sampling variability. This chapter focuses on providing a robust sampling strategy for multitask weighted posterior distributions in single-mode scenarios, with potentially multiscale inference in the inverse parameters.

Secondly, while the standard deviations $\sigma_\bullet$ in (4.16) are critical parameters to select and are related to the uncertainties on the inherent tasks, most of the authors either assign them a given value or train them as additional hyperparameters [173, 207, 291]. This can lead to highly biased predictions, especially when setting the PDE-residual standard deviations $\sigma_f$ and $\sigma_h$ which introduce strong priors on the model adequacy. Recently Psaros *et al.* [249] discussed, *inter alia*, alternatives generalizing the adjustment of some of these parameters — mainly the data-fitting standard deviations — in the context of unknown and heteroscedastic noise distributions. They either rely on *offline learning* at the cost of a pre-trained GAN or *online learning* of the weights based on additional parameter training. In particular, the number of these additional parameters may increase drastically when considering location-dependent variances, as suggested in [249], for realistic applications and consequently suffer from computational costs. The open question remains on how to deal with such unknown (homo- or hetero-scedastic) noise distributions without adding computational complexity by learning additional hyperparameters. Finally, although the question of physical model misspecification was pointed out in the total uncertainty quantification, the latter has not been addressed in [249] when misleading model uncertainty is assumed on the physical constraints $\mathcal{F}$ and $\mathcal{H}$. As a result, the issue of not introducing strong priors on the model adequacy by hand-tuning the hyperparameters $\sigma_f$ and $\sigma_h$, usually unknown or prescribed, is still a challenging task. Therefore, we consider the question of how to adaptively set the weights in multitask Bayesian inference problems such that we do not rely on a-priori manual calibration of the noise magnitude, task scaling, or model adequacy.

In view of this, we test in the next Sect. 4.3.3 the robustness of the usual BPINNs-HMC approach, as introduced in Sect. 4.3.1, on a test case demonstrating the issues arising from the multi-objective and multiscale nature of the sampling using Sobolev training of neural networks.

### 4.3.3 Sobolev training for BPINNs failure mode

Sobolev training is a special case of multi-objective BPINN sampling that likely leads to stiff learning due to the disparate scales involved [187]. Nevertheless, it is commonly used in the machine learning community to improve the prediction efficiency and generalization of neural networks, by adding information about the target function derivatives to the loss or its equivalent potential energy [94, 277, 308, 335]. This special training provides a baseline for testing the robustness of the present BPINNs-HMC method against the failure mode of vanishing task-specific gradi-

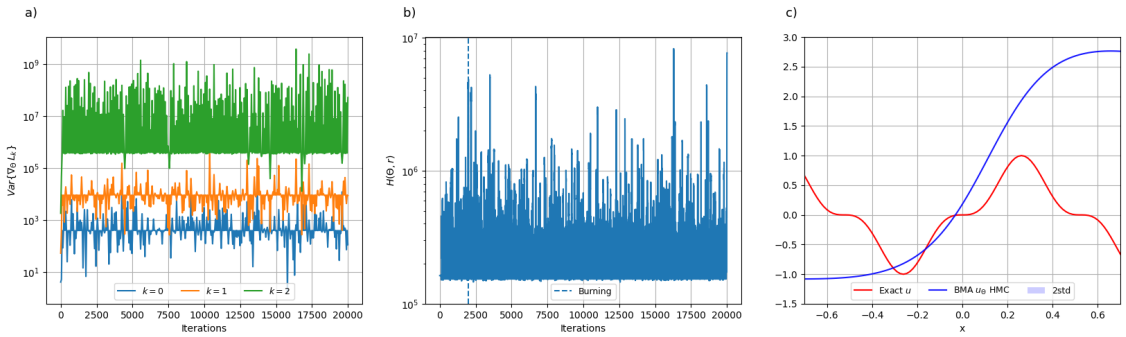


**Figure 4.1: HMC uniform-weighting failure mode for Sobolev training up to second-order derivatives:** a) Variances of the effective gradient $\nabla_\Theta L_k$ distributions ($k = 0, 1, 2$), plotted with respect to the ($N_s \times L$) HMC iterations, showing strong imbalances between the tasks. b) Non-conservative Hamiltonian that illustrates the resulting instabilities issues. c) Extremely poor approximation of the function and non-existent uncertainty estimates due to the massive rejection.

ents [187]. It also offers the opportunity to benchmark against the analytically $\varepsilon$-optimal weights that are known for Sobolev multi-objective optimization [187].

The BPINNs-HMC sampling is tested here on a Sobolev regression task, which means the dataset is restricted to $\mathcal{D} = \mathcal{D}^u$ involving measurements of a function and its derivatives $D_x^k$, $k \geq 1$ up to order $K$, such that the target posterior distribution is

$$P(\Theta|\mathcal{D}) \propto \prod_{k=0}^{K} P(\mathcal{D}^u, D_x^k u|\Theta) P(\Theta) \tag{4.17}$$

and the potential energy hence has the general form

$$U(\Theta) = \sum_{k=0}^{K} \left[ \frac{\lambda_k}{2\sigma_k^2} \|D_x^k u_\Theta - D_x^k u\|^2 \right] + \frac{\lambda_{K+1}}{2\sigma_{K+1}^2} \|\Theta\|^2 := \sum_{k=0}^{K+1} \lambda_k \mathcal{L}_k(\Theta) \tag{4.18}$$

where $L_k = \lambda_k \mathcal{L}_k$ refers to the weighted $k^{th}$ objective term, with $\lambda_k$ some positive weighting parameters to define (see Sect. 4.4.1). In this section, we use only a uniform weighting strategy, with $\lambda_k = 1, \forall k$, which corresponds to the classical BPINNs-HMC formulation. For sake of readability, equation (4.18) gathers the log-prior terms of the neural network and inverse parameters, assuming they all have the same prior distribution.

We first introduce a 1D Sobolev training up to second-order derivatives, with a test function $u(x) = \sin^3(\omega x)$ defined on the spatial domain $\Omega = [-0.7, 0.7]$ for $\omega = 6$. We use 100 training points, set the leapfrog parameters $L = 100$ and $\delta t = 1\text{e}{-3}$ for the number of iterations and time step respectively, and perform $N_s = 200$ sampling iterations. We also restrict the test to a function approximation problem so that subsequently $\Theta$ refers only to the neural network parameters. In the following and unless otherwise indicated, all the $\sigma_k$ are equal to one since in practice we do not have access to the values of these parameters for the derivatives or residual PDE terms, but rather to the observation noise on the data field $u$ only, if available.

Similarly to PINNs , this test case with uniform weights $\lambda_k$ leads to imbalanced gradient variances between the different objective terms. In particular, the higher-order derivatives present dominant gradient variances that contribute to the vanishing of the other tasks and lead to biased exploration of the posterior distribution. In Figure 4.1a we see that the term $\text{Var}\{\nabla_\Theta L_2\}$ corresponding to the higher-order derivative quickly develops two orders of magnitude greater than the other effective gradient variances. In addition to inefficient exploration of the Pareto front, we also face instability issues, generated by the highest order derivative terms, that result in a lack of conservation of the Hamiltonian along the leapfrog trajectories (see Figure 4.1b). The HMC sampler with uniform weighting strategy fails on this test case, resulting in poor prediction of the surrogate model $u_\theta$ (see Figure 4.1c). Indeed, none of the proposed samples are accepted according to the Metropolis-Hasting criterion. Hence, there are neither uncertainty estimates nor adjustments of the

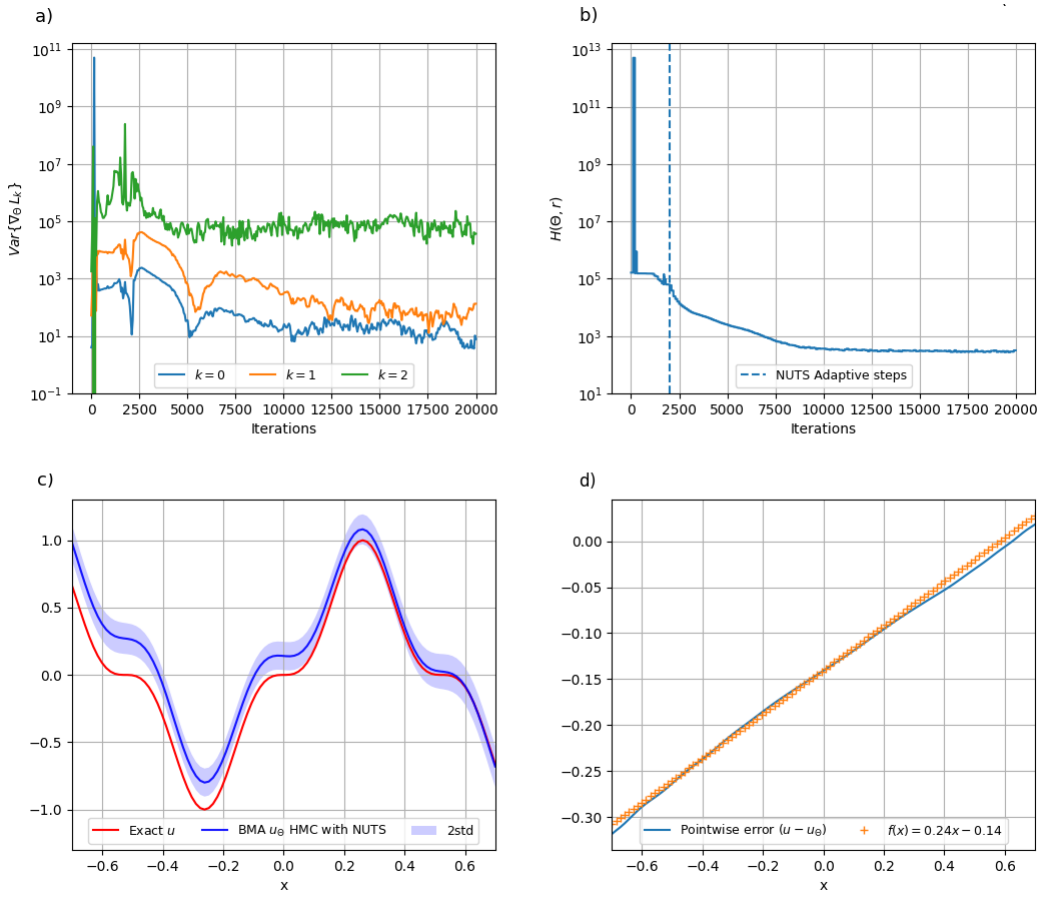


**Figure 4.2: Failure mode of NUTS step-size adaptation in Sobolev training up to second order derivatives:** a) Variances of the effective gradient $\nabla_\Theta L_k$ distributions, showing task imbalances. b) Hamiltonian evolution along the sampling, resulting in a weak exploration of the energy levels. The vertical dotted line delimits the number of adaptive steps in the NUTS sampler. c) BMA signal reconstruction with its uncertainty. d) Pointwise error between the surrogate BMA reconstruction $u_\Theta$ and the function $u$, highlighting the linear deviation of $u_\Theta$ and biased inference of the distinct tasks.

predictive BMA distribution. Both are solely based on the surrogate model corresponding to the prior distributions of the neural network parameters (Figure 4.1c). As specified in Sect. 4.3.1, such divergence pathologies on the classical HMC with uniform weighting are powerful diagnostics of bias in the resulting estimators and raise suspicions about the validity of the latter.

An alternative to counteract these effects consists in reducing the time step $\delta t$ to balance the order of magnitude of the derivative terms and improve the Metropolis-Hasting acceptance rate of the BPINNs-HMC. However, a small time step within the leapfrog iterations is more likely to generate pathological random walk behaviors or biased sampling [48, 132]. To this aim, we attempt an adaptive strategy by using the No-U-Turn sampler (NUTS) with step-size adaptation, as detailed in Algorithm 5 from Hoffmann and Gelman [132] and implemented in the Python Open Source package Hamiltorch [84]. We consider the same exact set of leapfrog parameters as previously — in order to comply with the same assumptions — and we impose $N = 20$ adaptive steps that lead to a final adapted time step of $\delta t = 1.29\text{e}{-4}$. In this case, we again reached a configuration where we were not efficiently exploring the Pareto front, as evidenced by the variances of the effective gradients in Figure 4.2a. This resulted in a better approximation of the second derivative compared to the signal itself and demonstrated biased sampling in the sense that the signal $u$ is determined up to a linear function due to the prevalence of the higher derivative term. This linear deviation is also shown in Figure 4.2d. This confirms that the NUTS time-step adaptation focuses rather on the prevailing conservation of the higher-order derivative which induced the stiffness.

In short, even a simple 1D Sobolev training with trivial uniform weights induces major failure of the classical BPINNs-HMC approaches because of the sensitivity of the posterior distribution to the higher-order derivatives that generate instabilities. Consequently, such divergence in the Hamiltonian conservation renders the sampling approach inoperative. Moreover, the alternatives ensuring the Hamiltonian conservation are ineffective because they face either inefficient exploration of the energy levels or a strong imbalance in the multitask and multiscale sampling. This suggests that the Hamiltonian Markov chain cannot adequately explore the Pareto front of the target distribution resulting from this potential energy and that strong imbalanced conditions cannot be overcome with the usual methodologies.

The purpose is therefore to develop a strategy to provide balanced conditions between the different tasks, independently of their scales, by looking for an appropriate weighting formulation. This approach is essential regardless of the usual HMC concerns about the adaptive settings of the leapfrog parameters and presents the advantage of reducing the instabilities without needlessly decreasing the time step.

## 4.4 An Adaptive Weighting Strategy for Unbiased Uncertainty Quantification in BPINNs

Conventional BPINN formulations exhibit limitations regarding multi-objective inferences, such as stability and stiffness issues, pathological conflicts between tasks, and biased exploration of the Pareto-optimal front. These problems cannot be tackled merely by adaptively setting the leapfrog parameters, as in the NUTS sampler, nor by hand-tuning the standard deviations $\sigma_k$, which introduces additional computational costs or energy waste. We, therefore, investigate another adaptive approach that focuses instead on the direct regularization of the target distribution: it aims to balance task weighting by automatically adapting the critical $\sigma_k$ parameters.

### 4.4.1 An Inverse Dirichlet Adaptive Weighting algorithm: AW-HMC

The development of a new alternative considering the limits of the HMC-BPINN approach — previously discussed in Sect. 4.3 — becomes crucial, especially in the case of complex multi-objective problems arising from real-world data. This strategy must address the main pathologies identified by: 1) ensuring the exploration of the Pareto front of the target posterior distribution, 2) managing the scaling sensitivity of the different terms, and 3) controlling the Hamiltonian instabilities.

Independently of these pathological considerations, there remains the issue of setting the critical $\sigma_k$ parameters, particularly when the level of noise on the data and the confidence in the PDE model are not prior knowledge. While manual tuning of these parameters is still commonplace, we could rely on the weight adaptations to implicitly determine the noise and inherent task uncertainties rather than introduce strong priors on the model adequacy that may lead to misleading predictions. Indeed, the weights $\lambda_k$ involved in the following general expression of the multi-potential energy (4.16):

$$U(\Theta) = \sum_{k=0}^{K} \lambda_k \mathcal{L}_k(\Theta) + \lambda_{K+1} \|\Theta\|^2 \tag{4.19}$$

are positive parameters integrating various sources of uncertainties. In this sense, the deterministic PDE model is completed by stochastic representations of the model discrepancy, and the data-fitting likelihood is itself supplemented by stochastic modeling of the experimental noise, both affecting the critical parameters $\lambda_k$. This intends to capture and estimate the various sources of uncertainties whether aleatoric — arising from variability or randomness in the observations like sensor noise — or epistemic — caused by imperfect modeling hypothesis or ignorance in the model adequacy. Therefore, we suggest considering automatic management of these uncertainties based on the appropriate and adaptive setting of the critical weighting parameters.

In order to fulfill all these requirements, we consider an Inverse-Dirichlet based approach that has demonstrated its effectiveness in the PINNs framework when dealing with balanced training and multiscale modeling [187]. It relies on adjusting the weights based on the variances of the loss term gradients, which can be interpreted as a training uncertainty with respect to the main descent direction in a high-dimensional multi-objective optimization problem. This strategy also offers considerable improvement in convergence over conventional training and avoids the vanishing of specific tasks.

The idea of developing an Inverse Dirichlet adaptively weighted algorithm for BPINNs is to incorporate such training uncertainties on the different tasks within the Bayesian framework so that it can simultaneously take into account the noise, the model adequacy and the sensitivity of the tasks, all while ensuring Pareto front exploration. Therefore, we are trying to determine the positive weighting parameters $\lambda_k$, $k = 0, ..., K$ in such a way that the weighted gradient

$$\nabla_\Theta L_k = \lambda_k \nabla_\Theta \mathcal{L}_k \tag{4.20}$$

distributions of the potential energy terms have balanced variances. We propose to ensure gradient distributions with the same variance

$$\gamma^2 := \mathrm{Var}\{\lambda_k \nabla_\Theta \mathcal{L}_k\} \simeq \min_{t=0..K} (\mathrm{Var}\{\nabla_\Theta \mathcal{L}_t\}), \quad \forall k = 0, ..., K \tag{4.21}$$

by setting the weights on an Inverse-Dirichlet based approach:

$$\lambda_k = \left( \frac{\min\limits_{t=0..K} \left(\mathrm{Var}\{\nabla_\Theta \mathcal{L}_t\}\right)}{\mathrm{Var}\{\nabla_\Theta \mathcal{L}_k\}} \right)^{1/2} = \left( \frac{\gamma^2}{\mathrm{Var}\{\nabla_\Theta \mathcal{L}_k\}} \right)^{1/2} \tag{4.22}$$

such that

$$\lambda_k \mathcal{N}(\mu_k, \mathrm{Var}\{\nabla_\Theta \mathcal{L}_k\}) = \left( \frac{\gamma^2}{\mathrm{Var}\{\nabla_\Theta \mathcal{L}_k\}} \right)^{1/2} \mathcal{N}(\mu_k, \mathrm{Var}\{\nabla_\Theta \mathcal{L}_k\}) = \mathcal{N}(\mu_k, \gamma^2). \tag{4.23}$$

Note that we do not discuss here the case of $\lambda_{K+1}$ corresponding to the prior $P(\Theta)$, since the log-prior term acts rather as a $\mathbb{L}^2$-regularization in the equivalent constrained optimization problem, such that the weight balancing approach focuses essentially on the log-likelihood terms of the potential energy. In fact, the sampling should enable us to efficiently explore the Pareto front corresponding to balanced conditions between the data-fitting and the different PDE-based likelihood terms. On the contrary, we do not want to rely on a non-informative prior to achieve task balancing, so we impose the following upper bound

$$\mathrm{Var}\{\lambda_{K+1} \nabla_\Theta \mathcal{L}_{K+1}\} \leq \gamma^2, \tag{4.24}$$

which can be achieved with setting $\lambda_{K+1} \leq \sigma_{K+1}$, related to the assumption on the prior $P(\Theta) \sim \mathcal{N}(0, \sigma_{K+1}^2 I)$. This comes from the observation that

$$\lambda_{K+1} \nabla_\Theta \mathcal{L}_{K+1}(\Theta^{t_\tau}) = \frac{\lambda_{K+1}}{\sigma_{K+1}^2} \Theta^{t_\tau} \tag{4.25}$$

such that

$$\mathrm{Var}\{\lambda_{K+1} \nabla_\Theta \mathcal{L}_{K+1}(\Theta^{t_\tau})\} = \frac{\lambda_{K+1}^2}{\sigma_{K+1}^4} \mathrm{Var}\{\Theta^{t_\tau}\} \leqslant \frac{1}{\sigma_{K+1}^2} \mathrm{Var}\{\Theta^{t_\tau}\} \tag{4.26}$$

with $\Theta^{t_\tau}$ the set of parameters sampled at iteration $\tau$. The latter upper bound also provides a dispersion indicator between the posterior variance of $\Theta$ and its prior distribution, that can be used to set the value of $\sigma_{K+1}$ given $\gamma^2$.

We investigate on-the-way methods to deal with the BPINNs-HMC failure mode, so that the weight adaptation strategy from equation (4.22) depends on the sampling iterations $\tau$. This results in a modified Hamiltonian Monte Carlo, denoted Adaptively Weighted Hamiltonian Monte Carlo

(AW-HMC) which is detailed in Algorithm 1. The weighting strategy is carried on until a number of adaptive iterations $N$, potentially different from the usual burn-in steps $N_{\text{burn}}$. It assumes that $N \leq N_{\text{burn}}$, and enables us to reach a weighted posterior distribution well-suited to the exploration of the Pareto front. Indeed, we aim to adaptively estimate a well-fitted posterior distribution that concentrates on the high probability-density region. This is achieved during the adaptive steps by leveraging gradient information of the different tasks and their respective sensitivities through variance-based weighting. Once the adaptive procedure converges, the weights stabilize, and we effectively sample from a well-fitted target distribution that mainly explores the region of highest posterior probability, characterized by the Pareto front neighborhood. Finite adaptation preserves ergodicity and asymptotic convergence of the chain while keeping $N \leq N_{\text{burn}}$ ensures the posterior distribution is drawn from the same weighted potential energy. In practice, the a-priori burn-in phase is closely linked to the number of adaptive steps by taking $N_{\text{burn}} = N$. We also introduce the notation $H_{\lambda_\tau}(\Theta, r)$ for the weighted Hamiltonian

$$H_{\lambda_\tau}(\Theta, r) = \sum_{k=0}^{K+1} \lambda_k(\tau)\mathcal{L}_k(\Theta) + \frac{1}{2} r^T \mathbf{M}^{-1} r \tag{4.27}$$

which defines the new transition probability for the Metropolis-Hasting acceptance criterion.

The question remains how to set the number of adaptive steps $N$. This is closely related to characterizing the convergence of the weighted posterior distribution toward the neighborhood where the posterior density is maximized, that is the Pareto front. To decide when to stop weights adaptation, we define a systematic stopping criterion based on the evolution of the Hamiltonian energy in equation (4.27).

In the following, we detail this criterion for stopping the adaptation procedure and activating the sampling from the weighted target distribution with balanced tasks, which mainly explores the region of the highest posterior probability. Our method for stopping weights adaptation is to reach either a maximum number of iterations $N_{\max}$ or ensuring the local variation of the Hamiltonian function, denoted $\overline{S}_\tau$, to be below a given threshold $S_{\min}$. Indeed, if there is no significant variation, there is no more evolution of weights and task values, and therefore adaptation can be stopped. This local variation is defined by the slope of the Hamiltonian function, which is computed as the averaged linear regression of its early history due to the strongly stochastic nature of the Hamiltonian transitions. Therefore, the significant variation in the Hamiltonian evolution is based on the locally averaged best slopes of the Hamiltonian function, whose statistical series is denoted $H_i$ related to the number of sampling iterations $X_i = i$. These best slopes $S_\tau$ are first computed by linear regression on a short sampling history, corresponding to the last $p_{\text{slope}}$ values of the Hamiltonian function (*e.g.* see the light colors curves on Fig 4.4):

$$S_\tau = \frac{\text{Cov}\left(\{H_i\}_{i=\tau-p_{\text{slope}}+1}^{\tau}, \{X_i\}_{i=\tau-p_{\text{slope}}+1}^{\tau}\right)}{\text{Var}\left(\{X_i\}_{i=\tau-p_{\text{slope}}+1}^{\tau}\right)}. \tag{4.28}$$

Then, these slopes are themselves denoised by local averaging on the last $p_{\text{mean}}$ values (*e.g.* see the solid colors curves on Fig 4.4) resulting in the following final expression of $\overline{S}_\tau$:

$$\overline{S}_\tau = \frac{1}{p_{\text{mean}}} \sum_{i=\tau-p_{\text{mean}}+1}^{\tau} S_i. \tag{4.29}$$

In practice, we choose $p_{\text{slope}} = p_{\text{mean}} = 4$. The effective number of adaptive steps $N$ is then the minimum value between $N_{\max}$ and the number of samplings $\tau$ required to reach the threshold $S_{\min}$. In addition to this criterion, the user must check that there are effective lower bounds on the weights (*e.g.* Figure 4.7 in Sobolev training) to verify that there is no singular behavior. Indeed in a singular case, the objective and the Hamiltonian could decrease solely by reducing of the weights to 0. This check is especially important since we allow auto-adaptation of weights. Applications of this criteria are detailed in Sect. 4.4.3 and Sect. 4.5.1 on the Sobolev benchmarks and Lotka-Voterra inverse problem.

**Algorithm 1:** Adaptively Weighted Hamiltonian Monte Carlo (AW-HMC)

**Input:** Initial $\Theta^{t_0}$, $N_s$ number of samples, $L$ number of leapfrog steps, $\delta t$ leapfrog step size, $N_{\max}$ maximum number of adaptive iterations, $N_{\text{burn}}$ burn-in steps and $\mathbf{M}$ the mass matrix.

*Sampling procedure:*
**for** $\tau = 1...N_s$ **do**
  Sample $r^{t_{\tau-1}} \sim \mathcal{N}(0, \mathbf{M})$;
  Set $(\Theta_0, r_0) \leftarrow (\Theta^{t_{\tau-1}}, r^{t_{\tau-1}})$;
  *Weights adaptation:*
  **if** $(\tau \leq N_{\max})$ **and** $(\overline{S}_\tau \geq S_{\min})$ **then**
    Compute $\lambda_k(\tau) = \left( \dfrac{\min\limits_{j=0..K} (\text{Var}\{\nabla_\Theta \mathcal{L}_j(\Theta_0)\})}{\text{Var}\{\nabla_\Theta \mathcal{L}_k(\Theta_0)\}} \right)^{1/2} \quad \forall k = 0..K$
    and $\lambda_{K+1}(\tau) = 1$;
  **else**
    $\lambda_k(\tau) = \lambda_k(\tau - 1) \quad \forall k = 0..K \quad$ and $\quad \lambda_{K+1}(\tau) = 1$
  **end**
  *Leapfrog:*
  **for** $i = 0...L-1$ **do**
    $r_i \leftarrow r_i - \dfrac{\delta t}{2} \sum\limits_{k=0}^{K+1} \lambda_k(\tau) \nabla_\Theta \mathcal{L}_k(\Theta_i)$;
    $\Theta_{i+1} \leftarrow \Theta_i + \delta t \mathbf{M}^{-1} r_i$;
    $r_{i+1} \leftarrow r_i - \dfrac{\delta t}{2} \sum\limits_{k=0}^{K+1} \lambda_k(\tau) \nabla_\Theta \mathcal{L}_k(\Theta_{i+1})$;
  **end**
  *Metropolis-Hastings:*
  Sample $p \sim \mathcal{U}(0, 1)$;
  Compute $\alpha = \min(1, \exp(H_{\lambda_\tau}(\Theta_0, r_0) - H_{\lambda_\tau}(\Theta_L, r_L))$ using (4.27);
  **if** $p \leqslant \alpha$ **then**
    $\Theta^{t_\tau} = \Theta_L$;
  **else**
    $\Theta^{t_\tau} = \Theta_0$;
  **end**
  Collect the samples after burn-in : $\left\{\Theta^{t_i}\right\}_{i=N_{\text{burn}}}^{N_s}$
**end**

Moreover, the present Inverse-Dirichlet balancing of the target distribution, based on the minimum variance of the gradients given by equation (4.22), can be interpreted as adjusting the weights with respect to the most likely or the least sensitive term of the multi-potential energy. It therefore offers the advantage of improving the convergence of the BPINNs toward the Pareto-optimal solution and also enhances the reliability of the uncertainty quantification of the output, whose samples are drawn from the Pareto front. Indeed, this weighting strategy induces an automatic increase in the uncertainty of the least likely task by adaptively adjusting the $\lambda$ parameters. Such observations arise from the development of upper bounds for each of the gradient variances, as detailed in the following Sect. 4.4.2, which involves prediction errors and PDE residuals, as well as sensitivity terms characterizing the variability of the mean gradient descent directions for each task. In light of this, we were able to provide an upper bound on the joint variance $\gamma^2$ which is developed in equation (4.36) in a basic and general perspective.

Last but not least, the Inverse-Dirichlet based adaptive weighting relieves us from an unrea-

sonable decrease in the time step, which no longer has to meet all the stiff scaling requirements to ensure Hamiltonian conservation. This approach then renders the sampling free of excessive tuning adaptation of the leapfrog hyperparameters $\delta t$ and $L$. In addition, this prevents pathological random-walk or divergence behaviors in the sampling since it enables the use of optimal integration time, both in terms of convergence rate and adequacy of the time step to the distinct learning tasks. Overall, our novel AW-HMC strategy overcomes the limitations of the usual BPINN methodologies, and we demonstrate its effectiveness in robustly addressing Bayesian Inference problems throughout the following sections.

### 4.4.2 Upper bound on the Inverse-Dirichlet weighting variance

The Inverse-Dirichlet Adaptively Weighted HMC algorithm, developed in Sect. 4.4.1, guarantees that the gradients of the multi-potential energy terms have balanced distributions throughout the sampling, with their joint variance $\gamma^2$ defined in equation (4.21). In this section, we use a general case to demonstrate that $\gamma^2$ is upper bound and controlled by a reliability criterion which depends on the prediction errors or PDE residuals, the dispersion of their mean variability with respect to $\Theta$ and the setting of the $\sigma_k$ values.

This first states the necessity to adequately set the $\sigma_k$ parameters to avoid biased and imbalanced conditions on task gradient distributions, since these parameters critically and arbitrarily affect the gradient distributions control. This also highlights that manual tuning of the $\sigma_k$ values may be an extremely sensitive task, difficult to achieve in practice. Therefore, in all the applications presented in this chapter, we chose to set these parameters uniformly and instead rely on the $\lambda$ automatic adjustment to ensure, *inter alia*, the efficient exploration of the Pareto front. It avoids that these standard deviation parameters imply a strong constraint, potentially biased, on each gradient distribution — with respect to $\Theta$ — and so, impact each task uncertainty. In this sense, we ensure reliable and robust uncertainty estimates of the distinct tasks through automatic and adaptive weighing.

For the sake of readability, we used two-task sampling with a data-fitting term from a field $u$ and a PDE constraint, denoted $\mathcal{F}$, so the data set is decomposed into $\mathcal{D} = \mathcal{D}^u \cup \mathcal{D}^Q$, following the notations introduced in Sect. 4.3.2. The multi-potential energy thus reduces to :

$$U(\Theta) = \frac{\lambda_0}{2\sigma_0^2} \left\| u_\Theta - u \right\|^2_{\mathcal{D}^u} + \frac{\lambda_1}{2\sigma_1^2} \left\| \mathcal{F}(u_\Theta) \right\|^2_{\mathcal{D}^Q} + \frac{1}{2\sigma_\Theta^2} \left\| \Theta \right\|^2 := \sum_{k=0}^{K+1} \lambda_k \mathcal{L}_k(\Theta) \tag{4.30}$$

where we choose to keep the $\sigma_k$ notation for the demonstration and restrain $\Theta$ to the neural network parameters, even if the following holds in an inverse problem paradigm. As a reminder, the measurement data used for the training $\mathcal{D}^u$ can differ from the collocation points where we impose the PDE constraint $\mathcal{D}^Q$ and their respective numbers are denoted $N^u$ and $N^Q$. With the notations from Sect. 4.3.2, the gradients of the two-tasks potential energy write respectively:

$$\begin{aligned} \frac{\partial \mathcal{L}_0}{\partial \Theta_j}(\Theta) &= \frac{1}{\sigma_0^2 N^u} \sum_{i=0}^{N^u} \Big( u_\Theta(x_i) - u_i \Big) \frac{\partial u_\Theta}{\partial \Theta_j}(x_i) \\ \frac{\partial \mathcal{L}_1}{\partial \Theta_j}(\Theta) &= \frac{1}{\sigma_1^2 N^Q} \sum_{i=0}^{N^Q} \mathcal{F}\Big( u_\Theta(x_i) \Big) \frac{\partial \mathcal{F}(u_\Theta)}{\partial \Theta_j}(x_i) \end{aligned} \tag{4.31}$$

for $\Theta \in \mathbb{R}^p$ and we can thus decompose the variances $\mathrm{Var}_\Theta\big[\nabla_\Theta \mathcal{L}_k\big]$, $k = 0, 1$ with respect to these gradients. To do so, we first compute their mean with respect to $\Theta$ and get respectively

$$\begin{aligned} \mathbb{E}_\Theta\big[\nabla_\Theta \mathcal{L}_0\big] &= \frac{1}{N^p} \sum_{j=0}^{N^p} \frac{\partial \mathcal{L}_0}{\partial \Theta_j}(\Theta) = \frac{1}{\sigma_0^2 N^u} \sum_{i=0}^{N^u} \Big( u_\Theta(x_i) - u_i \Big) \mathbb{E}_\Theta\big[\nabla_\Theta u_\Theta\big](x_i) \\ &= \frac{1}{\sigma_0^2} \mathbb{E}_{\mathcal{D}^u}\Big[ (u_\Theta - u) \mathbb{E}_\Theta\big[\nabla_\Theta u_\Theta\big] \Big] \end{aligned} \tag{4.32}$$

and

$$\mathbb{E}_\Theta\big[\nabla_\Theta \mathcal{L}_1\big] = \frac{1}{\sigma_1^2}\mathbb{E}_{\mathcal{D}^Q}\big[\mathcal{F}(u_\Theta)\mathbb{E}_\Theta\big[\nabla_\Theta \mathcal{F}(u_\Theta)\big]\big] \tag{4.33}$$

with the special configuration $\nabla_\Theta \mathcal{F}(u_\Theta) = \mathcal{F}(\nabla_\Theta u_\Theta)$ if $\mathcal{F}$ is linear. Finally, we can extend it to the variance computations, as follows:

$$\begin{aligned}
\mathrm{Var}_\Theta\big[\nabla_\Theta \mathcal{L}_0\big] &= \frac{1}{N^p}\sum_{j=0}^{N^p}\left(\frac{\partial \mathcal{L}_0}{\partial \Theta_j} - \mathbb{E}_\Theta\big[\nabla_\Theta \mathcal{L}_0\big]\right)^2 \\
&= \frac{1}{N^p (N^u\sigma_0^2)^2}\sum_{j=0}^{N^p}\left[\sum_{i=0}^{N^u}\Big(u_\Theta(x_i) - u_i\Big)\left(\frac{\partial u_\Theta}{\partial \Theta_j}(x_i) - \mathbb{E}_\Theta\big[\nabla_\Theta u_\Theta\big](x_i)\right)\right]^2 \\
&= \frac{1}{(N^u\sigma_0^2)^2}\sum_{i=0}^{N^u}\sum_{k=0}^{N^u}\Big(u_\Theta(x_i) - u_i\Big)\Big(u_\Theta(x_k) - u_k\Big)\mathrm{Cov}_\Theta\big[\nabla_\Theta u_\Theta(x_i), \nabla_\Theta u_\Theta(x_k)\big] \\
&\leqslant \frac{1}{\sigma_0^4}\|u_\Theta - u\|^2_{\infty,\mathcal{D}^u}\mathrm{Cov}_\Theta\left[\frac{1}{N^u}\sum_{i=0}^{N^u}\nabla_\Theta u_\Theta(x_i), \frac{1}{N^u}\sum_{k=0}^{N^u}\nabla_\Theta u_\Theta(x_k)\right] \\
&= \frac{1}{\sigma_0^4}\|u_\Theta - u\|^2_{\infty,\mathcal{D}^u}\mathrm{Var}_\Theta\big[\mathbb{E}_{\mathcal{D}^u}\big[\nabla_\Theta u_\Theta\big]\big]
\end{aligned} \tag{4.34}$$

that provides an upper bound for the gradient variance of the data-fitting term. We then obtain, in the same way, the PDE constraint bound as:

$$\mathrm{Var}_\Theta\big[\nabla_\Theta \mathcal{L}_1\big] \leqslant \frac{1}{\sigma_1^4}\|\mathcal{F}(u_\Theta)\|^2_{\infty,\mathcal{D}^Q}\mathrm{Var}_\Theta\big[\mathbb{E}_{\mathcal{D}^Q}\big[\nabla_\Theta \mathcal{F}(u_\Theta)\big]\big]. \tag{4.35}$$

The notation $\|\cdot\|_{\infty,\mathcal{D}^\bullet}$ here refers to the discrete $\ell^\infty$-norm on the spatial domain composed of the $\mathcal{D}^\bullet$ training points, and $\mathbb{E}_{\mathcal{D}^\bullet}$ introduces the spatial mean on the corresponding data set. Hence, the gradient variances of the tasks are controlled by the crossed complex components $\mathrm{Var}_\Theta\mathbb{E}_{\mathcal{D}^\bullet}$ which can be interpreted as sensitivity terms evaluating the dispersion with respect to $\Theta$ of the gradient descent directions, averaged in space. Finally, since the $\sigma_k$ values are uniformly set to one to avoid biased sampling, it means that the $\lambda$ values are computed in such a way the joint variance of the gradient distributions is bounded by:

$$\gamma^2 \leqslant \min\left\{\|u_\Theta - u\|^2_{\infty,\mathcal{D}^u}\mathrm{Var}_\Theta\big[\mathbb{E}_{\mathcal{D}^u}\big[\nabla_\Theta u_\Theta\big]\big],\ \|\mathcal{F}(u_\Theta)\|^2_{\infty,\mathcal{D}^Q}\mathrm{Var}_\Theta\big[\mathbb{E}_{\mathcal{D}^Q}\big[\nabla_\Theta \mathcal{F}(u_\Theta)\big]\big]\right\} \tag{4.36}$$

which highlights the fact that the weights are adjusted with respect to the most likely task and thus improve the reliability in the uncertainty quantification. The present computations can straightforwardly be extended to more complex multi-potential energy terms for direct and inverse real-world problems, which concludes our analysis.

### 4.4.3 Sobolev training benchmark and convergence diagnostics

The current AW-HMC algorithm is first validated on a Sobolev training benchmark with different complexities, which presents the advantage of providing a basis for comparison with $\varepsilon$-optimality results. This also allows us to establish a new indicator for convergence diagnostics of the BPINNs, and investigate the performances of the proposed auto-weighted methodology. We first apply this new Adaptively Weighted strategy to the 1D Sobolev training, up to second-order derivatives, introduced in Sect. 4.3.3 and then extend it to third-order derivatives Sobolev training.

We consider the same exact set of hyperparameters as in Sect. 4.3.3. In particular, the number of adaptive steps is set to $N = 20$, as for the NUTS declination, to ensure an impartial comparison of the distinct sampler methodologies. However, given the stopping criterion developed in Sect. 4.4, with a threshold set to $S_{\min} = 1\mathrm{e}{-3}$, we would obtain different numbers of adaptive steps. Indeed, as shown in Fig 4.4, the Sobolev training with derivatives up to the second order

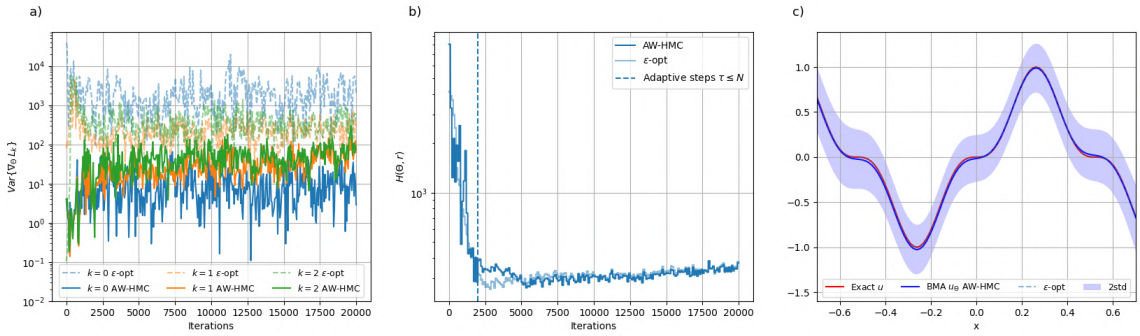


**Figure 4.3: Adaptively Weighted Hamiltonian Monte Carlo on Sobolev training up to second-order derivatives compared to $\varepsilon$-optimal weighting.** a) Effective gradient distributions variances $\mathrm{Var}\{\nabla_\Theta L_k\}$ with balanced conditions between the tasks. b) Hamiltonian evolution throughout the sampling satisfying energy conservation. c) Resulting field predictions with a comparison between $\varepsilon$-optimal results and AW-HMC strategy.

would exit after 28 iterations, and its formulation with derivatives up to the third order would exit after 15 iterations. It is though noticeable that the 28 iterations of the adaptation process — observed in Fig 4.4a for the second-order case — is a bit overestimated, due to the lag induced by the backward averaging, so stopping after a maximum number of iterations $N_{\max} = 20$ is totally acceptable, and ensure a fair comparison between the different samplers. Furthermore, Figure 4.7 confirms that the task weights have reached lower bounds for Sobolev training up to third-derivative, so all tasks are meaningfully balanced. In this case, the weights stabilization observed for iterations $\tau > 15$, in Figure 4.7, also confirms that the present stopping criterion is relevant, even if we consider a manual number of adaptive steps for the sake of fair comparisons.

In addition, we compare the predictions with a reference case where the weights $\lambda_k$ are set accordingly to $\varepsilon$-optimal analytical solution [306], which can only be provided for linear problems. Such analytical $\varepsilon$-optimal weights are available for the optimization problem of minimizing the multi-potential energy in equation (4.18). In the particular case of Sobolev training, these weights can be determined based on the following equation (see [187], for instance):

$$\lambda_k^\varepsilon = \frac{\prod_{j\neq k} \mathcal{I}_j}{\sum_{k=1}^{K} \prod_{j\neq k} \mathcal{I}_j} \quad \text{such that} \quad \mathcal{I}_k = \int_\Omega |D_x^k(u)|^2 \,\mathrm{d}x. \tag{4.37}$$

These theoretical weights, plotted in Figure 4.7b, alleviate stiffness issues that lead to vanishing gradient phenomena [187]. By doing so, these weights ensures that the objectives — or tasks — are minimized in an unbiased way, hence reaching Pareto optimal solution. Although we consider a marginalization process in the Bayesian context, these analytical weights provide an interesting baseline for comparison on stiff Sobolev problems. Indeed, appropriate weighting of the posterior distribution based on the $\varepsilon$-optimal rule (4.37) ensures effective sampling that we compare with our AW-HMC strategy. In this sense, $\varepsilon$-optimal weighting allows us to verify that our adaptive weighing strategy reaches the Pareto front neighborhood during the adaptive steps and hence efficiently samples the region of the highest posterior probability. We tested our methodology against this $\varepsilon$-optimal solution assuming observation noise $\xi_u \sim \mathcal{N}(0, \sigma_u^2 I)$ such that $\sigma_k = \sigma_u, \forall k$ with $\sigma_u = 0.1$. It provides good agreement between both approaches with a similar convergence of the Hamiltonian toward the same energy level, in Figure 4.3b: in fact, the $\mathbb{L}^2$-relative error on the Hamiltonian values between the $\varepsilon$-optimal and AW-HMC methods scales around $1\mathrm{e}{-4}$ after the adaptive steps. The AW-HMC method also provides $\mathbb{L}^2$-relative errors, compared to this optimal solution, ranging around $1\mathrm{e}{-3}$ for both the signal and its derivatives. Finally, we also point out in Figure 4.3a balanced gradient variances in the same way as observed with $\varepsilon$-optimal analytical weights. The AW-HMC methodology, therefore, provides similar results to $\varepsilon$-optimal solutions

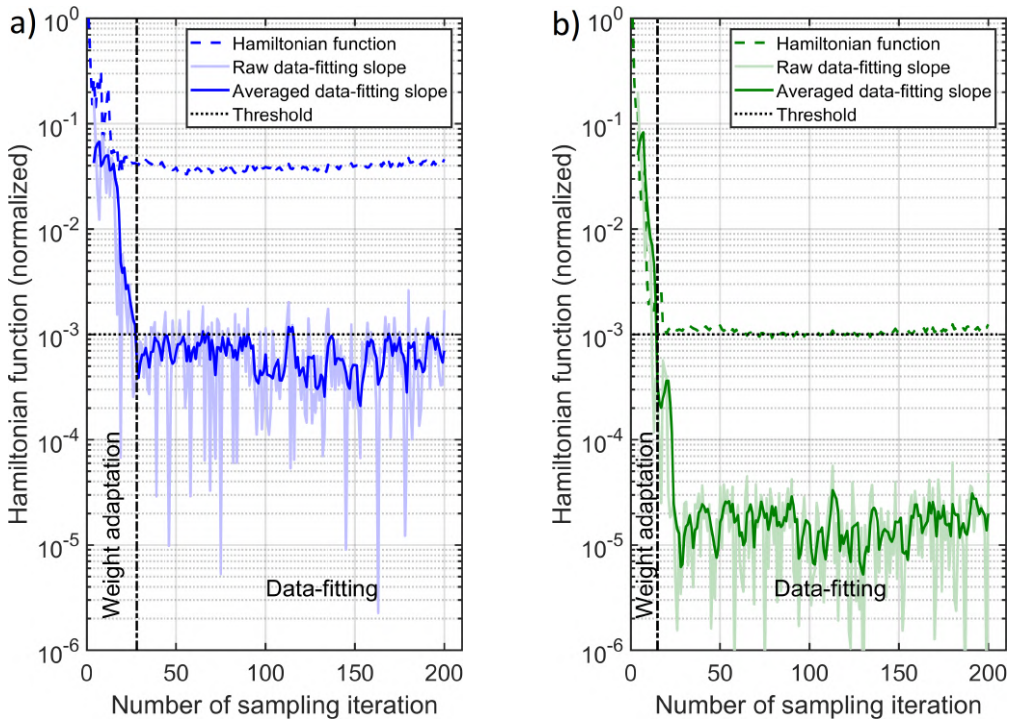


**Figure 4.4: Hamiltonian averaged slope used as stopping criterion for weight adaptation on 1D Sobolev training benchmarks.** The vertical dashed lines depict the start and the end of the weight adaptation process. a) Sobolev training with derivatives up to second order. b) Sobolev training with derivatives up to third order.

in terms of balance between the gradient variances, exploration of the Hamiltonian energy levels, and overall BMA predictions.

Our new approach shows exceptionally balanced conditions between the different tasks: the effective gradient distribution variances $\mathrm{Var}\{\nabla_\Theta L_k\}$ present the same orders of magnitude throughout the training, even with a finite number of adaptive steps. This means that the posterior distribution reached after the auto-adjustment of the weights is well-suited to converging toward the Pareto front exploration. This makes the sampling more efficient and comparable to sampling a weighted posterior based on the $\varepsilon$-optimal rule (4.37). Preventing strong imbalance behavior on the gradient variances, and therefore task-specific bias has considerably improved the marginalization of such multi-objective potential energy, in comparison with the conventional approaches that presented major failures in Sect. 4.3.3.

To further demonstrate the robustness of the method, we consider the third-order derivative extension of this test case, where even a NUTS adaptive strategy on the time step (reaching $\delta t = 1.36\mathrm{e}{-7}$) generates, here, pathological random-walk behavior making the sampling completely defective (see Figure 4.5 top row and Figure 4.6). Such a significant decrease in the time step is clearly explained by the enhanced stiffness induced by the third-order derivative term in this multitask learning. Indeed, the Hamiltonian trajectories are more likely to diverge during the deterministic steps due to this stiffness and require a small $\delta t$ to compensate for the divergence. To avoid the resulting pathological random walks, the overall integration time must be increased but this inevitably leads to excessive computational costs — under such a constraint on the leapfrog time step. This highlights the main limitation of NUTS when facing stiff multitask sampling that involves separate scales.

In contrast, our approach overcomes these major failures (see Figure 4.6) without additional constraints on $\delta t$ and provides balanced gradient variances between the different tasks as illustrated in Figure 4.5 (bottom row). We also compare the results of the AW-HMC methodology with analytical weights from $\varepsilon$-optimality and show great agreement between the approaches. In addition, in order to deal with the stochastic-induced process of the BPINNs induced by sampling variability, we perform various repetitions of the sampling with different initialization of the neural

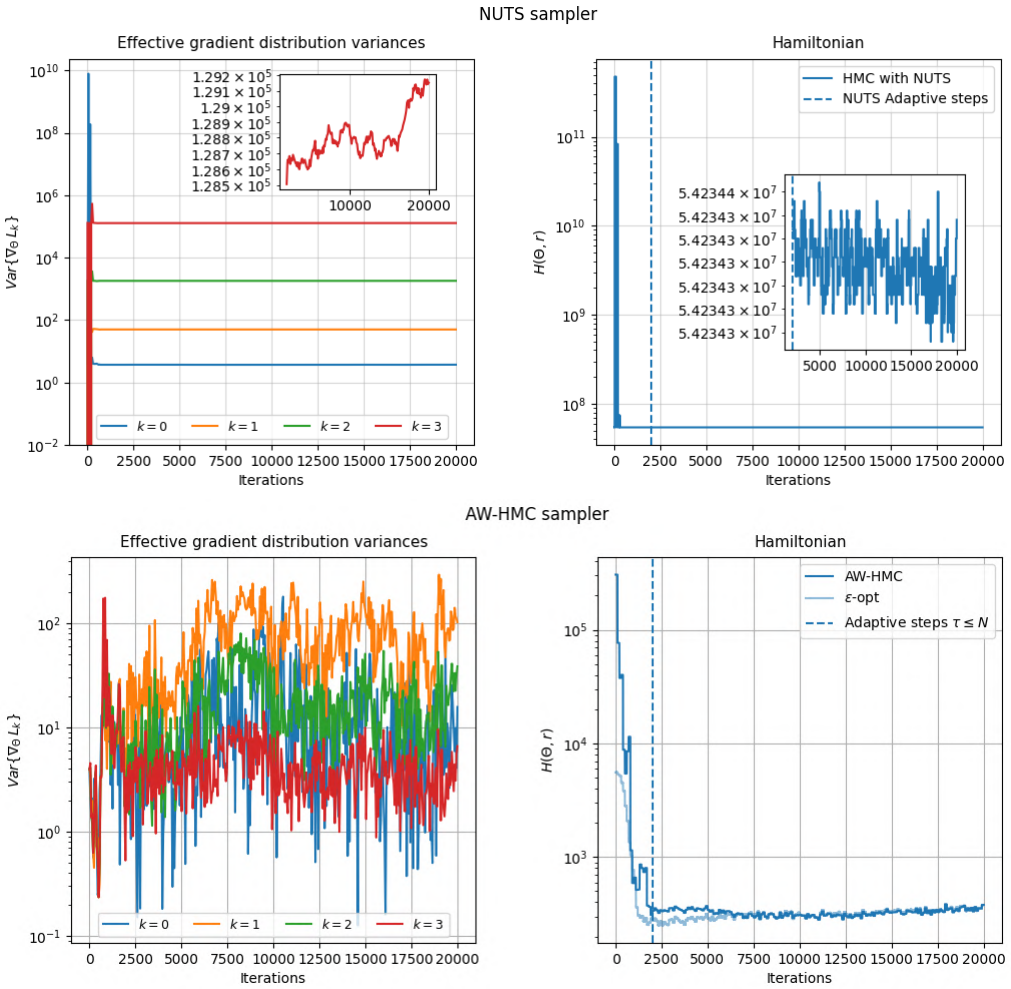


**Figure 4.5: Comparison between AW-HMC and NUTS samplers on Sobolev training up to third-order derivative:** Effective gradient distribution variances $\mathrm{Var}\{\nabla_\Theta L_k\}$ and Hamiltonian evolution. The NUTS formulation (top row) highlights strong imbalances between the learned tasks, on the left, and random-walk behaviors in exploring the energy level sets, on the right. AW-HMC strategy (bottom row) compared with $\varepsilon$-optimality.

network parameters and momentum. This leads to averaged weight evolution along the adaptive steps presented in Figure 4.7 that show similar order of magnitude as the analytical $\varepsilon$-optimal weights. The slight difference between the computed and analytical weights in Figure 4.7 can be explained by the difference of nature of both problems, respectively a marginalization process and an optimization one. Indeed, the weights determined by analytical $\varepsilon$-optimal analysis lead to the tightest upper bound in the corresponding optimization problem — that minimizes the multi-objective potential energy (4.18) — but do not incorporate any uncertainty quantification, unlike the computed weights based on Inverse-Dirichlet weighting in the AW-HMC sampler. Nonetheless, the comparison is interesting and illustrates that the overall scaling of the distinct tasks is well captured during the adaptive steps of AW-HMC (see Figure 4.7). The comparison of our adaptive weighting strategy with a posterior distribution weighted by the $\varepsilon$-optimal rule (4.37) shows similar convergence properties, driving the sampler close to a well-conditioned posterior distribution (see Figure 4.5 bottom-right). Therefore, the weighted posterior distribution determined by AW-HMC enables exploring of the optimal Pareto front neighborhood, avoids stiffness issues, and thus provides an efficient sampling of the highest posterior probability region.

Apart from these qualitative comparisons between the different methodologies and the analytical solution, we subsequently introduce a new metric that quantifies the quality of the predictions. This complements the usual metrics with a convergence quantification of the sampling along the marginalization process. The samples collected after the burn-in steps in the AW-HMC process

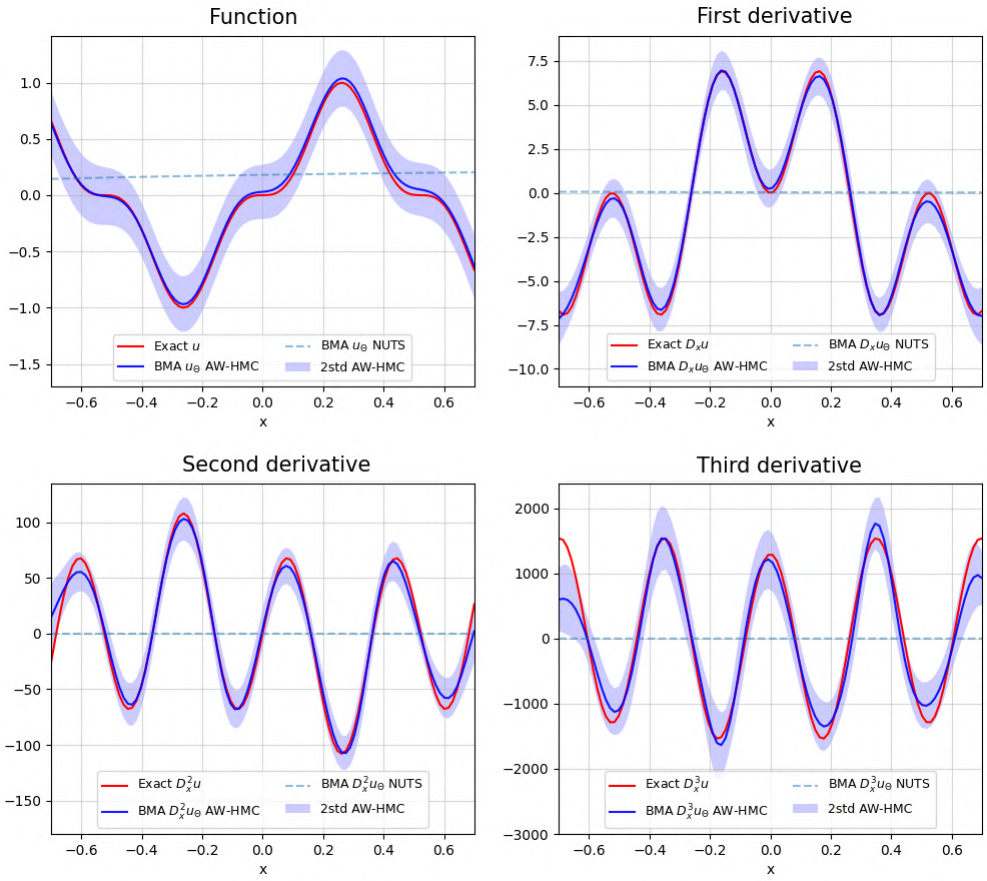


**Figure 4.6: Comparison of the BMA predictions (on the function and its derivatives) between the AW-HMC and NUTS formulations for 1D Sobolev training up to third-order derivative.** The imbalance between tasks and random walk behavior of NUTS (see Figure 4.5 top row) results in ineffective BMA predictions. The AW-HMC methodology overcomes these effects and significantly improves the sampling of the target distribution.

— i.e. all the instances of $\left\{\Theta^{t_\tau}\right\}_{\tau=N_{\text{burn}}}^{N_s}$ — are first used to determine a Bayesian Model Average estimation as defined in equation (4.3). Each sample provides a prediction $P(y|x,\Theta^{t_\tau})$, for the neural network characterised by $\Theta^{t_\tau}$, which is theoretically drawn from the posterior distribution $P(\Theta|\mathcal{D},\mathcal{M})$ such that the BMA is usually approximated by [319]:

$$P(y|x,\mathcal{D},\mathcal{M}) \simeq \frac{1}{N_s - N_{\text{burn}}} \sum_{\tau=N_{\text{burn}}}^{N_s} P(y|x,\Theta^{t_\tau}) \quad \text{with} \quad \Theta^{t_\tau} \sim P(\Theta|\mathcal{D},\mathcal{M}). \tag{4.38}$$

In Sobolev training, we consider as the neural network outputs, the prediction of the function itself and all its derivatives $y = \left\{D_x^k u_\Theta,\ k = 0...K\right\}$, such that we can compute, according to equation (4.38), relative BMA errors with respect to each output defined by :

$$\text{BMA-E}^k = \frac{\left\| P\left(D_x^k u_\Theta \,|\, x,\mathcal{D},\mathcal{M}\right) - D_x^k u \right\|^2}{\left\| D_x^k u \right\|^2}, \qquad \forall k = 0...K \tag{4.39}$$

where the notation $\|\cdot\|$ used here refers to the functional $\mathbb{L}^2$-norm. Based on the previous definition and in order to incorporate convergence on the BMA along the marginalization process, we introduce a new diagnostic called (relative) Bayesian Model Average Cumulative Error (BMA-CE), defined as follows:

$$\text{BMA-CE}^k(\tau) = \frac{\left\| \dfrac{1}{\tau - N} \displaystyle\sum_{i=N}^{\tau} P\left(D_x^k u_\Theta \,|\, x,\Theta^{t_i}\right) - D_x^k u \right\|^2}{\left\| D_x^k u \right\|^2}, \qquad \forall k = 0...K \tag{4.40}$$

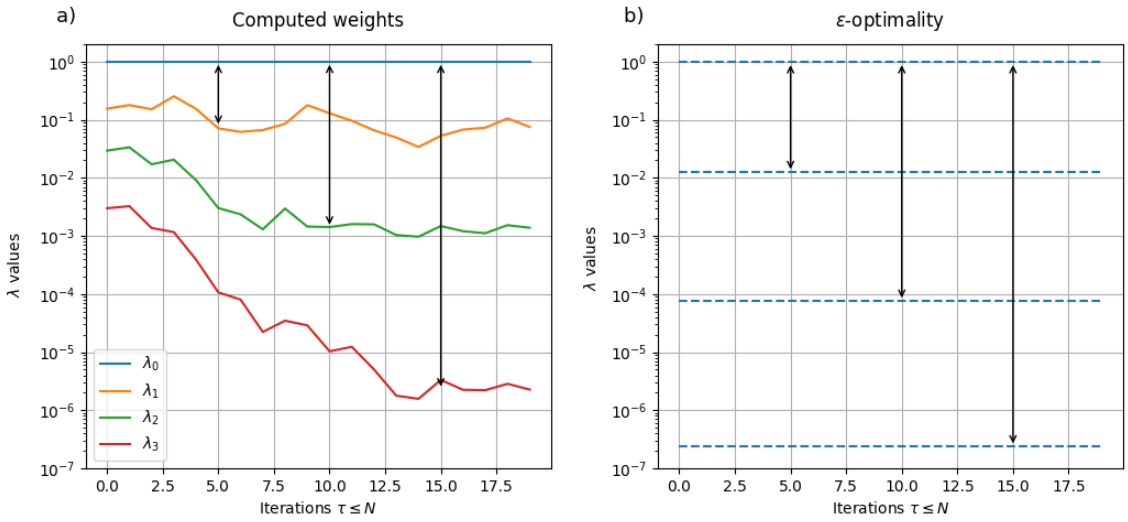


**Figure 4.7: $\lambda$ trajectories with AW-HMC and $\varepsilon$-optimal weighting strategies for Sobolev training up to third-order derivative:** a) Evolution of the $\lambda_k$ weights along the adaptive steps ($\tau \leq N$), averaged over several repetitions of the AW-HMC sampling. This is induced by different initializations of the neural network parameters and momentum to take into account sample variability. b) Comparison with analytical $\varepsilon$-optimal weights. The order of magnitude of the relative weights $\lambda_0/\lambda_i$, $i = 1...3$, in both methods, are represented by the double-headed arrows.

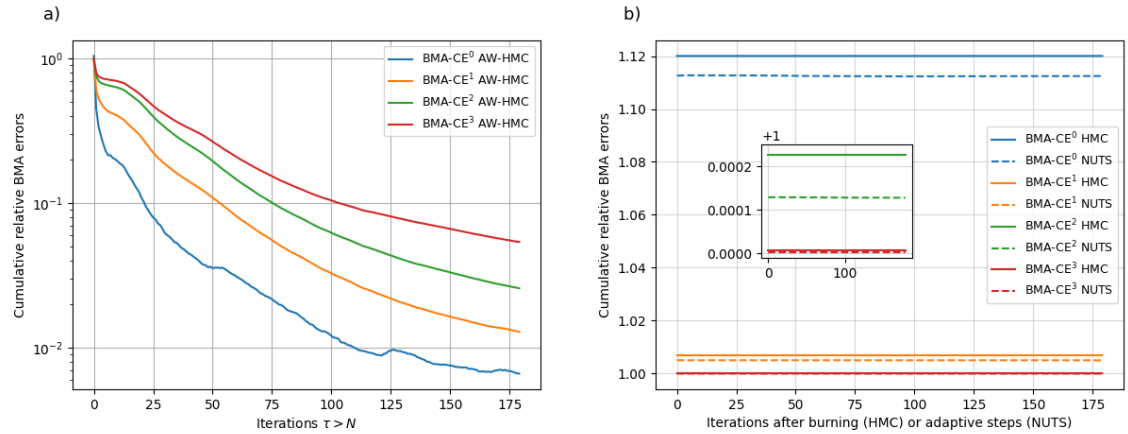


**Figure 4.8: Convergence diagnostics with the comparison between the HMC, NUTS, and AW-HMC samplers for Sobolev training up to third-order derivative:** a) Cumulative relative BMA errors, computed according to equation (4.40), plotted throughout the sampling iterations $\tau > N$ with the AW-HMC strategy. b) Cumulative relative BMA errors for the classical HMC and NUTS formulations. These quantities remain nearly constant in pathological cases, due either to massive rejection or pathological random walk, highlighting the lack of convergence in the usual BPINNs-HMC formulations.

depending on the sampling iterations after the adaptive steps, for $\tau > N$ in Algorithm 1. These formulae can be directly extended to all the neural network outputs, in a more general framework and quantify the sampling efficiency in terms of convergence rate. The cumulative BMA errors are represented in Figure 4.8 for the third-order extension of Sobolev training highlighting the convergence of the AW-HMC sampler for each of the functional tasks (Figure 4.8a). Instead, these quantities remain nearly constant for the pathological HMC and NUTS formulations, due to massive rejections and random-walk behavior, respectively (see Figure 4.8b).

### 4.4.4 2D Sobolev training benchmark

We finally extend the Sobolev training test case from Sect. 4.4.3 to several 2D benchmarks, where we study the impact of the functional complexity and the number of training points on the Bayesian Model Average errors. In this sense, we test the robustness and efficiency of the AW-HMC algorithm for the BPINNs on 2D Sobolev training constrained by gradient-based and Laplacian operators.

We define on the spatial domain $\Omega = [0, 2\pi]^2$ a target functional $u$, taken under the form:

$$u(x,y) = \sum_{i=1}^{N_{rep}} A_x^i \cos\left(2\pi L_x^{-1} l_x^i x + \varphi_x^i\right) A_y^i \sin\left(2\pi L_y^{-1} l_y^i y + \varphi_y^i\right) \tag{4.41}$$

which makes it possible to investigate a wide range of shape complexities and sharp interfaces, in addition to the stiffness introduced by the higher-order derivatives. We set the domain sizes to $L_x = L_y = 2\pi$, the number of repetitions $N_{rep} = 5$, while the parameters $A_x$ and $A_y$ are independently and uniformly sampled from the interval $[-2, 2]$, as are $\varphi_x$ and $\varphi_y$ from $[0, 2\pi]$. In order to treat several shape complexities, we consider a range of parameter $l$ such that the local length scales $l_x$ and $l_y$ are randomly sampled from the set $\{1, 2, ..., l\}$. The 2D spatial domain $\Omega$ is covered by a uniform grid with a resolution of $256 \times 256$, along with randomly-selected training points defining the dataset $\mathcal{D}$. We then study both the impact of the functional complexity, by setting different values of $l$, and the number of training points on the Bayesian Model Average resulting from our AW-HMC methodology. For this 2D Sobolev benchmark, we consider the multi-potential energy term defined by:

$$\begin{aligned} U(\Theta) = &\frac{\lambda_0}{2\sigma_0^2} \left\| u_\Theta - u \right\|_{\mathcal{D}}^2 + \frac{\lambda_1}{2\sigma_1^2} \left\| \left( \frac{\partial u_\Theta}{\partial x} + \frac{\partial u_\Theta}{\partial y} \right) - \left( \frac{\partial u}{\partial x} + \frac{\partial u}{\partial u} \right) \right\|_{\mathcal{D}}^2 \\ &+ \frac{\lambda_2}{2\sigma_2^2} \left\| \Delta u_\Theta - \Delta u \right\|_{\mathcal{D}}^2 + \frac{1}{2\sigma_\Theta^2} \|\Theta\|_{\mathbb{R}_p}^2. \end{aligned} \tag{4.42}$$

The results on the entire benchmark setup, presented in Figure 4.10, show a convergence trend with an increasing number of training points, and this independently of the $l$ values, even though the relative BMA errors reach higher bounds with additional shape complexity. These relative BMA errors are respectively computed according to the following relations for the functional surrogate model $u_\Theta$, the gradient-based term $\nabla u_\Theta$ and the Laplacian $\Delta u_\Theta$:

$$\begin{aligned} \text{BMA-E}^u &= \frac{\left\| P\left(u_\Theta \,|\, (x,y), \mathcal{D}, \mathcal{M}\right) - u \right\|^2}{\|u\|^2}, \\ \text{BMA-E}^{\nabla u} &= \frac{\left\| P\left( \frac{\partial u_\Theta}{\partial x} + \frac{\partial u_\Theta}{\partial y} \,\middle|\, (x,y), \mathcal{D}, \mathcal{M} \right) - \left( \frac{\partial u}{\partial x} + \frac{\partial u}{\partial y} \right) \right\|^2}{\left\| \frac{\partial u}{\partial x} + \frac{\partial u}{\partial y} \right\|^2}, \\ \text{BMA-E}^{\Delta u} &= \frac{\left\| P\left(\Delta u_\Theta \,|\, (x,y), \mathcal{D}, \mathcal{M}\right) - \Delta u \right\|^2}{\|\Delta u\|^2}, \end{aligned} \tag{4.43}$$

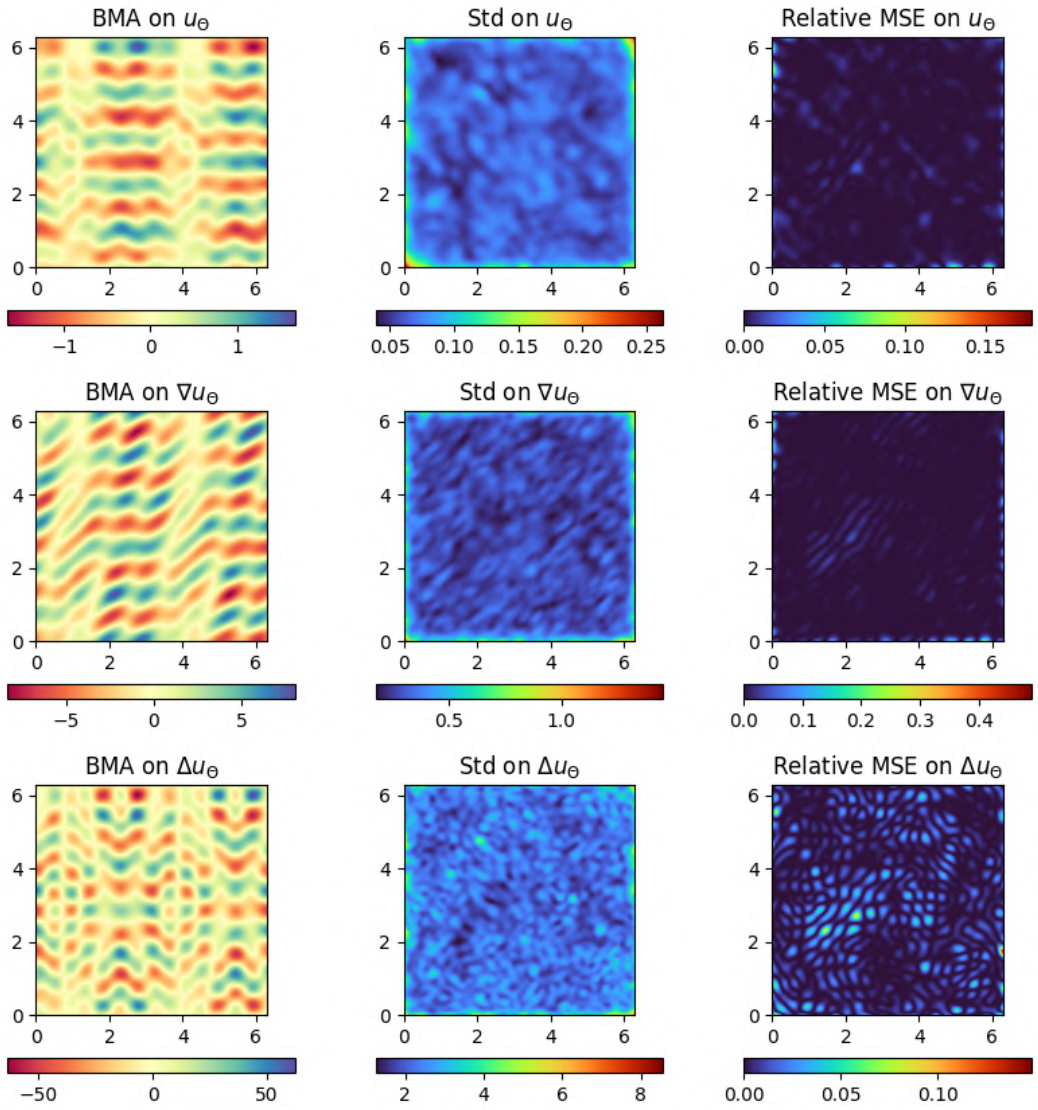


**Figure 4.9: 2D Sobolev training benchmark:** BMA predictions, predicted standard deviation, and relative MSE, presented locally for each term of the multi-objective potential energy (4.42). We worked on a limited case $l = 8$ with about $15\%$ of training points. The global relative mean squared errors, averaged over the whole domain $\Omega$, scale around $1.69e-3$, $3.42e-3$, and $5.6e-3$ respectively.

where the notation $\|\cdot\|$ refers to the functional $\mathbb{L}^2$-norm. The BMA errors are also average versions of different repetitions of Sobolev sampling, simultaneously running in parallel. In fact, in order to deal with the stochastic-induced process that may arise from the sampling variabilities themselves, we performed several realizations starting with distinct initializations of the neural network $\Theta^{t_0}$ and momentum $r^{t_0}$ parameters, which lead to different sampling realizations. We can potentially take into account these sampling variabilities to compute the standard deviation over these repetitions, as illustrated by the colored bands in Figure 4.10. We also represent in Figure 4.9 for each term of the multi-potential functional (4.42), respectively, their BMA predictions, their uncertainties based on the predictive standard deviations throughout the sampling, and the relative Mean Squared Errors (MSE) errors in the case $l = 8$ and with $10000$ training points, randomly sampled over the whole domain. The results here show enhanced uncertainties near the boundary walls where the higher errors are located and highlight the ability of our methodology to capture complex shape fields of different orders of magnitude at the same time. We can also emphasize that such a 2D Sobolev training benchmark was previously unachievable with the classical BPINNs-HMC formulation.

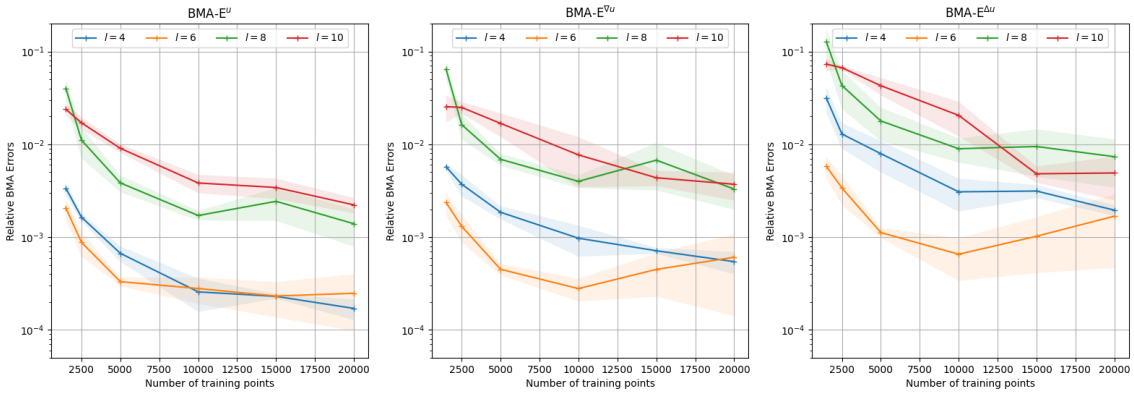


**Figure 4.10: 2D Sobolev training benchmark:** comparison of the relative BMA errors, as defined in equations (4.43), plotted with respect to the number of training points for each term of the multi-potential energy (4.42). We consider various shape complexities induced by the different values of $l$. The number of training points is increased until about $30\%$ of the whole data set is reached, for 20000 training points.

## 4.5 Validation on a multiscale Lotka-Volterra inverse problem

We demonstrate the use of AW-HMC on a more complex multitask and multiscale dynamical inverse problem to quantify the impact of the scaling. As Linka *et al.* [173] pointed out, sensitivity to scaling may hinder the performance of classical BPINNs, especially when considering nonlinear dynamical systems. In this section, we therefore compare the distinct BPINN methodologies, namely the usual HMC and NUTS formulations, with our novel adaptive weighting approach on a Lotka-Volterra multiscale inverse problem. The multiscale nature and stiffness resulting from real-world problems, where vanishing task-specific gradients are commonplace, is an interesting benchmark to quantify the robustness and efficiency of the present AW-HMC method.

### 4.5.1 Lotka-Volterra inverse problem formulation

In this context, we consider a Lotka-Volterra dynamical system with parameters of highly varying orders of magnitude defined by the following ODE system:

$$\begin{cases} \dfrac{\mathrm{d}u}{\mathrm{d}t} = \alpha u - \beta uv, \quad t \in \mathcal{T} \\ \dfrac{\mathrm{d}v}{\mathrm{d}t} = \delta uv - \gamma v, \quad t \in \mathcal{T} \\ u(0) = u_0,\ v(0) = v_0 \end{cases} \tag{4.44}$$

which characterizes the temporal evolution of predator-prey species. The notations $u(t)$ and $v(t)$ respectively refer to the prey and predator population size at a given time $t$, whereas the parameters $\alpha, \beta, \delta, \gamma \geq 0$ control the population dynamics, as growing and shrinkage rates. Thereafter, we set the initial populations to $u_0 = 100$ and $v_0 = 20$ with the following parameters $\alpha = 1$, $\beta = 0.1$, $\delta = 0.01$ and $\gamma = 0.5$ intentionally selected with different orders of magnitude. This sets up an inverse problem benchmark based on real-world dynamics with separate scales involved.

The observation data are first numerically generated by solving the ODE system (4.44) on a uniform temporal grid $\mathcal{T} = [0, 50]$ with a thin resolution of 400 points. The data are randomly sampled so as to consider only half in the training phase of the different samplers. The dataset $\mathcal{D}$ then involves these partial measurements of $u$ and $v$ at 200 different times, potentially with some added noise, and the same collocation points are kept to satisfy the ODE constraints. In this section, we focus on an inverse problem by inferring the unknown model parameters $\mathcal{P}_{\text{inv}} = \{\alpha, \beta, \delta, \gamma\}$ from these measurement data while recovering the whole species evolution on the original finer resolution. Although the overall Bayesian inference problem is multiscale by construction, each inverse parameter is assumed to follow single-mode posterior distributions.

Regarding the noticeable scaling difference between the two populations, we consider a predator-prey split of the tasks such that each field $u$ and $v$ satisfies a data-fitting likelihood term

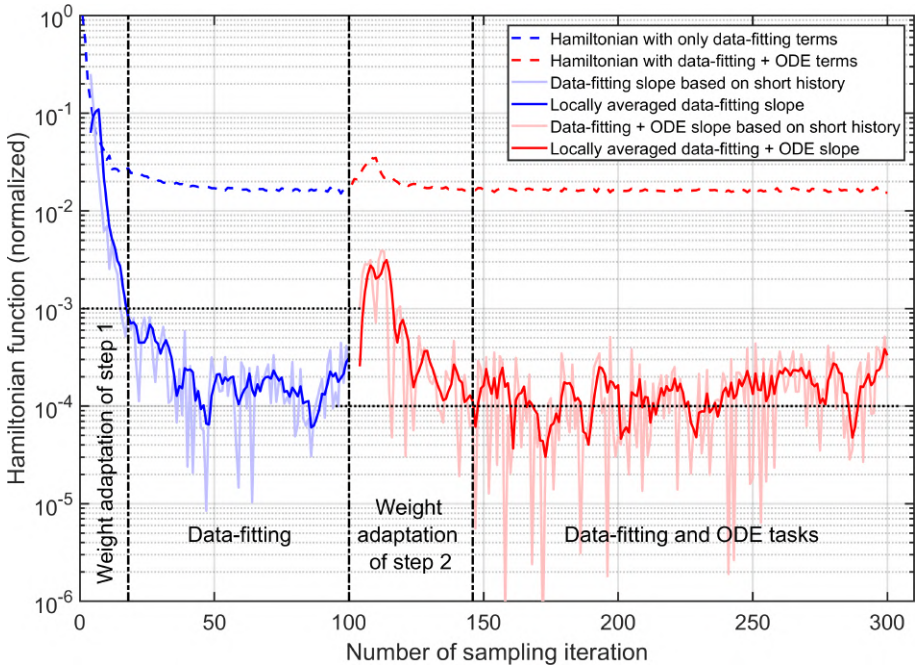


**Figure 4.11: Hamiltonian averaged slope used as stopping criterion for weight adaptation on Lotka-Volterra inverse problem.** The vertical dashed lines depict the start and the end of the weight adaptation process. The overall sampling has two sequential steps: first, data-fitting alone in blue (with a preliminary weight adaptation) and second, data-fitting together with the ODE constraints in red (with an updated weight adaptation).

and an ODE-residual likelihood term. We also assume log-normal prior distributions on $\mathcal{P}_{\text{inv}}$ to ensure positivity of the inverse parameters, as Yang *et al.* [328] have shown that such priors improve the inference, and we set independent normal distributions on the neural network parameters $\theta$. In practice though, we use a change of variable by introducing $\mathcal{P}_{\text{inv}} = e^{\widetilde{\mathcal{P}}_{\text{inv}}} := \left\{e^{\widetilde{\alpha}}, e^{\widetilde{\beta}}, e^{\widetilde{\delta}}, e^{\widetilde{\gamma}}\right\}$ for each of the inverse parameters, to infer $\widetilde{\mathcal{P}}_{\text{inv}}$ assuming normal prior distributions as well. For this test case, we impose weakly informed priors, especially on $\widetilde{\mathcal{P}}_{\text{inv}}$, since we expect our methodology to handle the multiscale inference due to the unbiased auto-weighting of the tasks. We therefore assume that both the neural network and inverse parameters all gather the same prior distribution, given by $\Theta \sim \mathcal{N}(0, \sigma_\Theta^2 I_{p+d})$ where we consider the newly set of parameter $\Theta = \left\{\theta, \widetilde{\mathcal{P}}_{\text{inv}}\right\}$.

Under these assumptions, we can define the multi-potential energy of the corresponding Hamiltonian system:

$$\begin{aligned} U(\Theta) = &\frac{\lambda_0}{2\sigma_0^2}\left\|u_\Theta - u\right\|_{\mathcal{D}}^2 + \frac{\lambda_1}{2\sigma_1^2}\left\|v_\Theta - v\right\|_{\mathcal{D}}^2 + \frac{\lambda_2}{2\sigma_2^2}\left\|\frac{\mathrm{d}u_\Theta}{\mathrm{d}t} - \alpha_\Theta u_\Theta + \beta_\Theta u_\Theta v_\Theta\right\|_{\mathcal{D}}^2 \\ &+ \frac{\lambda_3}{2\sigma_3^2}\left\|\frac{\mathrm{d}v_\Theta}{\mathrm{d}t} - \delta_\Theta u_\Theta v_\Theta + \gamma_\Theta v_\Theta\right\|_{\mathcal{D}}^2 + \frac{1}{2\sigma_\Theta^2}\|\Theta\|_{\mathbb{R}^{p+d}}^2 \end{aligned} \tag{4.45}$$

where the inferred inverse parameters are defined by $(\mathcal{P}_{\text{inv}})_\Theta = e^{(\widetilde{\mathcal{P}}_{\text{inv}})_\Theta} := \left\{e^{\widetilde{\alpha_\Theta}}, e^{\widetilde{\beta_\Theta}}, e^{\widetilde{\delta_\Theta}}, e^{\widetilde{\gamma_\Theta}}\right\}$. We also set all the $\sigma_k$ equal to one, as we do not wish to impose strong priors on the tasks and model uncertainty. As mentioned previously in Sect. 4.3.2, the norms are respectively the RMS and the Euclidean norm for the last term. The prior on the parameters is assumed to follow a Gaussian distribution with a larger standard deviation $\sigma_\Theta = 10$, in the sense that a slightly diffuse distribution induces weakly informed priors on the $\Theta$ parameters. This also ensures that the constraint (4.24) for a non-informative prior is satisfied (see Sect. 4.4.1).

For such inverse modeling, the sampling is decomposed using sequential training. This means that:

- First, the neural network parameters are sampled with an AW-HMC strategy to mainly target

the data-fitting likelihood terms (setting $\lambda_2 = \lambda_3 = 0$). This is referred to as sampling step 1, in the rest of the manuscript.

- We then introduce the ODE-residual tasks in (4.45) to provide estimations of the missing inverse parameters, using the AW-HMC algorithm with initial neural network parameters $\theta^{t_0}$ resulting from step 1. This is referred to as sampling step 2.

The BMA predictions and uncertainty quantification finally rely on this entire sampling procedure. In the two-step sequential training, the number of adaptive and sampling iterations are first given by $N = 19$ and $N_s = 100$ in step 1, and $N = 48$ and $N_s = 200$ in step 2. The number of adaptive steps, in particular, are determined according to the stopping criterion for the AW-HMC sampler developed in the methodological Sect. 4.4. For this Lotka-Volterra inverse problem, the maximum number of adaptations is set to $N_{\max} = 50$. We, however, distinguish the setting of the threshold $S_{\min}$ for the two sequential steps: in sampling step 1, the weight adaptation threshold is set to $S_{\min} = 1\text{e}{-3}$ and in sampling step 2, this threshold is set lower at $S_{\min} = 1\text{e}{-4}$ due to good preconditioning from the first sampling step. A new adaptation is still required, though, since the Hamiltonian function contains two more terms — the two residual values of the ODE expression. In Figure 4.11, the stopping criteria described above therefore lead to an exit after $N = 19$ adaptation iterations for the sampling step 1, and after $N = 48$ adaptive iterations for the sampling step 2, corresponding to the third dashed line. Besides, these parameters are kept identical for the other samplers, namely HMC and NUTS, to ensure impartial comparison between the distinct methodologies. The leapfrog parameters are meanwhile given by $L = 100$ and $\delta t = 5\text{e}{-4}$ and $2\text{e}{-4}$ respectively for the sampling steps 1 and 2. Finally, the neural network itself is composed of 4 layers with 32 neurons per layer and we use the sin activation function considering the periodic nature of the solution for the Lotka-Volterra system. Overall, this defines an interesting validation benchmark querying the impact of multiscale inverse problems and the robustness of the several Bayesian Inference methods.

### 4.5.2 Failure of the usual BPINN methodologies on multiscale inverse problem

We first consider the Lotka-Volterra inverse problem, introduced in the previous Sect. 4.5.1, to investigate the impact of multiscale dynamics on the usual BPINN methodologies as HMC with uniform weighting and NUTS. The sampling and leapfrog parameters are set accordingly to Sect. 4.5.1, where $N$ refers here to the burn-in and number of adaptive steps for the HMC and NUTS formulations, respectively. Therefore, we compare the different samplers assuming that, first, their time complexity is the same and, then, no informative priors on the inverse parameter scaling. In fact, the first condition states that different leapfrog parameters might improve the inference of these conventional methodologies. However, it implies a noticeable decrease in the leapfrog time step $\delta t$, thus slower exploration of the energy levels. Hence, these methods require either an increase in the integration time — by increasing $L$ — or using a large number of samples, to obtain suitable predictions. As a reminder, independently of this lack of efficiency in the posterior distribution sampling, poor choices on the weights of multi-potential energy can bias the sampler and deviate it from the Pareto front exploration. The second assumption is motivated by the willingness to address UQ on multiscale dynamics without any prior knowledge of the separate scales. This arises from an assertion by Linka *et al.* [173] indicating that sensitivity to scaling disrupts the performance of the BPINNs-HMC. Finally, we also consider the sequential training, corresponding to the two successive sampling steps, to provide an appropriate basis for comparison between the different methods.

We compare the predictive evolution of the populations to the exact solutions and compute relative BMA cumulative errors for both species to quantify the convergence of the distinct samplers. The results show a lack of convergence of the classical HMC with uniform weighting (in Figure 4.12c) and also, a strong imbalance between the tasks. The relative BMA-CE errors effectively characterize an extremely poor convergence of the predator population with respect to the prey population, which translates directly into an inefficient BMA prediction for the two-species populations (in Figure 4.12a and b). This failure mode is due essentially to the massive rejection

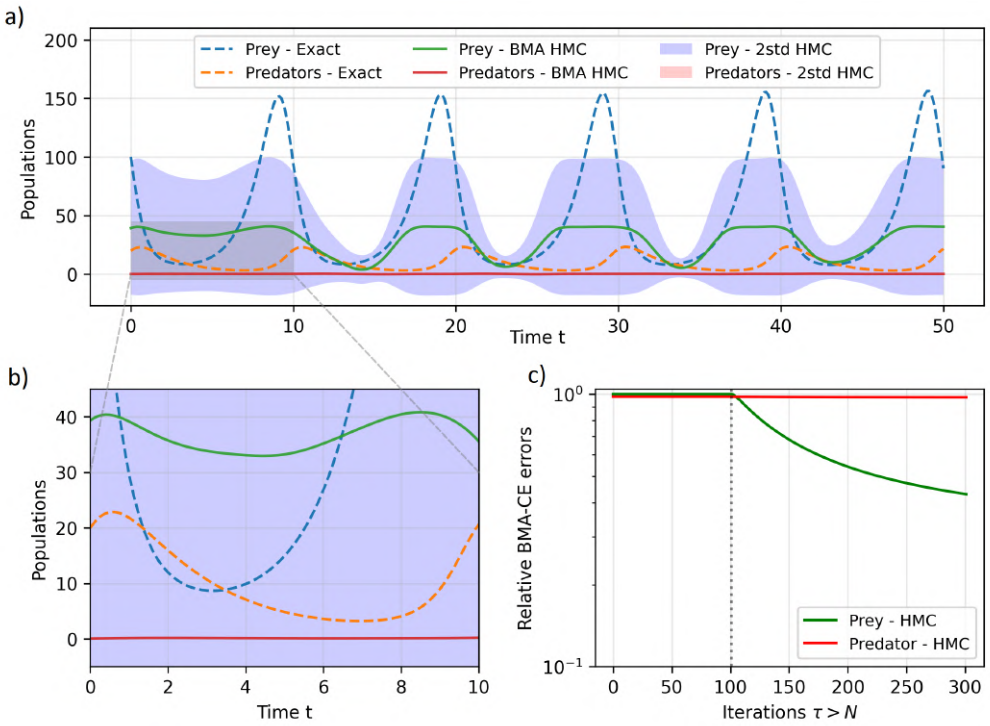


**Figure 4.12: Failure mode of classical HMC, with uniform weighting, on the Lotka-Volterra multiscale inverse problem defined in Sect. 4.5.3.** a) BMA predictions for the two-species populations along the physical time with their uncertainties, with a zoomed version in b). c) Relative BMA-CE errors throughout the sampling iterations illustrate the lack of convergence of the method.

of the samples — with an acceptance rate less than $1\%$ — due to non-conservation of the Hamiltonian trajectories along the leapfrog steps. Hence, this confirms the lack of robustness of the BPINNs-HMC paradigm when facing instability issues due to multiscale dynamics.

The NUTS alternative also struggles to converge on this multiscale inverse problem and results in inadequate predictions, especially for the predator population. Here the reason is not the massive sample rejection but rather a prohibitive decrease in the time step, reaching $\delta t = 8.26\text{e}{-5}$ and $2.81\text{e}{-5}$, respectively, at the end of the adaptive steps — nearly corresponding to a ten-fold drop in the time step, compared to AW-HMC. The relative BMA-CE errors (in Figure 4.13c) reveal that this time step adaptation is suitable for the convergence of the prey population since it appears to be the most sensitive task. This sensitivity should be understood in the sense that small variations with respect to $\Theta$ on the potential energy induce the strongest constraint on the Hamiltonian energy conservation. However, the time-step adaptation is not satisfactory for the predator population and even leads to inefficient forgetting of the neural network throughout the sequential training. This translates into misleading predictions on the evolution of the population (see Figure 4.13a and b) and unsuccessful inference of the inverse parameters. Indeed, Figure 4.14 represents the histograms of the marginal posterior distributions for the four inverse parameters, along with the phase diagrams of their trakectories troughout the sampling. These phase diagrams demonstrate the difficulties of the NUTS sampler in adequately identifying the modes resulting from separate scales. Overall, the NUTS sampler suffers from a lack of convergence toward the Pareto front and a misleading inference of the inverse parameters, subject to weakly-informed priors, due to its inability to capture multiscale behaviors.

### 4.5.3 Robust Bayesian Inference on multiscale Lotka-Volterra inverse problem

On such an inverse problem, we demonstrated the classical BPINNs-HMC algorithm faces massive rejection since the Hamiltonian trajectories are not conserved, which results in inoperative sampling. Even the adaptive strategies on the time step struggle to deal with the multiscale dynamics and require an extreme decrease in the $\delta t$ value to obtain some stability, as detailed in

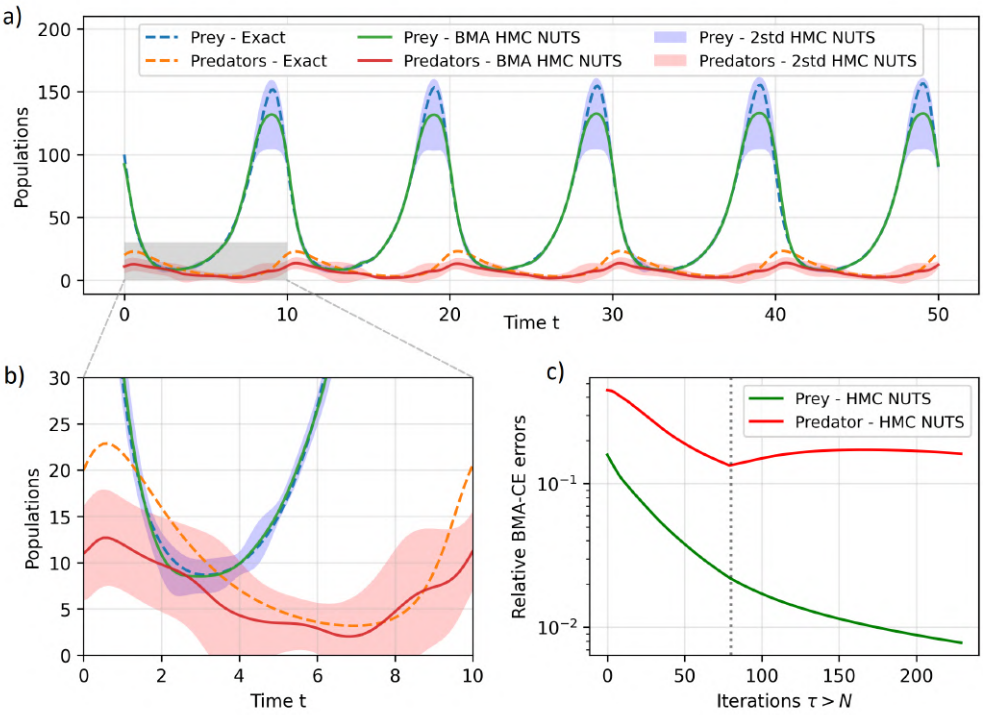


**Figure 4.13: Failure mode of HMC with NUTS adaptation on the Lotka-Volterra multiscale inverse problem defined in Sect. 4.5.3.** a) BMA predictions for the two-species populations along the physical time with their uncertainties, with a zoomed version in b). c) Relative BMA-CE errors throughout the sampling iterations showing an imbalance between the tasks and preferential adaptation of the prey population.

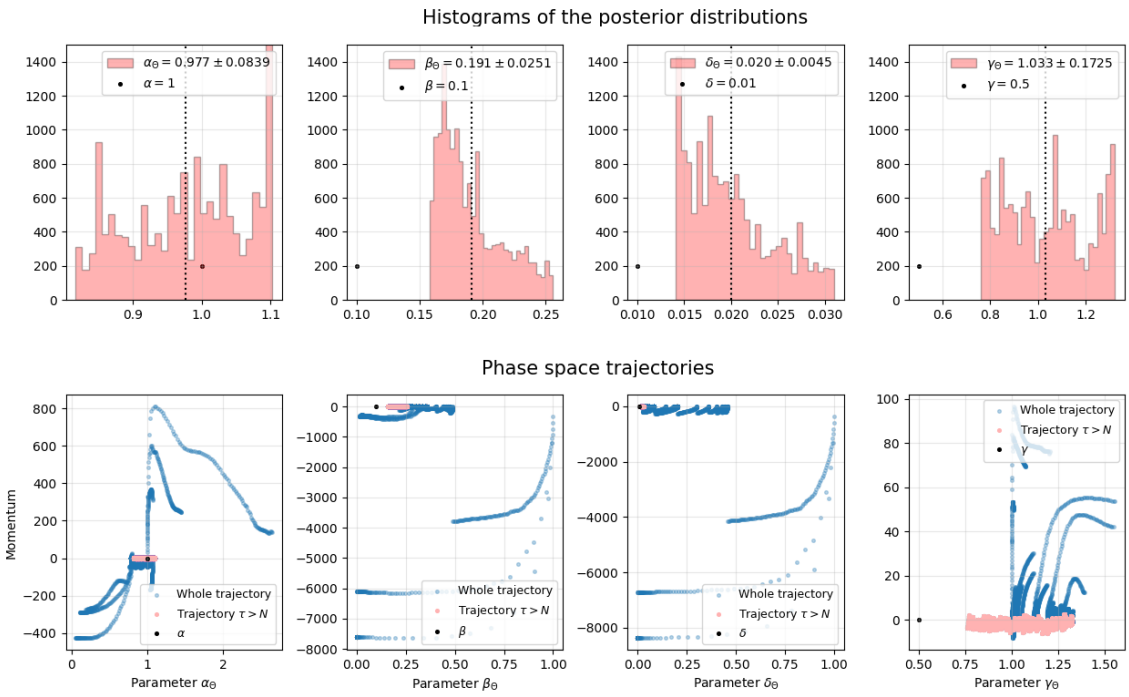


**Figure 4.14: Failure mode of HMC with NUTS on the Lotka-Volterra multiscale inference.** Top pictures show histograms of the marginal posterior distributions for the inverse parameters. Bottom pictures show phase diagrams of their trajectories throughout the sampling. The biased predictions from Figure 4.13 prevent proper inference of the inverse parameters, leading to random walk pathological behavior in the updated parameters.

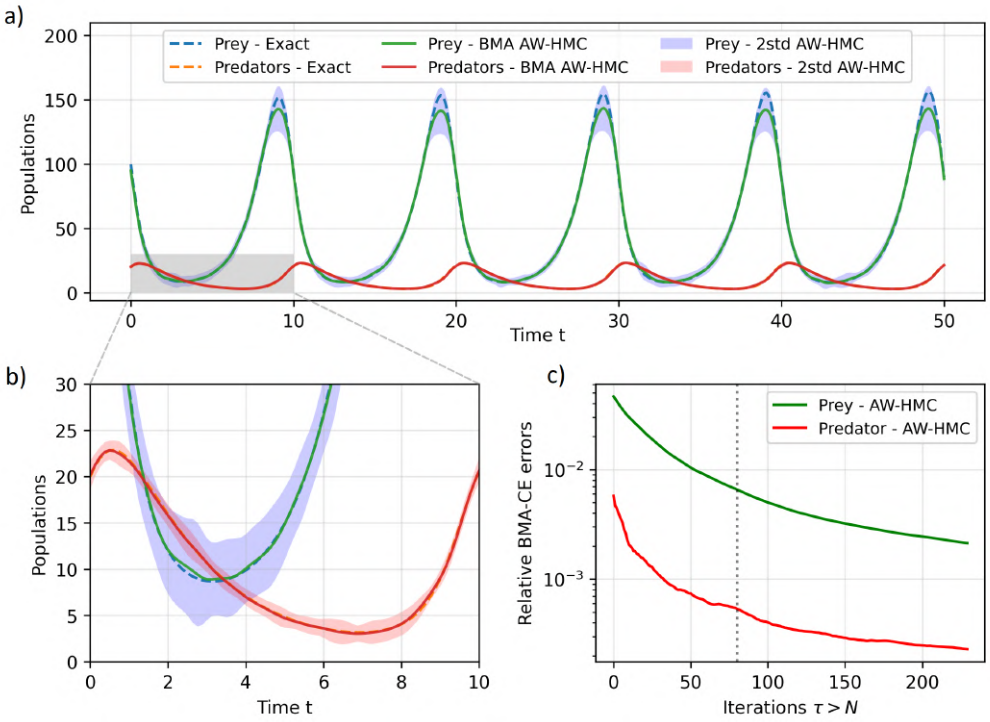


**Figure 4.15: Lotka-Volterra multiscale inference:** a) BMA predictions of the two-species populations along the physical time with their uncertainties, zoomed on b). c) Relative BMA-CE errors for the neural network outputs $y = (u_\Theta, v_\Theta)$ plotted throughout the sampling iterations. The dotted vertical line marks the introduction of the ODE-likelihood terms in the sequential training.

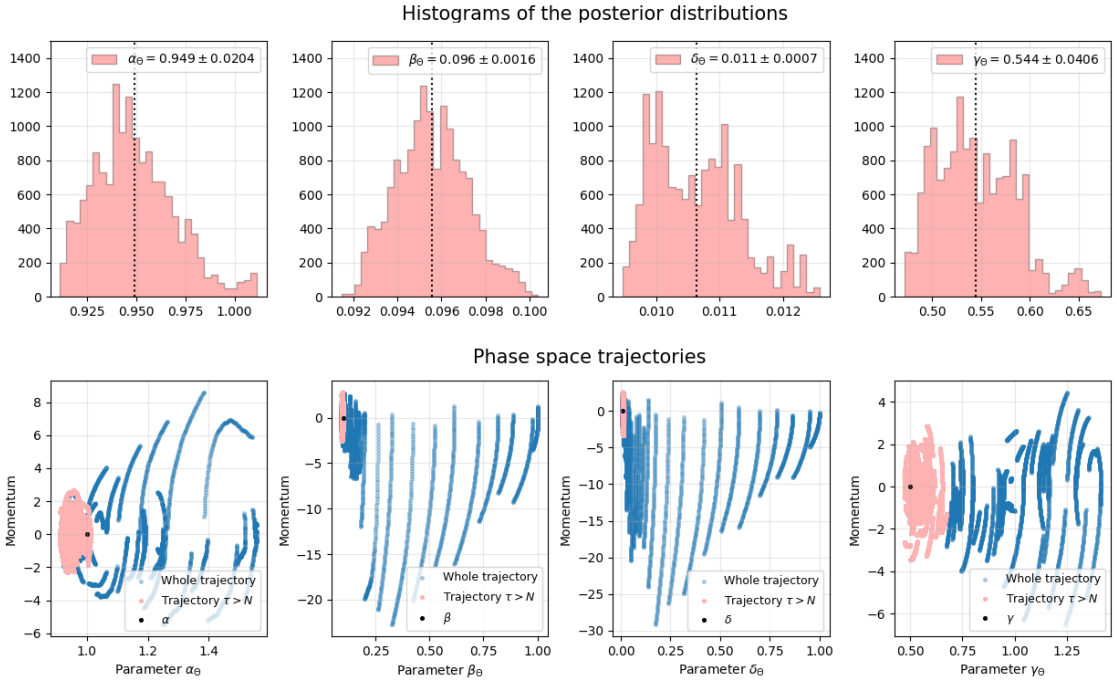


**Figure 4.16: Posterior distributions of the inverse parameters on the Lotka-Volterra multiscale inference**. Top pictures show histograms of the marginal posterior distributions for the inverse parameters $(\mathcal{P}_{\text{inv}})_\Theta = \{\alpha_\Theta, \beta_\Theta, \delta_\Theta, \gamma_\Theta\}$. Bottom pictures show phase diagrams of the parameter trajectories throughout the sampling that characterized convergence toward their respective modes during the adaptive steps (in blue) and efficient exploration of the mode neighborhood after the adaptive steps (in red). The ground truth parameters are respectively $\mathcal{P}_{\text{inv}} = \{\alpha, \beta, \delta, \gamma\} = \{1, 0.1, 0.01, 0.5\}$ and establish an inverse problem with separate scales.

| Seq. step \ $\lambda_k$ | $\lambda_0$ | $\lambda_1$ | $\lambda_2$ | $\lambda_3$ |
|---|---|---|---|---|
| Data-fitting (step 1) | 3.83e−2 | 1 | — | — |
| Data-fitting + ODE tasks (step 2) | 4.87e−2 | 1 | 9.16e−3 | 1.16e−1 |

| Seq. step \ $\widetilde{\sigma}_k$ | $\widetilde{\sigma}_0$ | $\widetilde{\sigma}_1$ | $\widetilde{\sigma}_2$ | $\widetilde{\sigma}_3$ |
|---|---|---|---|---|
| Data-fitting (step 1) | 5.109 | 1 | — | — |
| Data-fitting + ODE tasks (step 2) | 4.531 | 1 | 10.45 | 2.936 |

**Table 4.1:** Weight parameters $\lambda_k$ obtained after the adaptive steps in the Lotka-Volterra multiscale inverse problem, for each of the sequential steps (top rows). Effective standard deviations $\widetilde{\sigma}_k$ resulting from the weight adaptations and computed as $\widetilde{\sigma}_k = \sqrt{1/\lambda_k}$ for each of the sequential steps (bottom rows). This highlights enhanced uncertainties on the tasks related to the prey species. The splitting of the sequential steps is detailed in Sect. 4.5.1.

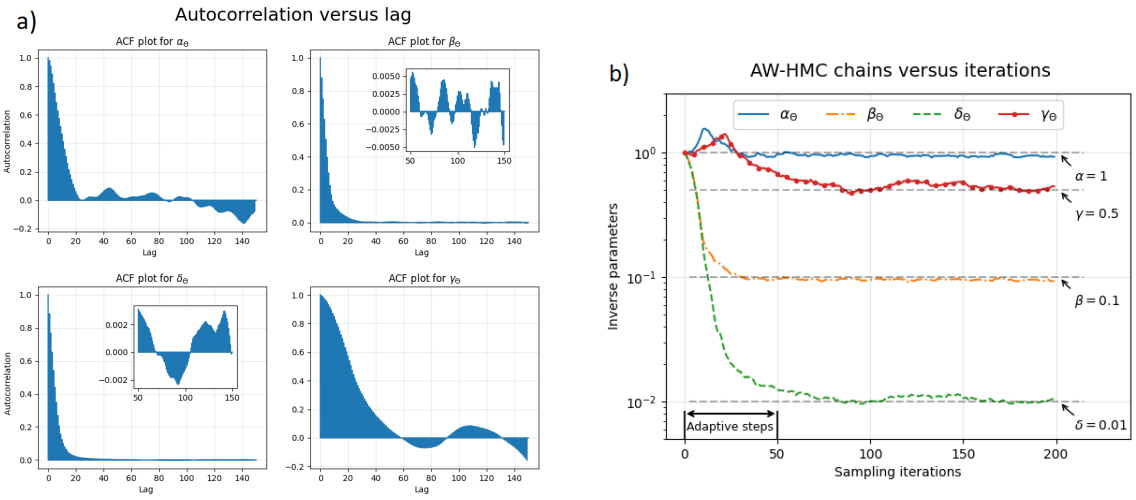


**Figure 4.17: Convergence diagnostics on the Lotka-Volterra multiscale inference problem:** a) Lag-k Autocorrelation Functions (ACF) of the inverse parameters $(\mathcal{P}_{\text{inv}})_\Theta = \{\alpha_\Theta, \beta_\Theta, \delta_\Theta, \gamma_\Theta\}$, plotted versus lag. b) Inverse parameters chain traces along the sampling iterations of the AW-HMC sampler, showing convergence toward their respective single modes during the adaptive steps. The groundtruth values of each parameter are respectively represented by the grey horizontal dotted lines.

Sect. 4.5.2. The natural implication of such constraints on the leapfrog time step is lack of convergence toward the Pareto front and poor inference of the inverse parameters, subject to weakly informed priors (see Figure 4.13 and 4.14 from Sect. 4.5.2). In fact, Linka *et al.* [173] addressed the same issue on learning COVID-19 dynamics and imposed (in Sect. 4.3 of [173]) log-normal prior distributions on the inverse parameters that already rely on appropriate scaling. The need for such appropriate scaling strongly impacts the inference in the sense that it requires prior knowledge which biases the sampling.

On the contrary, we assume independent priors with respect to the scaling and show that our AW-HMC approach is able to properly recover all the $\mathcal{P}_{\text{inv}}$ parameters as well as predict the species evolution with minimal tuning and decrease on $\delta t$. The recovery of separate scales no longer requires prior knowledge of the inverse parameter scaling to converge to their respective single modes. The results shown in Figure 4.16 represent both the marginal posterior distributions of each inferred inverse parameter $(\mathcal{P}_{\text{inv}})_\Theta$ and their trajectories when exploring the phase space distribution $\pi(\Theta, r)$. For the latter, we plotted the entire sampling trajectories that converge toward their respective mode during the adaptive steps, to finally sample around them as illustrated by the final trajectories for $\tau > N$. This confirms the ability of AW-HMC to quickly identify the separate modes of this inverse problem and manage such multiscale dynamics.

We also ensure that the number of overall samples is sufficient to provide meaningful estimates of the posterior distribution (in Figure 4.16) through a convergence diagnostic based on the autocorrelation of the samples. Therefore, we compute the lag-k Autocorrelation Function (ACF), identified as a standard metric for chain convergence characterization [134, 167, 259] and defined as the correlation between samples k steps apart. We apply it to the AW-HMC chains for the four inverse parameters in the Lotka-Volterra inference problem. Figure 4.17a shows the results of lag-k autocorrelation for their respective AW-HMC chain traces from Figure 4.17b. This diagnostic rapidly drops as k increases, indicating fast mixing of the chains and a fast decorrelation of the samples from the non-informative initializations. Hence, it suggests efficient convergence of the AW-HMC chains toward the inverse parameter modes and reliable estimation of the posterior distributions.

In order to quantify the effectiveness in identifying the parameters, we also measure the relative error in the inference of each inverse parameter $(\mathcal{P}_{\text{inv}})_\Theta = \{\alpha_\Theta, \beta_\Theta, \delta_\Theta, \gamma_\Theta\}$, with for instance:

$$E_{\alpha_\Theta} = \frac{|\alpha_\Theta - \alpha|}{|\alpha|} \tag{4.46}$$

where the prediction is given by $\alpha_\Theta = \dfrac{1}{N_s - N} \displaystyle\sum_{i=N}^{N_s} e^{\widetilde{\alpha_\Theta}^{t_i}}$. We show that these relative errors all scale around $5\text{e}{-2}$ for the four inverse parameters. The predictive evolution of the species populations is displayed in Figure 4.15, as a BMA on the neural network outputs $y = (u_\Theta, v_\Theta)$, and compared to the exact solutions in a qualitative and quantitative way. In this sense, we computed relative BMA cumulative errors for both the species, highlighting the convergence of the sampling, in Figure 4.15c. We see that the insertion of the ODE-residual likelihood terms in the two-step sequential training improves the convergence of the predictions when compared to pure data-based sampling.

This test case also reveals higher uncertainties on the evolution of the prey population characterized by effective standard deviations about four times greater (see Table 4.1). The enhanced uncertainty on these specific tasks is highlighted by smaller values of $\lambda_0$ and $\lambda_2$ at the end of the adaptive steps, compared to $\lambda_1$ and $\lambda_3$ in the potential energy (4.45). Therefore, the AW-HMC strategy benefits from its ability to adaptively weight the $\lambda$ parameters to intrinsically characterize the task uncertainties based on their gradient variances.

## 4.6 Application to Computational Fluid Dynamics: Stenotic Blood Flow

We illustrate the use of the methodology set out in Sect. 4.4.1 in a real-world problem from fluid mechanics, more precisely the study of inpainting and inverse problems on incompressible stenotic flows in asymmetric geometries. The objective is to demonstrate the generalization and performance of the present AW-HMC algorithm on more complex 2D geometries and nonlinear PDE dynamics under noise and sparsity of the data.

The measurement data are generated by randomly sampling the fully resolved CFD solutions on scattered locations. The direct numerical simulation of vascular flows in asymmetric stenotic vascular geometries is performed using a meshless solver based on a Discretization-Corrected Particle Strength Exchange (DC-PSE) method as detailed in [55].

### 4.6.1 Inpainting problem with sparse and noisy data

Inpainting problems have drawn increasing interest in MRI (Magnetic Resonance Imaging) or CT (Computed Tomography) medical imaging as an opportunity to reduce artifacts and recover missing information by using deep learning approaches [30, 192, 301]. Although the usual inpainting framework incorporates only measurement data in the image processing, Zheng *et al.* investigated a physics-informed version of the problem by incorporating the underlying physics

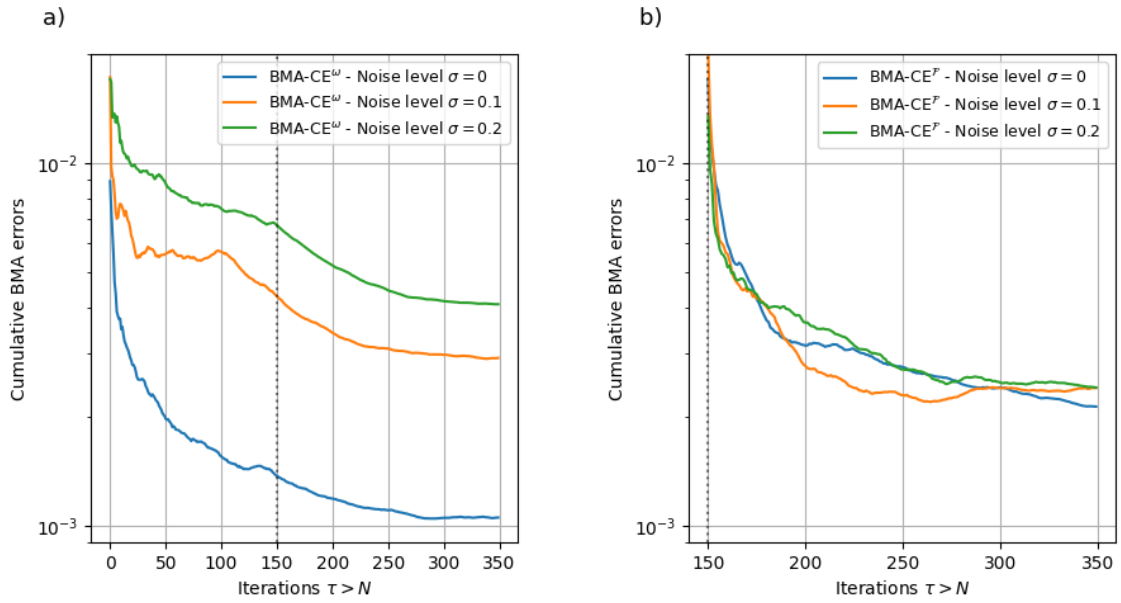


**Figure 4.18: Bayesian Model Average Cumulative Error diagnostics, as defined in (4.51), for the vorticity physics-informed inpainting problem:** a) BMA-CE on the vorticity field prediction throughout the sampling iterations and for different noise levels. b) BMA-CE on the PDE residual $\mathcal{F}$ satisfying (4.48) for different noise levels. The dotted vertical lines mark the introduction of the PDE constraint in the two-step sequential training.

as indirect measurements [340]. The present section falls within the same context: the idea is to infer the whole flow reconstruction based on sparse and noisy measurements while imposing PDE constraints on some complementary collocation points.

The governing equations of the stenotic flow dynamic are written here in a velocity $\mathbf{u} = (u, v)$ and vorticity $\omega$ formulation in two dimensions, satisfying an incompressible steady-state Navier-Stokes equation given by

$$(\mathbf{u} \cdot \nabla)\omega = Re^{-1}\Delta\omega, \quad \text{in } \Omega \tag{4.47}$$

or equivalently

$$u\frac{\partial \omega}{\partial x} + v\frac{\partial \omega}{\partial y} = \frac{1}{Re}\Delta\omega, \quad \text{in } \Omega \tag{4.48}$$

where $Re$ refers to the dimensionless Reynolds number, $\omega$ is the vorticity field $\omega = \dfrac{\partial v}{\partial x} - \dfrac{\partial u}{\partial y}$ and the incompressibility condition ensures $\operatorname{div} \mathbf{u} = 0$. We consider the 2D stenotic spatial domain $\Omega \subset [0, 10] \times [0, 1]$ and assume two different kinds of boundary conditions:

- the stenosis upper and lower walls, denoted $\partial\Omega_1$, where we impose no-slip conditions such that $\mathbf{u}_{\partial\Omega_1} = 0$ and $\omega = (\nabla \times \mathbf{u})_{\partial\Omega_1}$,
- the inlet and outlet boundaries, denoted $\partial\Omega_2$, with a prescribed parabolic profile and Neumann condition, respectively, on the velocity in the main flow direction.

These boundary conditions are detailed in Sect. 4.4 of the DC-PSE article [55]. We also first consider that the Reynolds number is known and set to $Re = 200$ according to the CFD simulations, such that the set of parameters to infer $\Theta$ is restricted here to the neural network weights and bias.

The measurement dataset, $\mathcal{D}$, is composed of noisy vorticity data on $\mathcal{D}^{\partial_1}$ and $\mathcal{D}^{\partial_2}$, defined as in (4.12) respectively for the boundary sets $\partial\Omega_1$ and $\partial\Omega_2$. We also consider sparse and noisy vorticity data on 1282 interior collocation points $\mathcal{D}^{\omega}$ that cover less than 2% of all the data required for the full vorticity field reconstruction on the spatial domain $\Omega$. We finally defined $\mathcal{D}^{\Omega}$ the dataset of 6408 interior points, representing 6% of the entire reconstructed data field, wherein the PDE

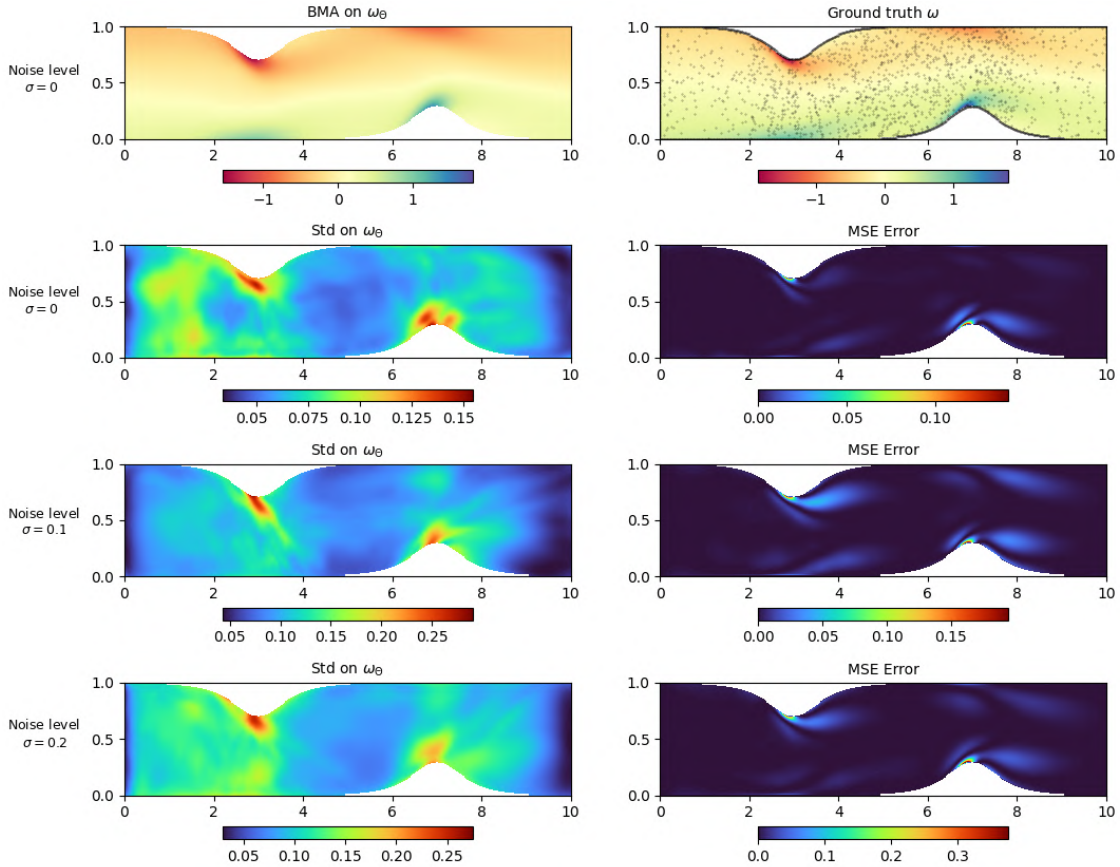


**Figure 4.19: Uncertainty quantification on the physics-informed inpainting problem:** BMA prediction of the vorticity field $\omega_\Theta$ in asymmetric stenosis without noise, compared to the ground truth solution $\omega$ (top row). The black dots on the exact field correspond to the training measurements of the dataset $\mathcal{D}$. Comparison of the uncertainty standard deviations (Std) and mean squared errors (MSE) on the predicted vorticity field $\omega_\Theta$ for different noise levels ($\sigma = 0, 0.1, 0.2$), shown in the bottom rows.

(4.48) is satisfied in this physically-constrained inpainting formulation. The multi-potential energy is then defined by:

$$U(\Theta) = \frac{\lambda_0}{2\sigma_0^2} \left\| \omega_\Theta - \omega \right\|_{\mathcal{D}^\omega}^2 + \frac{\lambda_1}{2\sigma_1^2} \left\| \omega_\Theta - \omega_{\,|\partial\Omega_1} \right\|_{\mathcal{D}^{\partial_1}}^2 + \frac{\lambda_2}{2\sigma_2^2} \left\| \omega_\Theta - \omega_{\,|\partial\Omega_2} \right\|_{\mathcal{D}^{\partial_2}}^2 + \frac{\lambda_3}{2\sigma_3^2} \left\| u_n \frac{\partial \omega_\Theta}{\partial x} + v_n \frac{\partial \omega_\Theta}{\partial y} - \frac{1}{Re} \Delta \omega_\Theta \right\|_{\mathcal{D}^\Omega}^2 + \frac{1}{2\sigma_\Theta^2} \left\| \Theta \right\|_{\mathbb{R}_p}^2 \tag{4.49}$$

with $u_n$ and $v_n$ noisy evaluations of the velocity field on the $\mathcal{D}^\Omega$ set. We then used sequential training by adding the PDE-residual likelihood term in the second sampling phase, such that the AW-HMC parameters are given first by $N = 50$ and $N_s = 200$, and then $N = 50$ and $N_s = 250$ for a leapfrog path length $L = 150$ and time step $\delta t = 5\text{e}{-4}$. As for the previous benchmarks, we set all the $\sigma_k$ equal to one and assume a centered normal distribution with the standard deviation $\sigma_\Theta = 10$ for the neural network parameters prior. The neural network is composed of 4 layers with 32 neurons per layer and is based on the hyperbolic tangent activation function. The velocity and vorticity CFD solutions $(\mathbf{u}, \omega)$ are both corrupted by additive Gaussian noise such that

$$\bullet_n = \bullet + \sigma\xi \quad \text{where} \quad \xi \sim \mathcal{N}(0, \psi^2) \tag{4.50}$$

is a vector of element-wise independent and identically-distributed Gaussian random numbers with mean zero and variance $\psi^2 = \mathrm{Var}\{\bullet\}$, and $\sigma$ refers to the level of added noise.

In this physics-informed inpainting problem, we investigate the impact of the level of noise $\sigma$ on the BMA predictions of the vorticity field, as well as on the physical constraint by extending the

| Noise level \ $\lambda_k$ | $\lambda_0$ | $\lambda_1$ | $\lambda_2$ | $\lambda_3$ |
|---|---|---|---|---|
| $\sigma = 0$ | 1 | 0.46 | 0.88 | 0.51 |
| $\sigma = 0.1$ | 1 | 0.19 | 0.35 | 0.29 |
| $\sigma = 0.2$ | 1 | 0.12 | 0.39 | 0.27 |

| Noise level \ $\widetilde{\sigma}_k$ | $\widetilde{\sigma}_0$ | $\widetilde{\sigma}_1$ | $\widetilde{\sigma}_2$ | $\widetilde{\sigma}_3$ |
|---|---|---|---|---|
| $\sigma = 0$ | 1 | 1.47 | 1.07 | 1.40 |
| $\sigma = 0.1$ | 1 | 2.29 | 1.69 | 1.86 |
| $\sigma = 0.2$ | 1 | 2.89 | 1.60 | 1.92 |

**Table 4.2:** Final $\lambda_k$ weight parameters for each noise level $\sigma$ in the physics-informed inpainting problem (top rows). Effective $\widetilde{\sigma}_k$ standard deviations resulting from the weight adaptations and computed as $\widetilde{\sigma}_k = \sqrt{1/\lambda_k}$ for each noise level (bottom rows). This highlights the overall adaptation of the effective standard deviations to the noise magnitude and the task sensitivities to the noise level. In particular, the wall-boundary conditions associated with $\lambda_1$ present the highest noise sensitivity.

notion of BMA convergence to the PDE residual. Hence, we compute the BMA-CE diagnostics for the field $\omega$ and the PDE constraint based on

$$\begin{aligned} \text{BMA-CE}^{\omega}(\tau) &= \left\| \frac{1}{\tau - N} \sum_{i=N}^{\tau} P\left(\omega_\Theta \,|\, x, \Theta^{t_i}\right) - \omega \right\|^2 \\ \text{BMA-CE}^{\mathcal{F}}(\tau) &= \left\| \frac{1}{\tau - N} \sum_{i=N}^{\tau} P\left(\mathcal{F}(\omega_\Theta) \,|\, x, \Theta^{t_i}\right) \right\|^2 \end{aligned} \tag{4.51}$$

with $\mathcal{F}(\omega_\Theta)$ the evaluation of the PDE residual from equation (4.48). The comparative curves for different noise levels are represented in Figure 4.18a and show sampling convergence toward final BMA errors on $\omega$ that scale about $1.05\text{e}{-3}$, $2.9\text{e}{-3}$ and $4.08\text{e}{-3}$, respectively, for noise levels $\sigma = 0,\ 0.1$ and $0.2$. In addition, we see in Figure 4.18b that the PDE residual constraints converge independently to the noise level, reaching final BMA errors around $2\text{e}{-3}$ in all cases.

To supplement the performance quantification of the inpainting formulation in recovering the entire vorticity field along with its uncertainty, we also use the Prediction Interval Coverage Probability (PICP) metric as defined by Yao *et al.* [331]. This consists of a quality indicator of the posterior approximation, which evaluates the percentage of the ground truth observations contained within 95% of the prediction interval, as given by:

$$PICP = \frac{1}{N_{\text{obs}}} \sum_{i=1}^{N_{\text{obs}}} \mathbb{1}_{(\omega_\Theta^l)_i \leq \omega_i \leq (\omega_\Theta^h)_i} \tag{4.52}$$

where $\omega_\Theta^l$ and $\omega_\Theta^h$ are respectively the 2.5% and 97.5% percentiles of the predictive distribution on the vorticity. In this case, the notation $N_{\text{obs}}$ refers to the total number of observations in the predictive dataset, in other words, the grid resolution of the computational domain $\Omega$. In our application, this PICP metric shows that more than 99% of the vorticity ground truth observations are covered by the posterior distribution of the neural network output $\omega_\Theta$, independently of the level of noise.

We also expect our self-weighted adaptation of $\lambda_k$ to be able to capture noise sensitivity with respect to the value of $\sigma$, and intrinsic task sensitivities to noise level without imposing any a-priori on the noise level estimation. This is the key point of our methodology since we intentionally decouple the setting of the parameters $\sigma_k$ in (4.49) from the noise magnitude, and rely on the self-weighted strategy to quantify their related uncertainties. On the contrary, when dealing with

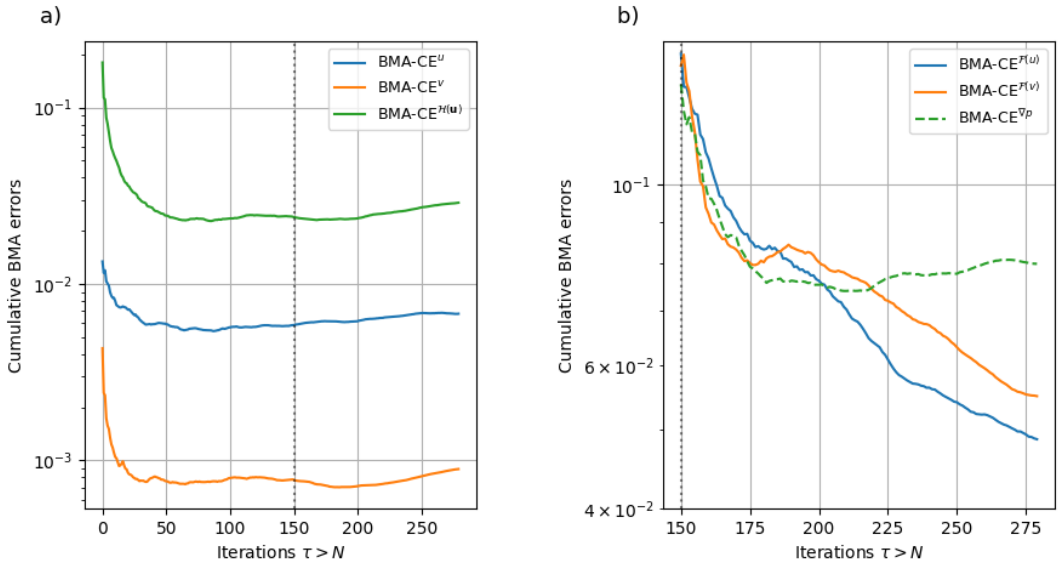


**Figure 4.20: Bayesian Model Average Cumulative Errors diagnostics for the CFD inverse problem:** a) BMA-CE throughout the sampling iterations for the velocity field components $\mathbf{u} = (u, v)$ and the divergence-free condition $\mathcal{H}(\mathbf{u})$. b) BMA-CE on the PDE residuals $\mathcal{F}(u)$ and $\mathcal{F}(v)$. The dotted curve represents the a-posteriori checking of pressure gradient norm BMA-CE error as defined in equation (4.57). The dotted vertical lines, in both figures, delimit the two stages of sequential training.

noisy measurement data in applications one frequently assumes the fidelity of each sensor to be known and sets the standard deviations $\sigma_k$ accordingly. They can also be defined as additional learnable parameters to be inferred. The latter is usually subject to additional computational costs in *online* learning or requires alternative neural network formalism used as pre-training in *offline* learning [249]. In contrast, the strength of the AW-HMC methodology relies on its similar computational cost compared to classical BPINNs-HMC. Moreover, AW-HMC improves convergence by drawing attention to exploring the Pareto front with optimal integration time. Therefore, it can shorten overall sampling requirements making this a competitive strategy in terms of computational cost.

The results presented in Figure 4.19 demonstrate the noise resistance of the AW-HMC approach and highlight sensitivity consideration with respect to the noise and tasks (see Table 4.2). We first noticed differences in the auto-adjustment of the lambda values relative to noise levels, leading to global enhanced uncertainties with increasing noise. We also observed various uncertainty adjustments depending on the sensitivity of the different tasks to the noise. In fact, the comparison of the local standard deviations on the vorticity field in Figure 4.19 shows that the wall boundary conditions are the most sensitive to noise, automatically increasing the uncertainties in these areas. The inlet and outlet boundaries are rather less sensitive. This is highlighted by a lower adaptation of their uncertainties to the noise level. In short, this application has shown the ability of our new adaptive methodology to automatically adjust the weights, and with them the uncertainties, to the intrinsic task sensitivities to the noise and to adapt the uncertainty to the noise magnitude itself.

### 4.6.2 Inverse problem with parameter estimation and latent field recovery

As a second CFD application, we consider a multi-objective flow inverse problem in an asymmetric and steep stenosis geometry. This aims to provide both a parameter estimation of the flow regime and recover a hidden field using our adaptively weighted strategy. Such considerations, motivated by real-world applications, use incomplete or corrupted measurement data in an attempt to derive additional information, which remains challenging or impractical to obtain straightforwardly.

With an emphasis on physical and biomedical problems, Raissi *et al.* investigated the ex-

traction of hidden fluid mechanics quantities of interest from flow visualizations, using physics-informed deep learning [255, 256]. The authors relied only on measurements of a passive scalar concentration that satisfied the incompressible Navier-Stokes equations, to infer the velocity and pressure fields in both external and internal flows.

In this direction, we focus on the velocity $\mathbf{u} = (u, v)$ and pressure $p$ formulation of the stenotic flow dynamics such that the continuity and momentum governing steady-state equations are written:

$$\begin{cases} (\mathbf{u} \cdot \nabla)\mathbf{u} = -\nabla p + Re^{-1}\Delta \mathbf{u}, & \text{in } \Omega \\ \quad \operatorname{div} \mathbf{u} = 0, & \text{in } \Omega \end{cases} \tag{4.53}$$

under the incompressibility condition on the stenotic domain $\Omega \subset [0, 10] \times [0, 1]$. We impose adherent boundary conditions on the wall interfaces such that $\mathbf{u}_{\partial\Omega_1} = 0$, and the following inlet/outlet boundary conditions respectively:

$$\begin{aligned} u = 4y - 4y^2,\ v = 0 \quad & \forall (x, y) \in \{0\} \times [0, 1] \\ \frac{\partial u}{\partial x} = 0,\ v = 0 \quad & \forall (x, y) \in \{10\} \times [0, 1]. \end{aligned} \tag{4.54}$$

The direct numerical simulation is performed using the DC-PSE formulation [55] with a Reynolds number set to $Re = 200$, as in the previous section. It is used to generate the observation data on $\Omega$ with a thin resolution. The $\mathcal{D}$ dataset is then composed of partial measurements of $\mathbf{u}$ randomly sampled to consider 9559 training points, representing less than 3% of the entire target resolution and respectively defining $\mathcal{D}^{\mathbf{u}}$ and $\mathcal{D}^{\partial}$ the sets of interior and boundary points. The same collocation points define $\mathcal{D}^{\Omega}$, where we impose the PDE constraints from the model (4.53), denoted $\mathcal{F}(\mathbf{u}) := (\mathcal{F}(u), \mathcal{F}(v))$, as well as the diverge-free condition $\mathcal{H}(\mathbf{u})$.

Finally, we set up the inverse problem by inferring the flow regime, considering the Reynolds number as an unknown model parameter $\mathcal{P}_{\text{inv}} = \{Re\}$. At the same time, we address the multitask problem to recover the latent pressure field $p_\Theta$ based upon partial measurements of the velocity field and fluid flow dynamics assumptions. The pressure field prediction, in particular, is adjusted throughout the sampling in such a way that its gradient satisfies the governing equations (4.53). As commonly established by the nature of the Navier-Stokes equation, the pressure is though not uniquely defined and, given the lack of precise boundary conditions on this field, is thus determined up to a constant.

Besides, the steep stenosis geometry considered in this problem generates sharp gradients at the wall interface. The latter needs to be adequately captured to obtain consistency in the inference of the latent pressure and inverse parameter. Hence, we complemented the training with some partial measurements of the first-order derivatives of the velocity. This enables us to ensure that the convective terms, in the PDE constraints (4.53), are consistent with the velocity data and therefore infer the corresponding pressure field. The multi-potential energy is thus written as:

$$\begin{aligned} U(\Theta) = & \frac{\lambda_0}{2\sigma_0^2} \left\| u_\Theta - u \right\|_{\mathcal{D}^{\mathbf{u}}}^2 + \frac{\lambda_1}{2\sigma_1^2} \left\| v_\Theta - v \right\|_{\mathcal{D}^{\mathbf{u}}}^2 + \frac{\lambda_2}{2\sigma_2^2} \left\| u_\Theta - u \right\|_{\mathcal{D}^{\partial}}^2 + \frac{\lambda_3}{2\sigma_3^2} \left\| v_\Theta - v \right\|_{\mathcal{D}^{\partial}}^2 \\ & + \frac{\lambda_4}{2\sigma_4^2} \left\| \partial_x u_\Theta - \partial_x u \right\|_{\mathcal{D}^{\mathbf{u}}}^2 + \frac{\lambda_5}{2\sigma_5^2} \left\| \partial_x v_\Theta - \partial_x v \right\|_{\mathcal{D}^{\mathbf{u}}}^2 + \frac{\lambda_6}{2\sigma_6^2} \left\| \partial_x u_\Theta - \partial_x u \right\|_{\mathcal{D}^{\partial}}^2 \\ & + \frac{\lambda_7}{2\sigma_7^2} \left\| \partial_x v_\Theta - \partial_x v \right\|_{\mathcal{D}^{\partial}}^2 + \frac{\lambda_8}{2\sigma_8^2} \left\| \partial_y u_\Theta - \partial_y u \right\|_{\mathcal{D}^{\mathbf{u}}}^2 + \frac{\lambda_9}{2\sigma_9^2} \left\| \partial_y u_\Theta - \partial_y u \right\|_{\mathcal{D}^{\partial}}^2 \\ & + \frac{\lambda_{10}}{2\sigma_{10}^2} \left\| Re_\Theta^{-1} \Delta u_\Theta - (u_\Theta \partial_x u_\Theta + v_\Theta \partial_y u_\Theta) - \partial_x p_\Theta \right\|_{\mathcal{D}^{\Omega}}^2 + \frac{\lambda_{11}}{2\sigma_{11}^2} \left\| \operatorname{div} u_\Theta \right\|_{\mathcal{D}^{\Omega}}^2 \\ & + \frac{\lambda_{12}}{2\sigma_{12}^2} \left\| Re_\Theta^{-1} \Delta v_\Theta - (u_\Theta \partial_x v_\Theta + v_\Theta \partial_y v_\Theta) - \partial_y p_\Theta \right\|_{\mathcal{D}^{\Omega}}^2 + \frac{1}{2\sigma_\Theta^2} \|\Theta\|_{R_{p+1}}^2 \end{aligned} \tag{4.55}$$

where the notation $\|\cdot\|$ refers to either the RMS norm on $\mathcal{D}^\bullet$ or the usual Euclidean norm on $\mathbb{R}^{p+1}$. Finally, the predictions of each of the QoI, namely the surrogate models on the velocity and pressure, are then recovered on the original finer resolution in Figure 4.21. As in Sect. 4.5.3, we select

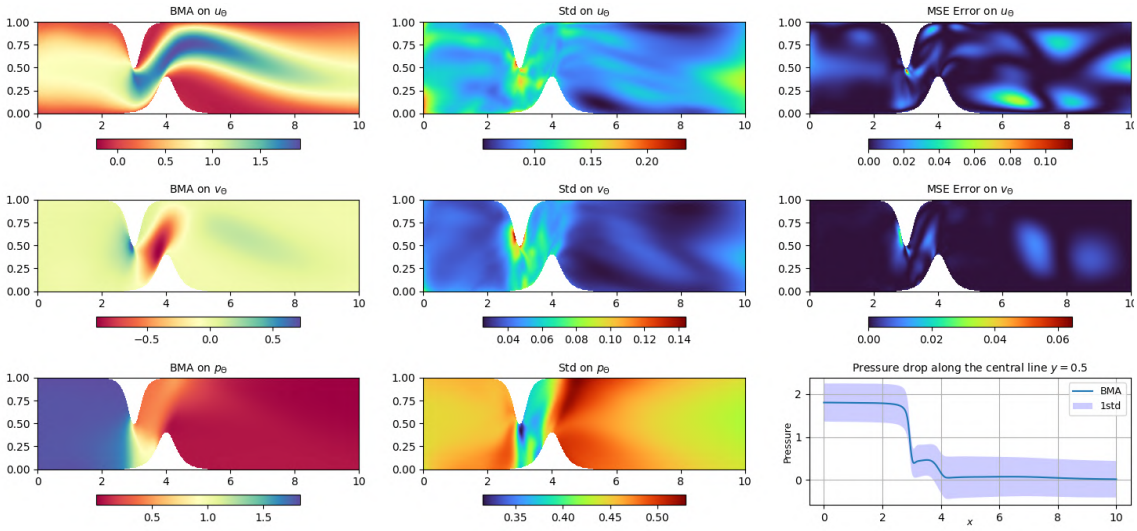


**Figure 4.21: Uncertainty quantification on the CFD inverse problem:** BMA predictions of the velocity field $\mathbf{u}_\Theta = (u_\Theta, v_\Theta)$ in asymmetric stenosis along with their uncertainty standard deviations (Std) and mean squared errors (MSE), at the top. BMA and uncertainty on the inferred latent pressure field with the pressure evolution plotted along the central line $y = 0.5$, leading to an average pressure drop of $1.78$ — bottom.

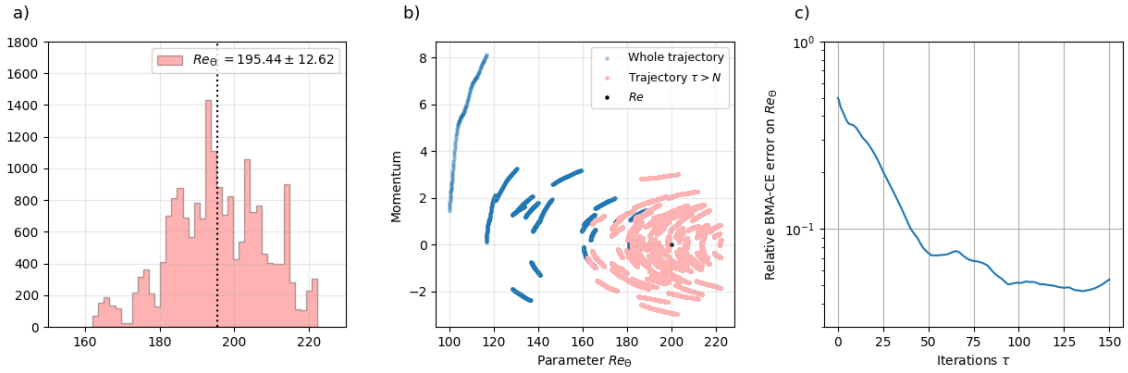


**Figure 4.22: Reynolds number posterior distribution and convergence diagnostic in CFD inverse problem:** a) Histogram of the marginal posterior distribution for the inverse Reynolds parameter. b) Phase diagram of its trajectory throughout the sampling, with the adaptive steps trajectories (in blue) and effective sampling (in red). c) BMA-CE error using the absolute relative norm as defined in (4.56). The relative BMA-CE error on $Re_\Theta$ is plotted over all the $\tau$ iterations of the second step sampling in the sequential training.

a log-normal prior distribution for the physical parameter and independent normal distributions for the neural network parameters, and we also use a sequential training approach, incorporating the PDE constraints in the second sampling phase.

The validation of the inference is first performed by computing the BMA-CE diagnostics for the velocity field components, the PDE constraints, and the incompressibility condition written in the same way as in equation (4.51). The results are provided in Figure 4.20 and highlight the convergence of each term toward final BMA errors scaling respectively about BMA-CE$^{u}(N_s) = 6.4\text{e}{-3}$, BMA-CE$^{v}(N_s) = 1\text{e}{-3}$, BMA-CE$^{\mathcal{F}(\mathbf{u})}(N_s) = (4.2\text{e}{-2}, 4.7\text{e}{-2})$ and BMA-CE$^{\mathcal{H}(\mathbf{u})}(N_s) = 2.9\text{e}{-2}$. The Bayesian Model Average predictions of the velocity field are then compared in Figure 4.21 with the ground truth observations providing local MSE that are embedded in their uncertainties and show enhanced standard deviations at the regions with higher errors. The PICP metric also enables to estimate that more than $95\%$ of the velocity field ground truth is recovered by the posterior distribution of $\mathbf{u}_\Theta$.

For the inverse parameter, we computed a BMA cumulative error based on the relative norm defined as follows

$$\text{BMA-CE}^{Re}(\tau) = \frac{\left| \dfrac{1}{\tau} \displaystyle\sum_{i=1}^{\tau} Re_{\Theta^{t_i}} - Re \right|}{|Re|}, \qquad \forall \tau = 1 ... N_s \tag{4.56}$$

where $Re_{\Theta^{t_i}}$ refers to the prediction of the Reynolds number for the sample characterized by the parameters $\Theta^{t_i}$. We show in Figure 4.22c that this relative error converges, reaching at the end of the sampling a residual of $5.4\text{e}{-2}$. We also represent in Figure 4.22 the histogram of the marginal posterior distribution of $Re_\Theta$ and its trajectory in the phase space illustrating the convergence toward its mode during the adaptive steps $\tau < N$. In fact, our approach leads to an estimate of the Reynolds number, inferred from the measurements data $\mathcal{D}$, which is consistent with the exact value and results in the following predictive interval $Re_\Theta \in [182.82, 208.06]$.

The latent pressure field BMA, inferred up to constant, is illustrated in Figure 4.21 with its uncertainty and is able to capture a sharp pressure drop — estimated in average to $1.78$ — arising from the steep stenosis geometry. In fact, it has been emphasized by Sun *et al.* in symmetric geometries, that such pressure drops turn to become nonlinear as the stenotic geometry becomes narrower [290], which is in line with what we obtain in our asymmetric case. As the pressure ground truth is unknown in this application, we complement the validation of the inverse problem with a-posteriori checking on the pressure gradient. In this sense, we provide a PICP estimate on the pressure recovery which stands around $91\%$ for its gradient norm, but also introduce the following posterior diagnostic on the pressure BMA-CE error:

$$\text{BMA-CE}^{\nabla p}(\tau) = \left\| \frac{1}{\tau - N} \sum_{i=N}^{\tau} \left| P\left(\nabla p_\Theta \,|\, x, \Theta^{t_i}\right) \right| - |\nabla p| \right\|^2 \tag{4.57}$$

where $|\cdot|$ denotes the vector norm, and $\nabla p$ is the evaluation of the exact gradient pressure from equation (4.53). The results are plotted, in dotted line, throughout the sampling iterations in Figure 4.20, and reach a residual error of $7.6\text{e}{-2}$. This illustrates good agreement between the ground truth and the predictive pressure gradient arising from our adaptively-weighted strategy.

Overall, the present AW-HMC methodology relies on multitask sampling to identify the flow regime through partial measurements of the velocity field and thus handles a complex flow inverse problem with latent field recovery that satisfies nonlinear physical PDE constraints.

## 4.7 Concluding remarks

BPINNs have recently emerged as a promising deep-learning framework for data assimilation and a valuable tool for uncertainty quantification [328]. This offers the opportunity to merge the predictive power of Physics-Informed Neural Networks with UQ in a Bayesian inference framework using Markov Chain Monte Carlo sampling. This makes it possible to quantify the confidence

in predictions under sparse and noisy data with physical model constraints, which is especially appealing for applications in complex systems. For this, Hamiltonian Monte Carlo has been established as a powerful MCMC sampler due to its ability to efficiently explore high-dimensional target distributions [48]. With it, BPINNs have extended the use of PINNs to a Bayesian UQ setting.

As we have shown here, BPINNs, however, share similar failure modes as PINNs: the multi-objective cost function translates to a multi-potential sampling problem in a BPINN. This presents the same difficulties in balancing the inference tasks and efficiently exploring the Pareto front as found in standard PINNs [258]. We illustrated this in a Sobolev training benchmark, which is prone to stiffness, disparate scales, and vanishing task-specific gradients. We emphasized that BPINNs are sensitive to the choice of the $\lambda$ weights in the potential energy, which can possibly lead to biased predictions or inoperative sampling. Hence, the standard weighting strategy appears to be inefficient in multiscale problems and multitask inference, while it turns out to be unsustainable to manually tune the weights in a reproducible and reliable way. Recently proposed alternatives [249] are subject to additional hyper-parameter tuning or pre-training of the weights with GAN, at the expense of increased computational complexity. Also, previous approaches mainly focused on measurement noise estimation and did not include physical model misspecification concerns which are also critical, especially when UQ modeling is the goal.

Robust automatic weighting strategies are therefore essential to apply BPINNs to multiscale and multitask problems and improve the reliability of the UQ estimates. Here, we have therefore proposed the AW-HMC BPINN formulation, which provides a plug-in automatic adaptive weighting strategy for standard BPINNs. AW-HMC effectively deals with multi-potential sampling, energy conservation instabilities, disparate scales, and noise in the data, as we have shown in the presented benchmarks.

We have shown that the present strategy ensures a weighted posterior distribution well-fitted to explore the Pareto front, providing balanced sampling by ensuring appropriate adjustment of the $\lambda$ weights based on Inverse Dirichlet weighting [187]. The weights can therefore directly be interpreted as training uncertainties, as measured by the variances of the task-specific training gradients. This leads to weights that are adjusted with respect to the model to yield the least sensitive multi-potential energy for BPINN sampling. This results in improved convergence, robustness, and UQ reliability, as the sampling focuses on the Pareto front. This enables BPINNs to effectively and efficiently address multitask UQ.

The proposed method is also computationally more efficient than previous approaches since it does not require additional hyperparameters or network layers. This also ensures optimal integration time and convergence in the leapfrog training. This prevents time steps from tending to zero or becoming very small, avoiding a problem commonly encountered in NUTS when attempting to avoid the pathologically divergent trajectories characteristic of HMC instabilities. The present methodology improves the situation since the time step no longer needs to meet all of the stiff scaling requirements to ensure energy conservation. As a result, it shortens overall integration time and sample number requirements, combining computational efficiency with robustness against sampling instabilities.

Our results also show that AW-HMC reduces bias in the sampling, since it is able to automatically adjust the $\lambda$ parameters, and with them the uncertainty estimates, according to the sensitivity of each term to the noise or inherent scaling. In classical approaches, this is prohibited by the bias and implicit prior introduced by manual weight tuning. In fact, we demonstrated the efficiency of the present method in capturing inverse parameters of different orders of magnitude in a multiscale problem, assuming completely independent priors with respect to the scaling. Previously, this would have been addressed by imposing prior distributions on these parameters that already rely on appropriate scaling. Otherwise, the classic BPINN formulation is prone to failure. The proposed adaptive weighting strategy avoids these issues altogether, performing much better in multiscale inverse problems.

We have demonstrated this in real-world applications from CFD of incompressible flow in asymmetric 2D geometries. We showed the use of AW-HMC BPINNs for CFD inpainting and

studied the impact of noise on multi-potential energy. This highlighted the robustness of the present approach to noisy measurements, but also its ability to automatically adjust the $\lambda$ values to accurately estimate the noise levels themselves. In this sense, we were able to show enhanced uncertainty with increasing noise, without any prior on the noise level itself, and to capture distinct intrinsic task sensitivities to the noise. Overall, this offers an effective alternative to automatically address multi-fidelity problems with measurements resulting from unknown heteroscedastic noise distributions.

Taken together, the present results render BPINNs a promising approach to scientific data assimilation. They now have the potential to effectively address multiscale and multitask inference problems, to couple UQ with physical priors, and to handle problems with sparse and noisy data. In all of these, the presented approach ensures efficient Pareto front exploration, the ability to correctly scale multiscale and stiff dynamics, and to derive unbiased uncertainty information from the data. Our approach involves only minimal assumptions on the noise distribution, the different problem scales, and the weights, and it is computationally efficient. This extends the application of BPINNs to more complex real-world problems that were previously not straightforwardly addressed.

Applications we expect to particularly benefit from these improvements include porous media research, systems biology, and the geosciences, where BPINNs now offer promising prospects for data-driven modeling. They could support and advance efforts for the extraction and prediction of morphological geometries [241, 271], upscaling and coarse-graining of material properties [14] and physical properties [263] directly from sample images. However, capturing these features from imperfect images remains challenging and is usually subject to uncertainties, *e.g.*, due to unavoidable imaging artifacts. This either requires the development of homogenization-based approaches [135] to bridge scales and quantify these uncertainties [238] or the use of data assimilation to compensate for the partial lack of knowledge in the images. The present BPINNs formulation with AW-HMC offers a potential solution.

CHAPTER 5

# Auto-weighted BPINNs for inverse problems in pore-scale imaging of calcite dissolution

## Contents



## 5.1 Motivation

In contrast to the straightforward upscaling method employed for assessing permeability deviations in Chapter 3, a more elaborate approach is necessary to evaluate the uncertainties on the micro-porosity field associated with $\mu$CT unresolved morphological features. In this sense, the current thesis, especially, targets data assimilation to provide an accurate local description of the porous medium by observing its dynamical dissolution through $\mu$CT experiments.

Pore-scale modeling of reactive flow offers, indeed, a valuable opportunity to investigate the evolution of macro-scale properties subject to dynamic processes. Yet, they suffer from imaging limitations arising from the associated X-ray microtomography process, which induces discrepancies in the properties estimates. Assessment of the kinetic parameters also raises challenges, as

reactive coefficients are critical parameters that can cover a wide range of values. We account for these two issues and ensure reliable calibration of pore-scale modeling, based on dynamical $\mu$CT images, by integrating uncertainty quantification in the workflow. In particular, we aim to combine $\mu$CT measurements, which come with their inherent deficiencies, with physics-based PDE models of reactive flows, which introduce uncertainties in the calibration of kinetic parameters to mitigate the limitations of each approach separately.

In this chapter, we present a novel data assimilation strategy in pore-scale imaging, based on the efficient framework developed in Chapter 4, and demonstrate that this makes it possible to robustly address reactive inverse problems incorporating Uncertainty Quantification. The present method is based on a multitasking formulation of reactive inverse problems combining data-driven and physics-informed techniques in calcite dissolution. This allows quantifying morphological uncertainties on the porosity field and estimating reactive parameter ranges through prescribed PDE models with a latent concentration field and dynamical $\mu$CT. The data assimilation strategy relies on sequential reinforcement incorporating successively additional PDE constraints and suitable formulation of the heterogeneous diffusion differential operator leading to enhanced computational efficiency. We guarantee robust and unbiased uncertainty quantification by straightforward adaptive weighting of Bayesian Physics-Informed Neural Networks, ensuring reliable micro-porosity changes during geochemical transformations.

## 5.2 Context and positioning

Pore-scale modeling in porous media is intrinsically related to X-ray $\mu$CT experiments. Advances in this imaging technique coupled with efficient numerical simulation offer a valuable opportunity to investigate dynamical processes and study the evolving macro-scale properties, such as the upscaled porosity and permeability [24, 211]. This is of great importance in the risk management perspective of $CO_2$ storage, and therefore ensuring the reliability of pore-scale modeling and simulation appears as crucial. Uncertainties, however, arise from the microtomography imaging process where artifacts, noise, and unresolved morphological features are intrinsic limitations inducing important deviations in the estimation of petrophysical properties [69, 238]. In particular, quantifying the impact of sub-resolution porosity in $\mu$CT images is identified as critical for geosciences applications [172, 276]. This limiting factor arises from the compromise between the field of view being investigated and the image resolution. For multi-scale porous media such as carbonate rocks, this trade-off can readily result in scan resolutions that do not fully resolve morphological features of the pore space. Intrinsic limiting factors remain in the X-ray $\mu$CT imaging process, as developed in Sect. 1.1.3 of Chapter 1, and investigating their effects and related uncertainties is fundamental to developing more accurate predictive models at the pore scale.

In addition to these imaging uncertainties, proper assessment of the kinetic parameters raises challenges in the pore-scale modeling of reactive flows. Mineral reactivities, including reactive surface area, are critical parameters to account though they commonly suffer from discrepancies of several orders of magnitude [217]. Providing uncertainty estimates on these kinetic parameters is essential to ensure reliable calibration of pore-scale models for $CO_2$ mineral storage assessment. Unsuitable characterization of the reactive surface area, for instance, will considerably affect the numerical model generating highly distinct behaviors that can become inconsistent with experimental investigations. Such concern is widely known, and several experimental works have developed potential solutions that address dynamical $\mu$CT imaging processes of carbonate dissolution [200, 218]. This relies on 4D $\mu$CT and differential imaging techniques to derive averaged reaction rates and provide local maps of mineral reactivity at the porous medium surface. However, dynamical $\mu$CT scans also suffer from trade-off issues that may disrupt the identification of these parameters [337]. In addition to potential sub-resolved porosity, one needs to consider the compromise between the acquisition time capturing the dynamical process and the image quality. This may result in noisy observation data or non-physical variations leading to misleading estimations of the kinetic parameters. Querying the reliability of reactive parameters involved in pore-scale modeling is crucial, and time-resolved experiments of dynamical processes offer such

an opportunity while suffering from imaging limitations.

Overall, we identify two current challenges to address reliable pore-scale modeling of reactive flows based on $\mu$CT images and ensure trustable evolutions of the macro-scale properties. The first challenge aims to quantify morphological uncertainties on the porous medium sample due to unresolved features resulting from X-ray $\mu$CT. Investigating the uncertainties in the micro-porosity field is a major concern, and neglecting these uncertainty effects can bias the determination of the evolving petrophysical properties in geological applications. The second challenge concerns the uncertainty quantification of the kinetic parameters for reactive processes. In this sense, providing reliable mineral reactivity from dynamical $\mu$CT remains critical in order to perform relevant direct numerical simulation at the pore scale. The present chapter addresses these two challenges and incorporates Uncertainty Quantification (UQ) concerns in the workflow of pore-scale modeling.

Accounting for these concerns, however, requires developing efficient data assimilation techniques to perform extensive parameter estimation studies, uncertainty quantification assessments, and improve model reliability. In fact, uncertainty quantification is commonly achieved through stochastic PDE models [86, 137] or probabilistic Markov Chain Monte Carlo (MCMC) methods embedding Bayesian inference [208, 274]. The main drawback being this requires numerous evaluations of the PDE model and can thus quickly become computationally expensive. To overcome such computational constraints, machine learning methods have appeared as a popular framework in geosciences and have shown effectiveness in building efficient surrogate models in PDE-based data assimilation problems [100, 314]. This offers alternatives and complementary means to traditional numerical methods to improve predictive modeling based on observation data and investigate uncertainty quantification within a Bayesian context. The development of machine-learning surrogate modeling incorporating uncertainty has, therefore, garnered increasing interest for a wide range of scientific applications [86, 103].

A popular framework combining physics-based techniques, data-driven methodology, and intrinsic uncertainty quantification are Bayesian Physics-Informed Neural Networks (BPINNs) [328]. This benefits from the advantages of neural network structures in building parameterized surrogate models and Bayesian inference standards in estimating probabilistic posterior distribution. BPINNs can, however, be prone to a range of pathological behaviors, especially in multi-objective and multiscale inverse problems, as developed in Chapter 4. This is because their training amounts to sample from a weighted multitask posterior distribution for which the setting of the weights parameters is challenging. Ensuring robust Bayesian inference, indeed, hinges on properly estimating these distinct task weights. We thus rely on the efficient BPINNs framework developed in the previous Chapter 4, which robustly addresses multi-objective and multiscale Bayesian inverse problems including latent field reconstruction. The strategy relies on an adaptive and automatic weighting of the target distribution parameters and objectives. It benefits from enhanced convergence and stability compared to conventional formulations and reduces sampling bias by avoiding manual tuning of critical weighting parameters [187]. The adjusted weights bring information on the task uncertainties, improve the reliability of the noise-related and model adequacy estimates and ensure unbiased uncertainty quantification. All these characteristics are crucial to address reliable reactive inverse problems of calcite dissolution, and we thus built the present methodology upon this efficient data-assimilation framework.

In this chapter, we focus on a multitask inverse problem for reactive flows at the pore scale through data assimilation that incorporates uncertainty quantification by means of the Bayesian Physics-Informed Neural Networks framework presented in Chapter 4. We intend to develop a novel approach for pore-scale imaging problems that combines dynamical microtomography and physics-based regularization induced by the PDE model of dissolution processes, for which the images are substantially noisy. To the best of our knowledge, investigating morphological and mineral reactivity uncertainties from the perspective of coupling physics-based models with data-driven techniques is the main novelty of this work. This formulation presents the joint ability to infer altogether kinetic parameters and quantify the residual micro-porosity generated by unresolved features in the $\mu$CT images. Overall, we aim to ensure reliable calibration of the PDE model and account for the morphological imaging uncertainty to provide meaningful evolution of

the petrophysical properties due to the reactive process.

The present methodology relies on sequential reinforcement of the target posterior distribution, which successively incorporates additional constraints from the PDE model into the data assimilation process. This sequential splitting formulation arises from the strong coupling, in the reactive model, between the micro-porosity field related to the $\mu$CT observations and the solute concentration, which is a latent field. Therefore, we consider successive sampling steps dedicated to 1) preconditioning the micro-porosity surrogate model with pure regression on the dynamical $\mu$CT images, 2) preconditioning the latent reactive fluid and inferring a first reactive parameter through PDE-constrained tasks, and 3) considering the overall data assimilation problem with two inverse parameters, a predictive posterior distribution on the micro-porosity and insight on the latent concentration field. We also propose a differentiation strategy wherein we consider a reformulation of the heterogeneous diffusion differential operator involved in the PDE model. This enhances the computational efficiency of the BPINNs surrogate model and shows that suitable differential operator expressions considerably improve the computational cost, especially when dealing with complex non-linear operators.

The main contributions of this chapter are summarized below:

1. We infer reactive inverse parameter uncertainty ranges in prescribed PDE models through suitable dimensionless formulations in inverse problems, for which we identify and define the corresponding dimensionless numbers.

2. We couple image-based and physics-informed techniques in dynamical dissolution processes from a pore-scale perspective.

3. We improve the relevance and reliability of predictions in dynamical systems through data-driven approaches and robust Bayesian Inference methodology.

4. We provide reliable quantification of the micro-porosity changes during geochemical transformations, with a focus on calcite dissolution processes, whose image acquisition is subject to a strong noise level.

5. We built an intrinsic data assimilation strategy for pore-scale imaging inverse problems relying on a sequential reinforcement approach and a formulation of the heterogeneous diffusion differential operator, which is suitable for an efficient HPC framework.

The remainder of this chapter is organized as follows: In Sect. 5.3, we review the current challenges arising from uncertainty quantification concerns in pore-scale modeling of reactive flows, with a focus on $\mu$CT limitations and model reliability issues. We also develop in Sect. 5.3.1 the direct formulation of pore-scale modeling of reactive flows we consider to study the dynamical dissolution of calcite. Sect. 5.4 describes the dimensionless expressions of the dissolution PDE model for direct and inverse problems. We identify the main differences in their formulations and establish in Sect. 5.4.3 the dimensionless inverse problem on calcite dissolution we address in the data assimilation approach, which ends up with equation (5.12). Sect. 5.5 is dedicated to describing the proposed data assimilation strategy for pore-scale imaging inverse problems, with sequential reinforcement of the target posterior distribution and computational strategy for the differential operator expressions. This relies on the efficient adaptive framework for Bayesian Physics-Informed Neural Networks, which has been developed in the previous Chapter 4. We validate this strategy in Sect. 5.6 on several 1D+Time test cases of calcite dissolution based on synthetic $\mu$CT images. This particularly demonstrates successful Bayesian inference of the reactive parameters with posterior distributions on the dimensionless numbers. This also highlights consistent UQ on the micro-porosity field with uncertainty ranges on the residual micro-porosity, potentially unresolved, arising from the $\mu$CT dynamical images. Finally, we apply in Sect. 5.7 our methodology to a more realistic 2D+Time data assimilation problem of calcite dissolution with heterogeneous porosity levels and synthetic $\mu$CT dynamical observations.

## 5.3 Uncertainty Quantification in pore-scale modeling of reactive flows: context and motivation

Pore-scale modeling of reactive flows plays a crucial role in the long-term management of $CO_2$ capture and storage in natural underground reservoirs. Understanding the local geochemical interactions between the injected $CO_2$ and the aquifer structure and how it impacts the reservoir macro-scale properties is an active field in porous media research [21, 169, 197, 286]. These geochemical effects include mineral trapping through precipitation and crystallization but also dissolution reactions associated with flow, and transport mechanisms [7, 232]. Mathematical models of such processes, at the pore scale, are usually combined with direct numerical simulations of highly coupled and non-linear Partial Differential Equations. Such PDE systems characterize the local evolving interfaces and provide insight into reservoir safety submitted to chemical interactions [200, 205, 220]. In this risk management perspective, ensuring the reliability of pore-scale modeling and simulation of reactive flows is therefore essential, and this requires embedding UQ concerns.

### 5.3.1 Modeling of pore-scale dissolution

The study of geochemical processes related to $CO_2$ capture and storage is crucial in the context of risk management and investigation of the coupled mechanisms occurring within aquifers. In particular, the dissolution of the carbonate rock architecture by the injected $CO_2$ may compromise the integrity of the geological reservoir. Pore-scale modeling of dissolution phenomena in porous media, therefore, remains an extensive research area [204, 280]. These mathematical models require a thin description of the highly heterogeneous pore structure in order to account for local interactions. The present chapter focus on the pore-scale dissolution of calcite subject to acidic transport in the subsoil. We, therefore, target the following irreversible chemical reaction with uniform stoichiometric coefficients:

$$\mathrm{CaCO_3\,(s)} + \mathrm{H^+} \longrightarrow \mathrm{Ca^{2+}} + \mathrm{HCO_3^-} \tag{5.1}$$

In this section, the mathematical model used to simulate the calcite dissolution process (5.1) at the pore scale will rely on a two-scale description of the local heterogeneities trough the Darcy-Brinkman Stokes formulation with superficial velocity, developed in Chapter 2 (see equation (2.11) from Sect. 2.3.2). We use the same notations as in Sect. 2.3.1 to define the spatial domain $\Omega$ corresponding to the porous medium description at the pore scale, which is decomposed into the void-space $\Omega_F$, the porous matrix $\Omega_S$ and the internal interface $\Sigma$ (*e.g.* see Figure 1.1). The micro-porosity field $\varepsilon$, defined on $\Omega$, is also assumed to have a strictly positive lower bound $\varepsilon(x,t) \geqslant \varepsilon_0 > 0$ for all $(x,t)$ in the spatiotemporal domain $\Omega \times [0, T_f]$. In fact, this lower bound $\varepsilon_0$ characterizes the residual, potentially unresolved, porosity of the porous matrix.

In the context of the current chapter, we are not interested in monitoring the dissolution products of (5.1) (*i.e* the $Ca^{2+}$ and $HCO_3{}^-$ ions), hence we mainly focus on the concentrations of the acid and calcium carbonate species respectively denoted $C(x,t) = [\mathrm{H^+}]$ and $C_{\mathrm{CaCO_3}(s)}(x,t)$. The solid concentration is linked to the porosity through the molar volume of calcite $\upsilon$ by the relation $C_{\mathrm{CaCO_3}(s)} = (1-\varepsilon)/\upsilon$ with $\upsilon = 36.93\,\mathrm{cm^3.mol^{-1}}$. The evolution of the acid phase (*i.e* the concentration field $C$) follows the equation (2.7) from Chapter 2, and the evolution of the solid phase with superficial concentration $C_{\mathrm{CaCO_3}(s)}$ is given by the same equation without transport nor diffusion, recalled here:

$$\frac{\partial C_{\mathrm{CaCO_3}(s)}}{\partial t} = R(C). \tag{5.2}$$

The reaction rate $R(C)$ — related to the chemical reaction (5.1) — is written:

$$R(C) = -K_s A_s \gamma_{\mathrm{H^+}} C \mathbb{1}_{\{(1-\varepsilon)>0\}} \tag{5.3}$$

where $K_s$ is the dissolution rate constant, $A_s$ the specific reactive area, and $\gamma_{\mathrm{H^+}}$ the activity coefficient of the acid, whose physical units are respectively $\mathrm{mol.m^{-2}.s^{-1}}$, $\mathrm{m^{-1}}$ and $\mathrm{m^3.mol^{-1}}$ (such

that the chemical activity $a_{H^+} = \gamma_{\mathrm{H}^+} C$ is dimensionless). Such reaction rates for the calcite dissolution are commonly established by the Transition State Theory [156] and involve both far-from equilibrium terms coupled with a term which express the dependence on the Gibbs free energy $\Delta G$ for close to the equilibrium conditions (*e.g.* see [190, 205]). In our work, we consider far-from the equilibrium assumption on the dissolution process and, therefore, the reaction rate reduces to the expression (5.3) previously introduced. One should also notice that the dissolution rate is normalized by the reactive surface area of the mineral $A_s$, which is often considered a calibration parameter to match with the experiments. However, this can readily generate significant discrepancies in the modeling of the chemical processes and bias the predictions. The notation $\mathbb{1}$ refers to a characteristic or activation function and ensures the rate of the chemical reaction is non-zero only in the presence of solid minerals. Along with boundary and initial conditions, we define the pore-scale direct formulation of the calcite dissolution problem (5.1) through the following PDE system [206, 285]:

$$\begin{cases} -\mathrm{div}(2\mu D(u)) + \mu\kappa_b^{-1}\dfrac{(1-\varepsilon)^2}{\varepsilon^2}u = \varepsilon(f - \nabla p), & \text{in } \Omega\times]0,T_f[ \\ \dfrac{\partial C}{\partial t} + \mathrm{div}(\varepsilon^{-1}uC) - \mathrm{div}\left(D_m\varepsilon^{1+\eta}\nabla(\varepsilon^{-1}C)\right) = -K_s A_s \gamma_{\mathrm{H}^+} C \mathbb{1}_{\{(1-\varepsilon)>0\}}, & \text{in } \Omega\times]0,T_f[ \\ \dfrac{\partial \varepsilon}{\partial t} = \upsilon\, K_s A_s \gamma_{\mathrm{H}^+} C \mathbb{1}_{\{(1-\varepsilon)>0\}}, & \text{in } \Omega\times]0,T_f[ \\ + \text{adequate boundary and initial conditions, along with } \mathrm{div}\, u = 0 \end{cases} \tag{5.4}$$

where $D_m$ is the molecular diffusion of the acid.

Appropriate model calibration of the kinetic input parameters, such as the specific surface area $A_s$ or the dissolution rate constant $K_s$, that compare with experimental results remains challenging. This comes from the observation these reactive constants can span over a wide range of orders of magnitude, inducing highly different behaviors in the chemical PDE system. Quantifying the uncertainties on these kinetic parameters thereby appears as a necessity to provide reliable reactive flow models at the pore scale.

### 5.3.2 Dynamical microtomography: mineral reactivity and imaging morphological uncertainties

Accounting for the $\mu$CT morphological uncertainties and sub-resolution porosity, introduced in Sect 1.1.3 of Chapter 1, is essential in providing reliable pore-scale simulations of reactive flows. This is of primary importance when considering risk assessment and predicting meaningful evolution of the rock macro-properties under geochemical effects. The study of these overall X-ray imaging limitations, therefore, raises concerns in the research community, and investigations are conducted on quantifying their implications on the effective properties. In fact, sub-resolution porosity may lead to a misleading estimation of the pore-space connectivity that disrupts the flow description within the REV and induces significant deviations in the computed permeability. Several modeling approaches, mainly based on upscaling principles, aim at quantifying these deviations. They cover DBS formulation altogether with the Kozeny-Carman equation (see equation (2.2) in Chapter 2), which estimates the permeability of the micro-porous domain through a heuristic relation with the residual micro-porosity [278]. However, in the absence of prior knowledge of this unresolved residual porosity, the setting of the micro-porous permeability becomes controversial. Alternatives rely on appropriate boundary conditions to model the unresolved features and wall roughness through slip-length formalism, and range from theoretical implications [2, 159, 161] to the practical computation of the permeability deviations on real 3D $\mu$CT scans as developed in Chapter 3. Apart from the modeling quantification of the effective properties uncertainties, experimental and imaging approaches are developed to resolve the sub-resolution porosity. This involves differential imaging techniques based on comparisons between several enhanced contrast scans [172], statistical studies based on $\mu$CT histograms [341], or deep learning methodologies such as CNN and GAN that provide super-resolved segmented images [16, 330].

Overall, uncertainty quantification of the X-ray $\mu$CT limitations either relies on appropriate mathematical modeling with the estimation of computed deviations or experimental approaches based on image treatment analysis of the $\mu$CT scans.

The reliability of pore-scale modeling related to X-ray $\mu$CT scans is questioned due to its inherent imaging limitations and morphological uncertainties. At the same time, proper assessment of the kinetic parameters in dynamic phenomena, including mineral reactivity and reactive surface area, also raise challenges. Actually, mineral reactivity is a critical parameter to account for in many geosciences applications though discrepancies of several orders of magnitude can be found in the literature [51, 108]. However, these parameters are usually regarded as input in the numerical models and eventually tuned to aggregate experimental results. Providing reliable uncertainty estimates on these kinetic parameters is, therefore, of great interest to provide trustable pore-scale reactive simulations. Such concern has received attention over the past decades, and considering dynamic imaging processes subsequently appears as a necessity. Several experimental works have already focused on 4D imaging techniques of carbonate dissolution to provide fundamental information on mineral reaction rates [218]. These kinetic characterization studies mostly rely on voxel-to-voxel subtraction of consecutive images in order to quantify the change of greyscale values, hence the evolution of the dissolution process and calcite retreat. This is referred to, in the literature, as differential imaging techniques and has been investigated for different imaging techniques such as X-ray $\mu$CT and Atomic Force Microscopy (AFM) [172, 273]. These approaches enable to capture heterogeneous spatial distributions of calcite dissolution rates through successive real-time measurements. They provide local maps of mineral reactivity at the crystal surfaces and quantification of their morphological evolutions [217, 273]. Menke *et al.* [200] also performed *in situ* time-resolved experiments of carbonate dissolution under reservoir conditions (in terms of pressure and temperature) to derive averaged reaction rates and evaluate dynamical changes in the effective properties. Investigation of mineral surface reactivity is another challenging concern to ensure reliable calibration of pore-scale models for $CO_2$ dissolution and is usually achieved through dynamical $\mu$CT experiments.

Nonetheless, dealing with dynamical $\mu$CT images brings its own challenges [337]. In addition to the unresolved features, dynamical imaging of chemical processes requires making a compromise between the acquisition time and the image quality. Indeed, capturing fast-dissolution processes, for instance, imposes short acquisition times and could result in highly noisy data since statistically, the number of photons reaching the detector would be reduced. In such a case, differential imaging makes it difficult to distinguish between true morphological changes and the derivation of highly noisy data. On top of that, any additional movement in the sample, not related to the dissolution process but rather resulting from instrumentation artifacts, makes it challenging to work with dynamical samples only to characterize $\mu$CT errors and uncertainty. Indeed, Zhang and al. [337] identified on a Bentheimer sampler that about 32% of the voxels have at least a 2% difference in greyscale values between two consecutive fast scans. These differences are not physical-based variations but rather intrinsic uncertainties measurements. They also show that such artifacts' uncertainties can be reduced by using slower acquisition time, though this is not always feasible to capture fast-dynamical processes. Time-resolved experiments of dynamical processes can provide insights into kinetic dissolution rates, though this also suffers from imaging limitations that can lead to misleading estimations.

Inferring reliable mineral reactivity from dynamical microtomography and quantifying imaging morphological uncertainties are identified as the major issues that can bias the determination of evolving petrophysical properties in geological applications. Current methodologies addressing these problems mainly fall into two categories: on one side, purely model-related approaches based on static $\mu$CT scans and upscaling principles, and on the other side, image treatment analysis relying on experimental static or dynamical images. Nonetheless, neither morphological uncertainty nor reaction rate quantification has been investigated from the perspective of coupling physics-based models with data-driven techniques. To the best of our knowledge, the development of data assimilation approaches on pore-scale imaging problems that combine dynamical microtomography and physical regularization induced by the PDE model of reactive processes is the main

novelty of the present chapter. The motivation for this formulation lies in its joint ability to infer mineral reactivity parameters and quantify the residual micro-porosity generated by unresolved features in the microtomography imaging process. Therefore, we assert that a proper balance between dynamical microtomography imaging and their PDE-based physical formulation could provide insights into the uncertainty quantification issues related to reactive pore-scale modeling. In this direction, we propose a novel methodology that uses a physics-based dissolution model as regularization constraints to dynamical data-driven microtomography inference. This aim at quantifying both the uncertainties on kinetic parameters to perform reliable model calibration and the morphological imaging uncertainty on the unresolved micro-porosity field.

## 5.4 Direct and inverse problem setup

This section is dedicated to setup the dimensionless versions of the dissolution PDE model for direct and inverse problems. We establish the main differences in their dimensionless formulations and define the modeling assumptions used in the present chapter.

### 5.4.1 Usual dimensionless formulation of the direct problem

The overall calcite dissolution PDE system, defined in equation (5.4), can model a wide range of dissolution regimes and patterns characterized by well-established dimensionless numbers. By setting $x^* = x/L$ and $t^* = tD_m/L^2$ and following the notations of Sect. 5.3.1 and Chapter 2, one can introduce the so-called Peclet and Reynolds numbers

$$\mathrm{Pe} = \overline{u}L/D_m \quad \text{and} \quad \mathrm{Re} = \rho\overline{u}L/\mu \tag{5.5}$$

where $\overline{u}$ and $L$ are respectively the characteristic velocity and length of the sample. In the context of pore-scale simulations, the inertial effects become negligible compared to viscous forces due to low Reynolds numbers — typically we have the assumption $\mathrm{Re} \ll 1$ throughout this chapter. Regarding the chemical reactions, two dimensionless numbers are defined: the catalytic Damköhler number denoted $\mathrm{Da}_{\mathrm{II}}$ and its inherited convective number $\mathrm{Da}_{\mathrm{I}}$, expressed as

$$\mathrm{Da}_{\mathrm{II}} = \frac{K_s A_s \gamma_{\mathrm{H}^+} L^2}{D_m} \quad \text{and} \quad \mathrm{Da}_{\mathrm{I}} = \frac{\mathrm{Da}_{\mathrm{II}}}{\mathrm{Pe}} = \frac{K_s A_s \gamma_{\mathrm{H}^+} L}{\overline{u}}. \tag{5.6}$$

The characteristic length $L$ is usually related to average pore throat diameters or $L^2$ can be set as the surface of a section divided by the average number of grains (*e.g.* see [135] for practical cases). Otherwise, it is possible to set the characteristic length of the problem as $L = \sqrt{\kappa_0}$, provided an experimental or numerical estimation of $\kappa_0$ [279]. All these dimensionless numbers are meaningful in direct dissolution problems to qualify the different dominant regimes in terms of diffusion, reaction, and advection.

Using the dimensionless variables $(x^*, t^*)$, the normalized concentration $C^* = C/C_0$ and velocity $u^* = u/\overline{u}$, one finally gets the dimensionless formulation of the overall reactive flow system (5.4) on the dimensionless spatiotemporal domain $\Omega^* \times [0, T_f^*]$. This leads to the usual PDE model:

$$\begin{cases} -\Delta u^* + L^2\kappa_b^{-1}\dfrac{(1-\varepsilon)^2}{\varepsilon^2}u^* = \varepsilon(f^* - \nabla p^*), & \text{in } \Omega^*\times]0, T_f^*[ \\ \dfrac{\partial C^*}{\partial t^*} + \mathrm{Pe}\,\mathrm{div}(\varepsilon^{-1}u^*C^*) - \mathrm{div}\left(\varepsilon^{1+\eta}\nabla(\varepsilon^{-1}C^*)\right) = -\mathrm{Da}_{\mathrm{II}}C^*\mathbb{1}_{\{(1-\varepsilon)>0\}}, & \text{in } \Omega^*\times]0, T_f^*[ \\ \dfrac{1}{\upsilon C_0}\dfrac{\partial \varepsilon}{\partial t^*} = \mathrm{Da}_{\mathrm{II}}C^*\mathbb{1}_{\{(1-\varepsilon)>0\}}, & \text{in } \Omega^*\times]0, T_f^*[ \\ + \text{adequate boundary and initial conditions, along with } \mathrm{div}\, u^* = 0 \end{cases} \tag{5.7}$$

obtained by means of multiplying the hydrodynamic DBS equation by $L/\rho\overline{u}^2$ and the chemical equations in (5.4) by $L^2/C_0D_m$. The notations $f^*$ and $p^*$ in the dimensionless DBS equation are

defined by $f^* = fL^2/(\mu\overline{u})$ and $p^* = pL/(\mu\overline{u})$, and finally $C_0$ is a characteristic constant for the acid concentration field. This PDE system defines the overall dimensionless formulation of the direct problem of calcite dissolution.

### 5.4.2 Modeling assumptions on the direct and inverse problems

In the applications Sect. 5.6 and 5.7, we consider inverse problems in the dissolution process of calcite cores with heterogeneous porosity levels for 1D and 2D spatial configurations. Although the 1D+Time test case is purely synthetic and aims to validate the method developed in Sect. 5.5, the 2D+Time application addresses a more realistic problem that can be applied to isotropic porous samples. Several modeling assumptions are, though, made to address both the reactive direct and inverse problems. These modeling assumptions are detailed hereafter and determine the dissolution regime considered in the applications.

The dimensionless numbers $\mathrm{Re}$ and $\mathrm{Pe}$ are common to both the direct and inverse formulations and respectively establish the viscosity-dominated regime and the convective or diffusive transport regime. At the initial state in the dynamic imaging process, we assume that the porous medium is completely saturated with the acid by capillary effect. The amount of reactant at the pore interface is initially homogeneously distributed, and therefore we expect, at first, a cylindrical dissolution regime of the calcite core with spherical symmetry. Subsequently, the dissolution process may deviate from this cylindrical pattern due to local heterogeneities in the micro-porosity field $\varepsilon$. We also suppose a low Peclet hypothesis $\mathrm{Pe} \ll 1$, so that the reactant diffusion is dominant over the advection phenomena resulting in more homogeneous dissolution rates at the interface (*e.g.* see [279] for the dissolution regimes characterization). In this sense, continuous acid injection is maintained at a given fluid flow rate to ensure a diffusive-dominated regime for the dissolution. Consequently, we neglect the advection effects in the present chapter and focus on the following reaction-diffusion system:

$$\begin{cases} \dfrac{\partial C^*}{\partial t^*} - \operatorname{div}\left(\varepsilon^{1+\eta}\nabla(\varepsilon^{-1}C^*)\right) = -\mathrm{Da}_{\mathrm{II}} C^* \mathbb{1}_{\{(1-\varepsilon)>0\}}, & \text{in} \quad \Omega^* \times ]0, T_f^*[ \\ \dfrac{1}{vC_0}\dfrac{\partial \varepsilon}{\partial t^*} = \mathrm{Da}_{\mathrm{II}} C^* \mathbb{1}_{\{(1-\varepsilon)>0\}}, & \text{in} \quad \Omega^* \times ]0, T_f^*[ \\ C^* = 1, & \text{on} \quad \partial\Omega^* \times ]0, T_f^*[ \\ C^*(x,0) = C_{\mathrm{init}}(x)/C_0 := C^*_{\mathrm{init}}, & \text{in} \quad \Omega^* \times \{0\} \end{cases} \tag{5.8}$$

written in its dimensionless form with the normalized concentration field $C^* = C/C_0$. The continuous acid injection is modeled through non-homogeneous Dirichlet boundary conditions on $C^*$, with the characteristic constant $C_0$ chosen as the value of the Dirichlet boundary conditions on $C$. The initial condition on the micro-porosity field $\varepsilon$ arises from the dry microtomography scan or the initial synthetic porous medium. Ultimately, we obtain a PDE model driven by one dimensionless number, namely the catalytic Damköhler number, characterizing the ratio of the reaction rate over the diffusion effects. The system (5.8) is, therefore, consistent with the standard dimensionless formulation of the direct problem, subject to a diffusive-dominated transport regime.

However, we merely cannot consider the dimensionless temporal variable $t^* = tD_m/L^2$ in a reactive inverse problem as it strongly depends on molecular diffusion $D_m$, which is among the unknown kinetic parameters to be estimated. In the next section, we focus on the challenge arising from the dimensionless formulation of a reactive inverse problem in the context of calcite dissolution.

### 5.4.3 Dimensionless inverse problem on calcite dissolution

In this chapter, we address pore-scale imaging inverse problems in dissolution processes. We aim to recover and quantify uncertainties both on the micro-porosity field description $\varepsilon$ and the reactive parameters involved in the diffusion-reaction system. Among these inverse kinetic parameters,

one can find the molecular diffusion $D_m$, the tortuosity index $\eta$, the dissolution rate constant $K_s$, and even the specific surface area $A_s$ — usually estimated on the dry $\mu$CT scan. Consequently, these parameters – in particular $D_m$ – cannot be used for the non-dimensionalization of the model since they are to be determined. Apart from special considerations of the tortuosity index of the sample, the other inverse parameters characterize the dissolution regime of the dynamical $\mu$CT experiment. In this sense, they provide insight into the physical catalytic Damköhler number $\mathrm{Da}_{\mathrm{II}}$, though the direct dimensionless formulation (5.8) is inappropriate for an inverse problem. The dimensionless temporal variable $t^*$ in the PDE system (5.8) is, indeed, closely related to the unknown molecular diffusion, compromising its application to inverse modeling. Establishing the dimensionless formulation of the inverse dissolution problem is not straightforward and therefore requires a different dimensionless time.

In the inverse problem, we consequently introduce the new temporal variable

$$t^* = \frac{tD_{\mathrm{ref}}}{L^2}, \tag{5.9}$$

where $D_{\mathrm{ref}}$ is a scaling factor of the dimensionless formulation for the chemical kinetics. This scaling factor can also be defined as $D_{\mathrm{ref}} = L^2/T$ introducing $T$ the characteristic time for the dimensionless problem, which is not the physical characteristic time for the diffusion since the latter is unknown. In practice, we can rely on a rough estimation of physical dissolution time $T_f$ — determining the dynamical process end — and a given dimensionless final time — usually $T_f^* = 1$ — to set the factor $D_{\mathrm{ref}}$. The estimations of this scaling parameter will be detailed on a case-by-case basis throughout the applications developed in Sect. 5.6 and 5.7. Using the new dimensionless variables $(x^*, t^*)$, the normalized concentration $C^* = C/C_0$ along with the definition of $D_{\mathrm{ref}}$, one can obtain the dimensionless formulation of the reaction-diffusion system in the context of inverse modeling, which leads to:

$$\begin{cases} \dfrac{\partial C^*}{\partial t^*} - D_m^* \mathrm{div}\left(\varepsilon^{1+\eta}\nabla(\varepsilon^{-1}C^*)\right) = -\mathrm{Da}_{\mathrm{II}}^* C^* \mathbb{1}_{\{(1-\varepsilon)>0\}}, & \text{in} \quad \Omega^*\times]0,T_f^*[ \\ \dfrac{1}{\upsilon C_0}\dfrac{\partial \varepsilon}{\partial t^*} = \mathrm{Da}_{\mathrm{II}}^* C^* \mathbb{1}_{\{(1-\varepsilon)>0\}}, & \text{in} \quad \Omega^*\times]0,T_f^*[ \\ C^* = 1, & \text{on} \quad \partial\Omega^*\times]0,T_f^*[ \\ C^*(x,0) = C_{\mathrm{init}}^*, & \text{in} \quad \Omega^*\times\{0\}. \end{cases} \tag{5.10}$$

In reactive inverse problems, we thus obtain a PDE model driven by two dimensionless numbers denoted $\mathrm{Da}_{\mathrm{II}}^*$ and $D_m^*$ which are defined as:

$$\mathrm{Da}_{\mathrm{II}}^* := K_s A_s \gamma_{\mathrm{H}^+} T = \frac{K_s A_s \gamma_{\mathrm{H}^+} L^2}{D_{\mathrm{ref}}} \quad \text{and} \quad D_m^* := \frac{D_m T}{L^2} = \frac{D_m}{D_{\mathrm{ref}}}. \tag{5.11}$$

Finally, the physical Damköhler number corresponding to the dynamical $\mu$CT experiment is recovered as the a-posteriori ratio $\mathrm{Da}_{\mathrm{II}} = \mathrm{Da}_{\mathrm{II}}^*/D_m^*$. From now on, we consider this dimensionless formalism and forget the star notation on the differential operator, domains, and field descriptions for the sake of readability. This results in the following inverse dimensionless PDE system:

$$\begin{cases} \dfrac{\partial C}{\partial t} - D_m^* \mathrm{div}\left(\varepsilon^{1+\eta}\nabla(\varepsilon^{-1}C)\right) = -\mathrm{Da}_{\mathrm{II}}^* C \mathbb{1}_{\{(1-\varepsilon)>0\}}, & \text{in} \quad \Omega\times]0,T_f[ \\ \dfrac{1}{\upsilon C_0}\dfrac{\partial \varepsilon}{\partial t} = \mathrm{Da}_{\mathrm{II}}^* C \mathbb{1}_{\{(1-\varepsilon)>0\}}, & \text{in} \quad \Omega\times]0,T_f[ \\ C = 1, & \text{on} \quad \partial\Omega\times]0,T_f[ \\ C(x,0) = C_{\mathrm{init}}, & \text{in} \quad \Omega\times\{0\} \end{cases} \tag{5.12}$$

with $\mathrm{Da}_{\mathrm{II}}^*$ and $D_m^*$ the inverse parameters to estimate, and $C_0$ and $\upsilon$ constant parameters. The tortuosity index $\eta$ is either set through a-priori estimation on the porous sample, modeling through the empirical Archie law, or regarded as an additional inverse parameter. Especially, the index

$\eta = 1$ is often considered for porous media with strong pore connections [279, 311] although practical upscaling of the diffusion can result in intermediate index values [135].

In addition to inferring the reactivity parameters $\mathrm{Da}_{\mathrm{II}}^*$ and $D_m^*$, we aim to estimate the spatial variability on the porosity field $\varepsilon$. In this sense, we develop a data assimilation approach on pore-scale imaging that combine dynamical $\mu$CT experiments of calcite dissolution and physical regularization induced by the dimensionless PDE model (5.12). It benefits from the joint ability to quantify the ranges of mineral reactivity and the residual micro-porosity generated by unresolved features in the microtomography imaging process. This formulation also relevantly combines the advantages of experimental and modeling approaches and overcomes their own limitations. On the one hand, the dissolution process observation will bring insights into the unresolved morphological features and lead to a better characterization of the sample's initial state. On the other, the PDE model regularization can efficiently substitute the differential imaging approach, which is controversial for fast-dynamical processes subject to poor imaging quality. Therefore, one can address mineral reactivity inference for highly noisy dynamical $\mu$CT resulting from the compromise between scan quality and time resolution, as introduced in Sect. 5.3.2. The major challenge of this data assimilation formulation, though, relies on the PDE constraint for the concentration field as the $\mu$CT experiments do not provide information on the flow, transport, or diffusion of the chemical reactant. In the reactive inverse problem, the acid concentration is thus a latent field whose only the dimensionless boundary conditions are known in equation (5.12) through the normalizing constant $C_0$. In the next section, we will develop the methodology adopted to solve such a dissolution inverse problem, accounting for all the established modeling assumptions.

## 5.5 Data assimilation strategy: sequential reinforcement and operator differentiation

In this present work, we focus on a multitask inverse problem for reactive flows at the pore scale involving two inverse parameters ($\mathrm{Da}_{\mathrm{II}}^*$ and $D_m^*$) and a latent concentration field $C$. This novel approach combines dynamical imaging data of calcite dissolution and physics-based regularization induced by the dimensionless PDE model (5.10). We build the current data assimilation approach upon the efficient AW-HMC framework for Bayesian Physics-Informed Neural Networks, presented in Sect. 4.4.1 of Chapter 4, to quantify both morphological and chemical parameter uncertainties. In this section, we present the data assimilation method developed to handle this pore-scale imaging inverse problem. Our methodology emphasizes the sequential reinforcement of the multi-potential energy and the efficient computation of the heterogeneous diffusion operator arising from Archie's law. This requires to set up first a few dedicated notations.

### 5.5.1 Domain decomposition and sampling notation setup

Dynamical synthetic or experimental $\mu$CT images are available on the overall spatiotemporal domain $\Omega \times [0, T_f]$, and provide dissolution observations subject to noise and imaging limitations (see Sect. 1.1.3 in Chapter 1 and 5.3.2): we introduce the two-index set $\mathfrak{Im}_{i,j}$ of image intensities (dissolution measurements) defined for the whole image voxels. Then, we define a subset of this image for sampling purposes, involving the positions $\mathcal{D}$ as a subset of $\overline{\Omega} \times [0, T_f]$ together with their image intensities $\mathrm{Im}$, corresponding to $N_{\text{obs}}$ partial and corrupted training observations:

$$\mathcal{D} = \{(x_k, t_k), \quad k = 1...N_{\text{obs}}\} \tag{5.13}$$

On this set of discrete points, there exists mappings $i$ and $j$ such as the image intensity satisfies

$$\mathrm{Im}_k := \mathfrak{Im}_{i(k),j(k)} = 1 - \varepsilon(x_k, t_k) + \xi(x_k, t_k), \quad k = 1...N_{\text{obs}} \tag{5.14}$$

where the noise $\xi \sim \mathcal{N}(0, \sigma^2 I)$ for which the standard deviation $\sigma$ is automatically estimated in the AW-HMC sampler by means of the $\lambda_k$ adjustment in the weighted multi-potential energy $U(\Theta)$ (see equation (4.19) and Sect. 4.3.2 in Chapter 4 for detailed development). This relationship

between the microtomography images $\mathrm{Im}$ and $\varepsilon$ comes from the correlation between the $\mu$CT values and the material local attenuation. Indeed, in a greyscale tomographic scan, the minimum signal corresponds to the least attenuating or the least dense areas (in $\Omega_F$ where $\varepsilon = 1$), while the maximum signal refers to the most attenuating areas (in $\Omega_S$ where $0 < \varepsilon_0 \leqslant \varepsilon < 1$). Due to the micro-continuum description of the medium based on the two-scale porosity assumption, each distinct region of the domain — namely $\Omega_S$ and $\Omega_F$ — is though regarded as a different term in the multi-potential energy definition. Such a distinction is prescribed since there is no guarantee that the data corruption is uniform: the measurement variability can differ locally when facing heteroscedastic noise. In particular, the artifact limitations tend to enhance the blurring effects at the material fluid/solid interface $\Sigma$. This motivates the special consideration of this interface neighborhood to account for the unresolved features and provide reliable morphological uncertainties.

In this sense, we introduce the Reactive Area of Interest (RAI) as the evolving fluid/mineral interface along the dissolution process that is defined by:

$$\mathrm{RAI} = \left\{(x_k, t_k) \in \Omega \times [0, T_f] \text{ such that } \mathfrak{Im}_{i(k)+1,j(k)} < \mathfrak{Im}_{i(k),j(k)} \text{ and } 0.1 < \mathrm{Im}_k < 0.9\right\} \tag{5.15}$$

where the imaging extreme values are ignored, as a correction criterion, to avoid integrating noise derivation artifacts into the definition of the RAI. These thresholds rely on the analysis of the $\mu$CT histogram of the initial porous medium dataset. We also define:

- The extended Reactive Area of Interest, denoted $\mathrm{RAI}^+$, as the RAI augmented by a fluid tubular neighborhood of the RAI both in space and time, that is to say, the fluid region close to the evolving interface in $\Omega \times [0, T_f]$,
- The reduced Reactive Area of Interest, denoted $\mathrm{RAI}^-$, based on the acceptability criterion — positivity of the $D_m^*$ estimations — defined thereafter and related to the relations (5.21)-(5.22).

Moreover, we introduce several discrete domains $\mathcal{D}^\bullet$ defined as the intersection between the non-reactive part of $\mathcal{D}$ and their respective time-dependent regions: fluid, solid, reactive, or boundary. For instance, one gets $\mathcal{D}^F = (\mathcal{D} \cap Q_F) \setminus \mathrm{RAI}$ with $Q_F$ the evolving fluid region defined as

$$Q_F = \{(x, t) \in \Omega \times [0, T_f] \quad \text{such that} \quad x \in \Omega_F(t)\}\,. \tag{5.16}$$

In the same way, $\mathcal{D}^S = (\mathcal{D} \cap Q_S) \setminus \mathrm{RAI}$ where $Q_S$ is the evolving solid region and $\mathcal{D}^\partial = \mathcal{D} \cap \{\partial\Omega \times [0, T_f]\}$. The overall domain $\Omega \times [0, T_f]$ is decomposed into several regions and respective training datasets that are involved in the sequential reinforcement of the multi-potential energy.

Finally, these different domains satisfy the following properties:

- $\mathrm{RAI}^- \subset \mathrm{RAI} \subset \mathrm{RAI}^+$,
- $\Omega_F \cup \Omega_S = \Omega$, where $\Omega_F = \mathbb{1}_{(\varepsilon<1)}$ in $\Omega$ is an open set,
- $\mathcal{D} = \mathcal{D}^F \cup \mathcal{D}^S \cup \mathcal{D}^\partial \cup \mathrm{RAI}$ .

### 5.5.2 Sequential reinforcement of the multi-potential energy

The data assimilation strategy developed in the present chapter relies on a sequential design of the multi-potential energy $U(\Theta)$, which will be reinforced to incorporate additional constraints through dedicated sampling steps. The overall process is illustrated in Figure 5.1. This sequential splitting is necessary due to the strong coupling between the porosity field $\varepsilon$, related to the $\mu$CT imaging process, the latent concentration field $C$, and the two unknown inverse parameters $\mathrm{Da}_{\mathrm{II}}^*$ and $D_m^*$. The first sampling step is, therefore, dedicated to providing a-priori estimations of the micro-porosity field through data-fitting terms only.

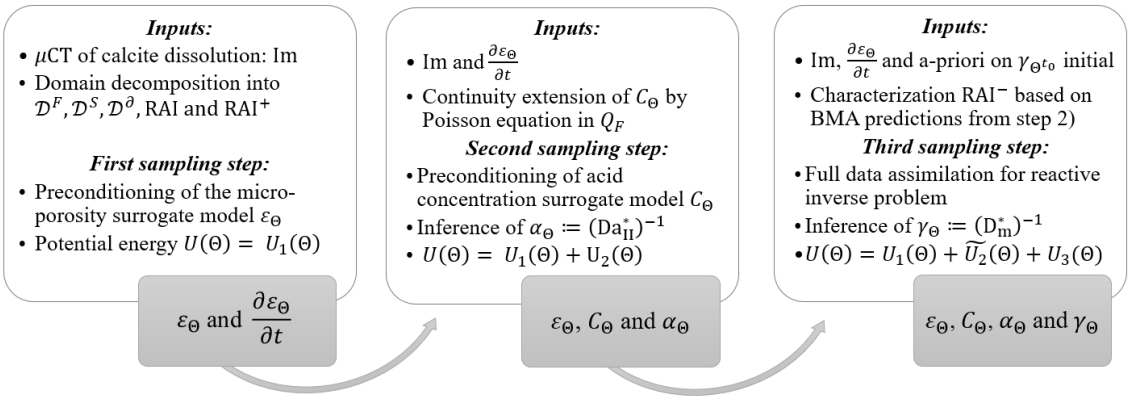


**Figure 5.1: Sequential graph of the potential energy reinforcement:** our data assimilation strategy incorporates additional physics-based constraints arising from the PDE model (5.12) through successive sampling steps. The notations are defined in Sect. 5.5.2.

### Step 1: Preconditioning by pure regression on image data

The first sampling step 1 of the sequential splitting strategy aims to provide a preconditioning description of the surrogate micro-porosity field $\varepsilon_\Theta$. We consider a task differentiation between $\mathcal{D}^S$ and RAI$^+$ and hence, we discard from the training the fluid measurements which are far from the mineral interface — as they are of no interest in this first step to characterize morphological uncertainty on $\varepsilon$. The resulting potential energy term writes:

$$U_1(\Theta) = \frac{\lambda_0}{2\sigma_0^2} \|1 - \varepsilon_\Theta - \mathrm{Im}\|^2_{\mathcal{D}^S} + \frac{\lambda_1}{2\sigma_1^2} \|1 - \varepsilon_\Theta - \mathrm{Im}\|^2_{\mathrm{RAI}^+} + \frac{1}{2\sigma_\Theta^2}\|\Theta\|^2 \tag{5.17}$$

where $\sigma_k$ are unknown standard deviations characterizing the noise distributions on their respective areas, and we assume a prior distribution on $\Theta$ given by $P(\Theta) \sim \mathcal{N}(0, \sigma_\Theta^2 I_{p+d})$. The notation $\|\cdot\|$ refers to either the RMS (root mean square) norm — inherited from the functional $\mathbb{L}^2$-norm — for the two first log-likelihood terms or to the usual Euclidean norm for the last log-prior term. In practice, we do not rely on a-priori manual calibration of the noise magnitudes — all $\sigma_k$ are set to be equal — but rather use the AW-HMC sampler to automatically and adaptively estimate these uncertainties through adjustments of the $\lambda_k$. This is especially meaningful in the neighborhood of the evolving fluid/solid interface (corresponding to the RAI$^+$) to study edge-enhancement implications and in the pure solid region to quantify the unresolved features. At the end of step 1, one gets a first a-priori estimation of the field $\varepsilon$, which presents the advantage of being denoised compared to the $\mu$CT images and hence is more suitable to differentiate. In this sense, we now have access to the time derivative of the surrogate porosity $\varepsilon_\Theta$ that is subsequently used to provide some preconditioning of the latent concentration field $C$.

### Step 2: Preconditioning of the latent reactive fluid

The second sampling step 2 relies on this first insight of the Bayesian neural network parameters obtained through step 1. We hence restart an adaptive weighting procedure with the AW-HMC sampler by adding additional constraints arising from the PDE model (5.12). As the acid concentration is a latent unknown field in our reactive inverse problem, we benefit from this second sampling step to provide a surrogate estimation $C_\Theta$ of this field and identify a first reactive parameter, namely $\mathrm{Da}^*_{\mathrm{II}}$. In this sense, we impose a physics-based regularization linking the porosity derivative to the surrogate concentration field through the PDE equation:

$$\frac{1}{\upsilon C_0}\frac{\partial \varepsilon_\Theta}{\partial t} - \mathrm{Da}^*_{\mathrm{II}} C_\Theta \mathbb{1}_{\{(1-\varepsilon)>0\}} = 0 \tag{5.18}$$

where the calcite molar volume $\upsilon$ and $C_0$ are constant parameters — we assume the concentration $C_0$ of continuous acid injection, defining the Dirichlet boundary conditions on $C$, to be known. In

a direct formulation, equation (5.18) is imposed over the whole domain $\Omega \times [0, T_f]$, though the PDE constraint in inverse modeling mainly brings meaningful information on the RAI. Indeed, we have $\dfrac{\partial \varepsilon_\Theta}{\partial t} \simeq -\dfrac{\partial \mathrm{Im}}{\partial t} > 0$ on the reactive area of interest, which is useful to characterize the reaction regime through the $\mathrm{Da}^*_{\mathrm{II}}$ dimensionless number. In the pure solid region where $\dfrac{\partial \varepsilon_\Theta}{\partial t} = 0$, the PDE constraint (5.18) translates into low acid penetration in $Q_S$ that we impose through the condition $C_\Theta = c_0 = 1\mathrm{e}{-7}$. In the fluid region $Q_F$, the latent acid concentration field is a solution of the following heat equation:

$$\frac{\partial C_\Theta}{\partial t} - D^*_m \Delta C_\Theta = 0 \tag{5.19}$$

with initial and boundary conditions, respectively unknown in the inverse formulation and non-homogeneous Dirichlet boundary conditions (see the dimensionless PDE model (5.12) from Sect. 5.4.3). Following the modeling assumptions of Sect. 5.4.2, especially on the diffusive dominated regime with $\mathrm{Pe} \ll 1$, we though assume as a first approximation that the surrogate acid concentration field $C_\Theta$ is driven by the quasi-stationary Poisson equation $\Delta C_\Theta = 0$ in $Q_F$. This behaves as a continuity extension of the surrogate concentration field from the domain boundary to the mineral evolving interface defined by the RAI. Along with the PDE equation (5.18) in the RAI, this defines augmented multi-potential energy for the second sampling step:

$$\begin{aligned} U(\Theta) &= U_1(\Theta) + \frac{\lambda_2}{2\sigma_2^2} \left\| (\upsilon C_0)^{-1} \alpha_\Theta \frac{\partial \varepsilon_\Theta}{\partial t} - C_\Theta \right\|^2_{\mathrm{RAI}} + \frac{\lambda_3}{2\sigma_3^2} \left\| \Delta C_\Theta \right\|^2_{\mathcal{D}^F} \\ &+ \frac{\lambda_4}{2\sigma_4^2} \left( \|1 - C_\Theta\|^2_{\mathcal{D}^\partial} + \|c_0 - C_\Theta\|^2_{\mathcal{D}^S} \right) + \frac{1}{2\sigma^2_\Theta} \|\Theta\|^2 \\ &:= U_1(\Theta) + U_2(\Theta) \end{aligned} \tag{5.20}$$

where the constant constraints on the boundary $\mathcal{D}^\partial$ and solid $\mathcal{D}^S$ datasets are gathered as a single term. The notation $\alpha_\Theta$ here refers to the first inverse parameter effectively sampled, with $\alpha_\Theta := (\mathrm{Da}^*_{\mathrm{II}})^{-1}$. This second step reinforces the sampling of the surrogate micro-porosity $\varepsilon_\Theta$ by providing insight into the latent concentration field $C_\Theta$ on the RAI and posterior distribution on the inverse parameter $\mathrm{Da}^*_{\mathrm{II}}$.

**Step 3: Overall data assimilation potential with full reactive model**

Finally, the third sampling step 3 will address the overall reactive inverse problem, to refine the micro-porosity and acid concentration predictions accounted for the fully coupled PDE model (5.12) and provide uncertainty quantification on the inverse parameters $\mathrm{Da}^*_{\mathrm{II}}$ and $D^*_m$. The extension by continuity of the acid concentration — from the Poisson equation in $Q_F$ — is replaced by its corresponding heat equation term (5.19) (see equation 5.23 bellow). We also use the diffusion-reaction PDE coupling $\varepsilon_\Theta$ and $C_\Theta$ to infer the dimensionless number $D^*_m$:

$$\frac{\partial C_\Theta}{\partial t} - D^*_m \mathrm{div}\left( \varepsilon_\Theta^{1+\eta} \nabla(\varepsilon_\Theta^{-1} C_\Theta) \right) + \mathrm{Da}^*_{\mathrm{II}} C_\Theta = \frac{\partial C_\Theta}{\partial t} - D^*_m \mathrm{div}\left( \varepsilon_\Theta^{1+\eta} \nabla(\varepsilon_\Theta^{-1} C_\Theta) \right) + \frac{1}{\upsilon C_0} \frac{\partial \varepsilon_\Theta}{\partial t} = 0 \tag{5.21}$$

which is theoretically valid on the whole RAI for the inverse modeling. Nonetheless, the heterogeneous diffusion term $\mathcal{D}_i(\varepsilon, C) := \mathrm{div}\left(\varepsilon^{1+\eta} \nabla(\varepsilon^{-1} C)\right)$ arising from Archie's law becomes highly sensitive at the mineral boundary due to jumps in the porosity derivatives at the interface. This may disrupt the identification of the inverse parameter $D^*_m$. The PDE constraint (5.21) therefore needs to be imposed on a reduced neighborhood of the reactive area of interest, namely the $\mathrm{RAI}^-$ domain.

This restricted RAI is then defined by the eligible points of the RAI domain where $D^*_m$ is predicted positive. From the overall samples of step 2, we compute the predictive BMA distributions of the two operators

$$\frac{\partial C_\Theta}{\partial t} + \frac{1}{\upsilon C_0} \frac{\partial \varepsilon_\Theta}{\partial t} \quad \text{and} \quad \mathcal{D}_i(\varepsilon_\Theta, C_\Theta) \tag{5.22}$$

on the domain $\Omega \times [0, T_f]$ and then estimate $D_m^*$ through equation (5.21) to define the RAI$^-$ domain.

From this procedure, one also gets an estimate of the posterior distribution of $D_m^*$ after sampling step 2 which is regarded as an initial a-priori on this inverse parameter in step 3. This will be further detailed in the applications (see Sect. 5.6 and 5.7). Taken together, the fully reinforced multi-potential energy for the third sampling step writes:

$$\begin{aligned} U(\Theta) &= U_1(\Theta) + \frac{\lambda_2}{2\sigma_2^2}\left\|(\upsilon C_0)^{-1}\alpha_\Theta\frac{\partial \varepsilon_\Theta}{\partial t} - C_\Theta\right\|_{\text{RAI}}^2 + \frac{\lambda_3}{2\sigma_3^2}\left\|\gamma_\Theta\frac{\partial C_\Theta}{\partial t} - \Delta C_\Theta\right\|_{\mathcal{D}^F}^2 \\ &+ \frac{\lambda_4}{2\sigma_4^2}\left(\|1 - C_\Theta\|_{\mathcal{D}^\partial}^2 + \|c_0 - C_\Theta\|_{\mathcal{D}^S}^2\right) \\ &+ \frac{\lambda_5}{2\sigma_5^2}\left\|\gamma_\Theta\left(\frac{\partial C_\Theta}{\partial t} + (\upsilon C_0)^{-1}\frac{\partial \varepsilon_\Theta}{\partial t}\right) - \operatorname{div}\left(\varepsilon_\Theta^{1+\eta}\nabla(\varepsilon_\Theta^{-1}C_\Theta)\right)\right\|_{\text{RAI}^-}^2 + \frac{1}{2\sigma_\Theta^2}\|\Theta\|^2 \\ &:= U_1(\Theta) + \widetilde{U_2}(\Theta) + U_3(\Theta) \end{aligned} \tag{5.23}$$

where $\gamma_\Theta := (D_m^*)^{-1}$ such that the set of inverse parameters we infer in practice is $(\mathcal{P}_{\text{inv}})_\Theta = \{\alpha_\Theta, \gamma_\Theta\}$. The data assimilation strategy developed in the present chapter incorporates successive physics-based constraints using a sequential reinforcement of the multi-potential energy $U(\Theta)$. This is achieved by splitting the sampling steps, which is required due to the strong coupling of the overall PDE system (5.12) involving latent field and unknown parameters. This overall algorithm is summarized in Figure 5.1.

### 5.5.3 Computational strategy for differential operator expression

This section is dedicated to the development of a differentiation strategy for efficient computation of the heterogeneous diffusion $\mathcal{D}_i(\varepsilon, C)$ arising from Archie's law. Indeed, the third sampling step in the sequential reinforcement of the multi-potential energy (see Sect. 5.5.2) involves the computation of this diffusion operator through a neural network surrogate model. This implies the use of Automatic Differentiation (AD) which is a prevalent technique in deep-learning frameworks such as Physics-Informed Neural Networks and Bayesian Physics-Informed Neural Networks. Such an automatic differentiation relies on gradient backpropagation to compute the derivatives of the neural network functional outputs with respect to its inputs, by using the chain rule principle. AD is thus a fast computational technique when it comes to the evaluation of first and second-order derivatives of the output fields, namely the spatial gradient and Laplacian operators, and the temporal partial derivatives. More complex non-linear operators resulting from two successive differentiation of non-trivial functional compositions — as this is the case for the $\mathcal{D}_i(\varepsilon, C)$ operator — can though readily lead to high-computational cost. This observation leads to reconsidering the heterogeneous diffusion term as a succession of sum and product of first and second-order operators. Consequently, we consider the diffusion operator $\mathcal{D}_i(\varepsilon, C)$ under two formulations: its compact form (5.24a) and its developed form (5.24c) reading

$$\mathcal{D}_i(\varepsilon, C) = \operatorname{div}\left(\varepsilon^{\eta+1}\nabla(\varepsilon^{-1}C)\right) \tag{5.24a}$$

$$= \operatorname{div}\left(\varepsilon^{\eta}\nabla C - \varepsilon^{\eta-1}C\nabla\varepsilon\right) = \operatorname{div}\left(\varepsilon^{\eta-1}(\varepsilon\nabla C - C\nabla\varepsilon)\right) \tag{5.24b}$$

$$= \varepsilon^{\eta-1}\left(\varepsilon\Delta C - C\Delta\varepsilon\right) + (\eta-1)\varepsilon^{\eta-1}\,\nabla\varepsilon\cdot\nabla C + (\eta-1)\varepsilon^{\eta-2}\,C\,\nabla\varepsilon\cdot\nabla\varepsilon \tag{5.24c}$$

Then we replace the expression of the diffusion in the multi-potential energy (5.23) with the novel operator formulation (5.24c). This makes possible to reduce the computational cost of evaluating this diffusion operator through merely the auto differentiation of the following terms: $\nabla\varepsilon_\Theta$, $\nabla C_\Theta$, $\Delta\varepsilon_\Theta$, and $\Delta C_\Theta$. Finally, we observe on the developed expression (5.24c) that the case $\eta = 1$ even results in a more straightforward expression of Archie's law which then writes $\mathcal{D}_i(\varepsilon, C) = \varepsilon\Delta C - C\Delta\varepsilon$. This is particularly convenient as the tortuosity index $\eta = 1$ can be regarded as

a) Comparison of diffusion operators on the 1D+Time

| | $T_{\text{CPU}}$ (ms) | Speedup $S$ | $T_{\text{GPU}}$ (ms) | Speedup $S$ |
|---|---|---|---|---|
| Original operator $\mathcal{D}_i(\varepsilon, C)$ | 37.13 | 1 | 11.32 | 3.28 |
| Developed operator (5.24c) with $\eta \neq 1$ | 24.78 | 1.49 | 6.985 | 5.32 |
| Developed operator (5.24c) with $\eta = 1$ | 10.66 | 3.48 | 6.739 | 5.51 |

b) Comparison of diffusion operators on the 2D+Time

| | $T_{\text{CPU}}$ (ms) | Speedup $S$ | $T_{\text{GPU}}$ (ms) | Speedup $S$ |
|---|---|---|---|---|
| Original operator $\mathcal{D}_i(\varepsilon, C)$ | 83.88 | 1 | 13.69 | 6.12 |
| Developed operator (5.24c) with $\eta \neq 1$ | 72.63 | 1.16 | 10.63 | 7.89 |
| Developed operator (5.24c) with $\eta = 1$ | 68.99 | 1.22 | 10.59 | 7.92 |

**Table 5.1: Computational times of the diffusion operators on the 1D+Time and 2D+Time inverse problem:** comparison between several expressions of the differential operator for CPU and GPU implementations. The Speedup is computed as $S = T_0/T_\bullet$ with $T_0 := T_{\text{CPU}}$ for the original expression $\mathcal{D}_i(\varepsilon, C) = \text{div}\left(\varepsilon^{\eta+1}\nabla(\varepsilon^{-1}C)\right)$. All the computational times are expressed in milliseconds (ms) and are averaged on several evaluations of the diffusion operator during the sampling procedure.

an approximation of the effective diffusivity in pore-scale models (*e.g.* see [279]). Furthermore, this reduced expression confirms the high sensitivity of the heterogeneous diffusion term at the mineral boundary $\sigma$ due to the micro-porosity Laplacian involved in Archie's law. Considering suitable differential operator expressions can enhance the surrogate model efficiency by reducing the automatic differentiation cost.

We perform some validations of this first insight through computational time measurements for the different expressions of the heterogeneous diffusion term. We hence compare the original formulation of $\mathcal{D}_i(\varepsilon, C)$ with the developed operator (5.24c) for tortuosity coefficients $\eta = 0.5$ — to consider the most general form — and $\eta = 1$ that leads to the reduced evaluation of the heterogeneous diffusion. We account for computational times on both CPU and GPU devices and perform several evaluations of the diffusion operator expressions to provide averaged computational times along the sampling procedure of step 3. These results are summarized in Table 5.1 for the 1D+Time test case (Table 5.1.a) and 2D+Time application (Table 5.1.b) explicitly developed in the validation Sect. 5.6 and application Sect. 5.7. We define in each case the reference computational cost $T_0$ as the CPU time necessary to evaluate the original operator expression $\mathcal{D}_i(\varepsilon, C)$. This respectively leads to $T_0 = 37.13$ ms and $T_0 = 83.88$ ms for 1D+Time and 2D+Time applications. We then evaluate the speedup, denoted $S$, of the distinct operator formulations as $S = T_0/T_\bullet$ where $T_\bullet$ are their respective computational times. It results from this comparison an effective improvement of the computational costs, either on CPU or GPU, when considering the developed operator (5.24c) from equation (5.24) — even in its general form for $\eta \neq 1$ (see second rows of Table 5.1.a and 5.1.b). This highlights that the configuration that best optimizes the speedup is to use the operator (5.24c) on GPU devices. The improvement between the general and reduced form of the operator (5.24c) is, however, less significant especially in 2D+Time. This can be readily explained by the fact that most of the computational time is spent evaluating the gradient and Laplacian operators rather than their combination. In this sense, the general form (5.24c) can be used effectively regardless of the tortuosity index value $\eta$. Overall, the developed heterogeneous diffusion operator (5.24c) contributes to reducing the computational cost of its single evaluation.

Suitable choices in the differential operator expressions considerably improve the AD cost when considering complex non-linear operators with non-trivial functional compositions, as for Archie's law. This, therefore, reduces the computational time spent in evaluating one instance of these operators. Such improvements are meaningful, accounting for the numerous surrogate model evaluations required for an appropriate sampling of the target posterior distribution (see equation

(4.2) in Chapter 4) through MCMC samplers. Considering the developed formulation (5.24c) of the heterogeneous diffusion operator on GPU devices hence implies a significant enhancement of the overall computational time of the present data assimilation strategy.

## 5.6 Validation on synthetic 1D+Time calcite dissolution

In this chapter, we develop a novel data assimilation strategy to address reactive inverse problems in pore-scale imaging with uncertainty quantification. This aims to quantify morphological uncertainty on the micro-porosity field $\varepsilon$ and estimate reliable ranges of chemical parameters through dynamical $\mu$CT noisy observations augmented with PDE models of dissolution. The present strategy is based on the robust Bayesian framework presented in Chapter 4 along with the AW-HMC sampler (see Sect. 4.4.1 of Chapter 4) and relies on sequential reinforcement of the multi-potential energy.

In this section, we validate the present methodology on inverse problems of calcite dissolution with heterogeneous porosity in artificial 1D spatial configurations. All the $\mu$CT measurements that we consider are synthetic observations resulting from direct numerical simulations of reactive flows with noise perturbation, in order to validate our methodology in well-established test cases. The validation test case is a purely synthetic 1D+Time problem, for which we check two configurations with distinct tortuosity indices with $\eta = 1$ and $\eta = 0.5$.

### 5.6.1 Direct reactive model: problem set up

We consider two heterogeneous samples of 1D synthetic calcite cores whose initial geometries are characterized by the numerical $\mu$CT images presented in Figure 5.2 on a 'physical' spatial domain $\Omega$ of width $0.3$mm. These initial images correspond to normalized greyscale tomographic scans, corrupted with noise that either accounts for sensor noise or unresolved morphological features. Direct numerical simulations of reactive processes are then performed on these initial geometries to provide synthetic $\mu$CT dynamical images of dissolution. These observation data are generated by solving the reaction-diffusion system (5.8) by means of mesh-based and particle methods — namely a Backward Euler or Mid Point method for the time integration coupled with Particle Strength Exchanges scheme for the heterogeneous diffusion — on a Cartesian spatiotemporal grid of resolution $N_x = 200$ and $N_t = 240$. Continuous acid injection is maintained through non-homogeneous Dirichlet boundary conditions on the domain $\Omega$ to ensure a diffusive-dominated regime. Numerically, we consider a strong acid solution with $\mathrm{pH} = 0$ such that the normalizing constant $C_0$ equals 1. The characteristic length $L$ of these porous samples is set to $L = 0.1$mm and the reactive parameters are respectively defined by $K_s = 0.8913\,\mathrm{mol.m^{-2}.s^{-1}}$, $D_m = 1\mathrm{e}{-9}\,\mathrm{m^2.s^{-1}}$, and $\gamma_{\mathrm{H^+}} = 1\mathrm{e}{-3}\,\mathrm{m^3.mol^{-1}}$ — taken from the benchmark [204]. The reactive specific area $A_s$ is set to $A_s = 1\mathrm{e}3\,\mathrm{m^{-1}}$, and we do not account for the calcite molar volume $\upsilon$ in these test cases — as such 1D+Time examples do not mean to be physically consistent but rather serve validation purposes. We also consider distinct tortuosity indexes, namely $\eta = 1$ and $\eta = 0.5$, on the different geometries to address both the compact form (5.24a) and develop form (5.24c) of the diffusion operator $\mathcal{D}_i(\varepsilon, C)$ in the data assimilation problem. The DNS is performed until the overall calcite core is dissolved which corresponds to a characteristic final time $T_f = 24$ s. Taken together, one gets a sequence of synthetic $\mu$CT images $\mathfrak{Im}_{i,j}$, similar to Figure 5.2, characterizing the dissolution process of the two calcite cores on the 'physical' spatiotemporal domain $\Omega \times [0, T_f]$.

### 5.6.2 Dimensionless inverse problem and dimensionless numbers

From the setting of these reactive parameters, one identifies the dissolution regime of these test cases given by the dimensionless catalytic Damköhler $\mathrm{Da}_{\mathrm{II}} = 8.913$ from equation (5.6). The inference of this Damköhler number is though not straightforward in inverse problems, as developed in Sect. 5.4.3, and we define the dimensionless time $t^*$ such that the its related final time is $T_f^* = 1$.

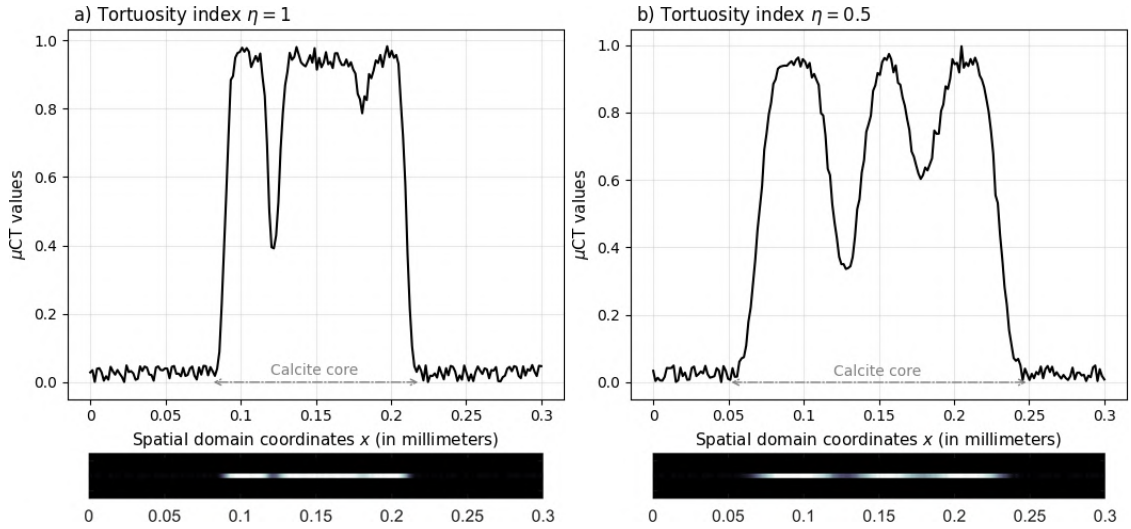


**Figure 5.2: Initial $\mu$CT images defining the porous sample geometries:** synthetic cases with tortuosity indices a) $\eta = 1$ and b) $\eta = 0.5$. The $\mu$CT measurements are normalized, corrupted with noise, and provide the dataset $\mathrm{Im}$ before the dissolution process. The calcite core regions are identified by the double-headed arrows, and correspond to the maximum intensity in the greyscale tomographic scans displayed below.

The dimensionless spatial variable $x^*$ is computed as in the dimensionless formulation of the direct problem using $x^* = x/L$. For the data assimilation, we hence consider the dimensionless domain $\overline{\Omega}^* \times [0, T_f^*] = [0,3] \times [0,1]$ to extract the observation dataset

$$\mathcal{D} = \{(x_k, t_k) \in [0,3] \times [0,1], \quad k = 1...N_{\text{obs}}\} \tag{5.25}$$

where the number of training points $N_{\text{obs}} = 7725$ represents about 16% of the data required for the full field reconstructions on $\Omega^* \times [0, T_f^*]$. The dataset $\mathcal{D}$ is divided into the corresponding datasets $\mathcal{D}^S$, $\mathcal{D}^F$, $\mathcal{D}^{\text{RAI}}$, $\text{RAI}^+$, $\text{RAI}^-$ and $\mathcal{D}^\partial$ that respectively cover around 50%, 4%, 15%, 13%, 10% and 8% of the $N_{\text{obs}}$ training measurements. One also determines the scaling dimensionless factor $D_{\text{ref}}$ which appears in the dimensionless inverse formulation (5.12):

$$D_{\text{ref}} = \frac{T_f^* L^2}{T_f} = 4.16\text{e}{-10}\,\text{m}^2.\text{s}^{-1} \tag{5.26}$$

according to the relation (5.9) and the estimations of $T_f$, $T_f^*$ and $L$. We characterize the dissolution regime in these reactive inverse problems by means of the two dimensionless numbers defined in (5.11), and one gets:

$$\text{Da}_{\text{II}}^* = 21.3912 \quad \text{and} \quad D_m^* = 2.4 \tag{5.27}$$

which are related to the inverse parameters to infer through $(\mathcal{P}_{\text{inv}})_\Theta = \{\alpha_\Theta, \gamma_\Theta\} = \left\{(\text{Da}_{\text{II}}^*)^{-1}, (D_m^*)^{-1}\right\}$. For such 1D+Time reactive inverse problems, the overall multi-potential energy finally writes in the case $\eta = 1$:

$$\begin{aligned} U(\Theta) = {} & \frac{\lambda_0}{2\sigma_0^2} \|1 - \varepsilon_\Theta - \text{Im}\|_{\mathcal{D}^S}^2 + \frac{\lambda_1}{2\sigma_1^2} \|1 - \varepsilon_\Theta - \text{Im}\|_{\text{RAI}^+}^2 + \frac{\lambda_2}{2\sigma_2^2} \left\| \alpha_\Theta \frac{\partial \varepsilon_\Theta}{\partial t} - C_\Theta \right\|_{\text{RAI}}^2 \\ & + \frac{\lambda_3}{2\sigma_3^2} \left\| \gamma_\Theta \frac{\partial C_\Theta}{\partial t} - \frac{\partial^2 C_\Theta}{\partial x^2} \right\|_{\mathcal{D}^F}^2 + \frac{\lambda_4}{2\sigma_4^2} \left( \|1 - C_\Theta\|_{\mathcal{D}^\partial}^2 + \|1\text{e}{-7} - C_\Theta\|_{\mathcal{D}^S}^2 \right) \\ & + \frac{\lambda_5}{2\sigma_5^2} \left\| \gamma_\Theta \left( \frac{\partial C_\Theta}{\partial t} + \frac{\partial \varepsilon_\Theta}{\partial t} \right) - \left( \varepsilon_\Theta \frac{\partial^2 C_\Theta}{\partial x^2} - C_\Theta \frac{\partial^2 \varepsilon_\Theta}{\partial x^2} \right) \right\|_{\text{RAI}^-}^2 + \frac{1}{2\sigma_\Theta^2} \|\Theta\|^2 \end{aligned} \tag{5.28}$$

and is sequentially reinforced, as presented in Sect. 5.5.2, through three successive sampling steps using the AW-HMC sampler. The hyperparameters setting of the sequential AW-HMC samplers together with the neural network architecture are detailed hereafter.

### 5.6.3 Deep learning configuration

Regarding the deep learning strategy for the overall data assimilation problem, we use two distinct neural network architectures to define the micro-porosity and acid concentration surrogate models. Each surrogate model has, therefore, one single output corresponding to $\varepsilon_\Theta$ and $C_\Theta$, respectively. This is preferred to merging the two outputs into a single neural network architecture to avoid a strong correlation between the output fields. Indeed, providing surrogate models not strongly correlated with a multiple-output neural network may require numerous hidden layers that straightforwardly impact the overall computational cost. On the contrary, using distinct neural networks makes it possible to build independent surrogate models while retaining few hidden layers and, therefore, a reasonable number of neural network parameters. Correlations between the two neural network architectures, and then the outputs fields $\varepsilon_\Theta$ and $C_\Theta$, are merely achieved through the PDE model defining the multi-potential energy (5.28). This deep learning configuration is more meaningful for such a reactive data assimilation problem since a high correlation — due to the neural network architecture — with the latent field $C_\Theta$ can highly disrupt the micro-porosity recovery. Relying on the PDE model to ensure relevant correlation hence appears as the most appropriate strategy.

The first neural network establishing the micro-porosity surrogate model $\varepsilon_\Theta$ is composed of 4 hidden layers with 32 neurons per layer and a hyperbolic tangent activation function. The output layer is complemented by a rectified hyperbolic tangent $\mathrm{Tanh}^r(z) = 0.5(\mathrm{Tanh}(z) + 1)$ to ensure output values between 0 and 1. This neural network complexity provides the best approximation of the micro-porosity during the first sampling step 1 while maintaining moderate computational costs. Indeed, we analyze in Figure 5.3 the impact of the neural network architecture both on the computational time spent on the sampling procedure and the BMA accuracy, computed as:

$$\text{BMA-E}^\varepsilon = \left\| P\left(\varepsilon_\Theta \,|\, (x,t), \mathcal{D}, \mathcal{M}\right) - \varepsilon \right\|^2_{\Omega^* \times [0, T_f^*]} \tag{5.29}$$

where the notation $\|\cdot\|$ used here refers to the functional $\mathbb{L}^2$-norm and $P\left(\varepsilon_\Theta \,|\, (x,t), \mathcal{D}, \mathcal{M}\right)$ is the BMA approximation from equation (4.3) in Chapter 4 (*e.g.* see [319]). For the optimal Neural Network (NN) configuration, one estimates the sampling computational cost, providing the overall samples of the posterior distribution based on the $N_{\text{obs}}$ training measurements, to about 17 min. The BMA prediction obtained through equation (4.3), over the whole computational domain $\Omega^* \times [0, T_f^*]$ is meanwhile immediate — less than 1 s on GPU and a few seconds on CPU. Recovering the latent concentration $C_\Theta$ will require less neural network expressivity compared to the micro-porosity field which needs to integrate noisy data, and unresolved morphological features in its reconstruction. In this sense, we assume that the second neural network defining the acid surrogate model is composed of 3 hidden layers with 32 neurons per layer and a hyperbolic tangent activation function. This is only one layer less compared to the first NN for $\varepsilon_\Theta$ but enables saving $1056$ parameters. The number of network parameters is, therefore, $3297$ for the first sampling and increases to $5538$ for the second and third sampling steps with the two additional inverse parameters.

The other hyperparameters concerning the AW-HMC sampler are summarized in Table 5.2 for the sequential sampling steps. These sampler parameters involve, *inter alia*, several adaptive steps $N$ during which the critical weights $\lambda_k$ are automatically adjusted through an Inverse Dirichlet basis (see equation (4.22) in Sect. 4.4.1 from Chapter 4), and a number of overall sampling steps $N_s$. The two other parameters, namely $L$ and $\delta t$, are intrinsically related to the Hamiltonian Monte Carlo structure of the AW-HMC sampler. Indeed, they are involved in the deterministic step that relies on the leapfrog symplectic integrator to solve for the Hamiltonian dynamical system (4.8) (see Sect. 4.3.1 in Chapter 4). We also refer to our methodological Chapter 4 for more details on these hyperparameters and especially to Algorithm 1 (Adaptively Weighted Hamiltonian Monte Carlo) for their respective role in the sampling phases.

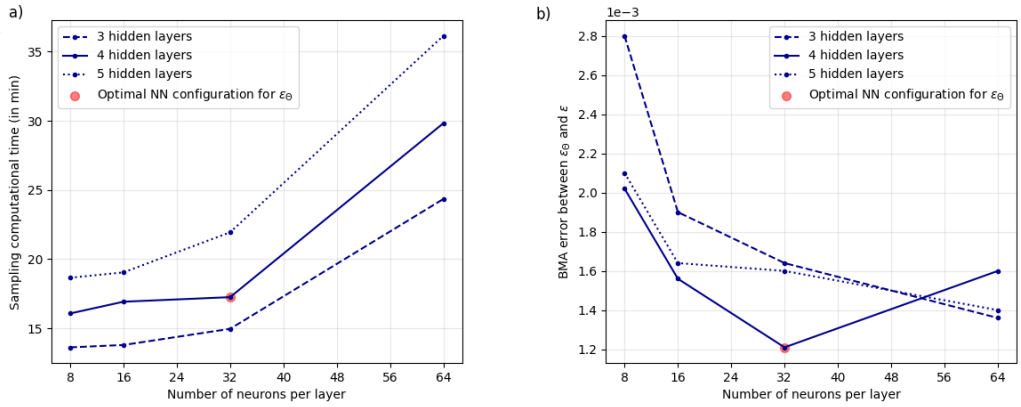


**Figure 5.3: Neural Network configuration choice for the surrogate model on the micro-porosity field:** a) Computational cost of sampling step 1 with respect to the neural network architectures both in terms of the number of hidden layers and neurons per layer. b) Bayesian Model Average (BMA) error between the surrogate model $\varepsilon_\Theta$ and groundtruth $\varepsilon$, computed as in equation (5.29), for different neural network architectures.

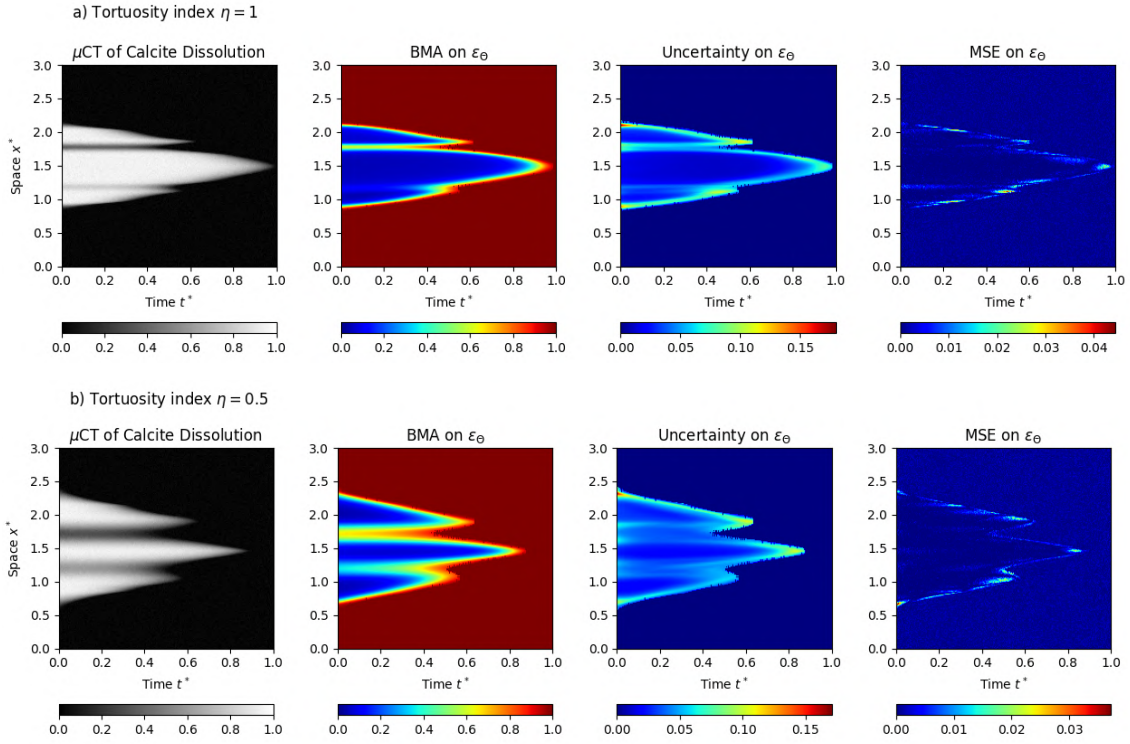


**Figure 5.4: Uncertainty Quantification on 1D+Time reactive inverse problem with data assimilation:** Bayesian Model Average (BMA) predictions on the micro-porosity field $\varepsilon_\Theta$ with their local uncertainties — given by the standard deviation on the posterior distribution of the predictions — and mean squared errors (MSE). The top row corresponds to the initial geometry from Figure 5.2a with tortuosity index $\eta = 1$. The bottom row is related to the initial porous sample from Figure 5.2b with $\eta = 0.5$.

| Sampling step | Number of adaptive steps $N$ | Number of samples $N_s$ | Number of leapfrog steps $L$ | Leapfrog time step $\delta t$ |
|---|---|---|---|---|
| 1) Preconditioning $\varepsilon_\Theta$ | 50 | 200 | 200 | 1e−3 |
| 2) Preconditioning $C_\Theta$ + Inference $\alpha_\Theta$ | 20 | 200 | 200 | 5e−4 |
| 3) Full data assimilation | 4 | 200 | 200 | 2e−4 |

**Table 5.2: AW-HMC hyperparameters on the 1D+Time reactive inverse problem:** Setting of the sampler hyperparameters for the three sequential sampling steps defined in Figure 5.1. The number of adaptive steps $N$ along with the leapfrog parameters $L$ and $\delta t$ are AW-HMC sampler-specific parameters.

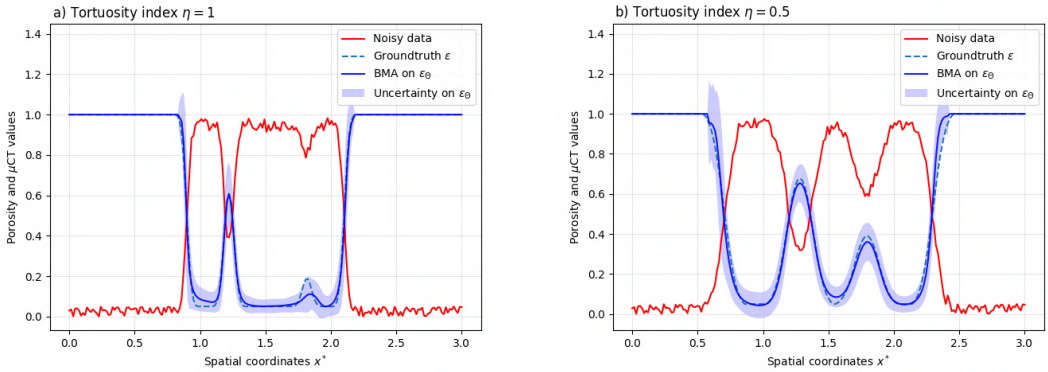


**Figure 5.5: Uncertainty Quantification on the micro-porosity field at the initial state ($t^* = 0$) for 1D+Time reactive inverse problem:** Corrupted $\mu$CT image before dissolution, groundtruth on $\varepsilon$, BMA prediction, and uncertainty on $\varepsilon_\Theta$ plotted along the spatial dimensionless coordinates $x^*$. Validation test cases with tortuosity indexes a) $\eta = 1$ and b) $\eta = 0.5$.

### 5.6.4 Numerical results

We demonstrate the validity of our data assimilation approach on synthetic inverse problems of calcite dissolution whose initial core geometries are characterized in Figure 5.2, and for which the dynamical $\mu$CT images are provided through DNS (see Sect. 5.6.1). In the data assimilation Bayesian framework, we first select log-normal prior distributions on $(\mathcal{P}_{\text{inv}})_\Theta = \{\alpha_\Theta, \gamma_\Theta\}$, which ensures the positivity of the inverse parameters, and independent normal distribution for the neural network parameters $\theta$. Nonetheless, appropriate change of variables on the inverse parameters, namely $\bullet_\Theta = e^{\widetilde{\bullet_\Theta}}$, makes it possible to consider Gaussian prior distributions on the newly defined set of parameter $\Theta = \{\theta, \widetilde{\mathcal{P}}_{\text{inv}}\}$ (*e.g.* see [328]). This is the underlying hypothesis considered when defining the log-prior term in the potential energy (5.28), where we assume $P(\Theta) \sim \mathcal{N}(0, \sigma_\Theta^2 I_{p+d})$. In practice, we use the standard deviation $\sigma_\Theta = 10$ in the applications such that slightly diffuse distribution induces weakly informed priors on the $\Theta$ parameters. We also impose weakly informed priors on the inverse parameters such that we do not rely on biased a-priori on their respective scaling. In this sense, we benefit from the AW-HMC sampler advantages to handle multiscale inverse problems with unknown informative priors. We also avoid hand-tuning of the distinct task uncertainties by setting all the $\sigma_k$, $k = 0...5$, to be equal in equation (5.28). On the contrary, automatic adjustment of the weighting parameters $\lambda_k$ will provide intrinsic task uncertainties during the sampling procedure.

From the overall sampling procedure, we first obtain a Bayesian Model Average prediction on the porosity field $\varepsilon_\Theta$ which is approximated by (*e.g.* see [319]):

$$P\left(\varepsilon_\Theta | (x,t), \mathcal{D}, \mathcal{M}\right) \simeq \frac{1}{N_s - N} \sum_{\tau=N}^{N_s} P\left(\varepsilon_\Theta | (x,t), \Theta^{t_\tau}\right) \tag{5.30}$$

where $P\left(\varepsilon_\Theta \,|\, (x,t), \Theta^{t_\tau}\right)$ is the surrogate model prediction of the micro-porosity resulting from

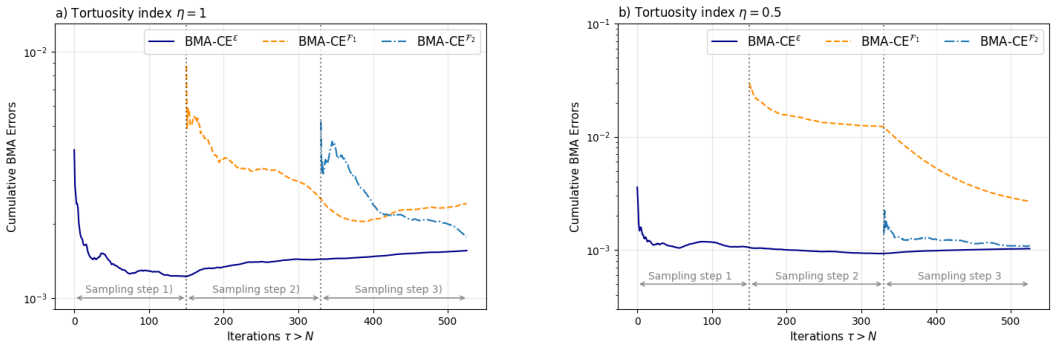


**Figure 5.6: Bayesian Model Average Cumulative Error diagnostics, as defined in equations (5.31)-(5.33), for 1D+Time reactive inverse problem:** BMA-CE on the micro-porosity field prediction $\varepsilon$ throughout the sampling iterations, and BMA-CE on the PDE constraint residuals $\mathcal{F}_1$ and $\mathcal{F}_2$ defined in (5.32) and introduced successively. The dotted vertical lines split the sampling steps in the sequential reinforcement of the multi-potential energy (5.28). Dissolution inverse problem on the initial geometries from a) Figure 5.2a with tortuosity index $\eta = 1$ and b) Figure 5.2b with tortuosity index $\eta = 0.5$.

the sampling iteration $\tau$ for the set of parameters $\Theta$ — including both the neural network and inverse parameters. Similarly, one can also compute local uncertainties on the output porosity field given the standard deviation metric on the posterior distribution of the predictions. These uncertainty quantification results are presented in Figure 5.4 along the whole dissolution time $t^*$ for both the initial core geometries with distinct tortuosity indexes. We also compare the local uncertainties on the micro-porosity field with the traditional MSE between the BMA surrogate prediction obtained by equation (5.30) and the groundtruth $\varepsilon$. This shows enhanced mean squared errors on the core edges during the calcite core dissolution which are, however, embedded in the local uncertainties. The latter uncertainties also tend to increase in these regions, characterizing the challenge of capturing reliable core interfaces from the dynamical $\mu$CT images. In this sense, one can query the confidence of mineral reactivity assessment using merely differential imaging techniques on the dynamical $\mu$CT scans. From the dynamical observation of the calcite core dissolution, we obtain uncertainties on the initial state geometry represented in Figure 5.5. This shows that the posterior prediction on $\varepsilon_\Theta$ covers the groundtruth micro-porosity field $\varepsilon$ and provides upper and lower bounds for the residual, potentially unresolved, micro-porosity $\varepsilon_0$ estimation in the porous matrix — *e.g.* $1.8\% \leqslant \varepsilon_0 \leqslant 9\%$ in the case $\eta = 1$ for the 95% confidence interval, corresponding to approximately two standard deviations.

Moreover, we rely on the Bayesian Model Average Cumulative Error metric, denoted BMA-CE and introduced in Sect. 4.4.3 of Chapter 4, to quantify the sampling efficiency in terms of convergence along the marginalization process. We first compute the BMA-CE diagnostics for the porosity field $\varepsilon$ based on:

$$\text{BMA-CE}^{\varepsilon}(\tau) = \left\| \frac{1}{\tau - N} \sum_{i=N}^{\tau} P\left(\varepsilon_\Theta \,|\, (x,t), \Theta^{t_i}\right) - (1 - \text{Im}) \right\|^2 \qquad \forall \tau > N. \tag{5.31}$$

Equation (5.31) hence defines for each sampling step $\tau$, after the adaptive steps, a cumulative error characterizing the convergence of the BMA model toward the groundtruth $\varepsilon$. Such a diagnostic is computed during the overall sampling procedure, covering the three successive steps of sequential reinforcement. In the same manner, we extend this notion of convergence to the PDE constraints by computing the BMA-CE metric on their respective residuals. We, therefore, introduce $\mathcal{F}_1$ and $\mathcal{F}_2$ the PDE constraints residuals arising from the reactive model (5.12) and involved in the multi-potential energy (5.28):

$$\begin{aligned} \mathcal{F}_1(\varepsilon_\Theta, C_\Theta) &:= \alpha_\Theta \frac{\partial \varepsilon_\Theta}{\partial t} - C_\Theta \\ \mathcal{F}_2(\varepsilon_\Theta, C_\Theta) &:= \gamma_\Theta \left( \frac{\partial C_\Theta}{\partial t} + \frac{\partial \varepsilon_\Theta}{\partial t} \right) - \left( \varepsilon_\Theta \frac{\partial^2 C_\Theta}{\partial x^2} - C_\Theta \frac{\partial^2 \varepsilon_\Theta}{\partial x^2} \right) \end{aligned} \tag{5.32}$$

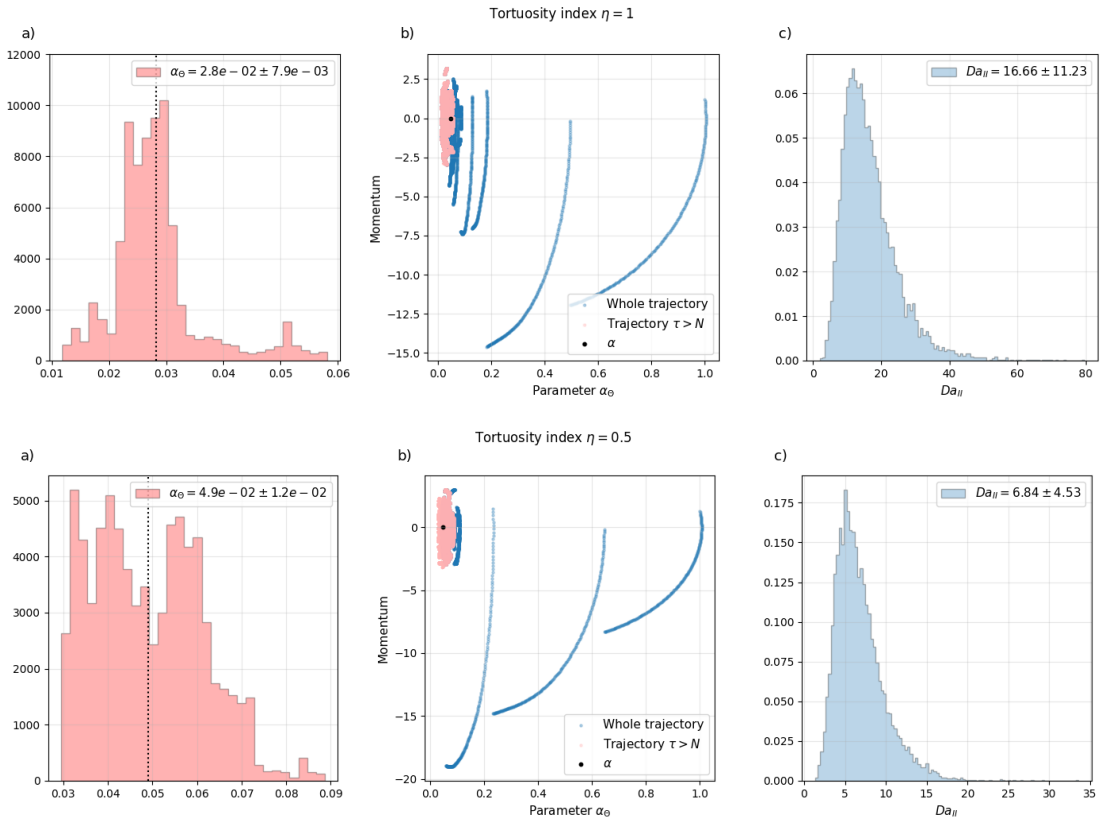


**Figure 5.7: Posterior distributions of 1D+Time reactive inverse problem:** a) Histogram of the marginal posterior distributions for the inverse parameter $\alpha_\Theta$. b) Phase diagrams of its trajectory throughout the sampling, with the adaptive steps trajectories (in blue) and effective sampling (in red). The groundtruth values of $\alpha$ are represented by the black dots. c) Resulting posterior distributions of the catalytic Damköhler number $\mathrm{Da}_{\mathrm{II}}$, determined through the log-normal distribution from relation (5.34). The top and bottom row respectively corresponds to the tortuosity indexes $\eta = 1$ and $\eta = 0.5$.

to finally define their corresponding diagnostics BMA-CE$^{\mathcal{F}_\bullet}$:

$$\text{BMA-CE}^{\mathcal{F}_\bullet}(\tau) = \left\| \frac{1}{\tau - N} \sum_{i=N}^{\tau} P\left(\mathcal{F}_\bullet(\varepsilon_\Theta, C_\Theta) \,|\, (x,t), \Theta^{t_i}\right) \right\|^2 \qquad \forall \tau > N. \tag{5.33}$$

These metrics are respectively computed on the sampling steps 2 and 3 for the residuals $\mathcal{F}_1$ and $\mathcal{F}_2$, and the resulting convergence curves are presented in Figure 5.6 for both initial geometries. Successively introducing the additional PDE constraints results in deviations in the BMA-CE$^\varepsilon$ curve compared to the purely data-fitting sampling step 1. This means that the PDE model brings information on the porosity field $\varepsilon$ recovery instead of providing overfitting predictions. One also gets that the PDE constraints are satisfied by the convergence of their residual BMA-CE curves.

Regarding the inverse parameters inference, we represent in Figure 5.7a the histograms of the marginal posterior distributions of $\alpha_\Theta := (\mathrm{Da}^*_{\mathrm{II}})^{-1}$ for the two initial geometries from Figure 5.2. These distributions are obtained throughout the sampling steps 2 and 3, and provide intrinsic uncertainties on the parameter estimations. One also gets from Figure 5.7b the parameter trajectories when exploring the phase space distribution $\pi(\Theta, r)$ (see equation (4.4) in Chapter 4), where the convergence toward the mode during the adaptive steps is represented in blue. The final sampling, corresponding to the phase diagram trajectories for $\tau > N$, thus ensures an efficient exploration of the parameter mode neighborhood. Following the sequential reinforcement strategy detailed in Sect. 5.5, one gets at the end of the sampling step 2 a description of the restricted RAI$^-$ domain altogether with an initial estimate on the distribution of $D^*_m$.

The latter is regarded as an initial a-priori on the parameter $\gamma_\Theta$ in step 3, and is obtained as follows:

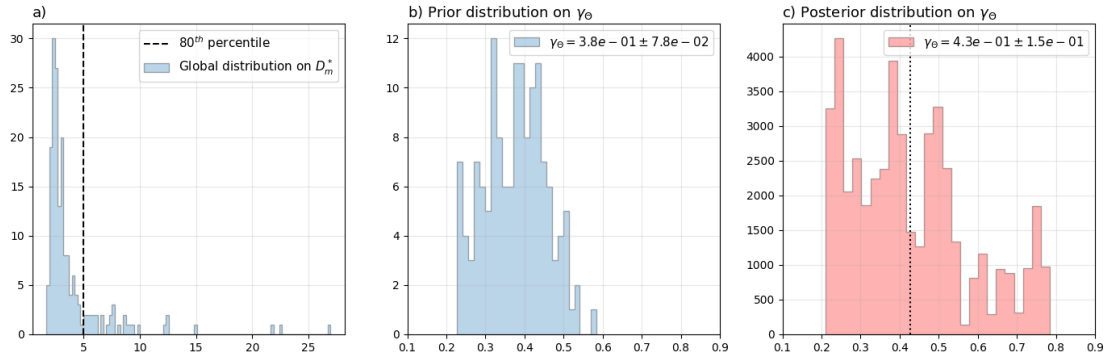


**Figure 5.8: Prior and posterior distributions on the inverse parameter $\gamma_\Theta$ for 1D+Time reactive inverse problem with tortuosity index $\eta = 1$:** a) Global distribution on the estimated parameter $D_m^*$ arising from a-posteriori analysis on the sampling step 2. We discard the distribution tail after the vertical dashed line corresponding to the $80^{\text{th}}$ percentile. b) Resulting prior distribution on the inverse parameter $\gamma_\Theta$, used as an a-priori in step 3. c) Posterior distribution on $\gamma_\Theta$ obtained from the overall data assimilation problem throughout sampling step 3.

- for the sampling iteration $\tau = N...N_s$ in step 2, we compute the (cumulative) predictive BMA distributions of the two operators

$$\frac{\partial C_\Theta}{\partial t} + \frac{1}{\upsilon C_0}\frac{\partial \varepsilon_\Theta}{\partial t} \quad \text{and} \quad \mathcal{D}_i(\varepsilon_\Theta, C_\Theta),$$

- we establish the $\text{RAI}_\tau^-$ as the admissible points of the RAI where $D_m^*$ is predicted positive for each sampling iteration $\tau > N$,

- we compute a spatially averaged estimation of the parameter $\left(\overline{D_m^*}\right)_\tau$ on this eligible domain, where

$$\left(\overline{D_m^*}\right)_\tau = \frac{1}{\#\text{RAI}_\tau^-} \sum_{k \in \text{RAI}_\tau^-} (D_m^*)_\tau(x_k, t_k) \qquad \forall \tau > N,$$

- we can estimate a global distribution on $D_m^*$ throughout the overall samples of step 2 where we discard the distribution tail after the $80^{\text{th}}$ percentile,

- we finally evaluate the prior distribution on the inverse parameter $\gamma_\Theta := (D_m^*)^{-1}$ with its mean value $\overline{\gamma_\Theta}$ used as an initial a-priori in step 3,

In the case $\eta = 1$ for instance, one gets the global distribution on $D_m^*$ shown in Figure 5.8a, which translates into the prior distribution on $\gamma_\Theta$ given by Figure 5.8b with $\overline{\gamma_\Theta} = 3.8\text{e}{-1}$. Finally, we obtain the posterior distribution from the overall data assimilation problem throughout sampling step 3. This results in the distribution on the inverse parameter $\gamma_\Theta$ represented in Figure 5.8c, with the uncertainty range $\gamma_\Theta \in [0.274, 0.582]$.

Finally, one can estimate the posterior distribution on the catalytic Damköhler number $\text{Da}_{\text{II}}$ resulting from the overall data assimilation problem on dynamical $\mu$CT images. This comes from the observation that each inverse parameter, namely $\alpha_\Theta$ and $\gamma_\Theta$, is sought according to a log-normal distribution through the change of variable $\bullet_\Theta = e^{\widetilde{\bullet_\Theta}}$. Hence, we obtain two normal posterior distributions on the random variables $X_1$ and $X_2$ respectively associated with $\ln(\alpha_\Theta)$ and $\ln(\gamma_\Theta)$ such that $X_1 \sim \mathcal{N}\left(\mu_\alpha, \sigma_\alpha^2\right)$ and $X_2 \sim \mathcal{N}\left(\mu_\gamma, \sigma_\gamma^2\right)$. This combines into a normal distribution on $\ln(\gamma_\Theta/\alpha_\Theta)$ given by $(X_1 - X_2) \sim \mathcal{N}\left(\mu_\gamma - \mu_\alpha, \sigma_\gamma^2 + \sigma_\alpha^2\right)$, which is nothing more than a log-normal posterior distribution on the Damköhler number $\text{Da}_{\text{II}}$. Indeed, one gets that the random variable $X$ related to the dimensionless $\text{Da}_{\text{II}}$ number follows

$$X \sim \text{Log}\text{–}\mathcal{N}\left(\mu_\gamma - \mu_\alpha, \sigma_\gamma^2 + \sigma_\alpha^2\right) := \text{Log}\text{–}\mathcal{N}\left(\mu, \sigma^2\right), \tag{5.34}$$

whose mean and variance are respectively computed as

$$\mathbb{E}[X] = e^{\mu+\sigma^2/2} \quad \text{and} \quad \text{Var}(X) = e^{2\mu+\sigma^2}\left(e^{\sigma^2}-1\right). \tag{5.35}$$

The resulting posterior distributions on the Damköhler number $\text{Da}_{\text{II}}$ are represented in Figure 5.7c for both the initial calcite core geometries with their related tortuosity indexes. We finally obtain the uncertainty ranges $\text{Da}_{\text{II}} \in [5.43, 27.89]$ and $\text{Da}_{\text{II}} \in [2.30, 11.37]$ for the tortuosity indexes $\eta = 1$ and $\eta = 0.5$ respectively.

## 5.7 Pore-scale imaging inverse problem of calcite dissolution: 2D+Time application

In this section, we apply the data assimilation methodology developed in Sect. 5.5 to inverse problems for calcite dissolution with heterogeneous porosity levels. We consider a more realistic application involving the dissolution of a 2D calcite core following the configuration of the benchmark developed in [204]. This test case can provide a basis for reactive inverse problems in isotropic porous samples, although the $\mu$CT measurements are still synthetic observations resulting from DNS altered with noise.

### 5.7.1 Problem set up and dimensionless inverse formulation

We consider a 2D calcite crystal with a cylindrical shape, heterogeneous porosity levels, and two apertures, whose initial geometry is defined by the numerical $\mu$CT image from Figure 5.9, corrupted with Gaussian noise. We define the physical domain $\Omega \subset \mathbb{R}^2$ of width 0.2mm corresponding to the two-dimensional flow channel surrounding the calcite core. We first solve the direct formulation of the dissolution process for this initial geometry on a Cartesian spatiotemporal grid of resolution $N_x = N_y = 100$ and $N_t = 350$. We assume a diffusive-dominated regime with continuous acid injection through non-homogeneous Dirichlet boundary conditions on $\partial\Omega$. We also consider, as in the 1D+Time validation test cases, a strong acid solution with $\text{pH} = 0$ such that the normalizing constant is given by $C_0 = 1\,\text{mol.L}^{-1}$. The characteristic length $L$ of these porous samples is set to $L = 0.1$mm and the reactive parameters are respectively defined by $K_s = 0.8913\,\text{mol.m}^{-2}\text{.s}^{-1}$, $D_m = 1\text{e}{-9}\,\text{m}^2\text{.s}^{-1}$, and $\gamma_{\text{H}^+} = 1\text{e}{-3}\,\text{m}^3\text{.mol}^{-1}$, taken from the benchmark [204]. The reactive specific area $A_s$ is set to $A_s = 1\text{e}3\,\text{m}^{-1}$ — which is slightly underestimated compared to the computed value around $7.4\text{e}3\,\text{m}^{-1}$. We account for the calcite molar volume $\upsilon = 36.93\text{e}{-3}\,\text{L.mol}^{-1}$, and set a tortuosity index $\eta = 0.5$. The DNS is performed until the overall calcite is dissolved which corresponds to a characteristic final time $T_f = 175$ s. Taken together, one gets a sequence of synthetic $\mu$CT images $\mathfrak{Im}_{i,j}$ characterizing the dissolution process of the calcite core on the spatiotemporal domain $\Omega \times [0, T_f]$.

Given these reactive parameters, we identify the same dissolution regime as in the 1D+Time test cases, with a catalytic Damköhler given by $\text{Da}_{\text{II}} = 8.913$. The inverse formulation, however, results in distinct dimensionless numbers, namely $\text{Da}^*_{\text{II}}$ and $D^*_m$, arising from the scaling dimensionless factor $D_{\text{ref}}$. This scaling factor is here determined by:

$$D_{\text{ref}} = \frac{T^*_f L^2}{T_f} = 5.714\text{e}{-11}\,\text{m}^2\text{.s}^{-1}, \tag{5.36}$$

where the final dimensionless time is $T^*_f = 1$. Therefore, one gets from equation (5.11) the following dimensionless numbers characterizing this 2D+Time reactive inverse problem:

$$\text{Da}^*_{\text{II}} = 155.9775 \quad \text{and} \quad D^*_m = 17.5 \tag{5.37}$$

which are related to the inverse parameters through $(\mathcal{P}_{\text{inv}})_\Theta = \{\alpha_\Theta, \gamma_\Theta\} = \left\{(\text{Da}^*_{\text{II}})^{-1}, (D^*_m)^{-1}\right\}$. We consider the dimensionless domain $\overline{\Omega}^* \times [0, T^*_f] = [0, 2] \times [-1, 1] \times [0, 1]$, given the characteristic length $L$, to extract the observation dataset

$$\mathcal{D} = \{(x_k, y_k, t_k) \in [0, 2] \times [-1, 1] \times [0, 1], \quad k = 1...N_{\text{obs}}\} \tag{5.38}$$

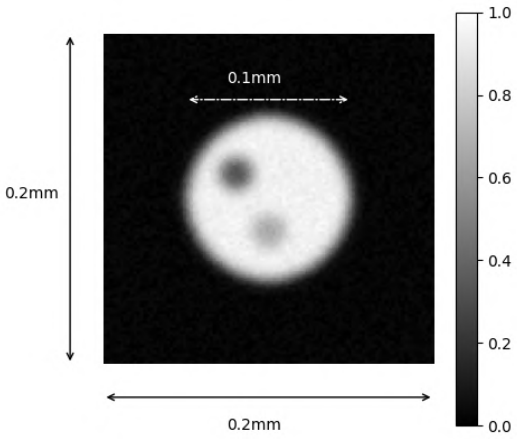


**Figure 5.9: Initial $\mu$CT image defining the 2D porous sample geometry:** Synthetic case with tortuosity index $\eta = 0.5$. The $\mu$CT measurements are normalized, corrupted with noise, and provide the observation dataset before the dissolution process. The cylindrical calcite core has a radius equal to $0.05$mm.

where the number of training points $N_{\text{obs}} = 15907$ represents less than $1\%$ of the data required for the full field reconstructions on the spatiotemporal domain $\Omega^* \times [0, T_f^*]$. This dataset $\mathcal{D}$ is then divided into $\mathcal{D}^S$, $\mathcal{D}^F$, $\mathcal{D}^{\text{RAI}}$, $\text{RAI}^+$, $\text{RAI}^-$ and $\mathcal{D}^\partial$ that respectively cover around $15.5\%$, $0.5\%$, $48\%$, $11\%$, $20\%$ and $5\%$ of the $N_{\text{obs}}$ training measurements. Finally, the multi-potential energy writes on this dataset decomposition:

$$
\begin{aligned}
U(\Theta) = \frac{\lambda_0}{2\sigma_0^2} \left\| 1 - \varepsilon_\Theta - \text{Im} \right\|_{\mathcal{D}^S}^2 + \frac{\lambda_1}{2\sigma_1^2} \left\| 1 - \varepsilon_\Theta - \text{Im} \right\|_{\text{RAI}^+}^2 + \frac{\lambda_2}{2\sigma_2^2} \left\| (\upsilon C_0)^{-1} \alpha_\Theta \frac{\partial \varepsilon_\Theta}{\partial t} - C_\Theta \right\|_{\text{RAI}}^2 \\
+ \frac{\lambda_3}{2\sigma_3^2} \left\| \gamma_\Theta \frac{\partial C_\Theta}{\partial t} - \Delta C_\Theta \right\|_{\mathcal{D}^F}^2 + \frac{\lambda_4}{2\sigma_4^2} \left( \left\| 1 - C_\Theta \right\|_{\mathcal{D}^\partial}^2 + \left\| 1\text{e}{-7} - C_\Theta \right\|_{\mathcal{D}^S}^2 \right) \\
+ \frac{\lambda_5}{2\sigma_5^2} \left\| \gamma_\Theta \left( \frac{\partial C_\Theta}{\partial t} + (\upsilon C_0)^{-1} \frac{\partial \varepsilon_\Theta}{\partial t} \right) - \mathcal{D}_i(\varepsilon_\Theta, C_\Theta) \right\|_{\text{RAI}^-}^2 + \frac{1}{2\sigma_\Theta^2} \left\| \Theta \right\|^2
\end{aligned}
\tag{5.39}
$$

where the heterogeneous diffusion operator $\mathcal{D}_i(\varepsilon_\Theta, C_\Theta)$ is computed in its developed form (5.24c) with $\eta = 0.5$. This overall potential energy is sequentially reinforced throughout three successive sampling steps, as detailed in Sect. 5.5.2 and validated in Sect. 5.6 on 1D+Time data assimilation problems.

### 5.7.2 Deep learning framework and computational efficiency

Regarding the deep learning strategy, the framework is kept identical to the 1D+Time validation test cases (see Sect. 5.6.3). In this sense, we consider two distinct neural network architectures, for the micro-porosity and acid concentration surrogate models, which are respectively composed of 4 and 3 hidden layers with 32 neurons per layer. The number of network parameters is, therefore, $3297$ for the first sampling and $5538$ for the second and third sampling steps with the two additional inverse parameters. The setting of the AW-HMC sampler hyperparameters is also summarized in Table 5.3 for the successive sampling steps.

Besides, we investigate the impact of the problem dimensionality by analyzing the computational efficiency of the present data assimilation approach with sequential reinforcement process. In this sense, we compare the computational costs of the three successive sampling steps on the 1D+Time and 2D+Time reactive inverse problems. The results of these computational time measurements are presented in Table 5.4 for both configurations. The first columns compare the sampling times, which is the time required to provide the overall samples of the posterior distributions using the AW-HMC sampler. This training phase is performed on the $N_{\text{obs}}$ observation data which are randomly selected and non-uniformly distributed on the whole Cartesian grids — respectively

| Sampling step | Number of adaptive steps $N$ | Number of samples $N_s$ | Number of leapfrog steps $L$ | Leapfrog time step $\delta t$ |
|---|---|---|---|---|
| 1) Preconditioning $\varepsilon_\Theta$ | 50 | 200 | 150 | 1e−3 |
| 2) Preconditioning $C_\Theta$ + Inference $\alpha_\Theta$ | 40 | 200 | 150 | 5e−4 |
| 3) Full data assimilation | 10 | 200 | 150 | 3e−4 |

**Table 5.3: AW-HMC hyperparameters on the 2D+Time reactive inverse problem:** Setting of the sampler hyperparameters for the three sequential sampling steps defined in Figure 5.1. The number of adaptive steps $N$ along with the leapfrog parameters $L$ and $\delta t$ are AW-HMC sampler-specific parameters.

a) Computational times for 1D+Time data assimilation

| | Sampling time $T_{\text{GPU}}$ (in hh:mm:ss) | Prediction time $T_{\text{CPU}}$ (in hh:mm:ss) |
|---|---|---|
| Sequential step 1 | 00:17:13 | 00:00:04 |
| Sequential step 2 | 01:38:01 | 00:00:13 |
| Sequential step 3 | 02:38:58 | 00:00:14 |

b) Computational times for 2D+Time data assimilation

| | Sampling time $T_{\text{GPU}}$ (in hh:mm:ss) | Prediction time $T_{\text{CPU}}$ (in hh:mm:ss) |
|---|---|---|
| Sequential step 1 | 00:16:26 | 00:04:59 |
| Sequential step 2 | 01:21:01 | 00:34:34 |
| Sequential step 3 | 02:41:10 | 00:41:18 |

**Table 5.4: Computational times of the successive sequential steps on the 1D+Time and 2D+Time inverse problem:** Comparison of the sampling times on GPU devices (first columns), and the prediction times on CPU devices (second columns) between 1D+Time and 2D+Time configurations. All the computational times are expressed under the form hh:mm:ss to ease the readability.

$N_x \times N_t = 200 \times 240$ in 1D+Time and $N_x \times N_y \times N_t = 100 \times 100 \times 350$ in 2D+Time. All the successive sampling steps are performed on GPU devices, and the computational times are expressed in hours, minutes and seconds (hh:mm:ss). In these sampling/training phases, the present methodology does not suffer from the curse of dimensionality. The 1D+Time and 2D+Time data assimilation problems present similar computational times, although the number of training observations is two times larger in 2D+Time. This establishes that most of the computational cost of the problem is correlated to the number of neural network parameters — as already confirmed in Sect. 5.6.3 and more specifically in Figure 5.3 — rather than the number of training points. Since it appears that the same neural network architecture as in 1D+Time is significant to describe the 2D+Time inverse problem, the computational efficiency of this 2D+Time data assimilation is significantly improved.

The second columns of Table 5.4 then compare the prediction time on CPU devices. This corresponds to the computational time necessary for the potential energy estimation and output field predictions on the whole domain $\Omega^* \times [0, T_f^*]$, along with the computation of the main differential operators required as additional outputs. Among the additional outputs, one finds the porosity time derivative at the end of step 1, and all the first-order derivatives and Laplacian operators for the porosity and concentration field at the end of step 2 — which are used to evaluate the initial a-priori on $\gamma_\Theta$. The first-order derivatives and Laplacian operators are also considered as output in step 3 to perform the a-posterior analysis based on the BMA-CE diagnostics. In contrast to the sampling phase, the computational time devoted to these predictions is larger when dimensionality increases. This comes from the observation that one needs to evaluate the output fields and

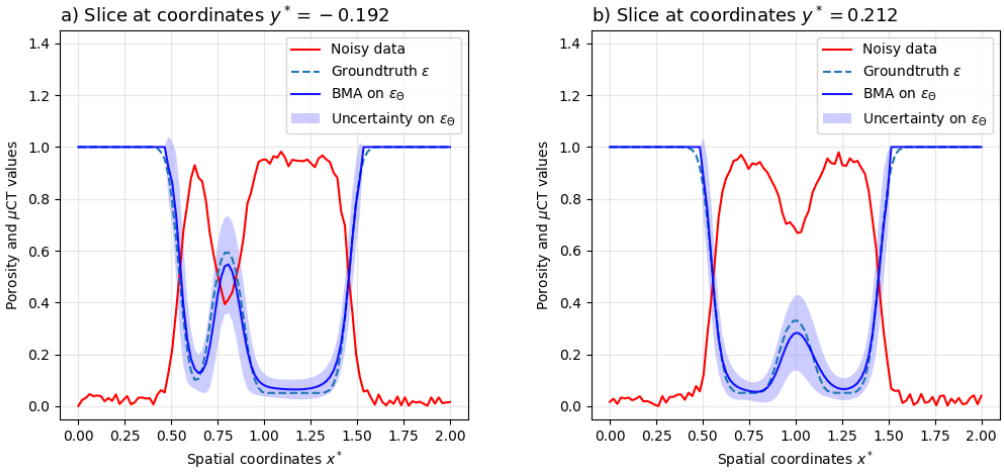


**Figure 5.10: Uncertainty Quantification on the micro-porosity field at the initial state ($t^* = 0$) for 2D+Time reactive inverse problem:** Corrupted $\mu$CT image before dissolution, groundtruth on $\varepsilon$, BMA prediction, and uncertainty on $\varepsilon_\Theta$. The results are plotted along the horizontal white dashed lines from Figure 5.11, at spatial coordinates a) $y^* = -0.192$ and b) $y^* = 0.212$.

additional differential operators on a Cartesian grid which is about 72 times larger in 2D+Time. The predictions of all these differential operators on the overall domain $\Omega^* \times [0, T_f^*]$ are achieved through automatic differentiation and hence are consistent with their evaluations along the training phase. This can straightforwardly be replaced by other standard differential schemes — as finite differences or PSE schemes — to evaluate these operators on the Cartesian grid, using merely the predictive porosity and acid concentration fields. However, the computational improvement of the process may not be that significant, since one needs to evaluate these operators for all the $N_s$ samplings steps — basically 600 times — to take into account their intrinsic uncertainties. This means that it only takes a few seconds per sample to evaluate these differential operators through automatic differentiation, which is thus comparable to other usual schemes. On top of that, the prediction phases here occur on CPU devices due to memory usage that is not marginal. Typically the micro-porosity field prediction on its own required the storage of $N_s \times N_x \times N_y \times N_t$ floats in 2D+Time, which is equivalent to about 1.9GB. In this sense, both memory usage and computational efficiency of this prediction phase could be improved, and efforts must be made in this direction. In prospect, we would like to benefit from the parallel architecture of GPU devices by investigating and using appropriate domain decompositions of $\Omega^* \times [0, T_f^*]$.

### 5.7.3 Results and discussion

We apply our data assimilation approach with sequential reinforcement of the multi-potential energy on this 2D+Time reactive inverse problem of calcite dissolution, based on synthetic dynamical $\mu$CT observations generated by DNS. We guarantee the positivity of the inverse parameter inference by selecting log-normal prior distributions and applying the same change of variable $\bullet_\Theta = e^{\widetilde{\bullet_\Theta}}$ as in the validation Sect. 5.6. This is combined with independent normal distribution on the neural network parameters, such that we assume the overall prior distribution $P(\Theta) \sim \mathcal{N}(0, \sigma_\Theta^2 I_{p+d})$. We also impose weakly informed priors on the inverse parameters since we do not impose a-priori information on their respective scaling.

At the end of the sequential sampling, one gets the Bayesian Model Average prediction on the porosity field $\varepsilon_\Theta$, approximated as in equation (5.29), along with its local uncertainties during the whole dissolution process. These uncertainty quantification results are presented in Figure 5.11 for several dissolution times, including the initial condition for $t^* = 0$ in Figure 5.11a. We compare these results with the synthetic $\mu$CT images and mean squared errors computed between the BMA surrogate prediction and the groundtruth $\varepsilon$. We observe enhanced uncertainties on the calcite core interfaces, including the aperture edges, and this all along the dissolution process. The initial state exhibits heterogeneous uncertainty distribution on the whole calcite, with lower uncertainties on

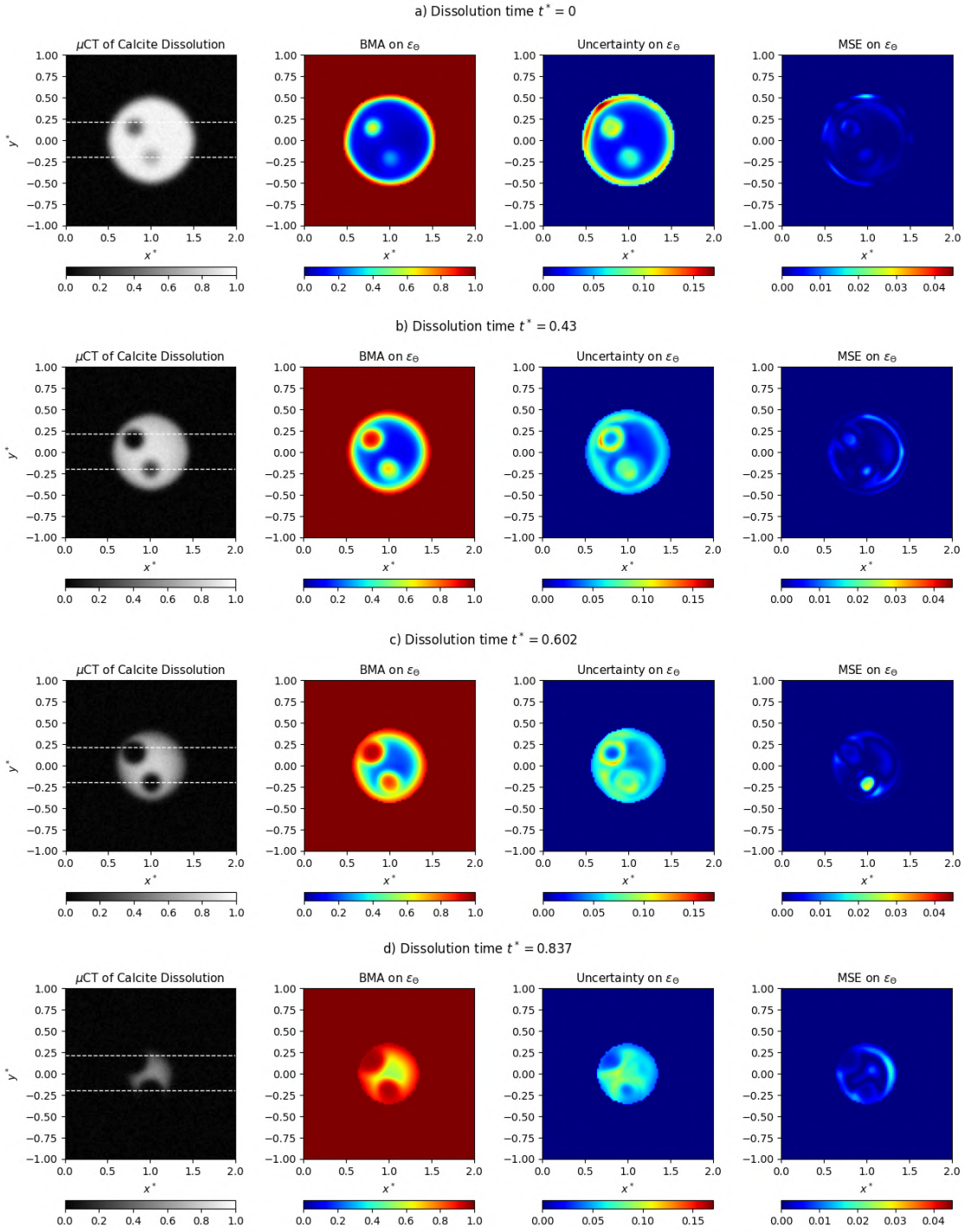


**Figure 5.11: Uncertainty Quantification on 2D+Time reactive inverse problem with data assimilation:** Bayesian Model Average (BMA) predictions on the micro-porosity field $\varepsilon_\Theta$ with their local uncertainties and mean squared errors (MSE). Comparison with the $\mu$CT dynamical images at several dissolution times, in the dimensionless formulation: a) Initial condition at $t^* = 0$. Intermediate dissolution times at b) $t^* = 0.43$, c) $t^* = 0.602$ and d) $t^* = 0.837$.

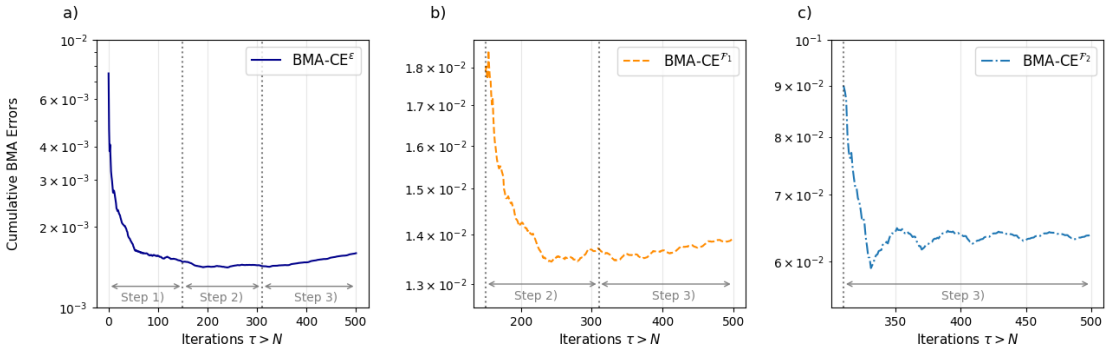


**Figure 5.12: Bayesian Model Average Cumulative Error diagnostics for 2D+Time reactive inverse problem:** BMA-CE on the micro-porosity field prediction $\varepsilon$ throughout the sampling iterations, and BMA-CE on the PDE constraint residuals $\mathcal{F}_1$ and $\mathcal{F}_2$ defined by equations (5.40) and introduced successively. The dotted vertical lines mark the sequential reinforcement of the multi-potential energy (5.39).

the pure solid region. As this mineral interface decreases due to the dissolution, the uncertainties tend to become more homogeneously distributed (see Figure 5.11c and 5.11d for instance). One can, however, notice that the local mean squared errors are significantly embedded in the micro-porosity uncertainties, ensuring reliable predictions. In Figure 5.10, we detail these results on the initial state geometry — for $t^* = 0$ — by plotting along the two dashed lines from Figure 5.11 the BMA and uncertainty on $\varepsilon_\Theta$, the groundtruth values, and the $\mu$CT observations. Considering the dynamical dissolution process also provide insight into the upper and lower bounds of the residual micro-porosity $\varepsilon_0$ for the initial calcite core geometry. In the porous matrix, we obtain the estimations $3\% \leqslant \varepsilon_0 \leqslant 10\%$ for the 95% confidence interval.

The validation of the inference is first performed using the Bayesian Model Average Cumulative Error on the micro-porosity field, which is computed along the three successive sampling steps of sequential reinforcement. We then introduce $\mathcal{F}_1$ and $\mathcal{F}_2$ the PDE constraints residuals arising from the reactive model (5.12) and involved in the multi-potential energy (5.39):

$$\begin{aligned} \mathcal{F}_1(\varepsilon_\Theta, C_\Theta) &:= (\upsilon C_0)^{-1} \alpha_\Theta \frac{\partial \varepsilon_\Theta}{\partial t} - C_\Theta \\ \mathcal{F}_2(\varepsilon_\Theta, C_\Theta) &:= \gamma_\Theta \left( \frac{\partial C_\Theta}{\partial t} + (\upsilon C_0)^{-1} \frac{\partial \varepsilon_\Theta}{\partial t} \right) - \mathcal{D}_i(\varepsilon_\Theta, C_\Theta) \end{aligned} \tag{5.40}$$

to estimate their BMA-CE$^{\mathcal{F}_\bullet}$ diagnostics on sampling steps 2 and 3. For the 2D+time data assimilation problem, the BMA-CE metrics on the micro-porosity field $\varepsilon$ and PDE residuals are straightforwardly extended from the formulae (5.31) and (5.33). The results are provided in Figure 5.12 and highlight the convergence of each term toward final BMA errors, at the sampling iteration $\tau = 500$, scaling respectively about BMA-CE$^{\varepsilon}(\tau) = 1.6\text{e}{-3}$, BMA-CE$^{\mathcal{F}_1}(\tau) = 1.4\text{e}{-2}$ and BMA-CE$^{\mathcal{F}_2}(\tau) = 6.4\text{e}{-2}$. From these convergence diagnostics, we observe a saturation of the PDE constraints that highlight the intrinsic uncertainties of their corresponding tasks in the multi-potential energy (5.39). In this sense, the PDE constraint $\mathcal{F}_2$ involving the heterogeneous diffusion operator (5.24c) is the most uncertain term due to its high sensitivity to porosity variations. Nonetheless, we notice, as in the validation test cases from Sect. 5.6, that successive introduction of the PDE constraints brings information on the porosity field recovery by preventing overfitting issues.

For the inverse parameters inference, we represent in Figure 5.13 the histograms of the marginal posterior distributions of $\alpha_\Theta := (\text{Da}^*_{\text{II}})^{-1}$ and its trajectory in the phase space illustrating the convergence toward its mode during the adaptive steps — represented in blue in Figure 5.13b. The latter shows that our data assimilation approach combined with the AW-HMC sampler from Chapter 4 makes it possible to capture the correct parameter range without prior knowledge of its scaling. Once the adaptive process ends, we effectively start sampling the inverse parameter mode neighborhood, represented by the phase space trajectories for $\tau > N$ in red. We then follow the same process as in Sect. 5.6.4 to estimate the prior distribution on the inverse param-

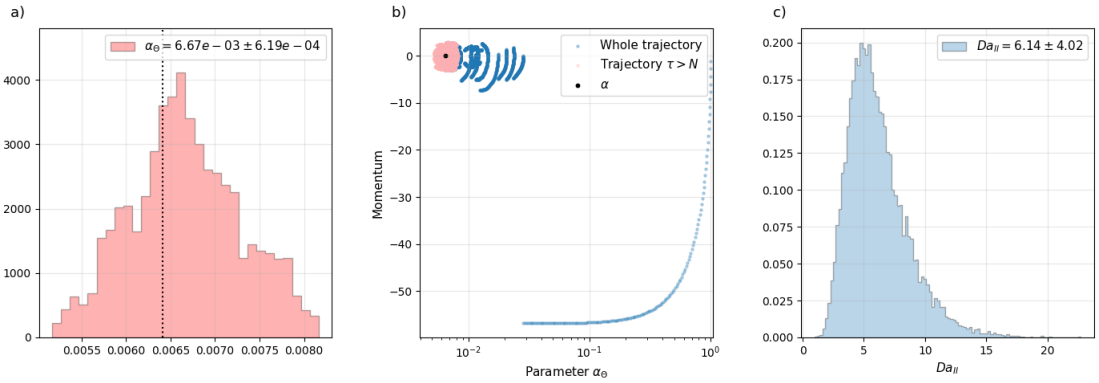


**Figure 5.13: Posterior distributions of 2D+Time reactive inverse problem:** a) Histogram of the marginal posterior distribution for the inverse parameter $\alpha_\Theta$. b) Phase diagram of its trajectory throughout the sampling, with the adaptive steps trajectories (in blue) and effective sampling (in red). The groundtruth value of $\alpha$ is represented by the black dot. c) Resulting posterior distribution of the catalytic Damköhler number $\mathrm{Da_{II}}$, determined through the log-normal distribution from relation (5.34).

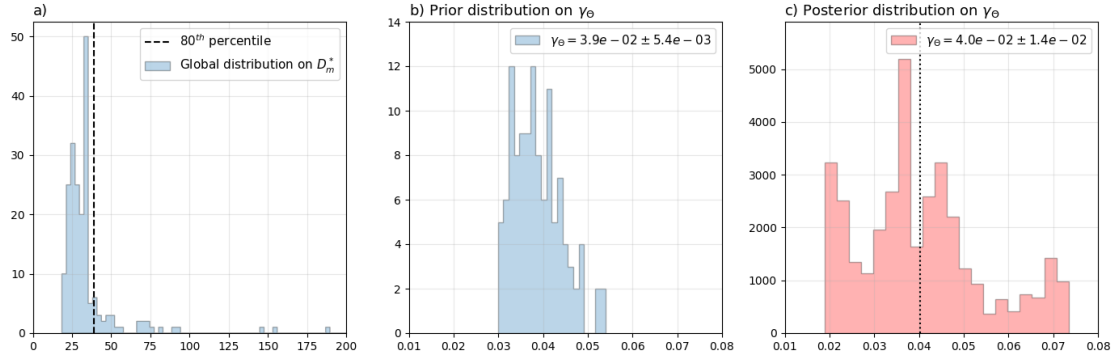


**Figure 5.14: Prior and posterior distributions on the inverse parameter $\gamma_\Theta$ for 2D+Time reactive inverse problem:** a) Global distribution on the estimated parameter $D_m^*$ arising from a-posteriori analysis on the sampling step 2. We discard the distribution tail after the vertical dashed line corresponding to the $80^{\text{th}}$ percentile. b) Resulting prior distribution on the inverse parameter $\gamma_\Theta$, used as an a-priori in step 3. c) Posterior distribution on $\gamma_\Theta$ obtained from the overall data assimilation problem throughout sampling step 3.

eter $\gamma_\Theta$, and we obtain $\overline{\gamma_\Theta} = 3.9\mathrm{e}{-2}$ which is used as an initial a-priori in the sampling step 3 (see Figure 5.14a and Figure 5.14b). The posterior distribution on the inverse parameter $\gamma_\Theta$, estimated throughout step 3, is represented in Figure 5.14c and provides the following predictive interval $\gamma_\Theta \in [2.6\mathrm{e}{-2}, 5.4\mathrm{e}{-2}]$. One can, finally, estimate the posterior distribution on the catalytic Damköhler number $\mathrm{Da_{II}}$ according to the log-normal distribution obtained by the relation (5.34). This results in the posterior distribution represented in Figure 5.13, and we obtain the uncertainty range $\mathrm{Da_{II}} \in [2.12, 10.16]$ for this data assimilation problem of calcite dissolution, which is consistent with the theoretical value.

## 5.8 Concluding remarks

This work intended to address two major challenges related to uncertainty quantification in pore-scale modeling of reactive flows, which plays a crucial role in the long-term management of $CO_2$ capture and storage. Providing reliable macro-properties changes due to geochemical processes, such as $CO_2$ mineral trapping and dissolution within the porous environment, is essential to query reservoir safety. In this sense, we aim to ensure that the evolving petrophysical properties provide meaningful characterizations of these chemical processes instead of intrinsic deviations arising from imaging limitations. Some intrinsic limiting factors remain when modeling pore-scale dynamical systems based on $\mu$CT scans and lead to several trade-offs that can bias the predictions. In particular, this results in unresolved micro-porosity, especially when the scan resolution does not fully capture morphological features of the pore space under the constraint of having a representative elementary volume (REV) of the sample. Quantifying sub-resolution porosity, which is a prevalent imaging artifact, was the first challenge we identified, and therefore we focused on quantifying morphological uncertainties in the micro-porosity field. Our second concern was to investigate the reliability of kinetic parameters, such as mineral reactivity, in the context of reactive processes. Indeed, these are critical parameters to account for in pore-scale modeling, though their experimental estimations can suffer from wide discrepancies. Estimating proper order of magnitude and uncertainty ranges appears essential to ensure reliable calibration of pore-scale models, and afterward trustable management of $CO_2$ mineral storage. The present article investigated both these issues by integrating uncertainty quantification concerns in the workflow of pore-scale modeling.

Current methodologies investigating these problems regard them independently and fall into pure image treatment analysis related to experimental static or dynamical $\mu$CT images. Deep learning methodologies, for instance, are used to address sub-resolution porosity quantification. Multi-scale image reconstruction, which extrapolates the latent information of the porous structure, is obtained with Generative Adversarial Networks [330]. One also gets super-resolved segmented images from static $\mu$CT scans through Convolutional Neural Networks [16], which compensate for the unresolved morphological features. Regarding the mineral reactivity assessment, experimental works have been conducted on dynamical 4D $\mu$CT of carbonate dissolution. This provides, through differential imaging techniques, insight into local reaction rates at the mineral interfaces [200, 218]. However, all these approaches do not consider incorporating uncertainty quantification in the estimates. In contrast, alternatives accounting for deviations in the petrophysical properties due to imaging limitations are mainly purely model-related approaches [238, 278].

The main novelty of our work, therefore, lay in its ability to address both morphological uncertainty and reaction rate quantification from the perspective of coupling physics-based models with data-driven techniques. In this sense, we have developed a data assimilation approach for pore-scale imaging problems that combines dynamical microtomography and physical regularization induced by PDE models of reactive processes. We integrated this novel data assimilation strategy into the Bayesian inference context through our efficient AW-HMC framework for BPINNs [237]. This also confirmed the great potential of this adaptive and self-balancing methodology and rendered BPINNs a promising approach to address complex data assimilation. In the pore-scale imaging context, in particular, we have focused on multitask inverse problems of calcite dissolution based on dynamical $\mu$CT images, along with two dimensionless inverse parameters and a latent concentration field. We have also assumed unknown informative priors on the different tasks scaling and relied on automatic adjustment of the uncertainties including noise-related estimations and model adequacy. In this sense, we provided reliable uncertainty quantification on the micro-porosity field description and reactive parameters. We also built our data assimilation upon a sequential reinforcement strategy of the multi-potential energy and thus the target posterior distribution. This involved successively integrating additional PDE constraints into the overall data assimilation process through dedicated sampling steps. Finally, we have also addressed computational concerns and have shown that suitable formulation of complex non-linear differential operators, especially the heterogeneous diffusion arising from Archie's law, can significantly reduce the computational costs of these operators. Taken together, we presented an intrinsic data

assimilation strategy for pore-scale imaging inverse problem and demonstrated its efficiency on several 1D+Time and 2D+time calcite dissolution problems.

Overall, our results confirmed enhanced morphological uncertainties localized on the calcite core edges throughout the dissolution process. This characterized the challenge of capturing reliable mineral interfaces from the dynamical $\mu$CT images, and therefore query the confidence of mineral reactivity assessment using merely differential imaging techniques on the $\mu$CT scans. Combining data-driven and physics-based approaches thus offers a promising alternative to overcome the limitations of each approach individually, and alleviate biased predictions. We also obtained reliable insight into the upper and lower bounds for the residual, potentially unresolved, micro-porosity $\varepsilon_0$ in the porous matrix. These estimations can then be incorporated into direct numerical simulation solvers to measure the impact of these micro-porosity variations on the other petrophysical properties, such as permeability. This can also ensure that the macro-scale porosity evolutions due to the reactive processes are significant compared to these intrinsic morphological uncertainties at the pore scale. Finally, we have obtained posterior distributions on the dimensionless reactive parameters characterizing the dissolution inverse problems. We have shown that our data assimilation approach combined with the AW-HMC sampler made it possible to capture the correct parameter ranges without prior knowledge of their scaling, which confirmed the robustness and reliability of the inferences. Last but not least, we have identified uncertainty ranges on the usual catalytic Damköhler number $\mathrm{Da}_{\mathrm{II}}$ resulting from the prescribed PDE model and dynamical observations of the dissolution process. This is of great interest to aggregate experimental investigations and direct numerical simulations, and therefore guarantee the reliability of pore-scale modeling and simulation of reactive flows. We now have the potential to effectively address robust and reliable uncertainty quantification in pore-scale imaging and to manage the impact of $\mu$CT limitations on the petrophysical properties and reactive parameters.

As future prospects, it would be interesting to apply the present data assimilation approach on real $\mu$CT dissolution scans and extend the inference to different kinds of dissolution regimes. This would bring further insights into the relationship between experiments and mathematical modeling theory, which would improve dramatically the trust in computational approaches of real-life reactive materials.

CHAPTER 6

# Conclusion and outlook

## Contents



This thesis investigates pore-scale modeling of reactive processes and presents several contributions toward the reliability concerns associated with such computational methodologies. In particular, we have addressed the challenge of understanding the intricate interplay between $\mu$CT experimental data and mathematical modeling theory to significantly enhance the confidence in DNS approaches in the context of $CO_2$ mineral storage modeling.

Ensuring the reliability of pore-scale modeling holds paramount importance in understanding the impacts of geochemical processes associated with $CO_2$ interactions within the aquifer environment and consistently managing changes in the macro-scale properties. Uncertainties, whether arising from morphological biases and imaging issues in the $\mu$CT data or the inaccurate calibration of kinetic parameters within the PDE model, influence the pore-scale flow dynamics, subsequently propagating uncertainties at the macro-scale during the upscaling process.

As a result, these uncertainties necessitate comprehensive exploration, and this thesis introduces an overall computational framework designed to address such a requirement. In this concluding chapter, we summarize the key contributions of this work and highlight several opportunities and prospects.

## 6.1 General conclusion

On one side, the current thesis addressed the development of suitable mathematical models and efficient DNS methods for modeling reactive hydrodynamics at the pore scale. A semi-Lagrangian formulation of the reactive systems is adopted, combining a particle description of the chemical transport equations with an underlying grid-based approach for flow modeling. The latter accounts for the involvement of the porous matrix in the overall flow process through a micro-continuum description of the medium and the Darcy-Brinkman Stokes model based on the superficial velocity formalism. The numerical implementation, within the HPC framework HySoP, hinged on an operator splitting strategy, coupled with high-order remeshing steps for grid-particle interpolations, and is provided on a hybrid computational environment, including CPU and GPU devices. This existing numerical framework is enhanced to account for the heterogeneous diffusion of the chemical species throughout the porous matrix, which arises from Archie's law in the two-scale description of the medium. A particle-based approximation of such diffusion operators is achieved

through a discrete renormalized Particle-Strength-Exchange (PSE) scheme, that makes it possible to fully address the superficial formulation of the chemistry on GPU devices.

This numerical framework is employed to investigate the effects of $CO_2$ mineral trapping, identify potential pore-clogging at the pore scale, and establish the macro-scale properties evolution due to such a geochemical process. In particular, a novel crystallization model is developed that relies on a two-step process, namely a homogeneous nucleation followed by a crystal growth step. A deterministic Transition State Theory (TST) formulation of the initial nucleation based on the supersaturation state is combined with a probabilistic view of the nuclei aggregation rates to the pore interface. These aggregation rates included a non-uniform probability of crystal attachment based on the local volume fraction of the surrounding material and adsorption frequencies. This incorporated geometrical dependency in the crystallization model, which is crucial to ensure accurate predictions of pore-clogging. Furthermore, we investigated the impact of several dominant regimes on the dynamical patterns of $CO_2$ mineral trapping and included the effects of nuclei aggregation by considering an additional dimensionless number in the overall crystallization regime characterization. This highlighted that considering the transport and nucleation rates, through the conventional $\mathrm{Pe}$ and $\mathrm{Da}_{\mathrm{II}}^{\mathrm{prec}}$ dimensionless numbers, is not sufficient to characterize pore-clogging at the pore scale and demonstrated that one should consider the effects of crystal aggregation on the reactive patterns of $CO_2$ mineral trapping.

On the other side, uncertainties in the calibration of the PDE models query the reliability of pore-scale modeling, especially considering the wide discrepancies observed in mineral reactivity and kinetic parameters in natural systems. The reactive specific area, in particular, is often used in pore-scale models as a calibration parameter to account for surface reaction rates. Furthermore, $\mu$CT morphological uncertainties including unresolved features on the micro-porosity field, unseen pore roughness, and approximate location of the pore interfaces render challenging the proper estimation of the macro-scale properties changes. Quantifying the deviations induced by these intrinsic limitations is essential to ensure reliable evolution of the macro-porosity and bulk permeability due to the geochemical processes.

Firstly, a direct numerical approach that hinges on upscaling these unresolved morphological features is addressed through a slip-length formalism and employed to investigate absolute permeability deviations on real rock geometries derived from X-ray $\mu$CT. We studied two uncertainty ranges at the macro-scale, namely the full deviation that stems from the modeling of Stokes flow with Navier boundary condition involving a prescribed slip length and the theoretical deviations at first and second orders, established by an asymptotic analysis. The latter determined the Stokes-like problems to solve at the successive orders that individually define slip-correction terms of the bulk permeability. An independent solver for Stokes is developed to robustly manage the distinct boundary conditions at the pore interface and ensure that the computed permeability deviations are representative of slip-length values characterizing the $\mu$CT uncertainties. This numerical framework is applied to quantify permeability ranges on several porous samples and this has highlighted the relevance of the second-order slip correction in explaining the apparent macroscopic effects on the permeability. We also established characteristic dimensionless ratios of the sample representativity based on the relative permeability deviations and specific area.

Finally, this thesis addressed morphological uncertainties in the micro-porosity field through inverse problems of reactive flows with the motivation of bringing an accurate description of porous media, observing their dynamical dissolution by $\mu$CT experiments. A dedicated data assimilation framework is developed to address such multitask inverse problems integrating uncertainty quantification (UQ) and a sequential reinforcement approach is introduced to incorporate additional physics-based PDE constraints into the workflow. This allowed the efficient combination of data-driven approaches based on imperfect dynamical experiments, with physics-based PDE models having their inherent uncertainties to provide insight into their respective limitations. Therefore, in addition to the morphological uncertainty quantification on the micro-porosity field arising from the $\mu$CT images, uncertainty ranges on the kinetic parameters are also provided, which renders reliable the calibration of the reaction rates in the PDE models for pore-scale DNS.

To achieve this objective, we have devised a novel deep-learning strategy that effectively tack-

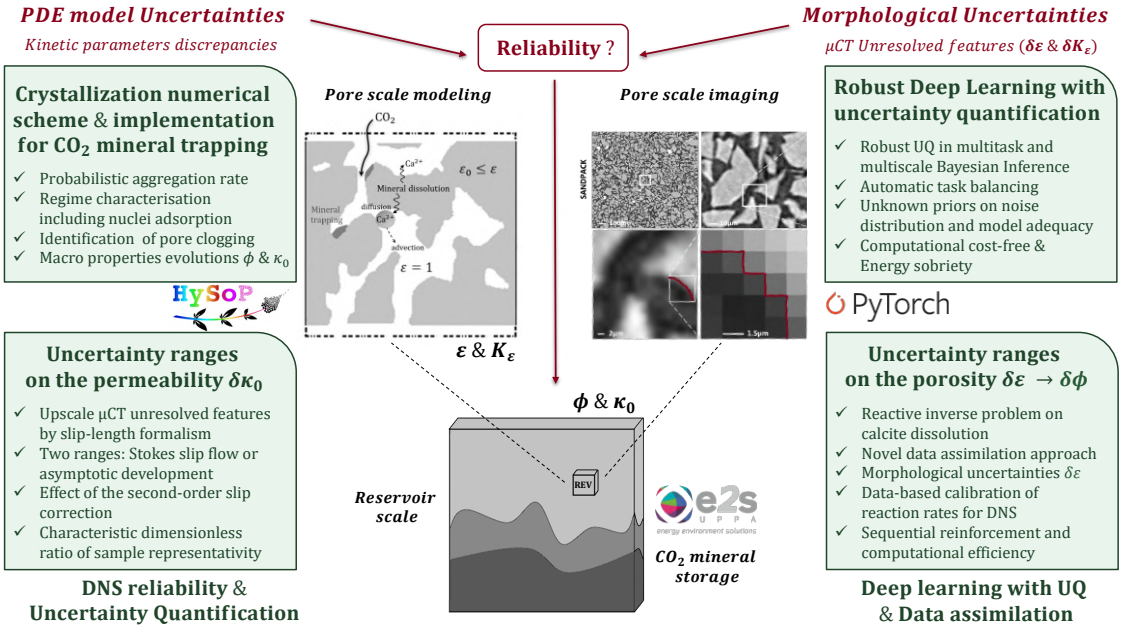


**Figure 6.1: Overview of the main contributions of the present thesis for $CO_2$ mineral storage applications, in relation to the identified concerns arising from pore-scale imaging and modeling.**

les physics-based and multi-task Bayesian inference problems while accommodating unknown priors on the measurement noise distribution and model adequacy. A Bayesian Physics-Informed Neural Network (BPINNs) formulation involving a robust MCMC sampler is developed to provide automatic and auto-weighted task balancing in multi-objective Bayesian Inference problems, which hinge on coupling PDE models and data observations as distinct tasks. The resulting Adaptively Weighted Hamiltonian Monte Carlo AW-HMC sampler demonstrated outstanding performances on several data assimilation problems of various complexity, efficiency in managing scaling sensitivities and the inherent uncertainties of the different objectives, and effectiveness in ensuring task balancing. Overall, this benefits from enhanced convergence and stability while improving reliability in the uncertainties estimates, which stems from a robust and unbiased sampling. Furthermore, this automatic task-balancing formulation of the BPINNs is cost-effective compared to ongoing alternatives, which either require a pre-trained Generative Adversarial Network (GAN) or a large number of additional parameters to infer. This novel strategy maintains reasonable computational costs by directly leveraging gradient information from the distinct tasks within the BPINNs framework and therefore aligns with energy sobriety concerns.

Overall, this work contributes significantly to the study of $CO_2$-related reactive processes in porous media by advancing computational methods, calibration techniques, and uncertainty quantification. Taken together, this enhances our ability to model and predict reliable changes in the macro-scale properties influenced by intricate geochemical processes at the pore scale in the context of $CO_2$ mineral storage in underground natural reservoirs.

In a broader scope, the presented data assimilation framework could offer valuable insights into reliability analyses involving inverse problems. This is particularly relevant when experimental data are abundant but multiple competing mathematical models are under consideration. In this context, incorporating robust uncertainty quantification into inferring interpretable inverse parameters related, *inter alia*, to physics, chemistry, or hydrodynamics could facilitate the discrimination among various models or numerical methods. At the same time, this process ensures reliable ranges for the inverse parameters inference, which guarantees a reasonable comparison between the different models.

## 6.2 Enhancement of DNS model and numerical framework

### 6.2.1 Exponential Integrators for more complex and stiff reactive systems

One way to enhance the numerical framework would rely on incorporating cutting-edge time integrators within the numerical framework HySoP, namely a dedicated class of Exponential Integrators. The latter consists of high-order integration method, which has been developed since the 1960s, though their use was limited due to the complexity of computing the exponential of an operator, which stands as an essential part of the approach. Over the past decades, advances in the numerical approximation of matrix exponentials have rendered Exponential Integrators an efficient alternative to commonly used implicit schemes for non-linear problems [294]. In particular, the method developed by Tokman *et al.* [179], which is derived from the EPIRK (Exponential Propagation Iterative method of Runge-Kutta type) class of Exponential Integrators, would make it possible to handle complex and stiff reactive systems with enhanced stability. Therefore, this would broaden the scope of modeling for geochemical processes and expand the DNS possibilities for $CO_2$ mineral storage applications. Such a formalism would also make it possible to incorporate divergence effects resulting, for instance, from crystal nucleation in processes where the characteristic time of fluid/solid interface changes is way faster than the hydrodynamics time scale.

### 6.2.2 Toward calcium free input process and transient models of $CO_2$ trapping

The numerical simulations of mineral trapping presented in Chapter 2 described a solution of dissolved $CO_2$ in an alkaline medium highly concentrated in calcium ions, continuously injected in the porous medium. To study $CO_2$ trapping without enhancing calcium concentration, which means using only the calcium available in the medium, we need to improve the accuracy of the schemes and enhance the modeling of the exchanges at walls. Indeed, calcium will be transported, diffused, and consumed totally but gradually, unlike $CO_2$, which is injected. The transport in the Poiseuille flow of the pores will cause calcium ions to spread and disperse (see the transport of an invasive front at the pore-scale in [135]), and the reaction will not occur close to the input. Instead, it will gradually propagate into the medium and should lead to a progressive wave of reaction/diffusion. Identification of different regimes of reaction with respect to Peclet and Damköhler numbers will be possible, investigating different processes and improving the first analysis provided in [236] and [297]. Such simulations and methods could also be translated into models of battery charge/discharge or studies of *in silico* drug delivery processes.

### 6.2.3 Reformulation of the PSE for heterogeneous diffusion

In future work, the stability and consistency of 3D Particle-Strength-Exchange methods will be investigated for space-variable diffusion operator, based on the DC-PSE analysis provided in [267]. New formulations of PSE will also be investigated based on other symmetric expressions of $\mathbf{M}$ managing the estimations of viscosity, molecular or effective diffusion for exchange formulae, rather than using the historical arithmetic averaging. Such extensions should help to satisfy physical constraints at porosity jumps with concentrations far from equilibrium. The inclusion of rheology as shear-thinning properties of precipitate, that is to say a model of non-linear viscosity computed by PSE schemes, will allow to investigate multi-factor mechanisms of pore clogging.

## 6.3 Advancing data assimilation for reactive hydrodynamics

### 6.3.1 Real experimental $\mu$CT data of calcite dissolution

The applications that we expect to particularly benefit from the advances of the data assimilation framework developed in the current thesis include the better characterization of real-life reactive materials, along with insights into the relationship between experiments and mathematical modeling. In this sense, investigating morphological bias on the micro-porosity and kinetic parameter uncertainty ranges on real experimental $\mu$CT data is one of the short-term prospects of this work.

We would target realistic 2D+Time calcite core dissolution, on the one hand, and dissolution of simplified porous geometries, on the other hand, resulting from the development of a dedicated reactive cell able to handle dynamical $\mu$CT scans at the DMEX Center for X-ray Imaging.

### 6.3.2 Investigation of other flow regimes

Together with the prospect of achieving data assimilation on real-like reactive materials, we would extend the current framework to different dissolution regimes, including advection dominant phenomena. This would require, especially, insights into the velocity field to integrate the overall reactive hydrodynamics PDE system within the data assimilation framework. Nonetheless, this implies the recovery of an additional latent field and inverse parameter, namely the velocity and a modified Peclet number $\mathrm{Pe}^* := \overline{u}L/D_{\mathrm{ref}}$, and therefore requires further investigations. One option would consist of using prior for the hydrodynamics through DNS formalism or fast surrogate modeling and fluid flow model proxy [18, 262] based on the morphological a-priori on the porous medium evolution from dynamical $\mu$CT. Subsequently, these priors could be incorporated and adjusted into the data assimilation problem involving mainly the constraints of the advection-diffusion-reaction PDE system, as a two-step sequential process. Moreover, the estimation of the bulk permeability of the Kozeny-Carman correlation is a real challenge since it drives the amount of concentration heading inside the solid matrix: it is a meaningful and fundamental physical quantity, but remains currently an open question.

### 6.3.3 Improvements of the deep-learning framework

Rendering deep learning approaches scalable to a wide variety of complex problems, including data assimilation on 4D real-life reactive material, requires developing efficient computational strategies. In this sense, the numerical framework for robust data assimilation with UQ developed in this thesis could benefit from enhanced parallelization on GPU devices. One can consider task parallelization on different processors during the sampling phase of a multi-objective data assimilation problem, or investigate potential coupling with the symmetric splitting approach of the standard Hamiltonian Monte Carlo suggested by Cobb *et al.* [84] which enables parallelization on data subsets during the training phase. Regarding the prediction step, one can also investigate appropriate standard domain decomposition distributed over several devices to enhance the computational efficiency. This should further improve the efficiency of the method with the idea of maintaining sustainable computational costs, which becomes crucial when addressing intricate real-world inverse problems and data assimilation.

### 6.3.4 Deep learning interpretability

Advances in AI and machine learning methodologies have led to their widespread scientific use in various application domains. Nonetheless, when such a performance relies on complex models, merely regarded as "black boxes", this raises concerns about their decision-making processes. Consequently, there is a need to gain deeper insights into the model interpretability in deep learning approaches by integrating more meaningful mathematical considerations of machine learning-based representations. In this sense, ongoing research focuses, for instance, on establishing mathematical frameworks for exploring the sensitivity analysis and optimization of neural network hyperparameters, as these parameters can significantly influence the network's performance [224]. This aims to enhance our understanding of machine learning approaches, making them more transparent and trustworthy.

# Bibliography


[1] Per Aagaard and Harold C. Helgeson. Thermodynamic and kinetic constraints on reaction rates among minerals and aqueous solutions; I, Theoretical considerations. *American Journal of Science*, 282(3):237–285, 1982. (Cited on page 46.)

[2] Yves Achdou, Olivier Pironneau, and Frederic Valentin. Effective boundary conditions for laminar flows over periodic rough boundaries. *Journal of Computational Physics*, 147:187–218, 1998. (Cited on pages 60, 62, 74 and 140.)

[3] Mark Adams, Phillip Colella, et al. Chombo. https://commons.lbl.gov/display/chombo/. (Cited on page 9.)

[4] Mehrdad Ahkami, Andrea Parmigiani, Paolo Roberto Di Palma, Martin O. Saar, and Xiang-Zhao Kong. A lattice-Boltzmann study of permeability-porosity relationships and mineral precipitation patterns in fractured porous media. *Computational Geosciences*, 24(5):1865–1882, 2020. (Cited on page 5.)

[5] Etienne Ahusborde, Michel Kern, and Viatcheslav Vostrikov. Numerical simulation of two-phase multicomponent flow with reactive transport in porous media: application to geological sequestration of CO2. *ESAIM: Proceedings and Surveys*, 50:21–39, 2015. (Cited on page 10.)

[6] Lateef T. Akanji and Stephan K. Matthai. Finite Element-Based Characterization of Pore-Scale Geometry and Its Impact on Fluid Flow. *Transport in Porous Media*, 81:241–259, 2010. (Cited on pages 8 and 69.)

[7] Fatima Al Hameli, Hadi Belhaj, and Mohammed Al Dhuhoori. CO2 sequestration overview in geological formations: Trapping mechanisms matrix assessment. *Energies*, 15(20), 2022. (Cited on pages 1 and 139.)

[8] Alex Alberts and Ilias Bilionis. Physics-informed information field theory for modeling physical systems with uncertainty quantification. *Journal of Computational Physics*, 486:112100, 2023. (Cited on page 14.)

[9] Grégoire Allaire. Homogenization of the Stokes flow in a connected porous medium. *Asymptotic Analysis*, 2:203–222, 1989. (Cited on page 66.)

[10] Grégoire Allaire and François Alouges. Analyse variationnelle des équations aux dérivées partielles. *Cours de l'École Polytechnique*, 2015. (Cited on page 68.)

[11] Grégoire Allaire and Hutridurga Hutridurga. Homogenization of reactive flows in porous media and competition between bulk and surface diffusion. *IMA Journal of Applied Mathematics*, 77(6):788–815, 2012. (Cited on page 21.)

[12] Grégoire Allaire, Robert Brizzi, Andro Mikelić, and Andrey Piatnitski. Two-scale expansion with drift approach to the Taylor dispersion for reactive transport through porous media. *Chemical Engineering Science*, 65(7):2292–2300, 2010. (Cited on page 21.)

[13] Ethem Alpaydin. *Introduction to Machine Learning*. The MIT Press, 2nd edition, 2010. (Cited on page 11.)

[14] Naif Alqahtani, Fatimah Alzubaidi, Ryan T. Armstrong, Pawel Swietojanski, and Peyman Mostaghimi. Machine learning for predicting properties of porous media from 2D X-ray images. *Journal of Petroleum Science and Engineering*, 184:106514, 2020. (Cited on pages 12 and 134.)

[15] Naif Alqahtani, Ryan T. Armstrong, and Peyman Mostaghimi. Deep learning convolutional neural networks to predict porous media properties. In *SPE Asia Pacific Oil and Gas Conference and Exhibition*, 2018. (Cited on page 12.)

[16] Naif J. Alqahtani, Yufu Niu, Ying Da Wang, Traiwit Chung, Zakhar Lanetc, Aleksandr Zhuravljov, et al. Super-Resolved Segmentation of X-ray Images of Carbonate Rocks Using

Deep Learning. *Transport in Porous Media*, 143(2):497–525, 2022. (Cited on pages 12, 58, 94, 101, 140 and 166.)

[17] M. Umer Altaf, Mohamad El Gharamti, Arnold W. Heemink, and Ibrahim Hoteit. A reduced adjoint approach to variational data assimilation. *Computer Methods in Applied Mechanics and Engineering*, 254:1–13, 2013. (Cited on page 13.)

[18] Shohreh Amini and Shahab Mohaghegh. Application of Machine Learning and Artificial Intelligence in proxy modeling for fluid flow in porous media. *Fluids*, 4(3), 2019. (Cited on pages 13 and 173.)

[19] Chérif Amrouche and M. Ángeles Rodríguez-Bellido. Stationary Stokes, Oseen and Navier-Stokes Equations with Singular Data. *Archive for Rational Mechanics and Analysis*, 199(2):597–651, 2011. (Cited on page 68.)

[20] Matthew Andrew, Branko Bijeljic, and Martin J. Blunt. Pore-scale imaging of geological carbon dioxide storage under in situ conditions. *Geophysical Research Letters*, 40(15):3915–3918, 2013. (Cited on pages 2 and 46.)

[21] Matthew Andrew, Branko Bijeljic, and Martin J. Blunt. Pore-scale imaging of trapped supercritical carbon dioxide in sandstones and carbonates. *International Journal of Greenhouse Gas Control*, 22:1–14, 2014. (Cited on pages 3 and 139.)

[22] Prisca Andriamananjaona. *Wettability in porous media – From macroscopic measurements to pore-scale characterization*. PhD thesis, Université de Pau et des Pays de l'Adour, 2020. (Cited on pages 79 and 88.)

[23] Heiko Andrä, Nicolas Combaret, Jack Dvorkin, Erik Glatt, Junehee Han, Matthias Kabel, et al. Digital rock physics benchmarks — Part I: Imaging and segmentation. *Computers & Geosciences*, 50:25–32, 2013. (Cited on pages xv and 5.)

[24] Heiko Andrä, Nicolas Combaret, Jack Dvorkin, Erik Glatt, Junehee Han, Matthias Kabel, et al. Digital rock physics benchmarks — Part II: Computing effective properties. *Computers & Geosciences*, 50:33–43, 2013. (Cited on pages xv, 5 and 136.)

[25] Philippe Angot, Charles-Henri Bruneau, and Pierre Fabrie. A penalization method to take into account obstacles in incompressible viscous flows. *Numerische Mathematik*, 81(4):497–520, 1999. (Cited on page 69.)

[26] Philippe Angot, Gilles Carbou, and Victor Péron. Asymptotic study for Stokes-Brinkman model with jump embedded transmission conditions. *Asymptotic Analysis*, 2015. (Cited on pages 3, 8 and 69.)

[27] Saeid Norouzi Apourvari and Christoph H. Arns. *An Assessment of the Influence of Microporosity for Effective Permeability Using Local Flux Analysis on Tomographic Images*. IPTC International Petroleum Technology Conference, 2014. (Cited on page 58.)

[28] Mauricio Araya-Polo, Faruk O. Alpak, Sander Hunter, Ronny Hofmann, and Nishank Saxena. Deep learning–driven permeability estimation from 2D images. *Computational Geosciences*, 24(2):571–580, 2020. (Cited on page 12.)

[29] Gustavus E. Archie. The electrical resistivity log as an aid in determining some reservoir characteristics. *Petroleum Transactions of AIME*, 146:54–62, 1942. (Cited on page 26.)

[30] Karim Armanious, Vijeth Kumar, Sherif Abdulatif, Tobias Hepp, Sergios Gatidis, and Bin Yang. ipA-MedGAN: Inpainting of Arbitrary Regions in Medical Imaging. In *2020 IEEE International Conference on Image Processing (ICIP)*, pages 3005–3009, 2020. (Cited on page 125.)

[31] D. Arumuga Perumal and Anoop K. Dass. A Review on the development of lattice Boltzmann computation of macro fluid flows and heat transfer. *Alexandria Engineering Journal*, 54(4):955–971, 2015. (Cited on page 10.)

[32] Yehuda Bachmat and Jacob Bear. On the Concept and Size of a Representative Elementary Volume (REV). In *Advances in Transport Phenomena in Porous Media*, pages 3–20. Springer Netherlands, 1987. (Cited on page 4.)

[33] Stefan Bachu. Review of CO2 storage efficiency in deep saline aquifers. *International Journal of Greenhouse Gas Control*, 40:188–202, 2015. (Cited on pages xv and 2.)

[34] Matthew Balhoff, Sunil Thomas, and Mary Wheeler. Mortar coupling and upscaling of pore-scale models. *Computational Geosciences*, 12:15–27, 2008. (Cited on page 69.)

[35] Ioannis Baltas, Anastasios Xepapadeas, and Athanasios N. Yannacopoulos. Robust control of parabolic stochastic partial differential equations under model uncertainty. *European Journal of Control*, 46:1–13, 2019. (Cited on page 13.)

[36] Uditha C. Bandara, Alexandre M. Tartakovsky, Mart Oostrom, Bruce J. Palmer, Jay Grate, and Cathery Zhang. Smoothed particle hydrodynamics pore-scale simulations of unstable immiscible flow in porous media. *Advances in Water Resources*, 62(Part C):356–369, 2013. (Cited on page 69.)

[37] John Banhart. *Advanced Tomographic Methods in Materials Research and Engineering*. Monographs on the Physics and Chemistry of Materials. Oxford University Press, 2008. (Cited on page 6.)

[38] Patrick Barreau, Didier Lasseux, Henri Berlin, and Alain Zaitowf. Effect of adsorbed polymers on relative permeability and capillary pressure: a pore scale numerical study. *WIT Transactions on Modelling and Simulation*, 10, 1970. (Cited on page 69.)

[39] Hélène Barucq, Henri Calandra, and Thibaut Maron. UW-PINN: Ultra-Weak PINNs for the acoustic wavesystem. Working paper or Preprint, hal-04052920, 2023. (Cited on page 13.)

[40] J. Thomas Beale and Andrew J. Majda. Rates of convergence for viscous splitting of the Navier-Stokes equations. *Mathematics of Computation*, 37:243–259, 1981. (Cited on page 31.)

[41] Héloïse Beaugendre, Serge Huberson, and Iraj Mortazavi. Coupling particle sets of contours and streamline methods for solving convection problems. *Applied Mathematics Letters*, 25(1):11–19, 2012. (Cited on pages 22 and 29.)

[42] Lauren E. Beckingham, Carl I. Steefel, Alexander M. Swift, Marco Voltolini, Li Yang, Lawrence M. Anovitz, et al. Evaluation of accessible mineral surface areas for improved prediction of mineral reaction rates in porous media. *Geochimica et Cosmochimica Acta*, 205:31–49, 2017. (Cited on page 10.)

[43] Aleksey V. Belyaev and Olga I. Vinogradova. Effective slip in pressure-driven flow past super-hydrophobic stripes. *Journal of Fluid Mechanics*, 652:489–499, 2010. (Cited on pages 60 and 76.)

[44] Marbe Benioug, Fabrice Golfier, Anne-Julie Tinet, Michel A. Buès, and Constantin Oltéan. Numerical efficiency assessment of IB–LB method for 3D pore-scale modeling of flow and transport. *Transport in Porous Media*, 109(1):1–23, 2015. (Cited on page 9.)

[45] William Benton. *Encyclopaedia Britannica*. University of Chicago Press, 1963. (Cited on page 58.)

[46] Steffen Berg, Arjen W. Cense, Jan P. Hofman, and Robert M.M. Smits. Two-phase flow in porous media with slip boundary condition. *Transport in Porous Media*, 74(3):275–292, 2008. (Cited on page 60.)

[47] Michael Bergdorf, Georges-Henri Cottet, and Petros Koumoutsakos. Multilevel adaptive particle methods for convection-diffusion equations. *Multiscale Modeling & Simulation*, 4(1):328–357, 2005. (Cited on pages 33 and 35.)

[48] Michael Betancourt. A Conceptual Introduction to Hamiltonian Monte Carlo. *arXiv*, 2018. arXiv:1701.02434. (Cited on pages xix, 14, 15, 95, 98, 99, 100, 104 and 133.)

[49] Michael Betancourt, Simon Byrne, and Mark Girolami. Optimizing The Integrator Step Size for Hamiltonian Monte Carlo. *arXiv*, 2014. arXiv:1411.6669. (Cited on page 99.)

[50] Michael Betancourt, Simon Byrne, Sam Livingstone, and Mark Girolami. The geometric foundations of Hamiltonian Monte Carlo. *Bernoulli*, 23(4):2257–2298, 2017. (Cited on page 98.)

[51] Jay R. Black, Susan A. Carroll, and Ralf R. Haese. Rates of mineral dissolution under CO2 storage conditions. *Chemical Geology*, 399:134–144, 2015. (Cited on page 141.)

[52] Martin J. Blunt, Branko Bijeljic, Hu Dong, Oussama Gharbi, Stefan Iglauer, Peyman Mostaghimi, et al. Pore-scale imaging and modelling. *Advances in Water Resources*, 51:197–216, 2013. (Cited on page 4.)

[53] Hinrich Bohn, Brian McNeal, and George O'Connor. Soil chemistry. *Soil Science*, 129(6), 1980. (Cited on page 45.)

[54] Matthieu Bonnivard, Anne-Laure Dalibard, and David Gérard-Varet. Computation of the effective slip of rough hydrophobic surfaces via homogenization. *Mathematical Models and Methods in Applied Sciences*, 24:2259–2285, 2014. (Cited on pages 62, 74 and 90.)

[55] George C. Bourantas, Bevan L. Cheeseman, Rajesh Ramaswamy, and Ivo F. Sbalzarini. Using DC PSE operator discretization in Eulerian meshless collocation methods improves their robustness in complex geometries. *Computers & Fluids*, 136:285–300, 2016. (Cited on pages 35, 125, 126 and 130.)

[56] Patrick Bousquet-Melou, Benoit Goyeau, Michel Quintard, Florian Fichot, and Dominique Gobin. Average momentum equation for interdendritic flow in a solidifying columnar mushy zone. *International journal of heat and mass transfer*, 45(17):3651–3665, 2002. (Cited on page 8.)

[57] Yann Brenier and Georges-Henri Cottet. Convergence of Particle Methods with random rezoning for the two-dimensional Euler and Navier–Stokes equations. *SIAM Journal on Numerical Analysis*, 32(4):1080–1097, 1995. (Cited on page 29.)

[58] Wim-Paul Breugem, Bendiks-Jan Boersma, and Rob E. Uittenbogaard. The influence of wall permeability on turbulent channel flow. *Journal of Fluid Mechanics*, 562:35–72, 2006. (Cited on page 60.)

[59] Henri C. Brinkman. A calculation of the viscous force exerted by a flowing fluid on a dense swarm of particles. *Flow, Turbulence and Combustion*, 1(1):27–34, 1949. (Cited on page 5.)

[60] Steven L. Brunton, Joshua L. Proctor, and J. Nathan Kutz. Discovering governing equations from data by sparse identification of nonlinear dynamical systems. *Proceedings of the National Academy of Sciences*, 113(15):3932–3937, 2016. (Cited on page 95.)

[61] Eurybiades Busenberg and L. Niel Plummer. A comparative study of the dissolution and crystal growth kinetics of calcite and aragonite. *Studies in diagenesis*, 1578:139–168, 1986. (Cited on page 46.)

[62] Eurybiades Busenberg and Niel Plummer. The kinetics of dissolution of dolomite in CO2-H2O systems at 1.5 to 65 degrees C and 0 to 1 atm PCO2. *American Journal of Science*, 282(1):45–78, 1982. (Cited on page 4.)

[63] Yunan Cai, Sheng Li, and Jianhua Lu. An improved immersed boundary-lattice Boltzmann method based on force correction technique. *International Journal for Numerical Methods in Fluids*, 87(3):109–133, 2018. (Cited on page 9.)

[64] Clément Cancès, Thomas Gallouët, Maxime Laborde, and Léonard Monsaingeon. Simulation of multiphase porous media flows with minimising movement and finite volume schemes. *European Journal of Applied Mathematics*, 30(6):1123–1152, 2019. (Cited on pages 8 and 69.)

[65] Gilles Carbou. Brinkmann model and double penalization method for the flow around a porous thin layer. *Journal of Mathematical Fluid Mechanics*, 10(1):126–158, 2008. (Cited on pages 8, 66 and 69.)

[66] Gilles Carbou and Pierre Fabrie. Boundary layer for a penalization method for viscous incompressible flow. *Advances in Differential Equations*, 8:1453–1480, 2003. (Cited on page 69.)

[67] Philip C. Carman. Fluid flow through granular beds. *Transactions, Institution of Chemical Engineers, London*, 15:150–166, 1937. (Cited on page 25.)

[68] W. David Carrier. Goodbye, Hazen; Hello, Kozeny-Carman. *Journal of Geotechnical and Geoenvironmental Engineering*, 129(11):1054–1056, 2003. (Cited on page 25.)

[69] Francisco J. Carrillo, Cyprien Soulaine, and Ian C. Bourg. The impact of sub-resolution porosity on numerical simulations of multiphase flow. *Advances in Water Resources*, 161:104094, 2022. (Cited on pages xvi, 6 and 136.)

[70] Michael A. Celia, Stefan Bachu, Jan M. Nordbotten, and Karl W. Bandilla. Status of CO2 storage in deep saline aquifers with emphasis on modeling approaches and practical simulations. *Water Resources Research*, 51(9):6846–6892, 2015. (Cited on page 1.)

[71] Philippe Chatelain, Georges-Henri Cottet, and Petros Koumoutsakos. Particle mesh hydrodynamics for astrophysics simulations. *International Journal of Modern Physics C*, 18(04):610–618, 2007. (Cited on pages 9, 22 and 29.)

[72] Philippe Chatelain, Alessandro Curioni, Michael Bergdorf, Diego Rossinelli, Wanda Andreoni, and Petros Koumoutsakos. Billion vortex particle direct numerical simulations of aircraft wakes. *Computer Methods in Applied Mechanics and Engineering*, 197(13–16):1296 – 1304, 2008. (Cited on pages 9, 28 and 29.)

[73] Robin Chatelin and Philippe Poncet. A hybrid grid-particle method for moving bodies in 3D stokes flow with variable viscosity. *SIAM Journal on Scientific Computing*, 35(4):B925–B949, 2013. (Cited on pages 9, 29, 31 and 69.)

[74] Li Chen, Qinjun Kang, Bill Carey, and Wen-Quan Tao. Pore-scale study of diffusion–reaction processes involving dissolution and precipitation using the lattice Boltzmann method. *International Journal of Heat and Mass Transfer*, 75:483–496, 2014. (Cited on page 9.)

[75] Zhao Chen, Vijay Badrinarayanan, Chen-Yu Lee, and Andrew Rabinovich. GradNorm: Gradient normalization for adaptive loss balancing in deep multitask networks. In *Proceedings of the 35th International Conference on Machine Learning*, pages 794–803. PMLR, 2018. (Cited on page 95.)

[76] Alexandre Joel Chorin. Numerical study of slightly viscous flow. *Journal of Fluid Mechanics*, 57(4):785–796, 1973. (Cited on page 31.)

[77] Lei Chou, Robert M. Garrels, and Roland Wollast. Comparative study of the kinetics and mechanisms of dissolution of carbonate minerals. *Chemical Geology*, 78(3):269–282, 1989. (Cited on pages 11, 23, 46, 47, 50 and 51.)

[78] Magali Christensen and Yukie Tanino. Enhanced permeability due to apparent oil/brine slippage in limestone and its dependence on wettability. *Geophysical Research Letters*, 44(12):6116–6123, 2017. (Cited on pages 60 and 76.)

[79] Jørgen Christoffersen and Margaret R. Christoffersen. Kinetics of spiral growth of calcite crystals and determination of the absolute rate constant. *Journal of Crystal Growth*, 100(1):203–211, 1990. (Cited on pages 48, 51 and 56.)

[80] Roberto Cipolla, Yarin Gal, and Alex Kendall. Multi-task Learning Using Uncertainty to Weigh Losses for Scene Geometry and Semantics. In *2018 IEEE/CVF Conference on Computer Vision and Pattern Recognition*, pages 7482–7491, 2018. (Cited on pages 95 and 96.)

[81] Holger Class, Anozie Ebigbo, Rainer Helmig, Helge K. Dahle, Jan M. Nordbotten, Michael A. Celia, et al. A benchmark study on problems related to CO2 storage in geologic formations. *Computational Geosciences*, 13(4):409–434, 2009. (Cited on pages xv, 1 and 21.)

[82] Adam D Cobb. Hamiltorch: A PyTorch-Based Library for Hamiltonian Monte Carlo. In *Proceedings of Cyber-Physical Systems and Internet of Things Week 2023*, CPS-IoT Week '23, page 114–115. Association for Computing Machinery, 2023. (Cited on page 15.)

[83] Adam D. Cobb et al. Hamiltorch. https://github.com/AdamCobb/hamiltorch. (Cited on page 15.)

[84] Adam D. Cobb and Brian Jalaian. Scaling Hamiltonian Monte Carlo inference for Bayesian neural networks with symmetric splitting. In *Proceedings of the Thirty-Seventh Conference on Uncertainty in Artificial Intelligence*, pages 675–685. PMLR, 2021. (Cited on pages 15, 97, 104 and 173.)

[85] Roger Cocle, Grégoire Winckelmans, and Goéric Daeninck. Combining the vortex-in-cell and parallel fast multipole methods for efficient domain decomposition simulations. *Journal of Computational Physics*, 227(21):9091–9120, 2008. (Cited on page 41.)

[86] Joffrey Coheur, Thierry E. Magin, Philippe Chatelain, and Maarten Arnst. Bayesian identification of pyrolysis model parameters for thermal protection materials using an adaptive gradient-informed sampling algorithm with application to a Mars atmospheric entry. *International Journal for Uncertainty Quantification*, 13(2), 2023. (Cited on pages 14 and 137.)

[87] Ricardo Cortez. Convergence of high-order deterministic particle methods for the convection-diffusion equation. *Communications on Pure and Applied Mathematics*, 50(12):1235–1260, 1997. (Cited on page 34.)

[88] Georges-Henri Cottet. A particle-grid superposition method for the Navier-Stokes equations. *Journal of Computational Physics*, 89(2):301–318, 1990. (Cited on pages 9, 22, 29 and 33.)

[89] Georges-Henri Cottet, Guillaume Balarac, and Mathieu Coquerelle. Subgrid particle resolution for the turbulent transport of a passive scalar. In *Advances in Turbulence XII*, pages 779–782, 2009. (Cited on page 39.)

[90] Georges-Henri Cottet, Jean-Matthieu Etancelin, Franck Pérignon, and Christophe Picard. High order Semi-Lagrangian particle methods for transport equations: Numerical analysis and implementation issues. *ESAIM: Mathematical Modelling and Numerical Analysis*, 48(4):1029–1060, 2014. (Cited on pages 32 and 40.)

[91] Georges-Henri Cottet and Petros Koumoutsakos. *Vortex Methods: Theory and Practice*. Cambridge University Press, 2000. (Cited on pages 29 and 31.)

[92] Georges-Henri Cottet, Petros Koumoutsakos, and Mohamed Lemine Ould Salihi. Vortex Methods with spatially varying cores. *Journal of Computational Physics*, 162(1):164–185, 2000. (Cited on pages 28 and 32.)

[93] Geroges-Henri Cottet and Sylvie Mas-Gallic. A particle method to solve the Navier-Stokes system. *Numerische Mathematik*, 57(1):805–827, 1990. (Cited on page 29.)

[94] Wojciech M. Czarnecki, Simon Osindero, Max Jaderberg, Grzegorz Swirszcz, and Razvan Pascanu. Sobolev Training for Neural Networks. In *Advances in Neural Information Processing Systems*, volume 30. Curran Associates, Inc., 2017. (Cited on page 102.)

[95] Anne-Laure Dalibard and David Gérard-Varet. Effective boundary condition at a rough surface starting from a slip condition. *Journal of Differential Equations*, 251(12):3450–3487, 2011. (Cited on pages 59 and 69.)

[96] Keith R. Daly and Tiina Roose. Multiscale modelling of hydraulic conductivity in vuggy porous media. *Proceedings of the Royal Society A: Mathematical, Physical and Engineering Sciences*, 470(2162), 2014. (Cited on page 61.)

[97] Jason Davies, Daniel Maynes, Brent W. Webb, and Brady Woolford. Laminar flow in a microchannel with superhydrophobic walls exhibiting transverse ribs. *Physics of fluids*, 18(8):087110, 2006. (Cited on page 60.)

[98] Anthony M.J. Davis and Eric Lauga. Hydrodynamic friction of fakir-like superhydrophobic surfaces. *Journal of Fluid Mechanics*, 661:402–411, 2010. (Cited on pages 60 and 76.)

[99] Pierre-Gilles de Gennes. On fluid/wall slippage. *Langmuir*, 18(9):3413–3414, 2002. (Cited on pages 60 and 76.)

[100] Denise Degen, Daniel Caviedes Voullième, Susanne Buiter, Harrie-Jan Hendriks Franssen, Harry Vereecken, Ana González-Nicolás, et al. Perspectives of physics-based machine

learning for geoscientific applications governed by partial differential equations. *Geoscientific Model Development Discussions*, 2023:1–50, 2023. (Cited on pages 13 and 137.)

[101] Pierre Degond and Sylvie Mas-Gallic. The weighted particle method for convection-diffusion equations. *Mathematics of Computation*, 53:485–526, 1989. (Cited on pages 32, 33 and 34.)

[102] Wim Degruyter, Olivier Bachmann, and Alain Burgisser. Controls on magma permeability in the volcanic conduit during the climactic phase of the Kos Plateau Tuff eruption (Aegean Arc). *Bulletin of Volcanology*, 72(1):63–74, 2010. (Cited on page 61.)

[103] Marta D'Elia, Hang Deng, Cedric Fraces, Krishna Garikipati, Lori Graham-Brady, Amanda Howard, et al. Machine Learning in Heterogeneous Porous Materials. *arXiv*, 2022. arXiv:2202.04137. (Cited on pages 12, 14, 95 and 137.)

[104] Hang Deng, Sergi Molins, David Trebotich, Carl Steefel, and Donald DePaolo. Pore-scale numerical investigation of the impacts of surface roughness: Upscaling of reaction rates in rough fractures. *Geochimica et Cosmochimica Acta*, 239:374–389, 2018. (Cited on page 10.)

[105] Paolo R. Di Palma, Nicolas Guyennon, Falk Heße, and Emanuele Romano. Porous media flux sensitivity to pore-scale geostatistics: A bottom-up approach. *Advances in Water Resources*, 102:99–110, 2017. (Cited on page 61.)

[106] Romain Dolbeau, François Bodin, and Guillaume Colin de Verdière. One OpenCL to rule them all? In *2013 IEEE 6th International Workshop on Multi-/Many-core Computing Systems (MuCoCoS)*, pages 1–6, 2013. (Cited on page 41.)

[107] Peng Du, Rick Weber, Piotr Luszczek, Stanimire Tomov, Gregory Peterson, and Jack Dongarra. From CUDA to OpenCL: Towards a performance-portable solution for multi-platform GPU programming. *Parallel Computing*, 38(8):391–407, 2012. (Cited on page 41.)

[108] Filip Dutka, Vitaliy Starchenko, Florian Osselin, Silvana Magni, Piotr Szymczak, and Anthony J.C. Ladd. Time-dependent shapes of a dissolving mineral grain: Comparisons of simulations with microfluidic experiments. *Chemical Geology*, 540:119459, 2020. (Cited on page 141.)

[109] Mohammad Ebadi, Denis Orlov, Ivan Makhotin, Vladislav Krutko, Boris Belozerov, and Dmitry Koroteev. Strengthening the digital rock physics, using downsampling for sub-resolved pores in tight sandstones. *Journal of Natural Gas Science and Engineering*, 89:103869, 2021. (Cited on page 58.)

[110] Mustapha El Ossmani and Philippe Poncet. Efficiency of multiscale hybrid Grid-Particle Vortex Methods. *Multiscale Modeling & Simulation*, 8(5):1671–1690, 2010. (Cited on pages 9, 28 and 31.)

[111] Jean-Matthieu Etancelin. *Couplage de modèles, algorithmes multi-échelles et calcul hybride*. PhD thesis, Université de Grenoble, 2014. (Cited on pages 32, 39, 40 and 42.)

[112] Jean-Matthieu Etancelin et al. HySoP. https://particle_methods.gricad-pages.univ-grenoble-alpes.fr/hysop-doc/. (Cited on pages xvii, 16 and 39.)

[113] Jean-Matthieu Etancelin, Peter Moonen, and Philippe Poncet. Improvement of remeshed lagrangian methods for the simulation of dissolution processes at pore-scale. *Advances in Water Resources*, 146:103780, 2020. (Cited on pages 9, 22, 28, 29, 30, 32, 40, 46 and 69.)

[114] Henry Eyring. The activated complex in chemical reactions. *The Journal of Chemical Physics*, 3(2):107–115, 1935. (Cited on page 46.)

[115] István Faragó. A modified iterated operator splitting method. *Applied Mathematical Modelling*, 32(8):1542–1551, 2008. (Cited on page 31.)

[116] Sara F. Farshidi, Yaqing Fan, Louis J. Durlofsky, and Hamdi A. Tchelepi. Chemical reaction modeling in a compositional reservoir-simulation framework. In *SPE Reservoir Simulation Symposium*, pages SPE–163677–MS, 2013. (Cited on page 10.)

[117] Salar Fattahi and Somayeh Sojoudi. Data-Driven Sparse System Identification. In *2018 56th Annual Allerton Conference on Communication, Control, and Computing (Allerton)*, pages 462–469. IEEE, 2018. (Cited on page 95.)

[118] Hossein Fazeli, Mohammad Masoudi, Ravi A. Patel, Per Aagaard, and Helge Hellevang. Pore-scale modeling of nucleation and growth in porous media. *ACS Earth and Space Chemistry*, 4(2):249–260, 2020. (Cited on page 48.)

[119] Lee A. Feldkamp, L. Craig Davis, and James W. Kress. Practical cone-beam algorithm. *Journal of the Optical Society of America A*, 1(6):612–619, 1984. (Cited on page 5.)

[120] Cedric G. Fraces and Hamdi Tchelepi. Physics Informed Deep Learning for flow and transport in porous media. In *SPE Reservoir Simulation Conference*, 2021. (Cited on page 13.)

[121] James Gabbard, Thomas Gillis, Philippe Chatelain, and Wim M. van Rees. An immersed interface method for the 2D vorticity-velocity Navier-Stokes equations with multiple bodies. *Journal of Computational Physics*, 464:111339, 2022. (Cited on page 9.)

[122] Marylou Gabrié, Grant M. Rotskoff, and Eric Vanden-Eijnden. Adaptive Monte Carlo augmented with normalizing flows. *Proceedings of the National Academy of Sciences*, 119(10):e2109420119, 2022. (Cited on page 102.)

[123] Mark Girolami and Ben Calderhead. Riemann manifold Langevin and Hamiltonian Monte Carlo methods. *Journal of the Royal Statistical Society: Series B (Statistical Methodology)*, 73(2):123–214, 2011. (Cited on pages 15 and 96.)

[124] Ian Goodfellow, Yoshua Bengio, and Aaron Courville. *Deep Learning*. MIT Press, 2016. (Cited on page 11.)

[125] Jeff Gostick, Mahmoudreza Aghighi, James Hinebaugh, Tom Tranter, Michael A. Hoeh, Harold Day, et al. OpenPNM: A Pore Network Modeling Package. *Computing in Science & Engineering*, 18(4):60–74, 2016. (Cited on pages 7 and 8.)

[126] Jeff Gostick et al. OpenPNM. https://openpnm.org/. (Cited on page 7.)

[127] Alex Graves. Practical Variational Inference for Neural Networks. In *Advances in Neural Information Processing Systems*, volume 24. Curran Associates, Inc., 2011. (Cited on page 95.)

[128] Bo Guo, Yashar Mehmani, and Hamdi A. Tchelepi. Multiscale formulation of pore-scale compressible Darcy-Stokes flow. *Journal of Computational Physics*, 397:108849, 2019. (Cited on page 8.)

[129] Parisa Heidary, Leila Farhadi, and Muhammad Umer Altaf. A reduced-adjoint variational data assimilation for estimating soil moisture profile from surface soil moisture observations. In *2021 IEEE International Geoscience and Remote Sensing Symposium IGARSS*, pages 6458–6460, 2021. (Cited on page 13.)

[130] Mads Mølholm Hejlesen, Petros Koumoutsakos, Anthony Leonard, and Jens Honoré Walther. Iterative Brinkman penalization for remeshed Vortex Methods. *Journal of Computational Physics*, 280:547–562, 2015. (Cited on page 28.)

[131] Helge Hellevang, Van T.H. Pham, and Per Aagaard. Kinetic modelling of CO2–water–rock interactions. *International Journal of Greenhouse Gas Control*, 15:3–15, 2013. (Cited on pages 11 and 23.)

[132] Matthew D. Hoffman and Andrew Gelman. The No-U-turn sampler: adaptively setting path lengths in Hamiltonian Monte Carlo. *The Journal of Machine Learning Research*, 15(1):1593–1623, 2014. (Cited on pages 15, 96, 99 and 104.)

[133] Matthew D. Hoffman, Alexey Radul, and Pavel Sountsov. An Adaptive-MCMC Scheme for Setting Trajectory Lengths in Hamiltonian Monte Carlo. In *Proceedings of The 24th International Conference on Artificial Intelligence and Statistics*, pages 3907–3915. PMLR, 2021. (Cited on page 99.)

[134] David W. Hogg and Daniel Foreman-Mackey. Data Analysis Recipes: Using Markov Chain Monte Carlo. *The Astrophysical Journal Supplement Series*, 236(1):11, 2018. (Cited on page 125.)

[135] Laurène Hume and Philippe Poncet. A velocity-vorticity method for highly viscous 3D flows with application to digital rock physics. *Journal of Computational Physics*, 425:109910, 2021. (Cited on pages 28, 31, 69, 88, 134, 142, 145 and 172.)

[136] IEA. Net zero by 2050. Technical report, IEA, Paris, 2021. https://www.iea.org/reports/net-zero-by-2050 License: CC BY 4.0. (Cited on page 1.)

[137] Baasansuren Jadamba, Akhtar A. Khan, Miguel Sama, Hans-Jorg Starkloff, and Christiane Tammer. A convex optimization framework for the inverse problem of identifying a random parameter in a stochastic partial differential equation. *SIAM/ASA Journal on Uncertainty Quantification*, 9(2):922–952, 2021. (Cited on pages 13 and 137.)

[138] Richard S. Jayne, Hao Wu, and Ryan M. Pollyea. Geologic CO2 sequestration and permeability uncertainty in a highly heterogeneous reservoir. *International Journal of Greenhouse Gas Control*, 83:128–139, 2019. (Cited on pages xv and 58.)

[139] Weiqi Ji, Weilun Qiu, Zhiyu Shi, Shaowu Pan, and Sili Deng. Stiff-PINN: Physics-informed neural network for stiff chemical kinetics. *The Journal of Physical Chemistry A*, 125(36):8098–8106, 2021. (Cited on page 97.)

[140] Pierre Joseph, Cécile Cottin-Bizonne, Jean-Michel Benoît, Christophe Ybert, Catherine Journet, Patrick Tabeling, et al. Slippage of water past superhydrophobic carbon nanotube forests in microchannels. *Physical Review Letters*, 97:156104, 2006. (Cited on pages 60, 74, 75 and 76.)

[141] Ramanzani Kalule, Hamid Ait Abderrahmane, Waleed Alameri, and Mohamed Sassi. Stacked ensemble machine learning for porosity and absolute permeability prediction of carbonate rock plugs. *Scientific Reports*, 13(1):9855, 2023. (Cited on page 12.)

[142] Qinjun Kang, Peter C. Lichtner, and Dongxiao Zhang. Lattice Boltzmann pore-scale model for multicomponent reactive transport in porous media. *Journal of Geophysical Research: Solid Earth*, 111(B5), 2006. (Cited on page 10.)

[143] Jean-Baptiste Keck. *Numerical modelling and High Performance Computing for sediment flows*. Theses, Université Grenoble Alpes, 2019. (Cited on pages 32, 39, 40, 41 and 42.)

[144] Richard A. Ketcham and William D. Carlson. Acquisition, optimization and interpretation of X-ray computed tomographic imagery: applications to the geosciences. *Computers & Geosciences*, 27(4):381–400, 2001. (Cited on page 6.)

[145] Siarhei Khirevich and Tadeusz W. Patzek. Behavior of numerical error in pore-scale lattice Boltzmann simulations with simple bounce-back rule: Analysis and highly accurate extrapolation. *Physics of Fluids*, 30:093604, 2018. (Cited on page 69.)

[146] Elena Konstantinovskaya, Jose A. Rivero, Valentina Vallega, John Brodylo, and Peter Coldham. 3D reservoir simulation of CO2 injection in a deep saline aquifer of the lower paleozoic potsdam sandstone of the st lawrence platform, gentilly block, quebec. *Geoenergy*, 1(1):2022–001, 2023. (Cited on page 3.)

[147] Josef Kozeny. Ueber kapillare Leitung des Wassers im Boden. *Sitzungsber Akad. Wiss., Wien*, 136(2a):271–306, 1927. (Cited on page 25.)

[148] David Krinsley and Patrick Trusty. Environmental Interpretation of Quartz Grain Surface Textures. In *Provenance of Arenites*, pages 213–229. Springer Netherlands, 1985. (Cited on page 76.)

[149] Timm Krueger, Halim Kusumaatmaja, Alexandr Kuzmin, Orest Shardt, Goncalo Silva, and Erlend Magnus Viggen. *The Lattice Boltzmann Method: Principles and Practice*. Graduate Texts in Physics. Springer, 2016. (Cited on page 10.)

[150] Ajitabh Kumar, Robin Ozah, Myeong H. Noh, Gary A. Pope, Steven L. Bryant, Kamy Sepehrnoori, et al. Reservoir simulation of CO2 storage in deep saline aquifers. *SPE Journal*, 10(3):336–348, 2005. (Cited on page 3.)

[151] Facebook Artificial Intelligence Research lab. PyTorch. https://pytorch.org/. (Cited on page 15.)

[152] Anthony J. C. Ladd and Piotr Szymczak. Reactive Flows in Porous Media: Challenges in Theoretical and Numerical Methods. *Annual Review of Chemical and Biomolecular Engineering*, 12(1):543–571, 2021. (Cited on page 10.)

[153] Peter Lai and Samuel Krevor. Pore scale heterogeneity in the mineral distribution and surface area of Berea sandstone. *Energy Procedia*, 63:3582–3588, 2014. (Cited on page 58.)

[154] Bishnu P. Lamichhane. A new Finite Element method for Darcy-Stokes-Brinkman equations. *ISRN Computational Mathematics*, 2013:798059, 2013. (Cited on page 28.)

[155] Shiwei Lan, Jeffrey Streets, and Babak Shahbaba. Wormhole Hamiltonian Monte Carlo. *Proceedings of the AAAI Conference on Artificial Intelligence*, 2014:1953–1959, 2014. (Cited on page 102.)

[156] Antonio C. Lasaga. Transition state theory. *Rev. Mineral.*, 8, 1981. (Cited on pages 11, 23, 46 and 140.)

[157] Antonio C. Lasaga. Chemical kinetics of water-rock interactions. *Journal of Geophysical Research: Solid Earth*, 89(B6):4009–4025, 1984. (Cited on page 46.)

[158] Didier Lasseux, Francisco J. Valdés Parada, and Mark L. Porter. An improved macroscale model for gas slip flow in porous media. *Journal of Fluid Mechanics*, 805:118–146, 2016. (Cited on pages 59, 69, 87 and 89.)

[159] Didier Lasseux, Michel Quintard, and Stephen Whitaker. Determination of permeability tensors for two-phase flow in homogeneous porous media: Theory. *Transport in Porous Media*, 24(2):107–137, 1996. (Cited on pages 25, 69 and 140.)

[160] Didier Lasseux, Francisco J. Valdés-Parada, and Alessandro Bottaro. Upscaled model for unsteady slip flow in porous media. *Journal of Fluid Mechanics*, 923, 2021. (Cited on page 59.)

[161] Didier Lasseux, Tony Zaouter, and Francisco J. Valdés-Parada. Determination of Klinkenberg and higher-order correction tensors for slip flow in porous media. *Phys. Rev. Fluids*, 8:053401, 2023. (Cited on pages 87 and 140.)

[162] Eric Lauga and Michael P. Brenner. Dynamic mechanisms for apparent slip on hydrophobic surfaces. *Physical Review E*, 70(2):026311, 2004. (Cited on pages 60 and 76.)

[163] Eric Lauga and Howard A Stone. Effective slip in pressure-driven Stokes flow. *Journal of Fluid Mechanics*, 489:55, 2003. (Cited on pages 60, 76 and 90.)

[164] Choongyeop Lee, Chang-Hwan Choi, and Chang-Jin Kim. Superhydrophobic drag reduction in laminar flows: a critical review. *Experiments in Fluids*, 57(12):176, 2016. (Cited on pages 61 and 76.)

[165] Joo Hwan Lee, Kaushik Patel, Nimit Nigania, Hyojong Kim, and Hyesoon Kim. OpenCL Performance Evaluation on Modern Multi Core CPUs. In *2013 IEEE International Symposium on Parallel & Distributed Processing, Workshops and Phd Forum*, pages 1177–1185, 2013. (Cited on page 41.)

[166] Randall J. LeVeque and Zhilin Li. The immersed interface method for elliptic equations with discontinuous coefficients and singular sources. *SIAM Journal on Numerical Analysis*, 31(4):1019–1044, 1994. (Cited on page 9.)

[167] Daniel Levy, Matt D. Hoffman, and Jascha Sohl-Dickstein. Generalizing Hamiltonian Monte Carlo with Neural Networks. In *International Conference on Learning Representations*, 2018. (Cited on page 125.)

[168] Dedong Li, Sebastian Bauer, Katharina Benisch, Bastian Graupner, and Christof Beyer. OpenGeoSys-ChemApp: a coupled simulator for reactive transport in multiphase systems and application to CO2 storage formation in northern germany. *Acta Geotechnica*, 9(1):67–79, 2014. (Cited on page 2.)

[169] Li Li, Catherine A. Peters, and Michael A. Celia. Upscaling geochemical reaction rates using pore-scale network modeling. *Advances in Water Resources*, 29(9):1351–1370, 2006. (Cited on pages 7, 22 and 139.)

[170] Nathalie Limodin, Julien Réthoré, Jean Yves Buffière, Anthony Gravouil, François Hild, and Stéphane G. Roux. Crack closure and stress intensity factor measurements in nodular graphite cast iron using three-dimensional correlation of laboratory X-ray microtomography images. *Acta Materialia*, 57:4090–4101, 2009. (Cited on page 5.)

[171] Guang Lin, Yating Wang, and Zecheng Zhang. Multi-variance replica exchange SGMCMC for inverse and forward problems via Bayesian PINN. *Journal of Computational Physics*, 460:111173, 2022. (Cited on page 97.)

[172] Qingyang Lin, Yousef Al-Khulaifi, Martin J. Blunt, and Branko Bijeljic. Quantification of sub-resolution porosity in carbonate rocks by applying high-salinity contrast brine using X-ray microtomography differential imaging. *Advances in Water Resources*, 96:306–322, 2016. (Cited on pages xvi, 6, 94, 136, 140 and 141.)

[173] Kevin Linka, Amelie Schäfer, Xuhui Meng, Zongren Zou, George Em Karniadakis, and Ellen Kuhl. Bayesian Physics Informed Neural Networks for real-world nonlinear dynamical systems. *Computer Methods in Applied Mechanics and Engineering*, page 115346, 2022. (Cited on pages xviii, 14, 95, 96, 97, 102, 118, 120 and 124.)

[174] Maria G. Lioliou, Christakis A. Paraskeva, Petros G. Koutsoukos, and Alkiviades C. Payatakes. Heterogeneous nucleation and growth of calcium carbonate on calcite and quartz. *Journal of Colloid and Interface Science*, 308(2):421–428, 2007. (Cited on page 47.)

[175] Sebastian Liska and Tim Colonius. A fast lattice Green's function method for solving viscous incompressible flows on unbounded domains. *Journal of Computational Physics*, 316:360 – 384, 2016. (Cited on page 69.)

[176] Dehao Liu and Yan Wang. Multi-Fidelity Physics-Constrained Neural Network and its application in materials modeling. *Journal of Mechanical Design*, 141(12), 2019. (Cited on pages 95 and 100.)

[177] Qiang Liu and Dilin Wang. Stein Variational Gradient Descent: A general purpose bayesian inference algorithm. In *Advances in Neural Information Processing Systems*, volume 29. Curran Associates, Inc., 2016. (Cited on pages 15 and 98.)

[178] Samuel Livingstone, Michael Betancourt, Simon Byrne, and Mark Girolami. On the geometric ergodicity of Hamiltonian Monte Carlo. *Bernoulli*, 25(4A):3109 – 3138, 2019. (Cited on page 98.)

[179] John Loffeld and Mayya Tokman. Implementation of Parallel Adaptive-Krylov Exponential Solvers for Stiff Problems. *SIAM Journal on Scientific Computing*, 36(5):C591–C616, 2014. (Cited on page 172.)

[180] Fei Lu, Matthias Morzfeld, Xuemin Tu, and Alexandre J. Chorin. Limitations of polynomial chaos expansions in the Bayesian solution of inverse problems. *Journal of Computational Physics*, 282:138–147, 2015. (Cited on page 14.)

[181] Ang Luo, Yongming Li, Xi Chen, Zhongyi Zhu, and Yu Peng. Review of CO2 sequestration mechanism in saline aquifers. *Natural Gas Industry B*, 9(4):383–393, 2022. (Cited on page 2.)

[182] Haishan Luo, Michel Quintard, Gérald Debenest, and Farid Laouafa. Properties of a diffuse interface model based on a porous medium theory for solid–liquid dissolution problems. *Computational Geosciences*, 16(4):913–932, 2012. (Cited on page 49.)

[183] Hans G. Machel. Concepts and models of dolomitization: a critical reappraisal. *Geological Society, London, Special Publications*, 235(1):7–63, 2004. (Cited on pages 10 and 27.)

[184] Suryanarayana Maddu, Bevan L. Cheeseman, Christian L. Müller, and Ivo F. Sbalzarini. Learning physically consistent differential equation models from data using group sparsity. *Physical Review E*, 103:042310, 2021. (Cited on page 95.)

[185] Suryanarayana Maddu, Bevan L. Cheeseman, Ivo F. Sbalzarini, and Christian L. Müller. Stability selection enables robust learning of differential equations from limited noisy data. *Proceedings of the Royal Society A*, 478(2262):20210916, 2022. (Cited on page 94.)

[186] Suryanarayana Maddu, Dominik Sturm, Bevan L. Cheeseman, Christian L. Müller, and Ivo F. Sbalzarini. STENCIL-NET for equation-free forecasting from data. *Scientific Reports*, 13(1):12787, 2023. (Cited on page 95.)

[187] Suryanarayana Maddu, Dominik Sturm, Christian L Müller, and Ivo F Sbalzarini. Inverse Dirichlet weighting enables reliable training of physics informed neural networks. *Machine Learning: Science and Technology*, 3(1):015026, 2022. (Cited on pages 95, 102, 103, 106, 111, 133 and 137.)

[188] Julien Maes, Cyprien Soulaine, and Hannah P. Menke. Improved Volume-Of-Solid Formulations for Micro-Continuum Simulation of Mineral Dissolution at the Pore-Scale. *Frontiers in Earth Science*, 10, 2022. (Cited on page 51.)

[189] Adrien Magni and Georges-Henri Cottet. Accurate, non-oscillatory, remeshing schemes for particle methods. *Journal of Computational Physics*, 231(1):152–172, 2012. (Cited on pages 9, 29, 30 and 32.)

[190] Kate Maher, Carl I. Steefel, Donald J. DePaolo, and Brian E. Viani. The mineral dissolution rate conundrum: Insights from reactive transport modeling of U isotopes and pore fluid chemistry in marine sediments. *Geochimica et Cosmochimica Acta*, 70(2):337–363, 2006. (Cited on pages 11, 56 and 140.)

[191] Oren Mangoubi, Natesh S. Pillai, and Aaron Smith. Does Hamiltonian Monte Carlo mix faster than a random walk on multimodal densities? *arXiv*, 2018. arXiv:1808.03230. (Cited on page 102.)

[192] José V. Manjón, José E. Romero, Roberto Vivo-Hernando, Gregorio Rubio, Fernando Aparici, Maria de La Iglesia-Vaya, et al. Blind MRI Brain Lesion Inpainting Using Deep Learning. In *Simulation and Synthesis in Medical Imaging*, pages 41–49. Springer International Publishing, 2020. (Cited on page 125.)

[193] Youssef M. Marzouk and Habib N. Najm. Dimensionality reduction and polynomial chaos acceleration of Bayesian inference in inverse problems. *Journal of Computational Physics*, 228(6):1862–1902, 2009. (Cited on page 14.)

[194] Mohammad Masoudi, Hossein Fazeli, Rohaldin Miri, and Helge Hellevang. Pore scale modeling and evaluation of clogging behavior of salt crystal aggregates in CO2-rich phase during carbon storage. *International Journal of Greenhouse Gas Control*, 111:103475, 2021. (Cited on pages 23 and 48.)

[195] Simon A. Mathias, Jon G. Gluyas, Gerardo J. González Martínez de Miguel, Steven L. Bryant, and David Wilson. On relative permeability data uncertainty and CO2 injectivity estimation for brine aquifers. *International Journal of Greenhouse Gas Control*, 12:200–212, 2013. (Cited on pages xv and 58.)

[196] Juerg M. Matter, Taro Takahashi, and David Goldberg. Experimental evaluation of in situ CO2-water-rock reactions during CO2 injection in basaltic rocks: Implications for geological CO2 sequestration. *Geochemistry, Geophysics, Geosystems*, 8(2), 2007. (Cited on page 1.)

[197] Yashar Mehmani, Tie Sun, Matthew T. Balhoff, Peter Eichhubl, and Steven Bryant. Multiblock pore-scale modeling and upscaling of reactive transport: Application to carbon sequestration. *Transport in Porous Media*, 95(2):305–326, 2012. (Cited on pages 7 and 139.)

[198] Yashar Mehmani and Hamdi Tchelepi. Pore-Network Modeling vs. Direct Numerical Simulation: a Comparative Study. In *AGU Fall Meeting Abstracts*, volume 2016, pages H51D–1519, 2016. (Cited on pages 7, 22 and 59.)

[199] Xuhui Meng, Hessam Babaee, and George Em Karniadakis. Multi-fidelity Bayesian neural networks: Algorithms and applications. *Journal of Computational Physics*, 438:110361, 2021. (Cited on pages 13, 14, 95, 96 and 100.)

[200] Hannah P. Menke, Branko Bijeljic, Matthew G. Andrew, and Martin J. Blunt. Dynamic Three-Dimensional Pore-Scale Imaging of Reaction in a Carbonate at Reservoir Conditions. *Environmental Science & Technology*, 49(7):4407–4414, 2015. (Cited on pages 22, 136, 139, 141 and 166.)

[201] Gregory Miller and David Trebotich. An embedded boundary method for the Navier–Stokes equations on a time-dependent domain. *Communications in Applied Mathematics and Computational Science*, 7(1):1 – 31, 2012. (Cited on page 9.)

[202] Chloé Mimeau, Iraj Mortazavi, and Georges-Henri Cottet. Passive control of the flow around a hemisphere using porous media. *European Journal of Mechanics - B/Fluids*, 65:213–226, 2017. (Cited on pages 9 and 39.)

[203] Sergi Molins. Reactive interfaces in direct numerical simulation of pore-scale processes. *Reviews in Mineralogy and Geochemistry*, 80(1):461–481, 2015. (Cited on page 8.)

[204] Sergi Molins, Cyprien Soulaine, Nikolaos I. Prasianakis, Aida Abbasi, Philippe Poncet, Anthony J. C. Ladd, et al. Simulation of mineral dissolution at the pore scale with evolving fluid-solid interfaces: review of approaches and benchmark problem set. *Computational Geosciences*, 25(4):1285–1318, 2021. (Cited on pages xv, 4, 22, 25, 28, 29, 32, 60, 69, 139, 151 and 159.)

[205] Sergi Molins, David Trebotich, Gregory H. Miller, and Carl I. Steefel. Mineralogical and transport controls on the evolution of porous media texture using direct numerical simulation. *Water Resources Research*, 53(5):3645–3661, 2017. (Cited on pages 11, 56, 139 and 140.)

[206] Sergi Molins, David Trebotich, Carl I. Steefel, and Chaopeng Shen. An investigation of the effect of pore scale flow on average geochemical reaction rates using direct numerical simulation. *Water Resources Research*, 48(3), 2012. (Cited on pages 9, 11, 23, 46, 69 and 140.)

[207] Joseph P. Molnar and Samuel J. Grauer. Flow field tomography with uncertainty quantification using a Bayesian physics-informed neural network. *Measurement Science and Technology*, 33(6):065305, 2022. (Cited on pages 14, 96, 97 and 102.)

[208] Anirban Mondal, Yalchin Efendiev, Bani Mallick, and Akhil Datta-Gupta. Bayesian uncertainty quantification for flows in heterogeneous porous media using reversible jump Markov chain Monte Carlo methods. *Advances in Water Resources*, 33(3):241–256, 2010. (Cited on page 137.)

[209] Yohei Morinishi, Thomas S. Lund, Oleg V. Vasilyev, and Parviz Moin. Fully Conservative Higher Order Finite Difference Schemes for Incompressible Flow. *Journal of Computational Physics*, 143(1):90–124, 1998. (Cited on page 69.)

[210] Lukas Mosser, Olivier Dubrule, and Martin J. Blunt. Reconstruction of three-dimensional porous media using generative adversarial neural networks. *Phys. Rev. E*, 96:043309, 2017. (Cited on page 11.)

[211] Peyman Mostaghimi, Martin J. Blunt, and Branko Bijeljic. Computations of absolute permeability on micro-CT images. *Mathematical Geosciences*, 45(1):103–125, 2013. (Cited on pages 59 and 136.)

[212] Nadja Müller. Supercritical CO2-brine relative permeability experiments in reservoir rocks —Literature Review and Recommendations. *Transport in Porous Media*, 87(2):367–383, 2011. (Cited on page 57.)

[213] Claude Louis M. H. Navier. Mémoire sur les lois du mouvement des fluides. *Mémoires de l'Académie Royale des Sciences de l'Institut de France*, 6(1823):389–440, 1823. (Cited on page 60.)

[214] Mathias Nehler, Ferdinand Stoeckhert, Anne Oelker, Jörg Renner, and Erik Saenger. Evaluating porosity estimates for sandstones based on X-ray micro-tomographic images. *Solid Earth Discussions*, pages 1–45, 2019. (Cited on pages xvi and 6.)

[215] Arne Erik Nielsen. Electrolyte crystal growth mechanisms. *Journal of Crystal Growth*, 67(2):289–310, 1984. (Cited on pages 48, 51 and 56.)

[216] Arne Erik Nielsen and Jens M. Toft. Electrolyte crystal growth kinetics. *Journal of Crystal Growth*, 67(2):278–288, 1984. (Cited on page 47.)

[217] Catherine Noiriel, Matthias Oursin, Giuseppe Saldi, and David Haberthür. Direct Determination of Dissolution Rates at Crystal Surfaces Using 3D X-ray Microtomography. *ACS Earth and Space Chemistry*, 3(1):100–108, 2019. (Cited on pages xvi, 5, 136 and 141.)

[218] Catherine Noiriel and François Renard. Four-dimensional X-ray micro-tomography imaging of dynamic processes in geosciences. *Comptes Rendus. Géoscience*, 354:255–280, 2022. (Cited on pages 4, 22, 136, 141 and 166.)

[219] Catherine Noiriel, Nicolas Seigneur, Pierre Le Guern, and Vincent Lagneau. Geometry and mineral heterogeneity controls on precipitation in fractures: An X-ray micro-tomography and reactive transport modeling study. *Advances in Water Resources*, 152:103916, 2021. (Cited on pages 23, 48 and 51.)

[220] Catherine Noiriel and Cyprien Soulaine. Pore-Scale Imaging and Modelling of Reactive Flow in Evolving Porous Media: Tracking the Dynamics of the Fluid–Rock Interface. *Transport in Porous Media*, 140(1):181–213, 2021. (Cited on pages xv, 4, 10, 22 and 139.)

[221] Catherine Noiriel, Carl I. Steefel, Li Yang, and Jonathan Ajo-Franklin. Upscaling calcium carbonate precipitation rates from pore to continuum scale. *Chemical Geology*, 318-319:60 – 74, 2012. (Cited on page 61.)

[222] Catherine Noiriel, Carl I. Steefel, Li Yang, and Dominique Bernard. Effects of pore-scale precipitation on permeability and flow. *Advances in Water Resources*, 95:125–137, 2016. (Cited on pages 11, 23, 48 and 61.)

[223] Mohammad Nooraiepour, Mohammad Masoudi, and Helge Hellevang. Probabilistic nucleation governs time, amount, and location of mineral precipitation and geometry evolution in the porous medium. *Scientific Reports*, 11(1):16397, 2021. (Cited on pages 11, 23 and 48.)

[224] Paul Novello, Gaël Poëtte, David Lugato, and Pietro Marco Congedo. Goal-Oriented Sensitivity Analysis of Hyperparameters in Deep Learning. *Journal of Scientific Computing*, 94(3):45, 2023. (Cited on page 173.)

[225] Sergey Oladyshkin, Holger Class, Rainer Helmig, and Wolfgang Nowak. An integrative approach to robust design and probabilistic risk assessment for CO2 storage in geological formations. *Computational Geosciences*, 15(3):565–577, 2011. (Cited on page 2.)

[226] Jan Oldenburg, Finja Borowski, Alper Öner, Klaus-Peter Schmitz, and Michael Stiehm. Geometry aware physics informed neural network surrogate for solving Navier–Stokes equation (GAPINN). *Advanced Modeling and Simulation in Engineering Sciences*, 9(1):8, 2022. (Cited on page 95.)

[227] Mohan K. R. Panga, Murtaza Ziauddin, and Vemuri Balakotaiah. Two-scale continuum model for simulation of wormholes in carbonate acidization. *AIChE Journal*, 51(12):3231–3248, 2005. (Cited on pages 4 and 22.)

[228] David L. Parkhurst, C. Anthony J. Appelo, et al. PHREEQC. https://www.usgs.gov/software/phreeqc-version-3. (Cited on page 11.)

[229] Sylvain Pasquier, Michel Quintard, and Yohan Davit. Modeling flow in porous media with rough surfaces: effective slip boundary conditions and application to structured packings. *Chemical Engineering Science*, 165:131–146, 2017. (Cited on pages 59, 60 and 62.)

[230] Anthony T. Patera. A spectral element method for fluid dynamics: Laminar flow in a channel expansion. *Journal of Computational Physics*, 54(3):468–488, 1984. (Cited on page 69.)

[231] Jaideep Pathak, Brian Hunt, Michelle Girvan, Zhixin Lu, and Edward Ott. Model-free prediction of large spatiotemporally chaotic systems from data: a reservoir computing approach. *Physical Review Letters*, 120:024102, 2018. (Cited on page 95.)

[232] Ryan L. Payton, Yizhuo Sun, Domenico Chiarella, and Andrew Kingdon. Pore scale numerical modelling of geological carbon storage through mineral trapping using true pore geometries. *Transport in Porous Media*, 141(3):667–693, 2022. (Cited on pages xv, 3, 21, 22 and 139.)

[233] Milutin Pejović, Mladen Nikolić, Gerard B.M. Heuvelink, Tomislav Hengl, Milan Kilibarda, and Branislav Bajat. Sparse regression interaction models for spatial prediction of soil properties in 3d. *Computers & Geosciences*, 118:1–13, 2018. (Cited on page 12.)

[234] Anna E. Peksa, Karl-Heinz A.A. Wolf, and Pacelli L.J. Zitha. Bentheimer sandstone revisited for experimental purposes. *Marine and Petroleum Geology*, 67:701–719, 2015. (Cited on page 88.)

[235] Joao P. Pereira-Nunes, Martin J. Blunt, and Branko Bijeljic. Pore-scale simulation of carbonate dissolution in micro-CT images. *Journal of Geophysical Research: Solid Earth*, 121:558–576, 2016. (Cited on pages 8 and 69.)

[236] Sarah Perez, Jean-Matthieu Etancelin, and Philippe Poncet. A semi-Lagrangian numerical method for the simulation of precipitation/crystallization at the pore scale of porous media. In *CrysPoM VII 2021*, Pau, France, 2021. (Cited on page 172.)

[237] Sarah Perez, Suryanarayana Maddu, Ivo F. Sbalzarini, and Philippe Poncet. Adaptive weighting of Bayesian physics informed neural networks for multitask and multiscale forward and inverse problems. *Journal of Computational Physics*, 491:112342, 2023. (Cited on pages 94 and 166.)

[238] Sarah Perez, Peter Moonen, and Philippe Poncet. On the Deviation of Computed Permeability Induced by Unresolved Morphological Features of the Pore Space. *Transport in Porous Media*, 141(1):151–184, 2022. (Cited on pages 58, 101, 134, 136 and 166.)

[239] Charles S. Peskin. Flow patterns around heart valves: A numerical method. *Journal of Computational Physics*, 10(2):252–271, 1972. (Cited on page 9.)

[240] Van T.H. Pham, Peng Lu, Per Aagaard, Chen Zhu, and Helge Hellevang. On the potential of CO2–water–rock interactions for CO2 storage using a modified kinetic model. *International Journal of Greenhouse Gas Control*, 5(4):1002–1015, 2011. (Cited on pages 11 and 23.)

[241] Johan Phan, Leonardo C. Ruspini, and Frank Lindseth. Automatic segmentation tool for 3D digital rocks by deep learning. *Scientific Reports*, 11(1):19123, 2021. (Cited on pages 12 and 134.)

[242] Philippe Angot. Well-posed Stokes/Brinkman and Stokes/Darcy coupling revisited with new jump interface conditions. *ESAIM: M2AN*, 52(5):1875–1911, 2018. (Cited on page 28.)

[243] Paul Ploumhans, Gregoire S. Winckelmans, John K. Salmon, Anthony Leonard, and Michael S. Warren. Vortex methods for Direct Numerical Simulation of three-dimensional bluff body flows: Application to the sphere at Re=300, 500, and 1000. *Journal of Computational Physics*, 178(2):427–463, 2002. (Cited on page 32.)

[244] L. Neil Plummer and Eurybiades Busenberg. The solubilities of calcite, aragonite and vaterite in CO2-H2O solutions between 0 and 90°C, and an evaluation of the aqueous model for the system CaCO3-CO2-H2O. *Geochimica et Cosmochimica Acta*, 46(6):1011–1040, 1982. (Cited on pages 46 and 51.)

[245] L. Neil Plummer, Tom M. L. Wigley, and David L. Parkhurst. The kinetics of calcite dissolution in CO2-water systems at 5 degrees to 60 degrees C and 0.0 to 1.0 atm CO2. *American Journal of Science*, 278(2):179–216, 1978. (Cited on pages 23, 45, 46 and 47.)

[246] Philippe Poncet. Finite difference stencils based on particle strength exchange schemes for improvement of vortex methods. *Journal of Turbulence*, 7(23), 2006. (Cited on pages 33 and 35.)

[247] Philippe Poncet. Analysis of direct three-dimensional parabolic panel methods. *SIAM Journal on Numerical Analysis*, 45(6):2259–2297, 2007. (Cited on page 69.)

[248] Philippe Poncet. Analysis of an immersed boundary method for three-dimensional flows in vorticity formulation. *Journal of Computational Physics*, 228(19):7268–7288, 2009. (Cited on page 9.)

[249] Apostolos F. Psaros, Xuhui Meng, Zongren Zou, Ling Guo, and George Em Karniadakis. Uncertainty quantification in scientific machine learning: Methods, metrics, and comparisons. *Journal of Computational Physics*, 477:111902, 2023. (Cited on pages 13, 14, 102, 129 and 133.)

[250] Michel Quintard and Stephen Whitaker. Two-phase flow in heterogeneous porous media: the method of large-scale averaging. *Transport in Porous Media*, 3(4):357–413, 1988. (Cited on pages xv, xvii, 3, 8, 22, 25, 26 and 64.)

[251] Michel Quintard and Stephen Whitaker. Transport in ordered and disordered porous media: volume-averaged equations, closure problems, and comparison with experiment. *Chemical Engineering Science*, 48(14):2537–2564, 1993. (Cited on pages xv, xvii and 3.)

[252] Ali Q. Raeini, Martin J. Blunt, and Branko Bijeljic. Direct simulations of two-phase flow on micro-CT images of porous media and upscaling of pore-scale forces. *Advances in Water Resources*, 74:116 – 126, 2014. (Cited on page 69.)

[253] Nasim Rahaman, Aristide Baratin, Devansh Arpit, Felix Draxler, Min Lin, Fred A. Hamprecht, et al. On the Spectral Bias of Neural Networks. In *Proceedings of the 36th International Conference on Machine Learning*, pages 5301–5310. PMLR, 2019. (Cited on page 95.)

[254] Maziar Raissi, Paris Perdikaris, and George Em Karniadakis. Physics-informed neural networks: A deep learning framework for solving forward and inverse problems involving nonlinear partial differential equations. *Journal of Computational Physics*, 378:686–707, 2019. (Cited on pages 11, 12 and 95.)

[255] Maziar Raissi, Alireza Yazdani, and George Em Karniadakis. Hidden Fluid Mechanics: A Navier-Stokes informed deep learning framework for assimilating flow visualization data. *arXiv*, 2018. arXiv:1808.04327. (Cited on page 130.)

[256] Maziar Raissi, Alireza Yazdani, and George Em Karniadakis. Hidden fluid mechanics: Learning velocity and pressure fields from flow visualizations. *Science*, 367(6481):1026–1030, 2020. (Cited on page 130.)

[257] Amir Raoof and S. Majid Hassanizadeh. A new method for generating pore-network models of porous media. *Transport in Porous Media*, 81(3):391–407, 2010. (Cited on page 7.)

[258] Franz M. Rohrhofer, Stefan Posch, and Bernhard C. Geiger. On the Pareto Front of Physics-Informed Neural Networks. *arXiv*, 2021. arXiv:2105.00862. (Cited on pages 95 and 133.)

[259] Vivekananda Roy. Convergence Diagnostics for Markov Chain Monte Carlo. *Annual Review of Statistics and Its Application*, 7(1):387–412, 2020. (Cited on page 125.)

[260] Youcef Saad and Martin H. Schultz. GMRES: a generalized minimal residual method for solving nonsymmetric linear systems. *SIAM Journal on scientific and statistical computing*, 7(3):856–869, 1986. (Cited on page 70.)

[261] David Sanchez, Laurène Hume, Robin Chatelin, and Philippe Poncet. Analysis of the 3D non-linear Stokes problem coupled to transport-diffusion for shear-thinning heterogeneous microscale flows, applications to digital rock physics and mucociliary clearance. *ESAIM: Mathematical Modelling and Numerical Analysis*, 53(4):1083–1124, 2019. (Cited on pages 24 and 69.)

[262] Javier E. Santos, Duo Xu, Honggeun Jo, Christopher J. Landry, Maša Prodanović, and Michael J. Pyrcz. PoreFlow-Net: A 3D convolutional neural network to predict fluid flow through porous media. *Advances in Water Resources*, 138:103539, 2020. (Cited on pages 11 and 173.)

[263] Javier E. Santos, Ying Yin, Honggeun Jo, Wen Pan, Qinjun Kang, Hari S. Viswanathan, et al. Computationally Efficient Multiscale Neural Networks Applied to Fluid Flow in

Complex 3D Porous Media. *Transport in Porous Media*, 140(1):241–272, 2021. (Cited on page 134.)

[264] Nishank Saxena, Ronny Hofmann, Faruk O. Alpak, Jesse Dietderich, Sander Hunter, and Ruarri J. Day-Stirrat. Effect of image segmentation and voxel size on micro-CT computed effective transport & elastic properties. *Marine and Petroleum Geology*, 86:972–990, 2017. (Cited on page 59.)

[265] Hayden Schaeffer. Learning partial differential equations via data discovery and sparse optimization. *Proceedings of the Royal Society A: Mathematical, Physical and Engineering Sciences*, 473(2197):20160446, 2017. (Cited on pages 12 and 95.)

[266] Steffen Schlüter, Adrian Sheppard, Kendra Brown, and Dorthe Wildenschild. Image processing of multiphase images obtained via X-ray microtomography: A review. *Water Resources Research*, 50(4):3615–3639, 2014. (Cited on page 6.)

[267] Birte Schrader, Sylvain Reboux, and Ivo F. Sbalzarini. Discretization correction of general integral PSE Operators for particle methods. *Journal of Computational Physics*, 229(11):4159–4182, 2010. (Cited on pages 33, 35 and 172.)

[268] Birte Schrader, Sylvain Reboux, and Ivo F. Sbalzarini. Choosing the best kernel: Performance models for diffusion operators in particle methods. *SIAM Journal on Scientific Computing*, 34(3):A1607–A1634, 2012. (Cited on page 32.)

[269] Eleonora Secchi, Sophie Marbach, Antoine Niguès, Derek Stein, Alessandro Siria, and Lydéric Bocquet. Massive radius-dependent flow slippage in carbon nanotubes. *Nature*, 537(7619):210–213, 2016. (Cited on page 60.)

[270] Ozan Sener and Vladlen Koltun. Multi-Task Learning as Multi-Objective Optimization. In *Advances in Neural Information Processing Systems*, volume 31. Curran Associates, Inc., 2018. (Cited on page 95.)

[271] Reza Shams, Mohsen Masihi, Ramin Bozorgmehry Boozarjomehry, and Martin J. Blunt. A hybrid of statistical and conditional generative adversarial neural network approaches for reconstruction of 3D porous media (ST-CGAN). *Advances in Water Resources*, 158, 2021. (Cited on pages 12 and 134.)

[272] Adrian Sheppard and Masa Prodanovic. Network Generation Comparison Forum. https://www.digitalrocksportal.org/projects/16, 2015. (Cited on pages 50, 65 and 80.)

[273] Martina Siena, Gianlorenzo Bussetti, Chiara Recalcati, Monica Riva, Lamberto Duò, and Alberto Guadagnini. Statistical characterization of heterogeneous dissolution rates of calcite from in situ and real-time AFM imaging. *Transport in Porous Media*, 140(1):291–312, 2021. (Cited on pages 22 and 141.)

[274] Martina Siena and Monica Riva. Impact of geostatistical reconstruction approaches on model calibration for flow in highly heterogeneous aquifers. *Stochastic Environmental Research and Risk Assessment*, 34(10):1591–1606, 2020. (Cited on page 137.)

[275] Harpreet Singh. Representative elementary volume (REV) in spatio-temporal domain: A method to find REV for dynamic pores. *Journal of Earth Science*, 28(2):391–403, 2017. (Cited on page 4.)

[276] Pavel Smal, Philippe Gouze, and Olivier Rodriguez. An automatic segmentation algorithm for retrieving sub-resolution porosity from X-ray tomography images. *Journal of Petroleum Science and Engineering*, 166:198–207, 2018. (Cited on pages 5, 6 and 136.)

[277] Hwijae Son, Jin Woo Jang, Woo Jin Han, and Hyung Ju Hwang. Sobolev Training for Physics Informed Neural Networks. *arXiv*, 2021. arXiv:2101.08932. (Cited on page 102.)

[278] Cyprien Soulaine, Filip Gjetvaj, Charlotte Garing, Sophie Roman, Anna Russian, Philippe Gouze, et al. The Impact of Sub-Resolution Porosity of X-ray Microtomography Images on the Permeability. *Transport in Porous Media*, 113(1):227–243, 2016. (Cited on pages 8, 58, 140 and 166.)

[279] Cyprien Soulaine, Sophie Roman, Anthony Kovscek, and Hamdi A. Tchelepi. Mineral dissolution and wormholing from a pore-scale perspective. *Journal of Fluid Mechanics*,

827:457–483, 2017. (Cited on pages 4, 5, 9, 22, 24, 25, 26, 49, 51, 69, 142, 143, 145 and 150.)

[280] Cyprien Soulaine, Sophie Roman, Anthony Kovscek, and Hamdi A. Tchelepi. Pore-scale modelling of multiphase reactive flow: application to mineral dissolution with production of $CO_2$. *Journal of Fluid Mechanics*, 855:616–645, 2018. (Cited on pages xv, 3, 22, 25, 69 and 139.)

[281] Vitaliy Starchenko, Cameron J. Marra, and Anthony J. C. Ladd. Three-dimensional simulations of fracture dissolution. *Journal of Geophysical Research: Solid Earth*, 121(9):6421–6444, 2016. (Cited on page 69.)

[282] Carl I. Steefel, C. Anthony J. Appelo, Bhavna Arora, Diederik Jacques, Thomas Kalbacher, Olaf Kolditz, et al. Reactive transport codes for subsurface environmental simulation. *Computational Geosciences*, 19(3):445–478, 2015. (Cited on pages 10, 11, 23 and 46.)

[283] Carl I. Steefel et al. CrunchFlow. https://www.e-education.psu.edu/png550/node/743. (Cited on page 11.)

[284] Carl I. Steefel and Antonio C. Lasaga. Evolution of dissolution patterns. In *Chemical Modeling of Aqueous Systems II*, volume 416 of *ACS Symposium Series*, pages 212–225. American Chemical Society, 1990. (Cited on page 51.)

[285] Carl I. Steefel and Antonio C. Lasaga. A coupled model for transport of multiple chemical species and kinetic precipitation/dissolution reactions with application to reactive flow in single phase hydrothermal systems. *American Journal of Science*, 294(5):529–592, 1994. (Cited on pages 10, 46 and 140.)

[286] Carl I. Steefel, Sergi Molins, and David Trebotich. Pore scale processes associated with subsurface CO2 injection and sequestration. *Reviews in Mineralogy and Geochemistry*, 77(1):259–303, 2013. (Cited on pages 11 and 139.)

[287] John E. Stone, David Gohara, and Guochun Shi. OpenCL: A Parallel Programming Standard for Heterogeneous Computing Systems. *Computing in Science & Engineering*, 12(3):66–73, 2010. (Cited on page 40.)

[288] Gilbert Strang. On the construction and comparison of difference schemes. *SIAM Journal on Numerical Analysis*, 5(3):506–517, 1968. (Cited on page 32.)

[289] Kazuhiko Suga, Yasuhiro Matsumura, Yu Ashitaka, Satoshi Tominaga, and Masayuki Kaneda. Effects of wall permeability on turbulence. *International Journal of Heat and Fluid Flow*, 31(6):974–984, 2010. (Cited on page 60.)

[290] Luning Sun, Han Gao, Shaowu Pan, and Jian-Xun Wang. Surrogate modeling for fluid flows based on physics-constrained deep learning without simulation data. *Computer Methods in Applied Mechanics and Engineering*, 361:112732, 2020. (Cited on pages 95 and 132.)

[291] Luning Sun and Jian-Xun Wang. Physics-constrained bayesian neural network for fluid flow reconstruction with sparse and noisy data. *Theoretical and Applied Mechanics Letters*, 10(3):161–169, 2020. (Cited on page 102.)

[292] Shiliang Sun, Jing Zhao, Minghao Gu, and Shanhu Wang. Variational Hybrid Monte Carlo for Efficient Multi-Modal Data Sampling. *Entropy*, 25(4), 2023. (Cited on page 102.)

[293] Piotr Szymczak and Anthony J. C. Ladd. Wormhole formation in dissolving fractures. *Journal of Geophysical Research: Solid Earth*, 114(B6), 2009. (Cited on page 10.)

[294] Antoine Tambue, Gabriel J. Lord, and Sebastian Geiger. An exponential integrator for advection-dominated reactive transport in heterogeneous porous media. *Journal of Computational Physics*, 229(10):3957–3969, 2010. (Cited on page 172.)

[295] Hua Tan, Reza Masoodi, Krishna M. Pillai, et al. PoreFlow. https://sites.uwm.edu/porousmedia/developed-softwares/poreflow/. (Cited on page 9.)

[296] Alexandre M. Tartakovsky, Paul Meakin, Timothy D. Scheibe, and Rogene M. Eichler West. Simulations of reactive transport and precipitation with smoothed particle hydrodynamics. *Journal of Computational Physics*, 222(2):654–672, 2007. (Cited on page 9.)

[297] Alexandre M. Tartakovsky, Paul Meakin, Timothy D. Scheibe, and Brian D. Wood. A smoothed particle hydrodynamics model for reactive transport and mineral precipitation in porous and fractured porous media. *Water Resources Research*, 43(5), 2007. (Cited on pages 9, 53 and 172.)

[298] Machine Intelligence team at Google Brain. TensorFlow. https://www.tensorflow.org/?hl=fr. (Cited on page 15.)

[299] Moussa Tembely, Ali M. AlSumaiti, and Waleed S. Alameri. Machine and deep learning for estimating the permeability of complex carbonate rock from X-ray micro-computed tomography. *Energy Reports*, 7:1460–1472, 2021. (Cited on page 12.)

[300] Jonathan Tompson and Kristofer Schlachter. An introduction to the OpenCL programming model. *Person Education*, 49:31, 2012. (Cited on page 41.)

[301] Minh-Trieu Tran, Soo-Hyung Kim, Hyung-Jeong Yang, and Guee-Sang Lee. Multi-Task Learning for Medical Image Inpainting Based on Organ Boundary Awareness. *Applied Sciences*, 11(9), 2021. (Cited on page 125.)

[302] David Trebotich et al. Chombo-Crunch. https://www.alcf.anl.gov/science/projects/chombo-crunch-advanced-simulation-subsurface-flow-and-reactive-transport-processes. (Cited on page 11.)

[303] David Trebotich, Brian Van Straalen, Daniel T. Graves, and Philip Colella. Performance of embedded boundary methods for CFD with complex geometry. *Journal of Physics: Conference Series*, 125(1):012083, 2008. (Cited on page 9.)

[304] Michael C. Turk, Xingzhao Shi, Dave A. J. Gonyer, and Dipankar Roy. Chemical and Mechanical Aspects of a Co-Cu Planarization Scheme Based on an Alkaline Slurry Formulation. *ECS Journal of Solid State Science and Technology*, 5(2):P88, 2015. (Cited on page 45.)

[305] Francisco J. Valdes-Parada, J. Alberto Ochoa-Tapia, and Jose Alvarez-Ramirez. On the effective viscosity for the Darcy–Brinkman equation. *Physica A: Statistical Mechanics and its Applications*, 385(1):69–79, 2007. (Cited on page 8.)

[306] Remco van der Meer, Cornelis W. Oosterlee, and Anastasia Borovykh. Optimally weighted loss functions for solving PDEs with Neural Networks. *Journal of Computational and Applied Mathematics*, 405:113887, 2022. (Cited on page 111.)

[307] Pantelis R. Vlachas, Jaideep Pathak, Brian R. Hunt, Themistoklis P. Sapsis, Michelle Girvan, Edward Ott, et al. Backpropagation algorithms and Reservoir Computing in Recurrent Neural Networks for the forecasting of complex spatiotemporal dynamics. *Neural Networks*, 126:191–217, 2020. (Cited on page 95.)

[308] Nikolaos N. Vlassis and WaiChing Sun. Sobolev training of thermodynamic-informed neural networks for interpretable elasto-plasticity models with level set hardening. *Computer Methods in Applied Mechanics and Engineering*, 377:113695, 2021. (Cited on page 102.)

[309] Martin Vohralík and Soleiman Yousef. A simple a posteriori estimate on general polytopal meshes with applications to complex porous media flows. *Computer Methods in Applied Mechanics and Engineering*, 331:728–760, 2018. (Cited on page 8.)

[310] Lars von Wolff, Felix Weinhardt, Holger Class, Johannes Hommel, and Christian Rohde. Investigation of crystal growth in enzymatically induced calcite precipitation by microfluidic experimental methods and comparison with mathematical modeling. *Transport in Porous Media*, 137(2):327–343, 2021. (Cited on pages 49, 51 and 56.)

[311] Noriaki Wakao and Jeffrey M. Smith. Diffusion in catalyst pellets. *Chemical Engineering Science*, 17(11):825 – 834, 1962. (Cited on pages 26 and 145.)

[312] Sifan Wang, Yujun Teng, and Paris Perdikaris. Understanding and mitigating gradient flow pathologies in physics-informed neural networks. *SIAM Journal on Scientific Computing*, 43(5):A3055–A3081, 2021. (Cited on page 95.)

[313] Sifan Wang, Xinling Yu, and Paris Perdikaris. When and why PINNs fail to train: a neural tangent kernel perspective. *Journal of Computational Physics*, 449:110768, 2022. (Cited on page 95.)

[314] Ying Da Wang, Martin J. Blunt, Ryan T. Armstrong, and Peyman Mostaghimi. Deep learning in pore scale imaging and modeling. *Earth-Science Reviews*, 215:103555, 2021. (Cited on page 137.)

[315] Henry Weller, Hrvoje Jasak, et al. OpenFOAM. https://www.openfoam.com/. (Cited on page 9.)

[316] Stephen Whitaker. Theory and applications of transport in porous media: the method of volume averaging. *The Netherlands: Kluwer Academic Publishers*, page 81, 1999. (Cited on page 3.)

[317] Marcus Wigand, James W. Carey, Hartmut Schütt, Eric Spangenberg, and Joerg. Erzinger. Geochemical effects of CO2 sequestration in sandstones under simulated in situ conditions of deep saline aquifers. *Applied Geochemistry*, 23(9):2735–2745, 2008. (Cited on pages 2 and 46.)

[318] Dorthe Wildenschild and Adrian P. Sheppard. X-ray imaging and analysis techniques for quantifying pore-scale structure and processes in subsurface porous medium systems. *Advances in Water Resources*, 51:217–246, 2013. (Cited on pages 6 and 59.)

[319] Andrew G Wilson and Pavel Izmailov. Bayesian Deep Learning and a Probabilistic Perspective of Generalization. In *Advances in Neural Information Processing Systems*, volume 33, pages 4697–4708. Curran Associates, Inc., 2020. (Cited on pages 95, 98, 114, 153 and 155.)

[320] Mariëtte Wolthers, Gernot Nehrke, Jon Petter Gustafsson, and Philippe Van Cappellen. Calcite growth kinetics: Modeling the effect of solution stoichiometry. *Geochimica et Cosmochimica Acta*, 77:121–134, 2012. (Cited on pages 11, 23, 47, 48, 51 and 56.)

[321] Brian D. Wood, Karen Radakovich, and Fabrice Golfier. Effective reaction at a fluid-solid interface: Applications to biotransformation in porous media. *Advances in water resources*, 30(6-7):1630–1647, 2007. (Cited on page 25.)

[322] Anqi Wu, Sebastian Nowozin, Edward Meeds, Richard E. Turner, José Miguel Hernández-Lobato, and Alexander L. Gaunt. Deterministic Variational Inference for Robust Bayesian Neural Networks. In *7th International Conference on Learning Representations*, 2019. (Cited on pages 14, 15 and 98.)

[323] Qingrong Xiong, Todor G. Baychev, and Andrey P. Jivkov. Review of pore network modelling of porous media: Experimental characterisations, network constructions and applications to reactive transport. *Journal of Contaminant Hydrology*, 192:101–117, 2016. (Cited on page 7.)

[324] Sheng Xu and Z. Jane Wang. An immersed interface method for simulating the interaction of a fluid with moving boundaries. *Journal of Computational Physics*, 216(2):454–493, 2006. (Cited on page 9.)

[325] Liang Yan and Tao Zhou. Adaptive multi-fidelity polynomial chaos approach to Bayesian inference in inverse problems. *Journal of Computational Physics*, 381:110–128, 2019. (Cited on pages 14 and 96.)

[326] Liang Yan and Tao Zhou. An Adaptive Surrogate Modeling Based on Deep Neural Networks for Large-Scale Bayesian Inverse Problems. *Communications in Computational Physics*, 28(5):2180–2205, 2020. (Cited on pages 14 and 96.)

[327] Fengchang Yang, Andrew G. Stack, and Vitalii Starchenko. Micro-continuum approach for mineral precipitation. *Scientific Reports*, 11(1):3495, 2021. (Cited on pages 11 and 53.)

[328] Liu Yang, Xuhui Meng, and George Em Karniadakis. B-PINNs: Bayesian physics-informed neural networks for forward and inverse PDE problems with noisy data. *Journal of Computational Physics*, 425:109913, 2021. (Cited on pages xviii, 14, 95, 97, 98, 119, 132, 137 and 155.)

[329] Yibo Yang and Paris Perdikaris. Adversarial uncertainty quantification in physics-informed neural networks. *Journal of Computational Physics*, 394:136–152, 2019. (Cited on page 95.)

[330] Yongfei Yang, Fugui Liu, Jun Yao, Stefan Iglauer, Mozhdeh Sajjadi, Kai Zhang, et al. Multi-scale reconstruction of porous media from low-resolution core images using conditional generative adversarial networks. *Journal of Natural Gas Science and Engineering*, 99:104411, 2022. (Cited on pages 12, 94, 140 and 166.)

[331] Jiayu Yao, Weiwei Pan, Soumya Shubhra Ghosh, and Finale Doshi-Velez. Quality of Uncertainty Quantification for Bayesian Neural Network Inference. *arXiv*, 2019. arXiv:1906.09686. (Cited on page 128.)

[332] Ting Yao, Beatrice A. Baudet, and Sérgio D. N. Lourenço. Quantification of the surface roughness of quartz sand using optical interferometry. *Meccanica*, 54(4-5):741–748, 2018. (Cited on page 76.)

[333] Christophe Ybert, Catherine Barentin, Cécile Cottin-Bizonne, Pierre Joseph, and Lydéric Bocquet. Achieving large slip with superhydrophobic surfaces: Scaling laws for generic geometries. *Physics of fluids*, 19(12):123601, 2007. (Cited on pages 60 and 76.)

[334] James J. De Yoreo and Peter G. Vekilov. *Principles of Crystal Nucleation and Growth*, pages 57–94. De Gruyter, 2003. (Cited on page 47.)

[335] Wentao Yuan, Qingtian Zhu, Xiangyue Liu, Yikang Ding, Haotian Zhang, and Chi Zhang. Sobolev Training for Implicit Neural Representations with Approximated Image Derivatives. In *Computer Vision – ECCV 2022*, volume 13675, pages 72–88. Springer Nature Switzerland, 2022. (Cited on page 102.)

[336] HouLin Zhang, Hao Yu, XinHeng Yuan, HengYu Xu, Marembo Micheal, JiaNing Zhang, et al. Permeability prediction of low-resolution porous media images using autoencoder-based convolutional neural network. *Journal of Petroleum Science and Engineering*, 208:109589, 2022. (Cited on page 11.)

[337] Yulai Zhang, Peyman Mostaghimi, and Ryan T. Armstrong. On the challenges of greyscale-based quantifications using X-ray computed microtomography. *Journal of Microscopy*, 275(2):82–96, 2019. (Cited on pages 136 and 141.)

[338] Zeyu Zhang, Sabine Kruschwitz, Andreas Weller, and Matthias Halisch. Enhanced pore space analysis by use of $\mu$-CT, MIP, NMR, and SIP. *Solid Earth*, 9:1225–1238, 2018. (Cited on page 79.)

[339] Lei Zhao, Heng Li, Jin Meng, and Dongxiao Zhang. Efficient uncertainty quantification for permeability of three-dimensional porous media through image analysis and pore-scale simulations. *Physical Review E*, 102:023308, 2020. (Cited on page 58.)

[340] Qiang Zheng, Lingzao Zeng, and George Em Karniadakis. Physics-informed semantic inpainting: Application to geostatistical modeling. *Journal of Computational Physics*, 419:109676, 2020. (Cited on page 126.)

[341] Li Zhuang, Hyu-Soung Shin, Sun Yeom, Chuyen Ngoc Pham, and Young-Jae Kim. A novel method for estimating subresolution porosity from CT images and its application to homogeneity evaluation of porous media. *Scientific Reports*, 12(1):16229, 2022. (Cited on pages 94 and 140.)

[342] B.F. Zwick, G.C. Bourantas, F. Alkhatib, A. Wittek, and K. Miller. Recovery by discretization corrected particle strength exchange (DC PSE) operators. *Applied Mathematics and Computation*, 448:127923, 2023. (Cited on page 35.)

UNIVERSITE DE PAU ET DES PAYS DE L'ADOUR

# ECOLE DOCTORALE 211 SEA

SCIENCES EXACTES ET LEURS APPLICATIONS

**Laboratory of Mathematics and their Applications of Pau, UMR CNRS-UPPA 5142**

UNIVERSITÉ DE PAU ET DES PAYS DE L'ADOUR

e2s UPPA

energy environment solutions